Geofluids

Geomechanics of Shale Oil Reservoirs

Lead Guest Editor: Bing Hou
Guest Editors: Jihui Ding, Amer Syed, Yukie Tanino, and Jihoon Wang

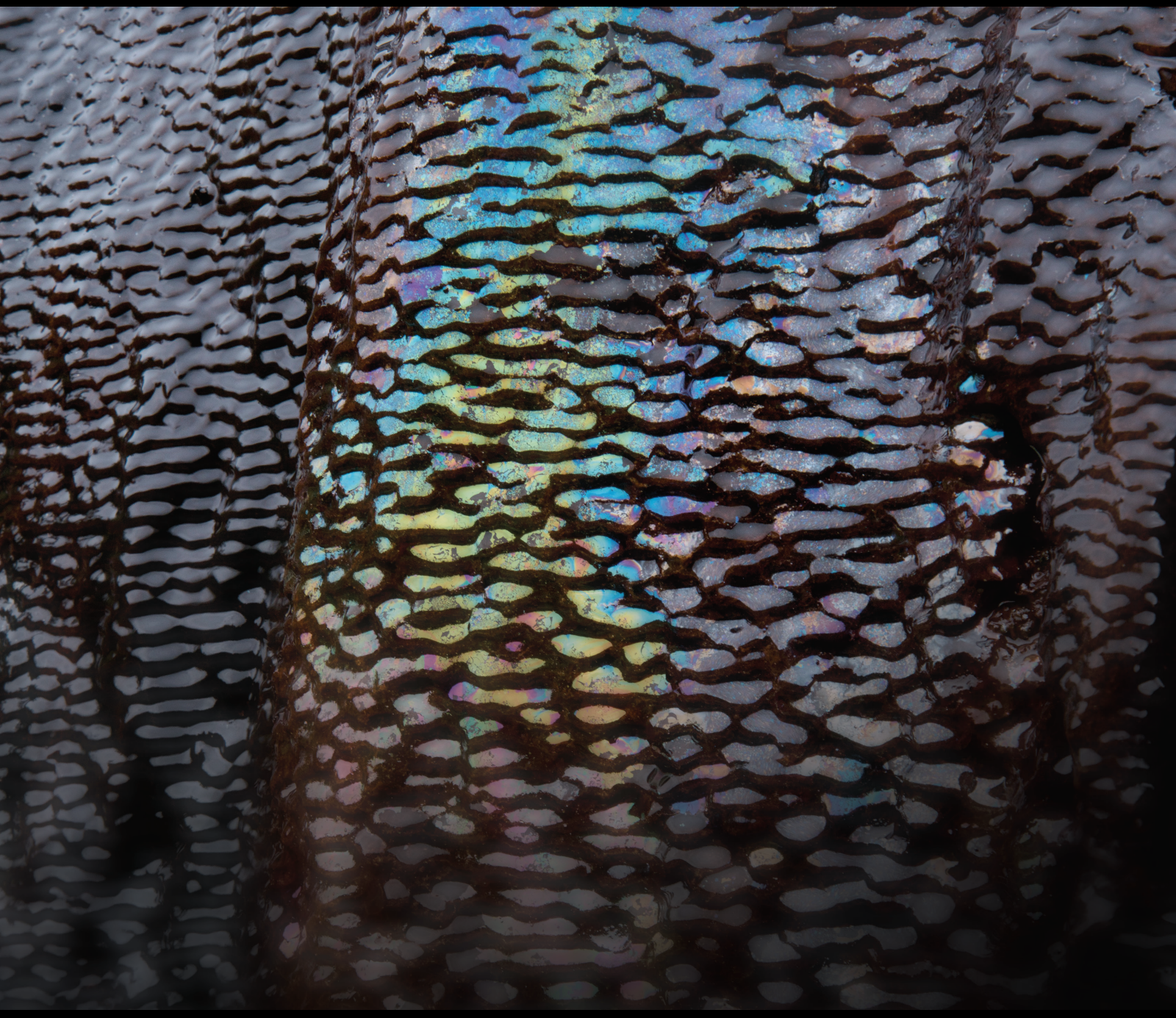

Geomechanics of Shale Oil Reservoirs

Geofluids

Geomechanics of Shale Oil Reservoirs

Lead Guest Editor: Bing Hou
Guest Editors: Jihui Ding, Amer Syed, Yukie Tanino, and Jihoon Wang

Contents

Hindawi
Geofluids
Volume 2023, Article ID 4030804, 13 pages
https://doi.org/10.1155/2023/4030804

Research Article

Porothermoelastic Response of a Borehole in Fluid-Saturated Medium Subjected to Thermal Osmosis Effect

Hai Lin,[1,2] **Jingen Deng**,[1] **Xiaocheng Zhang**,[2] **and Jiajia Gao**[3]

[1]*State Key Laboratory of Petroleum Resource & Prospecting, China University of Petroleum, Beijing 102249, China*
[2]*CNOOC China Limited, Tianjin Branch, Tianjin 300459, China*
[3]*Petroleum Engineering School, Southwest Petroleum University, Chengdu 610500, China*

Correspondence should be addressed to Jingen Deng; dengjingen@126.com

Received 19 October 2021; Revised 1 March 2022; Accepted 6 April 2023; Published 22 May 2023

Academic Editor: Basim Abu-Jdayil

With the thermo-hydro-mechanical coupling process considered, this paper derives a set of analytical porothermoelastic solutions to field variables including the stress, displacement, and pore pressure fields to evaluate the wellbore stability around a vertical borehole drilled through an isotropic porous rock. The thermal effect on the wellbore stability of the low-permeability saturated rock also introduces the thermal osmosis term. The wellbore problem is decomposed into axisymmetric and deviatoric loading cases considering the borehole subjected to a nonhydrostatic stress field. It obtains the time-dependent distributions of field variables by performing the inversion technique for Laplace transforms to the porothermoelastic solutions in the Laplace domain. The results suggest that the thermal osmosis effect should not be neglected on the premise that a lower permeability porous rock is characterized by the substantially large thermal osmotic coefficient and the small thermal diffusivity values. The case that the thermal osmosis effect reduces the undrained loading effect leads to the decrease of the mean shear stress that is determined by the effective maximum and minimum stress around a borehole, since, and accordingly contributes to the wellbore stability to resist the shear failure.

1. Introduction

When the deep-water and unconventional oil and gas resources are drilled in the high-temperature and high-pressure (HTHP) block, drilling a borehole experiences a large temperature difference between the drilling mud and formation fluid. The coupled thermo-hydraulic-mechanical (THM) effect of fluid-saturated porous media inevitably implicates time-dependent wellbore instability issues, since the thermal loading progressively reestablishes the induced stresses and pore pressure around a wellbore [1–23]. Moreover, the poroelastic effect associated with undrained loading [24, 25] also contributes to the remodifications of field variables after instantaneously drilling a borehole, especially for low-permeability porous medium.

Detournay and Cheng [24] adopted the field variables including displacement, stress, and pore pressure around a borehole to discuss the coupled hydromechanical effect. Three different modes are used to obtain the complete solution of field variables. Mode 1 is a classical elastic case and not related to the coupled issue. The content of mode 2 is purely pressure radial (or axisymmetric) diffusion around a borehole and is attributed to the partially coupled process. It means that the pore pressure induces the occurrence of stresses and displacement whereas the opposite process does not take place. Mode 3 is a fully coupled process. The pore pressure perturbation leads to the induced stresses and solid displacements; accordingly, the stress perturbation also induces a pore pressure built-up regime near the borehole wall due to the undrained loading. The undrained loading gives rise to the occurrence of the excess pore pressure case for low-permeability porous rock. This is because that the pore fluid is not allowed to have enough time to escape the current pore space delimited by the solid pore wall, when the undrained loading is quickly applied to the porous rock. The pore fluid naturally suffers the undrained loading effect and causes an excess pore pressure to generate in the pore-space. It refers the excess pore pressure case to as an

undrained state subjected by the low-permeability porous rock. This phenomenon exactly explains the poroelastic effect to embody the coupled solid deformation and fluid flow in the porous medium.

The thermal effect introduced by the coupled THM process is embodied in the radial diffusion problem and induces pore pressure and stresses around a wellbore. That is to say, the thermal effect alone appears in a developed mode 2 that differs from the aforementioned study of Detournay and Cheng [24] and renders the pore pressure diffusion to depend on the temperature variation [1–23]. Besides, the thermal osmosis effect is observed by conducting the experiment [26–31] or discussed in studies [6–8, 19–23].

Thermal osmosis effect accounts for the contribution of temperature gradient on the fluid flux and becomes significant for expected temperature gradients in the case of the clay barriers of waste disposal with extremely low hydraulic conductivity (10^{-10} and 10^{-14} m/s) [6, 29]. The thermal osmosis effect resembles the Sorêt effect in a chemical solution that causes a chemical flux proportional to the temperature gradient [2]. Besides, the indirect thermal osmosis flow may significantly contribute to mass transfer induced in semi-impermeable clays compared to the direct Darcian flow [28]. The studies [19–23] further support the viewpoint of Ghassemi and Diek [8]. Namely, a case associated with a substantially large thermoosmotic coefficient and a larger temperature gradient significantly facilitates the thermal osmosis effect to modify the change in pore pressure near a borehole. Both positive and negative values of the thermal osmosis coefficient K^{T} are possibly observed in rocks [26]. In the case of $K^{\mathrm{T}} < 0$, the osmotic flow direction is from warmer to cooler, while in the case of $K^{\mathrm{T}} > 0$, the flow is from cooler to warmer [31]. Nevertheless, the flow in both directions in laboratory tests is using compacted clays [27]. The absolute value of thermal osmotic coefficient K^{T} ranges from 10^{-14} to $10^{-10}\,\mathrm{m^2/(s{\cdot}K)}$ for different porous media [30].

Several relevant studies [2, 6, 7, 9, 10, 15, 16] neglected the nonlinear convective heat transfer term that couples temperature with pore pressure to obtain the engineering-oriented analytical linear-porothermoelastic solutions. However, this partially decoupled operation alone holds for low-permeability rocks [9]. Besides, the abovementioned porothermoelastic analytical solutions neglect the thermal osmosis effect [3–5, 10–16].

The present paper newly formulates coupled porothermoelastic solution with thermal osmosis for a vertical borehole in a nonhydrostatic stress field. Accordingly, the results from this paper could provide theoretical guidance for effectively dealing with the complicated issues during drilling through the low permeability and low porosity formation.

2. General Formulations

The governing equations in the present model are presented as follows.

2.1. Constitutive Equations. Introducing the thermal effect into the work of Detournay and Cheng [32] or extending the study of Zimmerman [33], the constitutive Equations (1) and (2) take the following forms to accurately show the coupled thermo-hydro-mechanical behavior when the isotropic fluid saturated porous medium deforms in the elastic state. Besides, the constitutive Equations (1) and (2) are written as that the positive stress denotes compression in line with the rock mechanics convention.

$$\sigma_{ij} = 2G\varepsilon_{ij} + \lambda\varepsilon + \alpha p\delta_{ij} + \beta^s T\delta_{ij}, \tag{1}$$

$$\zeta = -\alpha\varepsilon + \frac{p}{M} - \beta^{fs}T. \tag{2}$$

The abovementioned equations include total stresses tensor σ_{ij}, pore pressure p, temperature variations T, strain tensor for the solid rock ε_{ij}, volumetric strain $\varepsilon = \varepsilon_{ii}$, and the variation of fluid content per unit reference volume ζ. The material constants include drained Poisson's ratio ν, rock shear modulus G, and the Lame constant λ defined by $\lambda = 2G\nu/(1-2\nu)$. δ_{ij} is the Kronecker delta. Besides, Biot coefficient α and modulus M are written as follows:

$$\alpha = 1 - \frac{K}{K_s}, \frac{1}{M} = \frac{\alpha - \phi}{K_s} + \frac{\phi}{K_f}, \tag{3}$$

where the rock bulk modulus K is defined by $3K = 2G(1+\nu)/(1-2\nu)$. K_s and K_f are the bulk modulus of solid grain and fluid, respectively. ϕ is rock intrinsic porosity.

The thermic coefficients related to solid skeleton β^s and solid-fluid β^{fs} are read as follows [11]:

$$\begin{aligned} \beta^s &= 3K\alpha^s, \\ \beta^{fs} &= 3\alpha\alpha^s + \phi\left(\alpha^f - 3\alpha^s\right), \end{aligned} \tag{4}$$

where the symbols α^s and α^f are the linear expansion coefficient for solid matrix and volumetric expansion coefficient for fluid, respectively.

2.2. Field Equations. In the case of the infinitely long borehole and constant boundary condition along the borehole axis direction, both fluid and heat flux components will disappear along the direction of the borehole axis [11]. With Equation (2) and thermal osmosis term considered into fluid flux [8], the fluid diffusive equation for weakly compressive and thermally expansible fluid reads as follows:

$$\frac{1}{M}\frac{\partial p}{\partial t} - \alpha\frac{\partial \varepsilon}{\partial t} - \beta^{fs}\frac{\partial T}{\partial t} - \kappa\nabla^2 p + K^{\mathrm{T}}\nabla^2 T = 0, \tag{5}$$

where the permeability coefficient κ is expressed as $\kappa = k/\mu$ in which k is the intrinsic permeability tensor and μ is the fluid viscosity. K^{T} denotes the thermal osmosis coefficient. The linear differential operator ∇^2 is written as follows:

$$\nabla^2 = \frac{1}{r}\frac{\partial}{\partial r}\left(r\frac{\partial}{\partial r}\right) + \frac{\partial^2}{r^2\partial\theta^2}. \tag{6}$$

Provided that the assumption of instantaneous local temperature equilibrium holds, the heat diffusive field equation takes the form of Wang and Papamichos [4]:

$$\rho_m c_m \frac{\partial T}{\partial t} - k^{\mathrm{T}}\nabla^2 T = 0, \tag{7}$$

where ρ_m and c_m, respectively, denote the total mass density and specific heat capacity, and k^{T} is the thermal conductivity of porous rock. It holds that the effect of the strain and pore pressure on the temperature is commonly ignored [23, 33] considering the strain and coupled parameters with much smaller values. Gao et al. [19] concluded that the thermal filtration effect depending on the pressure gradient Equation (6) has a weak influence on the temperature diffusion, such that it is also ignored.

3. Borehole Problem Description and the Solution

3.1. Borehole Problem Description. A circular vertical borehole is drilled in a porous rock formation subjected to a non-hydrostatic horizontal in situ stress field; see Figure 1. It is assumed that one of the three in situ principal stresses is parallel to the borehole axis, and x - and y -axes correspond to the directions of two other in situ principal stresses.

It follows that the total stresses acting on a circular boundary are given by the following:

$$\begin{aligned} \sigma_r &= \sigma_m + \sigma_d \cos 2\theta, \\ \sigma_\theta &= \sigma_m - \sigma_d \cos 2\theta, \\ \tau_{r\theta} &= -\sigma_d \sin 2\theta, \end{aligned} \tag{8}$$

with the mean stress σ_m and shear stress σ_d are, respectively, defined by $\sigma_m = (\sigma_H + \sigma_h)/2$ and $\sigma_d = (\sigma_H - \sigma_h)/2$, in which the symbols σ_H and σ_h, respectively, are the maximum and minimum horizontal in situ stress.

The generalized plane strain assumption may be appropriate to extrapolate the solutions under a two-dimensional case to a general three-dimensional one, assuming that the geomechanics is characterized by geometries in which boundary conditions are constant along the direction of the infinitely long borehole axis [11]. In line with the loading decomposition scheme proposed by Abousleiman and Cui [34], this problem is disassembled into two separate resolved subproblems, since the antiplane shear stresses disappear in a vertical borehole. Two subproblems include a modified poroelastic plane strain problem (Problem I) and an elastic unaxial problem (Problem II). Finally, the principle of superposition to consider the linearity problem is employed to obtain the complete solutions.

3.2. Solution to Modified Poroelastic Plane Stain Problem. The boundary conditions including stress components, pore pressure, and temperature acting at borehole wall after instant drilling are described as for Problem I:

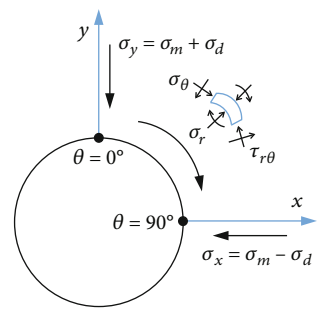

Figure 1: Schematic of borehole stress analysis.

$$\Delta\sigma_r|_{r=r_w} = p_w - [\sigma_m + \sigma_d \cos 2\theta], \tag{9a}$$

$$\Delta\tau_{r\theta}|_{r=r_w} = \sigma_d \sin 2\theta, \tag{9b}$$

$$\Delta p|_{r=r_w} = p_w - p_0, \tag{9c}$$

$$\Delta T|_{r=r_w} = T_w - T_0, \tag{9d}$$

where p_w is the wellbore pressure. T_w and T_0, respectively, are the wellbore fluid temperature and the formation temperature.

Furthermore, two separate boundary conditions at the borehole wall for each of the loading modes may be defined as follows, respectively.

(i) Axisymmetric loading:

$$\Delta\sigma_r^{(a)}\Big|_{r=r_w} = p_w - \sigma_m, \tag{10a}$$

$$\Delta\tau_{r\theta}^{(a)}\Big|_{r=r_w} = 0, \tag{10b}$$

$$\Delta p^{(a)}\Big|_{r=r_w} = p_w - p_0, \tag{10c}$$

$$\Delta T|_{r=r_w} = T_w - T_0. \tag{10d}$$

(ii) Deviatoric loading:

$$\Delta\sigma_r^{(d)}\Big|_{r=r_w} = -\sigma_d \cos 2\theta, \tag{11a}$$

$$\Delta\tau_{r\theta}^{(d)}\Big|_{r=r_w} = \sigma_d \sin 2\theta, \tag{11b}$$

$$\Delta p^{(d)}\Big|_{r=r_w} = 0. \tag{11c}$$

The boundary conditions of this problem imposed at the far field, i.e., $r \longrightarrow \infty$, are expressed as follows:

$$\begin{aligned}
\sigma_r &= \sigma_m + \sigma_d \cos 2\theta,\\
\tau_{r\theta} &= -\sigma_d \sin 2\theta,\\
\sigma_z &= 2\nu\sigma_m + (1-2\nu)(\alpha p_0 + \beta^s T_0),\\
p &= p_0,\\
T &= T_0.
\end{aligned} \tag{12}$$

Introducing the rotation of displacement field ω, the equilibrium equation ($\sigma_{ij'j} = 0,\ i, j \in (r, \theta)$) is written in terms of volumetric strain $\varepsilon(\varepsilon = \varepsilon_r + \varepsilon_\theta)$, variation of fluid content ζ, and temperature T:

$$\begin{aligned}
&\left(\lambda + 2G + \alpha^2 M\right)\frac{\partial \varepsilon}{\partial r} - G\frac{1}{r}\frac{\partial \omega}{\partial \theta} + \alpha M \frac{\partial \zeta}{\partial r}\\
&\quad + \left(\beta^s + \alpha M \beta^{sf}\right)\frac{\partial T}{\partial r} = 0,
\end{aligned} \tag{13}$$

$$\begin{aligned}
&\left(\lambda + 2G + \alpha^2 M\right)\frac{1}{r}\frac{\partial \varepsilon}{\partial \theta} + G\frac{\partial \omega}{\partial r} + \alpha M \frac{1}{r}\frac{\partial \zeta}{\partial \theta}\\
&\quad + \left(\beta^s + \alpha M \beta^{sf}\right)\frac{1}{r}\frac{\partial T}{\partial \theta} = 0,
\end{aligned} \tag{14}$$

where ε and ω, respectively, are defined by the following:

$$\varepsilon = \frac{1}{r}\frac{\partial}{\partial r}(r u_r) + \frac{\partial u_\theta}{r \partial \theta}, \tag{15}$$

$$\omega = -\frac{1}{r}\frac{\partial u_r}{\partial \theta} + \frac{\partial}{r \partial r}(r u_\theta). \tag{16}$$

Furthermore, the diffusive equation in terms of the variation of fluid content ζ is written as an alternative form, through combining Equations (2) and (5) with the transforms to Equations (13) and (14).

$$\frac{\partial \zeta}{\partial t} - c^* \nabla^2 \left[\zeta + \left(\bar{c}^* - \frac{K^{\mathrm{T}}}{c^*}\right) T\right] = 0, \tag{17}$$

where

$$\begin{aligned}
c^* &= \frac{\kappa M(\lambda + 2G)}{\alpha^2 M + (\lambda + 2G)},\\
\bar{c}^* &= \beta^{fs} - \frac{\alpha \beta^s}{\lambda + 2G}.
\end{aligned} \tag{18}$$

The boundary conditions in Equations ((10a)), ((10b)), ((10c)), and ((10d)) and ((11a)), ((11b)), and ((11c)) suggest the dependence of the displacement, stress, pore pressure, and temperature upon the polar angle could be sought of which has the following form [35]:

$$\left(\tilde{\zeta}, \tilde{\varepsilon}, \tilde{u}_r, \tilde{\sigma}_r, \tilde{\sigma}_\theta, \tilde{p}, \tilde{T}\right) = \left(\tilde{Z}, \tilde{\Xi}, \tilde{U}_r, \tilde{S}_r, \tilde{S}_\theta, \tilde{P}, \tilde{H}\right) \cos m\theta, \tag{19a}$$

$$\left(\tilde{\omega}, \tilde{u}_\theta, \tilde{\tau}_{r\theta}\right) = \left(\tilde{W}, \tilde{U}_\theta, \tilde{S}_{r\theta}\right) \sin m\theta, \tag{19b}$$

with $m = 0$ for axisymmetric loading and $m = 2$ for deviatoric loading. $\tilde{Z}$, $\tilde{\Xi}$, $\tilde{U}_r$, $\tilde{U}_\theta$, $\tilde{S}_r$, $\tilde{S}_\theta$, $\tilde{S}_{r\theta}$, $\tilde{P}$, $\tilde{W}$, and $\tilde{H}$ are the functions of time t and radial distance r only. Besides, the sign"~" represents the Laplace integral transforms with respect to t and is defined by the following:

$$\tilde{f}(r, s) = \int_0^\infty f(r, t)\, e^{-st} dt, \tag{20}$$

where s is a parameter for the Laplace transform.

3.2.1. Solutions to Axisymmetric Loading

(1) Solution for Temperature. Under axis-symmetric thermal loading, Equation (8) is solved by the following initial and boundary conditions in the Laplace transformed forms:

$$\frac{\tilde{T}^{(a)}(r_w, t)}{T_m - T_0} = \frac{1}{s} \quad \frac{\tilde{T}^{(a)}(r, 0)}{T_m - T_0} = 0 \quad \frac{\tilde{T}^{(a)}(\infty, t)}{T_m - T_0} = 0, \tag{21}$$

and therefore reads as follows:

$$\tilde{T}^{(a)} = m_0(s)\frac{K_0(\xi_T)}{K_0(\beta_T)}, \tag{22}$$

where

$$\begin{aligned}
m_0(s) &= \frac{T_m - T_0}{s},\\
\beta_T &= r_w \sqrt{\frac{s}{c_h}},\\
\xi_T &= r\sqrt{\frac{s}{c_h}},\\
c_h &= \frac{k_T}{\rho_m c_m}.
\end{aligned} \tag{23}$$

$K_n(xr)$ is the modified Bessel function of the second kind of order "n".

(2) Solutions for Pore Pressure, Radial Displacement, and Stresses. Taking into consideration of Equation (2), a simplified uncoupled pore pressure diffusion expression could be written as Equation (24) when the assumption that displacement field is irrotational in semi-infinite domain holds the following:

$$\frac{\partial p}{\partial t} - c^* \left[\nabla_r^2 p + \frac{1}{\kappa}\left(\bar{c}^* \frac{\partial T}{\partial t} - K^{\mathrm{T}} \nabla_r^2 T\right)\right] = 0, \tag{24}$$

in which

$$\nabla_r^2 = \frac{1}{r}\frac{\partial}{\partial r}\left(r\frac{\partial}{\partial r}\right). \tag{25}$$

Equation (24) may be solved by the following Laplace transformed initial and boundary conditions:

$$\frac{\tilde{p}(r_w,t)}{p_w-p_0}=\frac{1}{s}\quad \frac{\tilde{p}(r,0)}{p_w-p_0}=0\quad \frac{\tilde{p}(\infty,t)}{p_w-p_0}=0, \tag{26}$$

and thus, the solution of the pore pressure in the Laplace domain reads under axis-symmetric loading

$$\tilde{P}^{(a)}=\frac{p_w-p_0}{s}\frac{K_0(\xi)}{K_0(\beta)}-\frac{c^*}{\kappa}\left[\frac{\bar{c}^*c_T-K^{\mathrm{T}}}{c_T-c^*}m_0(s)\cdot\left(\frac{K_0(\xi)}{K_0(\beta)}-\frac{K_0(\xi_T)}{K_0(\beta_T)}\right)\right], \tag{27}$$

where

$$\xi=r\sqrt{\frac{s}{c^*}},\qquad \beta=r_w\sqrt{\frac{s}{c^*}}. \tag{28}$$

One combines Equation (1) with Equation (15) and takes into consideration the Laplace transformed boundary condition (Equation (10a)), and thus, the radial displacement and stresses for axisymmetric loading are given as follows:

$$\frac{2G\tilde{u}_r^{(a)}}{r_w}=\frac{1-2\nu}{1-\nu}\left\{n_0(s)\left[\frac{K_1(\xi)}{\beta K_0(\beta)}-\frac{r_w}{r}\frac{K_1(\beta)}{\beta K_0(\beta)}\right]+n_1(s)\left[\frac{K_1(\xi_T)}{\beta_T K_0(\beta_T)}-\frac{r_w}{r}\frac{K_1(\beta_T)}{\beta_T K_0(\beta_T)}\right]\right\}-\frac{p_w-\sigma_m}{s}\frac{r_w}{r}, \tag{29a}$$

$$\tilde{\sigma}_r^{(a)}=-\frac{1-2\nu}{1-\nu}\left\{n_0(s)\left[\frac{r_w}{r}\frac{K_1(\xi)}{\beta K_0(\beta)}-\frac{r_w^2}{r^2}\frac{K_1(\beta)}{\beta K_0(\beta)}\right]+n_1(s)\left[\frac{r_w}{r}\frac{K_1(\xi_T)}{\beta_T K_0(\beta_T)}-\frac{r_w^2}{r^2}\frac{K_1(\beta_T)}{\beta_T K_0(\beta_T)}\right]\right\}+\frac{p_w-\sigma_m}{s}\frac{r_w^2}{r^2}, \tag{29b}$$

$$\tilde{\sigma}_\theta^{(a)}=\frac{1-2\nu}{1-\nu}\left\{n_0(s)\left[\frac{r_w}{r}\frac{K_1(\xi)}{\beta K_0(\beta)}-\frac{r_w^2}{r^2}\frac{K_1(\beta)}{\beta K_0(\beta)}+\frac{K_0(\xi)}{K_0(\beta)}\right]+n_1(s)\left[\frac{r_w}{r}\frac{K_1(\xi_T)}{\beta_T K_0(\beta_T)}-\frac{r_w^2}{r^2}\frac{K_1(\beta_T)}{\beta_T K_0(\beta_T)}+\frac{K_0(\xi_T)}{K_0(\beta_T)}\right]\right\}-\frac{p_w-\sigma_m}{s}\frac{r_w^2}{r^2}, \tag{29c}$$

where

$$n_0(s)=\alpha\left[\frac{p_w-p_0}{s}-\frac{c^*}{\kappa}\frac{\bar{c}^*c_T-K^{\mathrm{T}}}{c_T-c^*}m_0(s)\right], \tag{30a}$$

$$n_1(s)=m_0(s)\left(\frac{c^*}{\kappa}\frac{\bar{c}^*c_T-K^{\mathrm{T}}}{c_T-c^*}\alpha+\beta^s\right). \tag{30b}$$

3.2.2. Solutions for Pore Pressure, Stresses, and Displacements under Deviatoric Loading. Considering Equation (18), the transforms to Equations (13), (14), and (17) while omitting the terms related to thermal effect result in the following equations in the Laplace transform domain:

$$\chi\frac{\tilde{\Xi}}{r}-\frac{1}{4}\frac{d\tilde{W}}{dr}+\frac{\alpha M}{2G}\frac{\tilde{Z}}{r}=0, \tag{31a}$$

$$\left(r^2\frac{d^2}{dr^2}+r\frac{d}{dr}-4\right)\tilde{W}=0, \tag{31b}$$

$$\left[r^2\frac{d^2}{dr^2}+r\frac{d}{dr}-\left(\frac{s}{c^*}r^2+4\right)\right]\tilde{Z}=0, \tag{31c}$$

in which $\chi=(1/2G)(\lambda+2G+\alpha^2M)$. Meanwhile, Equations (15) and (16) can degenerate to a nonhomogeneous linear differential equation set of order 2 with respect to constant coefficient.

$$\frac{d}{rdr}\left(r\tilde{U}_r^{(d)}\right)+2\frac{\tilde{U}_\theta^{(d)}}{r}=\tilde{\Xi}, \tag{32}$$

$$\frac{d}{rdr}\left(r\tilde{U}_\theta^{(d)}\right)+2\frac{\tilde{U}_r^{(d)}}{r}=\tilde{W}. \tag{33}$$

Noted that the solution regarding Equations (31a), (31b), and (31c)–(33) should remain to be bounded for vanishing $\tilde{Z}$, $\tilde{W}$, $\tilde{U}_r^{(d)}$, and $\tilde{U}_\theta^{(d)}$ at infinite boundaries.

After some manipulation, the solutions to displacement components, pore pressure, and stresses for deviatoric loading may be deduced from Equations (31a), (31b), and (31c)–(33) while considering the Laplace transformed boundary condition Equations (11a)–(11c).

$$\frac{2Gs\tilde{U}_r^{(d)}}{\sigma_d r_w}=\frac{C_1}{\beta}\left[K_1(\xi)+\frac{2}{\xi}K_2(\xi)\right]-C_2\frac{r_w}{2r}-C_3\left(\frac{r_w}{r}\right)^3 \tag{34a}$$

$$\frac{2Gs\tilde{U}_\theta^{(d)}}{\sigma_d r_w}=2\frac{C_1}{\beta^2}\frac{r_w}{r}K_2(\xi)+C_2\frac{1}{2\chi}\frac{r_w}{2r}-C_3\left(\frac{r_w}{r}\right)^3 \tag{34b}$$

$$-\frac{s\tilde{P}^{(d)}}{\sigma_d}=\frac{1-\nu}{1-2\nu}C_1K_2(\xi)+\frac{\alpha M}{4G\chi}C_2\left(\frac{r_w}{r}\right)^2 \tag{34c}$$

$$\frac{s\tilde{S}_r^{(d)}}{\sigma_d}=C_1\left[\frac{1}{\xi}K_1(\xi)+\frac{6}{\xi^2}K_2(\xi)\right]-\frac{1}{2(1-\psi)}C_2\left(\frac{r_w}{r}\right)^2-3C_3\left(\frac{r_w}{r}\right)^4 \tag{34d}$$

$$\frac{s\tilde{S}_{\theta}^{(d)}}{\sigma_d} = -C_1\left[\frac{1}{\xi}K_1(\xi) + \left(1 + \frac{6}{\xi^2}\right)K_2(\xi)\right] + 3C_3\left(\frac{r_w}{r}\right)^4 \tag{34e}$$

$$\frac{s\tilde{S}_{r\theta}^{(d)}}{\sigma_d} = 2C_1\left[\frac{1}{\xi}K_1(\xi) + \frac{3}{\xi^2}K_2(\xi)\right] - \frac{1}{4(1-\psi)}C_2\left(\frac{r_w}{r}\right)^2 - C_3\left(\frac{r_w}{r}\right)^4 \tag{34f}$$

where

$$C_1 = -\frac{4\beta(\psi - \nu)}{(D_2 - D_1)} \tag{35a}$$

$$C_2 = \frac{8(1-\psi)D_2}{D_2 - D_1}, \tag{35b}$$

$$C_3 = -\frac{\beta(D_2 + D_1) + 8(\psi - \nu)K_2(\beta)}{\beta(D_2 - D_1)} \tag{35c}$$

$$D_1 = 2(\psi - \nu)K_1(\beta) \tag{35d}$$

$$D_2 = \beta(1-\nu)K_2(\beta) \tag{35e}$$

with $\xi_3 = r\sqrt{s/c^*}$, $\beta_3 = r_w\sqrt{s/c^*}$, and $\psi = (1-\chi)/(1-2\chi)$.

When the relationship between shear strain and displacement defined by $\gamma_{r\theta} = (1/r)((\partial u_r/\partial\theta) + (\partial u_\theta/\partial r) - (u_\theta/r))$ and $\omega = (-1/r)((\partial u_r/\partial\theta) + (\partial/r\partial r)(ru_\theta))$ is adopted, it could be observed that the field variables in Equations ((29a)), ((29b)), ((29c)), ((34a)), ((34b)), ((34c)), ((34d)), ((34e)), and ((34f)) and the introduced transition variables in Equations (35a), (35b), (35c), (35d), and (35e) share the same fundamental expressions, excluding the negative sign appearing in the expressions of pore pressure compared to the one in the study of Detournay and Cheng [22]. The latter prescribes that the tension is positive. That is to say, the approach that Cui et al. [36] dealt with the whole variables with the negative sign to the corresponding formulas [37] is not appropriate.

The stress components in the time domain could be completed in favor of the numerical algorithm associated with the inversion technique for Laplace transforms offered by Stehfest [38], which has been adopted extensively in petroleum engineering.

Thus, the axial stress reads under plane strain condition

$$\begin{aligned}\tilde{\sigma}_z^{\mathrm{I}} = {} & \nu\left(2\frac{\sigma_m}{s} + \tilde{\sigma}_r^{(a)} + \tilde{\sigma}_r^{(d)} + \tilde{\sigma}_\theta^{(a)} + \tilde{\sigma}_\theta^{(d)}\right) \\ & + (1-2\nu)\left[\alpha\left(\frac{p_0}{s} + \tilde{p}^{(a)} + \tilde{p}^{(d)}\right) + \beta^s\left(\frac{T_0}{s} + \tilde{T}^{(a)}\right)\right].\end{aligned} \tag{36}$$

3.3. Solution to the Elastic Uniaxial Stress Problem. This problem is purely elastic, and no time-dependent pore pressure and stresses are generated [35], and hence, the solution is only related to axial stress and reads as follows:

$$\sigma_z^{\mathrm{II}} = \sigma_v - 2\nu\sigma_m - (1-2\nu)(\alpha p_0 + \beta^s T_0). \tag{37}$$

Ultimately, the complete porothermoelastic solutions for stresses, pore pressure, and temperature around a pressurized vertical borehole are obtained on the condition that positive stress denotes compression

$$\sigma_r = \sigma_m + \sigma_d \cos 2\theta + \sigma_r^{(a)} + \sigma_r^{(d)}, \tag{38a}$$

$$\sigma_\theta = \sigma_m - \sigma_d \cos 2\theta + \sigma_\theta^{(a)} + \sigma_\theta^{(d)}, \tag{38b}$$

$$\sigma_z = \sigma_{zz}^{\mathrm{I}} + \sigma_{zz}^{\mathrm{II}}, \tag{38c}$$

$$\tau_{r\theta} = -\sigma_d \sin 2\theta + \sigma_{r\theta}^{(d)}, \tag{38d}$$

$$p = p_0 + p^{(a)} + p^{(d)}, \tag{38e}$$

$$T = T_0 + T^{(a)}. \tag{38f}$$

4. Numerical Results and Discussions

The input parameters for modeling results are listed in Table 1. Assign the temperature difference between mud T_m and formation T_0 to $\Delta T = 25\circ$C (heating) and $\Delta T = -25\circ$C (cooling), respectively.

4.1. Sensitivity Analysis. This subsection conducts the sensitivity analysis of remarkable influencing factors including thermal osmosis coefficient K^{T}, thermal diffusivity c_h, and permeability coefficient κ on induced pore pressure.

Figures 2 and 3 show the induced pore pressure distributions where porothermoelastic osmosis solution, porothermoelastic, and pure poroelastic models occur at 10^{-4}day.

The undrained loading effect reflects the short-term behavior of low-permeability rock and is induced by deviatoric stress [24, 25]. For the pure poroelastic model [24] (see Figure 3(c)), the undrained loading effect does increase the pore pressure in regions near the wellbore wall.

As shown from Figure 2(a), in line with the common porothermoelastic (THM) model [11], heating the wellbore generates an increased pore pressure in regions near the borehole wall for smaller time intervals $t = 10^{-4}$day, since the thermal expansion of fluid is higher than that of the solid skeleton but the extremely low permeability of rock restricts the excess pore pressure to immediately dissipate. However, the present results suggest that heating (negative temperature gradient $\Delta T < 0$) does not always further guarantee a pore pressure building up. The reduced pore pressure associated with porothermoelastic osmosis (THMO) solution is attributed to the weakened phenomenon of the undrained loading effect by the thermal osmosis effect. This weaken phenomenon occurs where the thermal osmotic coefficient K^{T} is significantly large, and signs of K^{T} and temperature gradient ΔT share the opposite form, for example, $K^{\mathrm{T}} > 0$ and $\Delta T < 0$. This special case produces a backflow to pull the fluid out of formation and even exceedingly dehydrates rock [8]. Naturally, the lower pore pressure fortifies the effective stresses and then increases the rock strength to failure and therefore culminates in better condition to stabilize wellbore.

Table 1: List of input data ([8, 11, 39]).

Parameters	Value	Units
In situ conditions		
Overburden stress (σ_v)	29	kPa/m
Maximum horizontal in situ stress (σ_H)	25	kPa/m
Minimum horizontal in situ stress (σ_h)	20	kPa/m
Formation pore pressure (p_0)	9.8	kPa/m
Wellbore conditions		
Well depth (true vertical depth)	1000	m
Wellbore radius (r_w)	0.1	m
Formation pore pressure (p_w)	12	kPa/m
Material parameters		
Elastic modulus (E)	9.474	GPa
Possion's ratio (ν)	0.24	
Grain bulk modulus (K_s)	27.5	GPa
Grain bulk modulus (K_f)	2.15	GPa
Permeability coefficient (κ)	5.0×10^{-9}, 5.0×10^{-10}, 5.0×10^{-11}	$m^2/(MPa \cdot s)$
Reference porosity (ϕ)	0.14	
Linear expansion coefficient for solid skeleton (α^s)	6.0×10^{-6}	1/K
Volumetric expansion coefficient for pore fluid (α^f)	3.0×10^{-4}	1/K
Thermal diffusivity (c_h)	$7.15 \times 10^{-7}/1.6 \times 10^{-6}$	m^2/s
Thermal osmotic coefficient (K_T)	1×10^{-10}, 1×10^{-11}, 1×10^{-12}, 1×10^{-13}	$m^2/(s \cdot K)$
Cohesion of rock (C)	10	MPa
Internal friction angle (φ)	20	Degree

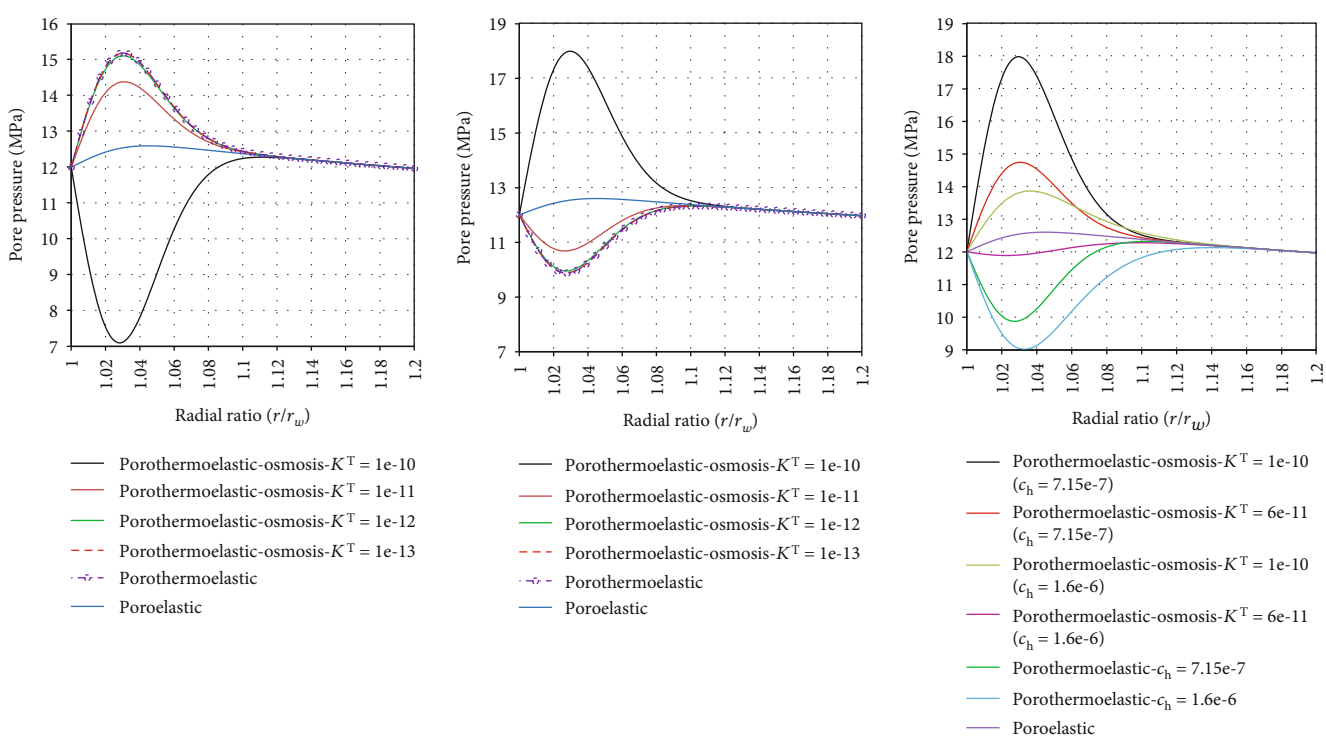

(a) (b) Cooling $c_h = 7.15e-7$ (c) Cooling

Figure 2: Induced pore pressure varying with r/r_w at $\theta = 90\circ$ wherein different conditions are prescribed.

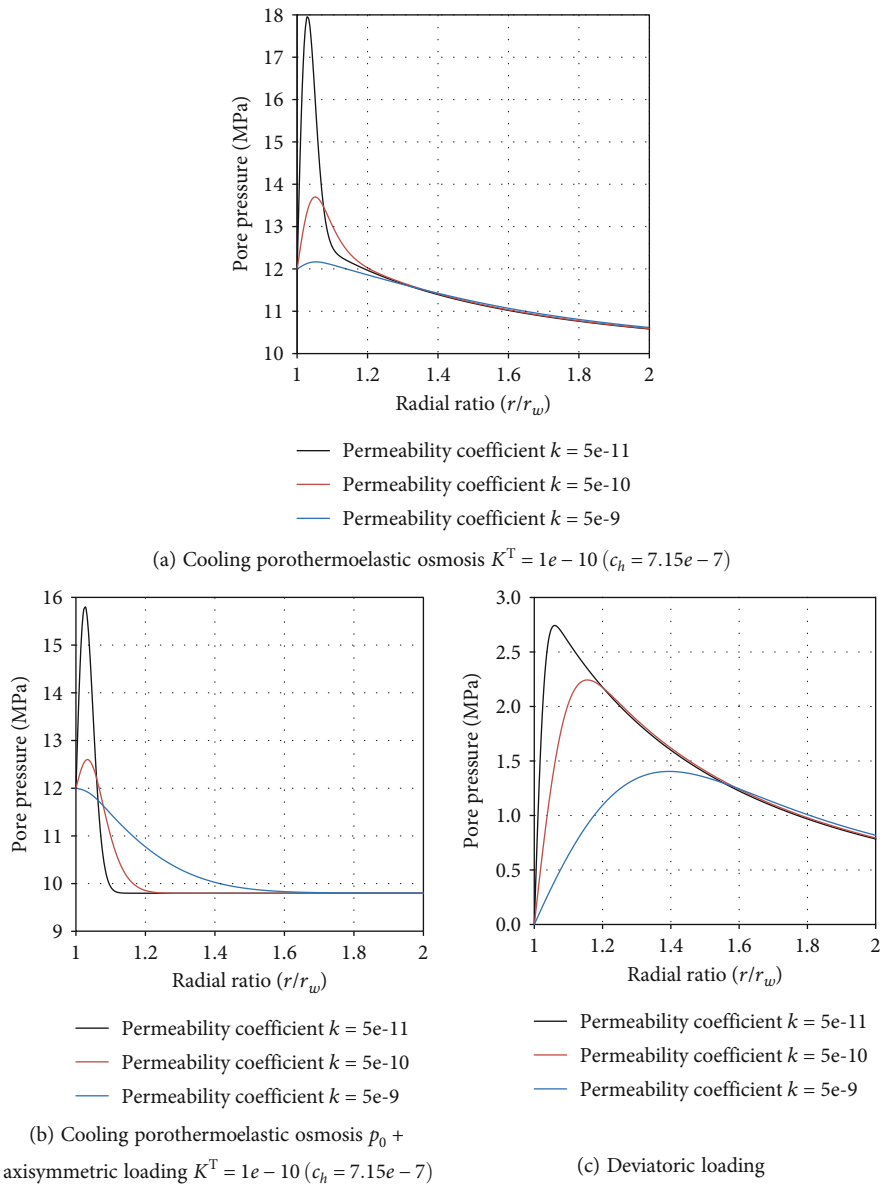

Figure 3: Induced pore pressure varying with r/r_w at $\theta = 90\circ$ wherein different permeability coefficients are prescribed.

The intensifying case (see Figure 2(b)) is stipulated as the same sign for cooling (positive temperature gradient $\Delta T > 0$) and the significantly large thermal osmosis coefficient $K^T > 0$. The intensifying case causes drilling fluid water in mud to flow into the formation. The increased pore pressure associated with this intensifying case reduces effective stresses and thus decreases the rock strength to failure. It deteriorates the wellbore stability. The previous investigator, i.e., Ghassemi and Diek [8], likewise testified the similar view that the thermal osmosis effect enhances or reduces the chemical osmosis effect that rests upon the sign between thermal osmotic coefficient and temperature gradient, and the magnitude of thermal osmotic coefficient as well. Besides, in the case of a considerably small thermal osmosis coefficient, the induced pore pressures share the approximatively identical significance compared THMO model with the THM one. Therefore, it is appropriate for neglecting the thermal osmosis effect.

When the same thermal osmotic coefficient is prescribed, the thermal osmosis effect enhancing the undrained loading effect is more significant for the rock characterized by the less value that of thermal diffusivity c_h (see Figure 2(c)). Also, the case of larger value that of thermal diffusivity and lower thermal osmotic coefficient would turn to the reduction of the undrained loading effect and further decrease pore pressure. Moreover, the thermal osmosis effect with a larger thermal osmotic coefficient is more vulnerable to undertake the role to enhance the undrained loading effect, when the same thermal diffusivity is stipulated.

With the THMO model considering the cooling effect, the total pore pressure as presented in Figure 3(a) equals the superposition of the original formation pore pressure and axisymmetric loading effect (see Figure 3(b)) and deviatoric loading (see Figure 3(c)). The thermal osmosis effect on the pore pressure is reduced in the case of a larger

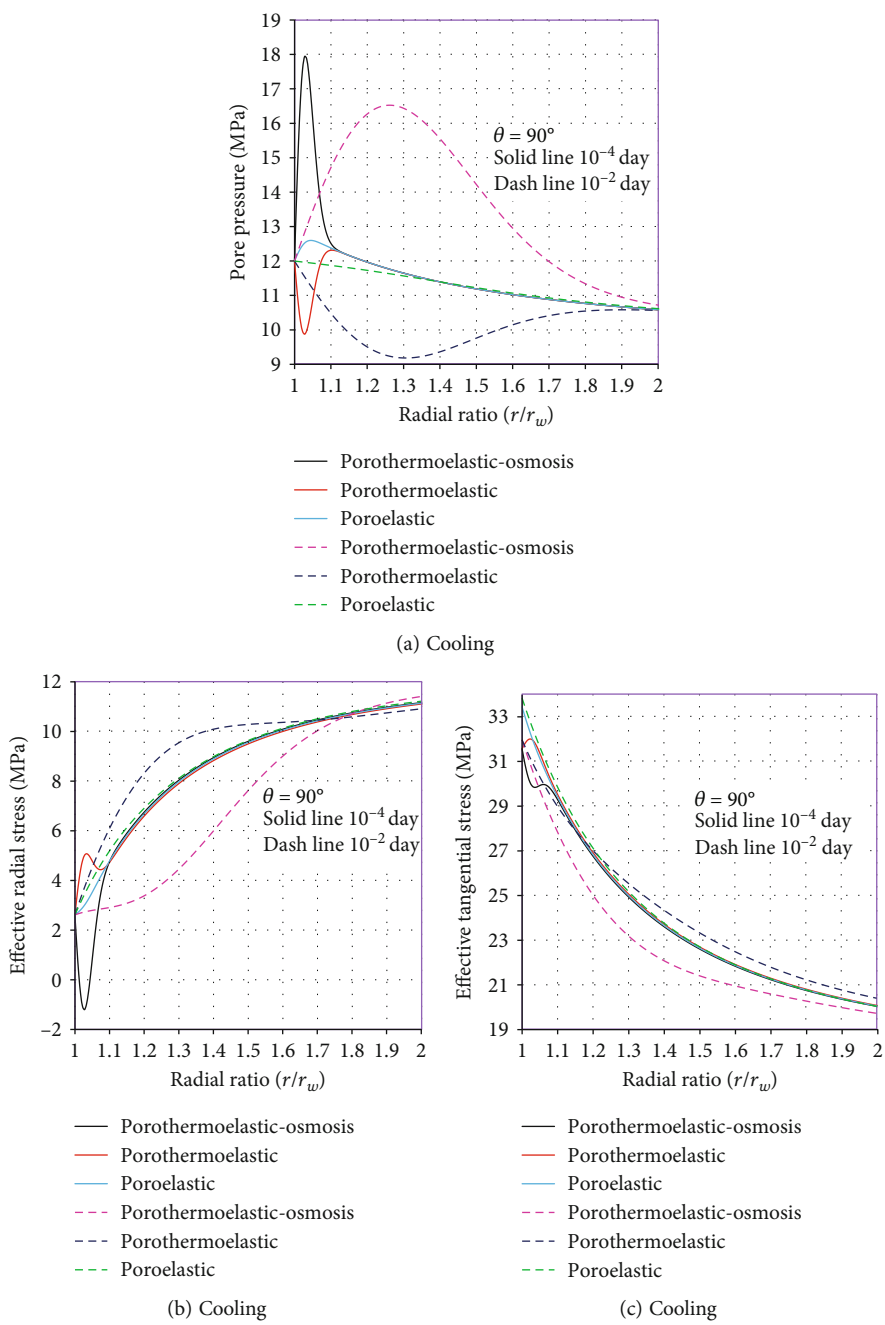

Figure 4: Induced pore pressure and effective stresses varying with r/r_w at $\theta = 90\circ$ wherein different conditions are prescribed.

permeability coefficient κ. On the contrary, the cases of lower magnitudes of permeability coefficient intensify the thermal osmosis effect to generate the more distinct back-flow phenomenon, so that the undrained loading effect is reduced and consequently the pore pressure drops.

4.2. Time Dependence of the Induced Pore Pressure and Effective Total Stresses. Figure 4 evaluates the induced pore pressure and effective stress profiles at different times when the THMO model and THM case where cooling and the pure poroelastic one are examined.

Figure 4 describes the induced pore pressure and effective total stresses including radial and tangential profiles (porothermoelastic osmosis solution, $c^h = 7.15 * 10^{-7}$, $K^{\mathrm{T}} = 1 * 10^{-10}$; porothermoelastic model, $c^h = 7.15 \times 10^{-7}$) and pure poroelastic model when wellbore is subjected to cooling or isothermal condition, respectively, at different times.

When the thermal osmosis effect intensifies the undrained loading effect, the thermally induced pore pressure and effective stresses including radial and tangential stresses of THMO model behave the opposite variation compared to the common THM one. Higher pore pressure leads to effective tensile radial stress and consequently produces the probability for borehole spalling inside the formation (or outburst) [40, 41] at smaller time interval after drilling a borehole (see Figure 4(b)). However, the

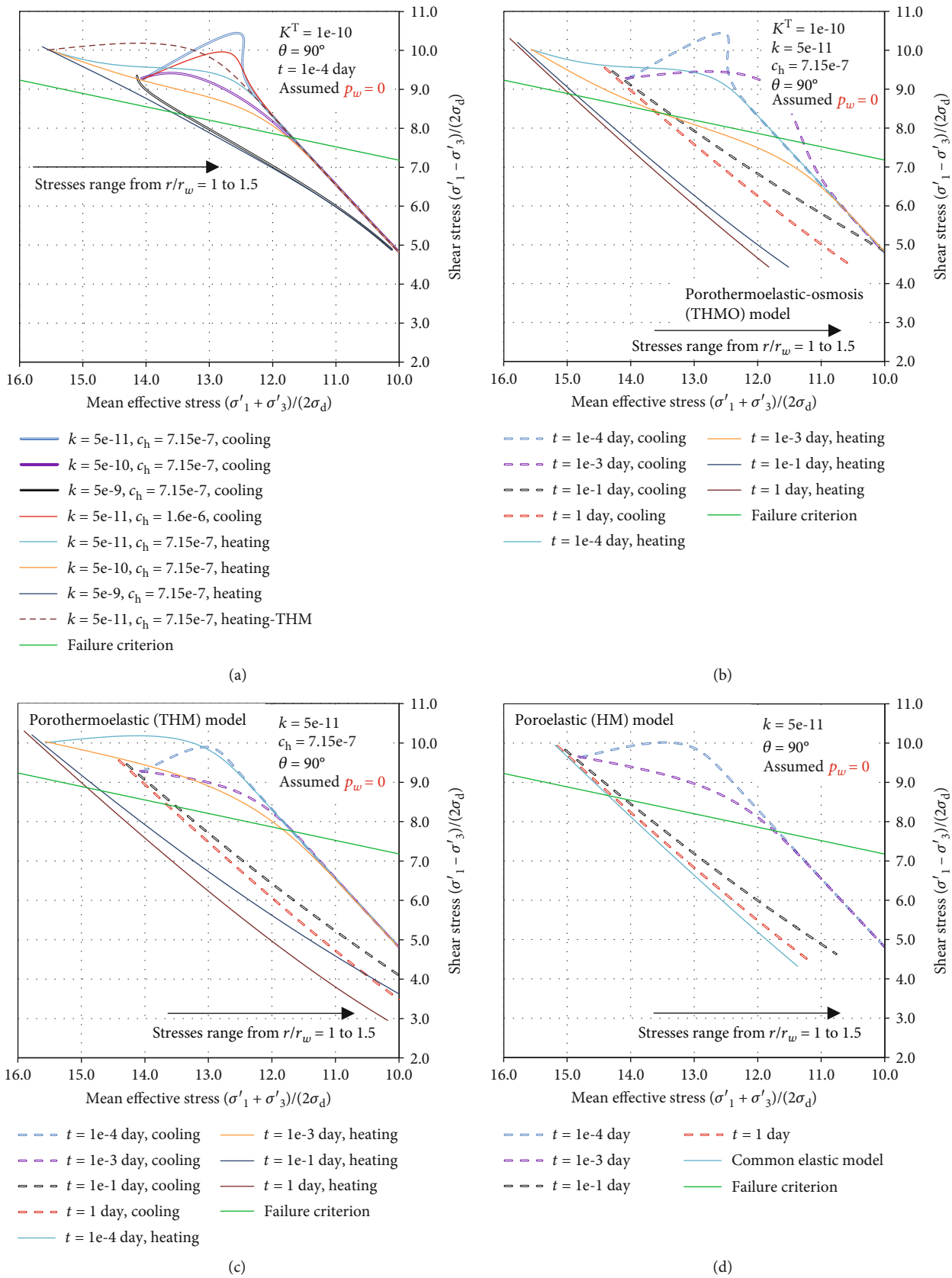

Figure 5: The time-dependent shear failure potentials against different models including porothermoelastic osmosis (THMO), porothermoelastic (THM), and pure poroelastic (HM).

values of pore pressure gradually shift inward the formation with diminishing magnitudes as time progress. This case also reduces effective stresses, and the shear failure zones are displaced into formation in nature. The more compressive effective radial stress which the regions of tensile spalling failure disappear can be observed at a later time. The cooling effect naturally reduces the stress as presented in the constitutive Equation (1); therefore, Figure 4(c) shows the pure poroelastic (HM) model has larger effective tangential stress than that of THMO and THM ones, especially the regions at or very close to the borehole wall. But, the increased pore pressure due to the thermal osmosis effect further reduces the magnitude of tangential stress near the borehole wall.

As time elapses, the common THM one indicates that the reduction and less minimum magnitude of pore pressure is a reverse analogy to that of the THMO solution and pure poroelastic model near the borehole wall region. Finally, the reduced shear stress in the form of a difference between effective tangential stress and effective radial stress stabilizes the wellbore with regard to shear failure in regions near the wellbore wall.

4.3. Time-Dependent Potential of Borehole Collapse. One illustrates the potential of borehole collapse for vertical borehole against different models in this subsection.

Mohr-Coulomb strength criterion is used to study the borehole stability. It is commonly expressed in terms of the shear stress $(\sigma_1' - \sigma_3')/2$ and mean effective stress $(\sigma_1' + \sigma_3')/2$ (the effective stress is defined by $\sigma_{ij}' = \sigma_{ij} - \alpha p \delta_{ij}$) to predict the failure of a geotechnical material [42].

$$\left(\frac{\sigma_1' - \sigma_3'}{2}\right) = C\cos\varphi + \left(\frac{\sigma_1' + \sigma_3'}{2}\right)\sin\varphi, \tag{39}$$

where C and φ, respectively, correspond to the intrinsic cohesive strength and internal friction angle of the rock. Besides, the abovementioned maximum and minimum principal stresses σ_1' and σ_3' correspond to the eigenvalues σ_n of the matrix of the effective stress tensor $(\sigma_{ij}',\ i, j \in (r, \theta, z)$ in Equations (34a)–(34f) around the borehole. One obtains the two principal stresses by solving the following characteristic equation:

$$\begin{vmatrix} \sigma_r' - \sigma_n & \tau_{r\theta} & \tau_{rz} \\ \tau_{r\theta} & \sigma_\theta' - \sigma_n & \tau_{\theta z} \\ \tau_{rz} & \tau_{\theta z} & \sigma_{zz}' - \sigma_n \end{vmatrix} = 0. \tag{40}$$

Note that a profile above the failure envelope implies failure.

On the whole, Figure 5 shows the borehole collapse related to the three aforementioned models is time-dependent. The locations of borehole collapse occur inside the formation (or next to the borehole wall) at an earlier time but are displaced at the borehole wall at a later time. The combination of effective compressive tangential stress and effective tensile radial stress renders the maximum magnitude of the shear stress $(\sigma_1' - \sigma_3')/2$ to occur inside the formation. Noted that the shear stress $\tau_{r\theta}$ of a vertical borehole appropriately has zero magnitudes at the borehole wall or the formation; thus, the effective maximum or minimum principal stress σ_1' and σ_3' can practically equal to the effective tangential stress and effective radial stress. The potential of borehole collapse occurring at the borehole wall increases with increasing time; this is because maximum effective tangential stress occurs at the borehole at a later time.

With the cooling cases considered, Figure 5(a) shows that the obvious thermal osmosis effect further enhances the undrained effect for lower permeability rock at a given thermal diffusion coefficient, and thus, the risk of borehole collapse increases and the failure location occurs inside the formation. Similarly, the strengthening effect of the thermal osmosis effect on the undrained effect for lower permeability rock corresponds to the rock with a smaller thermal diffusion coefficient at a given permeability coefficient. The cooling effect reduces the effective tangential stress, and thus, the mean effective stresses of the cooling cases are smaller than those of the heating cases. The potential of borehole collapse firstly occurs at the borehole wall for heating cases of the THMO model in Figure 5(a), but the location of borehole collapse could appear inside the formation for the THM model at a given earlier time. This is because the thermal osmosis effect reduces the undrained effect and renders the pore pressure to decrease, and thus, the effective compressive radial stress along the radial distance eliminates the possibility of the maximum shear stress occurring inside the formation.

With the case of the thermal osmosis effect strengthening the undrained effect considered, Figure 5(b) again confirms the view that the locations of borehole collapse occur inside the formation at an earlier time when the drilling mud cools the formation. However, Figure 5(c) indicates the aforementioned phenomenon corresponds to the heating borehole. The heat effect further increases the risk of borehole collapse compared to Figures 5(c) and 5(d). Also, Figure 5(d) shows the time-dependent effect disappears with increasing time and approaches the elastic case.

This study presents the effect of thermal osmosis effect on wellbore stability and can also be introduced to the discussion of thermal osmosis effect on hydraulic fracturing [43, 44].

5. Conclusions

Under plane strain condition, the present paper formulates a set of porothermoelastic analytical solutions of the vertical wellbore drilled through an isotropic porous rock formation subjected to thermal osmosis effect and nonhydrostatic remote stress.

(1) When a lower permeability rock is characterized by the substantially large thermal osmotic coefficient and the smaller thermal diffusivity, the thermal osmosis effect more significantly intensifies or weakens the undrained loading effect (poroelastic effect), and it is not appropriate for neglecting this effect

(2) In the case of the positive magnitude of the product of the significantly large thermal osmotic coefficient

and temperature gradient, the thermal osmosis effect intensifies the undrained loading effect and leads to a build-up of pore pressure. Accordingly, lower effective stresses increase the mean shear stress and tend to deteriorate wellbore stability. The weakening cases, on the contrary, can stabilize wellbore with respect to shear failure

(3) The predrilling mud-weight design is suggested to consider the time-dependent locations of borehole collapse since the locations firstly occur inside the formation, whereas it is displaced at the borehole wall

Data Availability

The reader can request the data by contacting the corresponding author.

Conflicts of Interest

The authors declare that they have no conflicts of interest.

Acknowledgments

This research is supported by the Research and demonstration of drilling and completion technology for extended reach wells exceeding 6000 meters in Laizhou Bay (No. CNOOC-KJ135ZDXM36TJ06TJGD202201).

References

[1] P. T. Delaney, "Rapid intrusion of magma into wet rock: groundwater flow due to pore pressure increases," *Journal of Geophysical Research B*, vol. 87, no. B9, pp. 7739–7756, 1982.

[2] D. F. McTigue, "Thermoelastic response of fluid-saturated porous rock," *Journal of Geophysical Research-Solid Earth*, vol. 91, no. B9, pp. 9533–9542, 1986.

[3] D. F. McTigue, "Flow to a heated borehole in porous, thermoelastic rock: analysis," *Water Resources Research*, vol. 26, no. 8, pp. 1763–1774, 1990.

[4] Y. Wang and E. Papamichos, "Conductive heat flow and thermally induced fluid flow around a well bore in a poroelastic medium," *Water Resources Research*, vol. 30, no. 12, pp. 3375–3384, 1994.

[5] X. Li, L. Cui, and J. C. Roegiers, "Thermoporoelastic analyses of inclined boreholes," in *Paper presented at the SPE/ISRM Rock Mechanics in Petroleum Engineering*, pp. 1–9, Trondheim, Norway, 1998.

[6] Y. Zhou, R. Rajapakse, and J. Graham, "Coupled consolidation of a porous medium with a cylindrical or a spherical cavity," *International Journal for Numerical and Analytical Methods in Geomechanics*, vol. 22, no. 6, pp. 449–475, 1998.

[7] Y. Zhou, R. Rajapakse, and J. Graham, "A coupled thermoporoelastic model with thermo-osmosis and thermal-filtration," *International Journal of Solids and Structures*, vol. 35, no. 34-35, pp. 4659–4683, 1998.

[8] A. Ghassemi and A. Diek, "Porothermoelasticity for swelling shales," *Journal of Petroleum Science and Engineering*, vol. 34, no. 1-4, pp. 123–135, 2002.

[9] Y. Wang and M. B. Dusseault, "A coupled conductive-convective thermo-poroelastic solution and implications for wellbore stability," *Journal of Petroleum Science and Engineering*, vol. 38, no. 3-4, pp. 187–198, 2003.

[10] G. Chen and R. T. Ewy, "Thermoporoelastic effect on wellbore stability," *SPE Journal*, vol. 10, no. 2, pp. 121–129, 2005.

[11] Y. Abousleiman and S. Ekbote, "Solutions for the inclined borehole in a porothermoelastic transversely isotropic medium," *Journal of Applied Mechanics*, vol. 72, no. 1, pp. 102–114, 2005.

[12] H. S. Farahani, M. Yu, S. Miska, N. Takach, and G. Chen, "Modeling transient thermo-poroelastic effects on 3D wellbore stability," in *Paper presented at the SPE Annual Technical Conference and Exhibition*, pp. 1–12, San Antonio, Texas, USA, 2006.

[13] Q. Tao and A. Ghassemi, "Poro-thermoelastic borehole stress analysis for determination of the in situ stress and rock strength," *Geothermics*, vol. 39, no. 3, pp. 250–259, 2010.

[14] B. Wu, X. Zhang, R. G. Jeffrey, and B. Wu, "A semi-analytic solution of a wellbore in a non-isothermal low-permeability porous medium under non-hydrostatic stresses," *International Journal of Solids and Structures*, vol. 49, no. 13, pp. 1472–1484, 2012.

[15] M. Gomar, I. Goodarznia, and S. R. Shadizadeh, "Transient thermo-poroelastic finite element analysis of borehole breakouts," *International Journal of Rock Mechanics and Mining Sciences*, vol. 71, pp. 418–428, 2014.

[16] M. F. Kanfar, Z. Chen, and S. S. Rahman, "Fully coupled 3D anisotropic conductive-convective porothermoelasticity modeling for inclined boreholes," *Geothermics*, vol. 61, pp. 135–148, 2016.

[17] Z. Q. Fan and R. Parashar, "Analytical solutions for a wellbore subjected to a non-isothermal fluid flux: implications for optimizing injection rates, fracture reactivation, and EGS hydraulic stimulation," *Rock Mechanics and Rock Engineering*, vol. 52, no. 11, pp. 4715–4729, 2019.

[18] Z. Q. Fan, R. Parashar, and Z. H. Jin, "Impact of convective cooling on pore pressure and stresses around a borehole subjected to a constant flux: implications for hydraulic tests in an enhanced geothermal system reservoir," *Interpretation*, vol. 8, no. 2, pp. SG13–SG20, 2020.

[19] J. Gao, J. Deng, K. Lan, Z. Song, Y. Feng, and L. Chang, "A porothermoelastic solution for the inclined borehole in a transversely isotropic medium subjected to thermal osmosis and thermal filtration effects," *Geothermics*, vol. 67, pp. 114–134, 2017.

[20] Z. Song, F. Liang, and S. Chen, "Thermo-osmosis and mechano-caloric couplings on THM responses of porous medium under point heat source," *Computers and Geotechnics*, vol. 112, pp. 93–103, 2019.

[21] Z. Song, Y. Hao, and H. Liu, "Analytical study of the thermo-osmosis effect in porothermoelastic responses of saturated porous media under axisymmetric thermal loadings," *Computers and Geotechnics*, vol. 123, article 103576, 2020.

[22] X. Zhai and K. Atefi-Monfared, "Explanation of early failure in porous media confined with flexible layers, considering thermo-osmosis, thermal-filtration and heat sink from fluid dilation," *Computers and Geotechnics*, vol. 122, article 103501, 2020.

[23] J. J. Gao, H. Lin, B. S. Wu, J. Deng, and H. Liu, "Porochemothermoelastic solutions considering fully coupled thermo-

hydro-mechanical-chemical processes to analyze the stability of inclined boreholes in chemically active porous media," *Computers and Geotechnics*, vol. 134, article 104019, 2021.

[24] E. Detournay and A. H. D. Cheng, "Poroelastic response of a borehole in a non-hydrostatic stress field," *International Journal of Rock Mechanics and Mining Science and Geomechanics Abstracts*, vol. 25, no. 3, pp. 171–182, 1988.

[25] G. Chen and R. T. Ewy, "Investigation of the undrained loading effect and chemical effect on shale stability," in *Paper presented at the SPE/ISRM Rock Mechanics Conference*, Irving, Texas, 2002.

[26] C. Dirksen, "Thermo-osmosis through compacted saturated clay membranes," *Soil Science Society of America Journal*, vol. 33, no. 6, pp. 821–826, 1969.

[27] D. H. Gray, *Coupled Flow Phenomena in Clay-Water Systems*, University of Michigan, 1966.

[28] C. L. Carnahan, "Thermodynamic coupling of heat and matter flows in near-field regions of nuclear waste repositories," *MRS Online Proceedings Library*, vol. 26, pp. 1023–1030, 1983.

[29] S. T. Horseman and T. J. McEwen, "Thermal constraints on disposal of heat-emitting waste in argillaceous rocks," *Engineering Geology*, vol. 41, no. 1-4, pp. 5–16, 1996.

[30] J. M. Soler, "The effect of coupled transport phenomena in the Opalinus Clay and implications for radionuclide transport," *Journal of Contaminant Hydrology*, vol. 53, no. 1-2, pp. 63–84, 2001.

[31] J. Gonçalvès and J. Trémosa, "Estimating thermo-osmotic coefficients in clay-rocks: I. Theoretical insights," *Journal of Colloid and Interface Science*, vol. 342, no. 1, pp. 166–174, 2010.

[32] E. Detournay and A. H. D. Cheng, "Fundamentals of poroelasticity," in *Analysis and Design Methods*, pp. 113–171, Elsevier, 1993.

[33] R. W. Zimmerman, "Coupling in poroelasticity and thermoelasticity," *International Journal of Rock Mechanics and Mining Sciences*, vol. 37, no. 1-2, pp. 79–87, 2000.

[34] Y. Abousleiman and L. Cui, "Poroelastic solutions in transversely isotropic media for wellbore and cylinder," *International Journal of Solids and Structures*, vol. 35, no. 34-35, pp. 4905–4929, 1998.

[35] J. P. Carter and J. R. Booker, "Elastic consolidation around a deep circular tunnel," *International Journal of Solids and Structures*, vol. 18, no. 12, pp. 1059–1074, 1982.

[36] L. Cui, Y. Abousleiman, A. H. D. Cheng, and J. C. Roegiers, "Time-dependent failure analysis of inclined boreholes in fluid-saturated formations," *Journal of Energy Resources Technology*, vol. 121, no. 1, pp. 31–39, 1999.

[37] L. Cui, A. H. D. Cheng, and Y. Abousleiman, "Poroelastic solution for an inclined borehole," *Journal of Applied Mechanics*, vol. 64, no. 1, pp. 32–38, 1997.

[38] H. Stehfest, "Algorithm 368: numerical inversion of Laplace transforms [D5]," *Communications of the ACM*, vol. 13, no. 1, pp. 47–49, 1970.

[39] http://www.pmi.ou.edu/images/Pbore%20pics/criticalregionwithbedding.jpg.

[40] L. Paterson, "A model for outbursts in coal," *International Journal of Rock Mechanics and Mining Science and Geomechanics Abstracts*, vol. 23, no. 4, pp. 327–332, 1986.

[41] A. H.-D. Cheng, Y. Abousleiman, and J. C. Roegiers, "Review of some poroelastic effects in rock mechanics," *International Journal of Rock Mechanics and Mining Science and Geomechanics Abstracts*, vol. 30, no. 7, pp. 1119–1126, 1993.

[42] J. C. Jaeger, N. G. W. Cook, and R. W. Zimmerman, *Fundamentals of Rock Mechanics*, John Wiley & Sons, 4rd ed. edition, 2007.

[43] Y. Wang, B. Hou, D. Wang, and Z. Jia, "Features of fracture height propagation in cross-layer fracturing of shale oil reservoirs," *Petroleum Exploration and Development*, vol. 48, no. 2, pp. 469–479, 2021.

[44] B. Hou, Y. F. Dai, C. L. Zhou, K. Zhang, and F. Liu, "Mechanism study on steering acid fracture initiation and propagation under different engineering geological conditions," *Geomechanics and Geophysics for Geo-Energy and Geo-Resources*, vol. 7, no. 3, pp. 1–14, 2021.

Hindawi
Geofluids
Volume 2022, Article ID 6711977, 12 pages
https://doi.org/10.1155/2022/6711977

Research Article

An Improved Model for Evaluating the Brittleness of Shale Oil Reservoirs Based on Dynamic Elastic Properties: A Case Study of Lucaogou Formation, Jimusar Sag

Yang Gao,[1,2] Yan Dong,[2] Lei Chen,[3] Yingyan Li,[2] Jianhua Qin,[2] and Zhenxue Jiang[1,3]

[1]*Unconventional Oil and Gas Research Institute, China University of Petroleum-Beijing, Beijing 102249, China*
[2]*Xinjiang Oilfield Company, PetroChina, Karamay, Xinjiang 834000, China*
[3]*State Key Laboratory of Petroleum Resources and Prospecting, China University of Petroleum-Beijing, Beijing 102249, China*

Correspondence should be addressed to Lei Chen; rawson163@163.com

Received 13 March 2022; Revised 14 April 2022; Accepted 20 April 2022; Published 4 May 2022

Academic Editor: Hasan N. Al-Saedi

Rock brittleness is a critical factor affecting the stimulation of shale oil reservoirs. For efficient development of the shale oil in Lucaogou Formation, Jimusar Sag, the brittleness of the sweet spots needs to be evaluated. In this paper, the triaxial compression, acoustic wave measurements, and three-point bending tests were carried out on the reservoir cores. Based on the prepeak energy characteristics of the stress-strain curve, the brittleness of different horizons was calculated, with the largest difference of 24.89%. An improved model based on dynamic elastic properties was proposed to evaluate the brittleness along the vertical pay zones, by which the continuous brittleness in the upper sweet spot was found more changeful than that in the lower sweet spot. The linear correlation coefficient between the brittleness from the improved model and that from the laboratory tests is 0.85, improving the accuracy by 21% and 27% respectively, compared with the conventional elastic property methods. From the characteristics of compression fractures and the length of the fracture process zone, it was found that the compression fractures were more complex and the fracture process zone length was shorter in a more brittle rock, verifying the reliability of the improvement model. The improved method based on dynamic elastic properties proposed in this paper is expected to guide the brittleness evaluation in other regions.

1. Introduction

With the increasing demand for oil and gas, unconventional energy sources, shale oil being one principle contributor, have become the focus of exploration and development [1–4]. As an effective measure to stimulate the reservoirs [5–7], fracturing technology, especially the stimulated reservoir volume fracturing, has played an important role in the exploitation of shale oil, improving the production of shale oil [8]. In fracturing design, the brittleness of reservoir rocks is an important parameter of concern, providing guidance for evaluating the feasibility of reservoir fracturing [9]. It is generally believed that the brittleness of reservoir rock would affect the complexity of the fracture. That is, the more brittle the rock is, the more complex the hydraulic fracture is [10].

At present, there is no unified standard in the evaluation of rock brittleness [11]. The evaluation of reservoir rock brittleness is mainly from lithology analysis, geophysical methods, and rock mechanics experiments [12–16]. The methods based on lithologic characteristics consider the content of brittle minerals [17, 18]. However, the previous research shows that mineral compositions could not accurately reflect the brittleness of rocks [12, 17, 19]. In addition, the scholars hardly unanimously agree on the classification criteria for brittle minerals [18–20]. In the geophysical method, the rock porosity or mineral component distribution of formation needs to be predicted in advance [15, 16], without comparing with laboratory tests. Brittleness evaluation based on mechanical experiments can be assessed with stress-strain curve analysis, rock mechanical strength evaluation, and calculation of the elastic properties [14, 21–24],

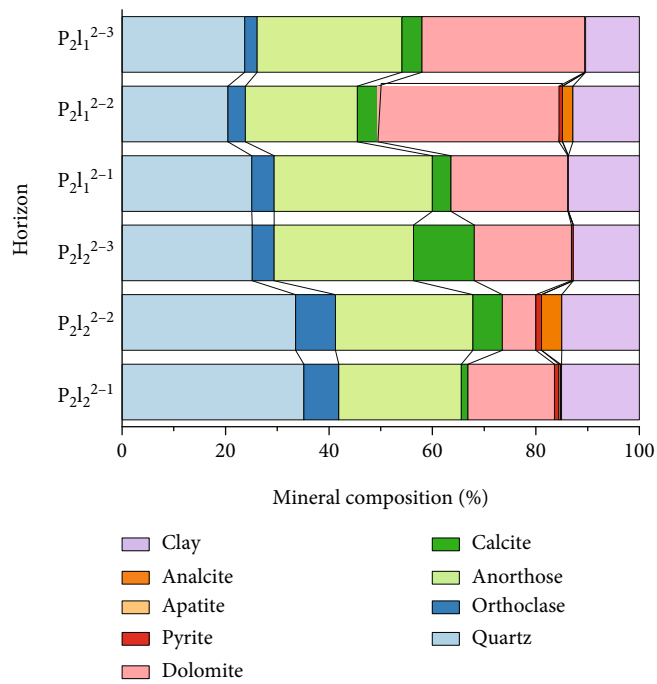

Figure 1: Mineral composition in different horizons.

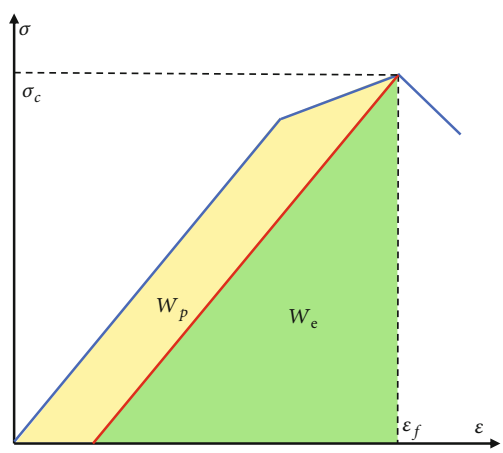

Figure 2: Evaluation of rock brittleness based on the prepeak energy.

among which the elastic property method is widely used [9]. The brittleness evaluation by rock mechanics would be limited by the number of specimen cores, so it is difficult to carry out the rock brittleness evaluation across the pay zones continuously. Therefore, it is necessary to evaluate the rock brittleness continuously using acoustic logging, where evaluating accuracy is an essential topic, especially those from elastic properties. The improvement of the evaluation method based on elastic properties still needs to be studied [9, 12].

The shale oil of Lucaogou Formation in Jimusar Sag, China, is a national demonstration area of continental shale, consisting of two sweet spots. With the characteristics of interlamination, the reservoirs are oil-bearing overall [25–28]. The rock mechanical properties of Lucaogou Formation present diversities in different horizons, and the factors influencing the complexity of hydraulic fractures remain to be studied. Especially when the sweet spots need to be developed as a whole, it is necessary to evaluate the stimulation feasibility of different horizons in the upper and lower sweet spots. The precondition for estimating the stimulation feasibility of reservoirs is the evaluation of brittleness [8, 29], especially the continuous brittleness.

In this paper, the reservoir cores of shale oil in Lucaogou Formation were selected to carry out the triaxial compression, acoustic wave, and three-point bending experiments. Based on the stress-strain curve, the brittleness of different horizons was evaluated. An improved model for evaluating the continuous brittleness by elastic properties was proposed, verified by the characteristics of compression fractures and the length of the fracture process zone. The improvement method proposed in this paper is expected to be a reference for the field when the brittleness needs to be estimated using acoustic logging data.

2. Geological Background

Jimusar Sag is located in the east of the Junggar Basin, China, bounded by the Santai Fault in the south and the Jimusar Fault in the north. It is a typical dustpan depression with depth in the west and shallowness in the east [25–28]. Shale oil in Jimusar Sag is mainly developed in the Permian Lucaogou Formation, which belongs to the continental liquid hydrocarbon shale, a typical representative of shale oil in the foreland salinized lake basin [25–28, 30]. Lucaogou Formation is simple in structure and stable in distribution. The formation thickness is 25 m~300 m, with an average of 200 m, and the buried depth is 800 m-4800 m, with an

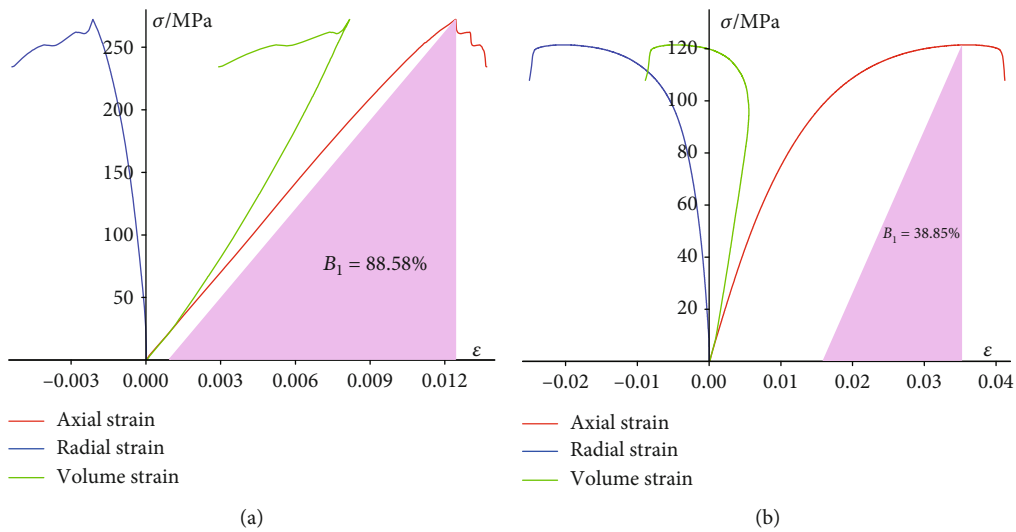

Figure 3: Typical stress-strain curves of higher and lower brittle rocks.

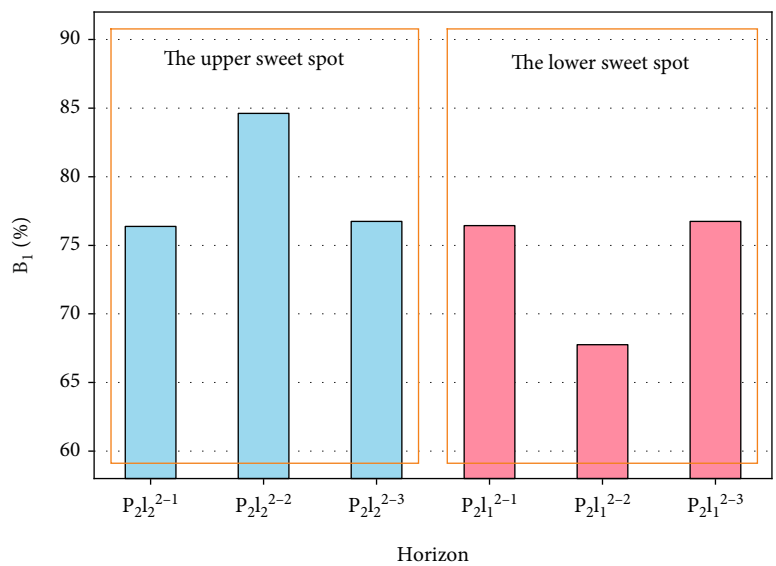

Figure 4: The brittleness distribution in different horizons.

average of 3570 m. Affected by the multisource mixed accumulation of volcanic rocks, clastic rocks, and carbonate rocks, the lithology of the reservoir is diverse, mainly including mudstone, fine silty sandstone, and microcrystalline dolomite [30].

The shale oil in the Lucaogou Formation is concentrated in two sections, where two sweet spots are developed with high porosity and stable distribution [30]. The upper sweet spot ($P_2l_2^2$) can be divided into three horizons ($P_2l_2^{2\text{-}1}$, $P_2l_2^{2\text{-}2}$, and $P_2l_2^{2\text{-}3}$), of which the superposition thickness is more than 18 m. The lower sweet spot ($P_2l_1^2$) can be divided into six horizons ($P_2l_1^{2\text{-}1}$~$P_2l_1^{2\text{-}6}$), but the oil is intensively developed in $P_2l_1^{2\text{-}1}$~$P_2l_1^{2\text{-}3}$, where the superposition thickness of the main area is greater than 17 m. The mineral composition analysis using X-ray diffraction was carried out on the rock cores of the Lucaogou Formation in Jimusar Sag. As shown in Figure 1, it is found that the rock mineral compositions of the upper and lower sweet spots are relatively similar, mainly including quartz, feldspar, calcite, dolomite, and clay.

3. Methods and Results in the Evaluation of Brittleness

3.1. Evaluation of Brittleness Based on the Prepeak Energy. In recent years, calculating the energy characteristics of the compression stress-strain curve has been a reasonable way to evaluate rock brittleness [19, 22, 31–36]. Some scholars used prepeak energy to evaluate rock brittleness from the stress-strain curve [36], describing the proportion of accumulative plastic energy [36]. Some scholars believe that estimating postpeak instability based on postpeak energy balance is a means to characterize rock brittleness [22]. In recent publications, the brittleness also was evaluated by

prepeak and postpeak energies [19]. At present, there is no consensus on which method is the most reliable [19, 22, 31–36]. In the postpeak methods, the characteristics of fracture generated after the peak would affect the pattern of the post stress-strain curve. Thus, we adopted the characteristics of prepeak energy [36] to calculate the rock brittleness of the Lucaogou Formation, which is more representative to evaluate the accumulation of elastic energy before failure.

As shown in Figure 2, during the process of rock compression, elastic deformation and plastic deformation would be generated. The elastic energy W_e together with elastic deformation is recoverable stored energy, and the plastic energy W_p during the plastic process is unrecoverable consumption energy. Previous studies show that dissipated energy W_p is an important parameter to measure the plastic characteristics of rock. The greater the W_p proportions, the more obvious the plastic characteristics would be, so the brittleness of the rock is lower, and the larger the W_e proportions, the greater the stored energy is, so the rock would be more brittle. The calculation of brittleness is shown in the following equation [36].

$$B_1 = \frac{W_e}{W_e + W_p}, \tag{1}$$

where B_1 is the brittleness index based on the prepeak energy of the stress-strain curve, W_e the elastic energy, and W_p the plasticity energy.

Figures 3(a) and 3(b) are the typical stress-strain curves of higher and lower brittleness of shale oil in the Lucaogou Formation. We could find that the elastic stage is dominant of the stress-strain curve in Figure 3(a), where the brittleness index is 88.58%. The stress-strain curve in Figure 3(b) presents prominent plastic characteristics, where the brittleness index is only 38.85%.

Based on Equation (1), the brittleness of shale oil among different horizons in Lucaogou Formation was obtained, as shown in Figure 4, and it was found that there were significant differences in rock brittleness of different horizons in the upper and lower sweet spots. In the upper sweet spot, the brittleness index of $P_2l_2^{2\text{-}2}$ is the largest, which is 84.61%. The brittleness index of $P_2l_1^{2\text{-}2}$ is smallest in the lower sweet spot, reaching 67.75%, and the brittleness of $P_2l_2^{2\text{-}1}$, $P_2l_2^{2\text{-}3}$, $P_2l_1^{2\text{-}1}$, and $P_2l_1^{2\text{-}3}$ is close, about 76%. The current fracturing practice of the upper sweet spot shows that shale oil production in the $P_2l_2^{2\text{-}2}$ horizon is best [37], which is consistent with the brittleness calculation results, indicating the rationality of brittleness evaluation on the characteristics of prepeak energy.

3.2. The Improved Brittleness Evaluation Model Based on Dynamic Elastic Properties. In the brittleness evaluation based on mechanical parameters, some scholars have found that there is a close relationship between rock brittleness and elastic modulus and Poisson's ratio: the rock would be more brittle when the elastic modulus is larger, and the Poisson's ratio is smaller, and the rock brittleness could be calculated as in Equation (2) [38] and Equation (3) [39], which could be called elastic property methods. Although the rock brittleness is related to the elastic constant [38–40], the present methods based on elastic properties were suspicious for the lack of comparison with other methods. The weighted average calculation of the elastic modulus and Poisson's ratio in Equation (2) lacks a theoretical basis, and the calculated value in Equation (3) will be unstable with the change of elastic constant [39]. Therefore, these two methods have been questioned by scholars [9, 12, 39].

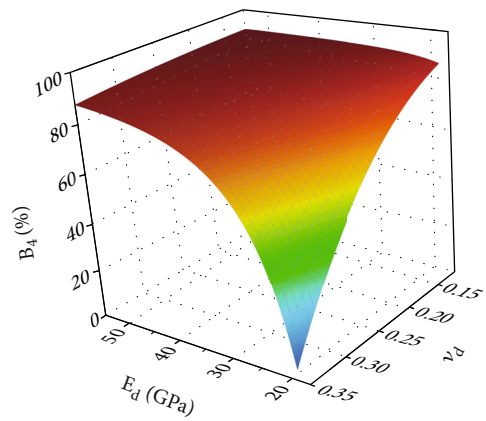

Figure 5: The three-dimensional function relationship of B_4, E_d, and ν_d.

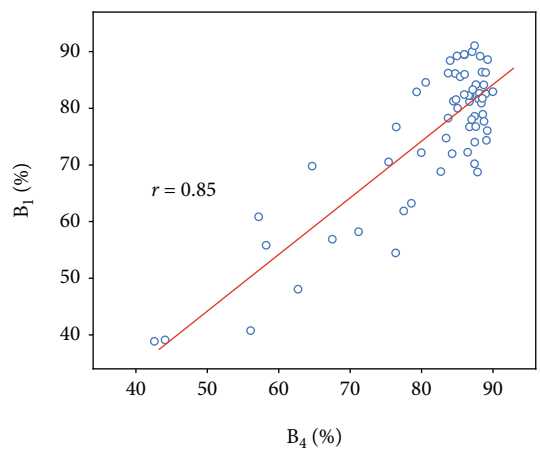

Figure 6: Linear relation between B_4 and B_1.

$$B_2 = \frac{1}{2}\left(\frac{E - E_{\min}}{E_{\max} - E_{\min}} + \frac{\nu - \nu_{\max}}{\nu_{\min} - \nu_{\max}}\right) \times 100\%, \tag{2}$$

$$B_3 = \frac{E}{\nu} \times 100\%, \tag{3}$$

where E is the modulus of elasticity, $E_{\max}$ is the largest value of elastic modulus in the measured area, $E_{\min}$ the smallest value of elastic modulus, ν is the Poisson's ratio, $V_{\max}$ is the largest value of the Poisson's ratio, and $V_{\min}$ is the smallest value of the Poisson's ratio.

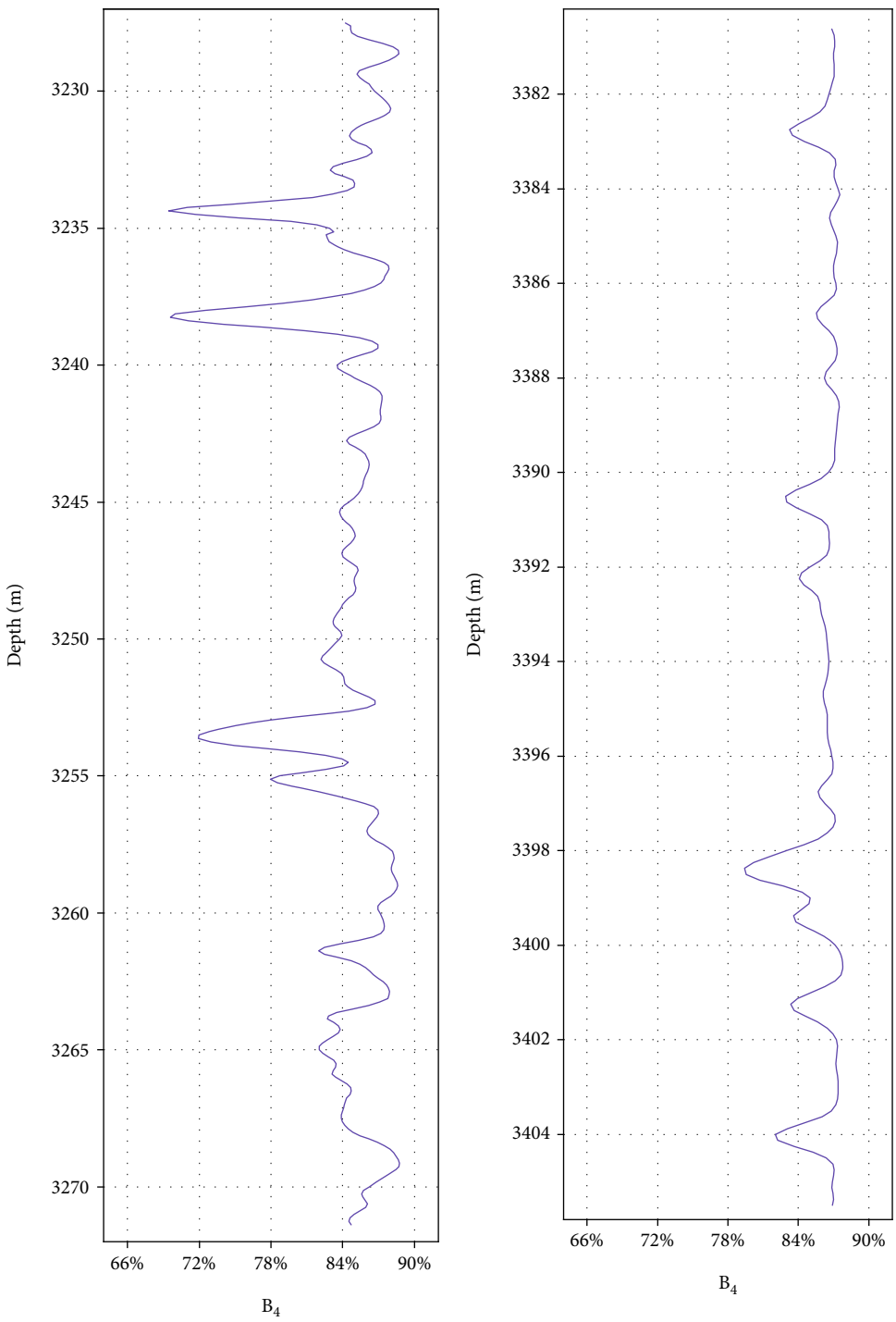

(a) The upper sweet spot of well J10014

(b) The lower sweet spot of well J10014

Figure 7: Continued.

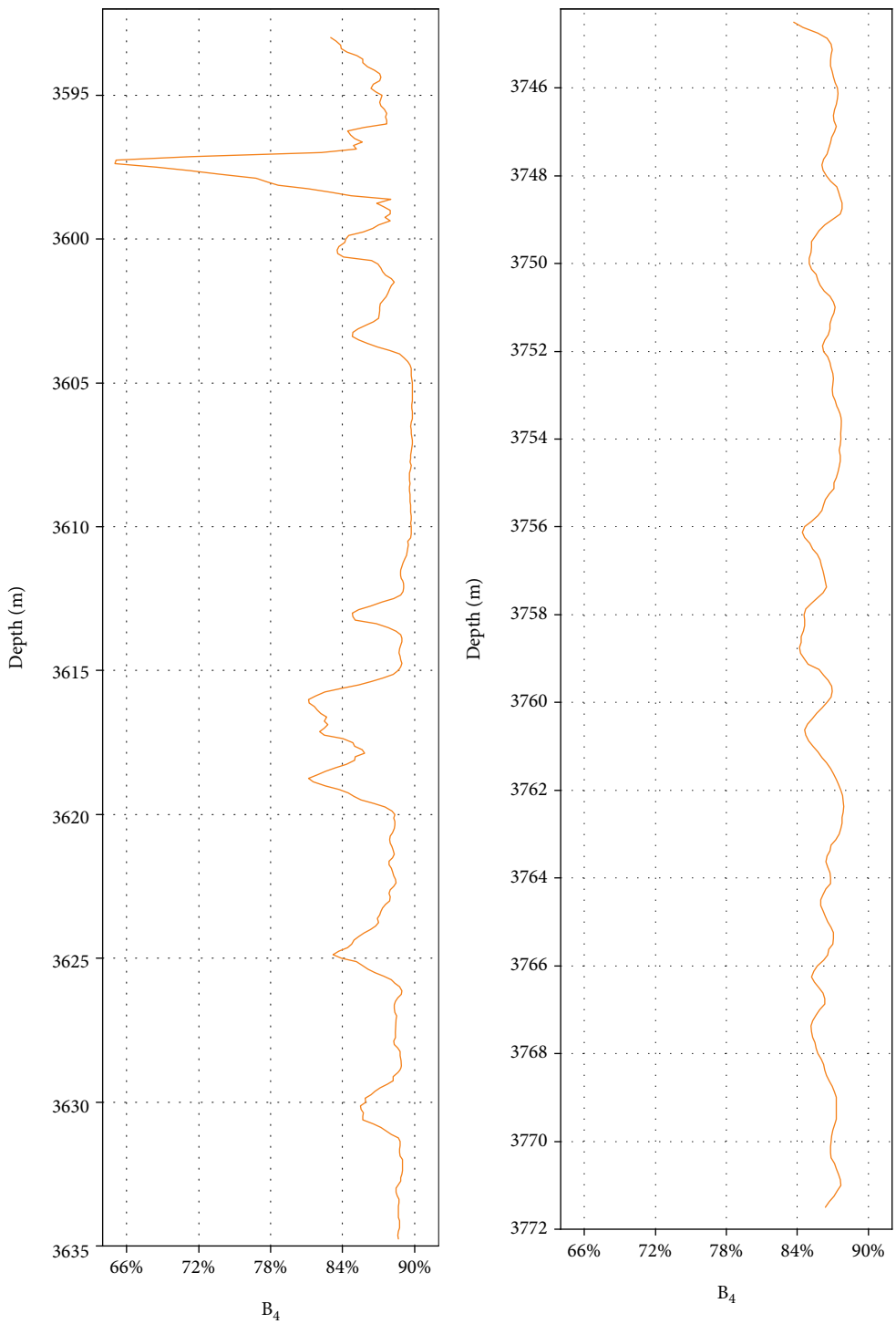

(c) The upper sweet spot of well J251

(d) The lower sweet spot of well J251

Figure 7: The vertical distribution of brittleness in wells J10014 and J251.

Although shortcomings exist in the present evaluation methods using elastic properties, the technique of brittleness evaluation based on elastic properties has significant advantages. Especially in the brittleness evaluation via acoustic logging data, a reasonable brittleness calculation model can provide bases for evaluating the continuous brittleness of reservoirs.

Exploring the relationship between dynamic elastic constant and brittleness of rocks could provide proper support for brittleness calculation from field acoustic logging data. The acoustic parameters of rock cores were tested, and the dynamic elastic modulus and dynamic Poisson's ratio were calculated from Equations (4) and (5) [41]. Referring to the previous research on the

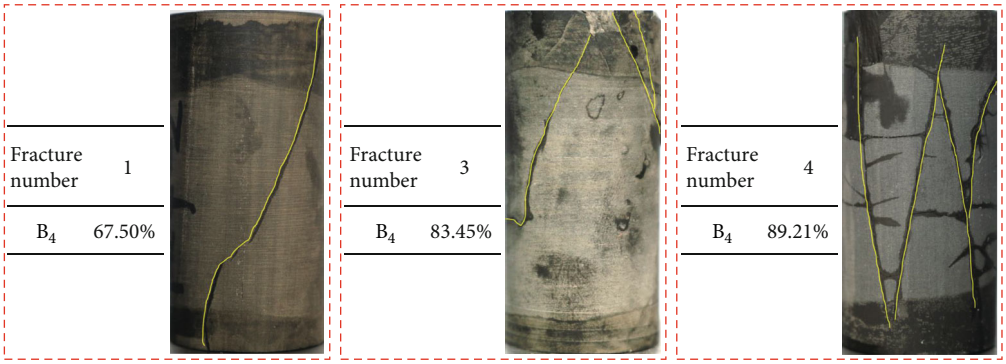

Figure 8: The typical fracture characteristics of shale oil cores after failure.

relationship of elastic constant and brittleness [38, 39], a three-parameter model for calculating the factor of rock brittleness was proposed in this paper, as shown in Equation (6), where α is related to the influence of the dynamic Poisson's ratio on brittleness and β would decide the proportion of the dynamic elastic modulus.

$$E_d = \frac{\rho V_s^2\left(3V_p^2 - 4V_s^2\right)}{V_p^2 - V_s^2}, \tag{4}$$

$$\nu_d = \frac{\left(V_p/V_s\right)^2 - 2}{2\left[\left(V_p/V_s\right)^2 - 1\right]}, \tag{5}$$

$$F_d = \alpha E_d^{\beta} \nu_d^{\gamma}, \tag{6}$$

where V_p is the longitudinal wave velocity, V_s the shear wave velocity, ρ the density of rock sample, E_d the dynamic elastic modulus, ν_d the dynamic Poisson's ratio, F_d the rock brittleness evaluation factor, and α, β, γ the relevant parameters for calculating rock brittleness.

In the three-parameter model for evaluating the brittleness factor, determining the values of the three parameters is the key. In order to improve the accuracy of brittleness evaluation based on dynamic elastic properties, the global optimization method was used to solve the parameters in this paper, aimed at the consistency with the results by the energy method. We defined r as the correlation coefficient between B_1 and F_d, as in Equation (7), where r is an equation containing parameters α, β, γ. If the brittleness evaluation model based on dynamic elastic constant was expected to present high consistency with the energy method, the correlation coefficient r should be sufficiently large. During the solution of parameters based on the global optimization algorithm, the optimal solution of α, β, γ could be obtained when r reaches the maximum value in Equation (8).

In this paper, the maximum value of the correlation coefficient r is found to be 0.85 when α is -2.478, β is -2.77, and γ is 2.65. The improved brittleness evaluation model based on dynamic elastic properties is shown in Equation (9). For the shale oil of Lucaogou Formation in Jimusar Sag, the brittleness evaluation model is shown in Equation (10).

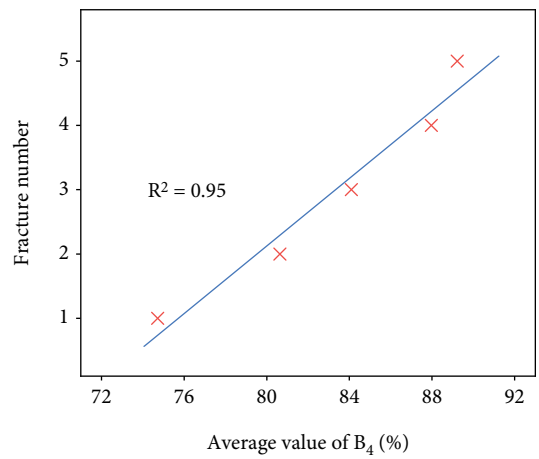

Figure 9: The relationship between B_4 and fracture number.

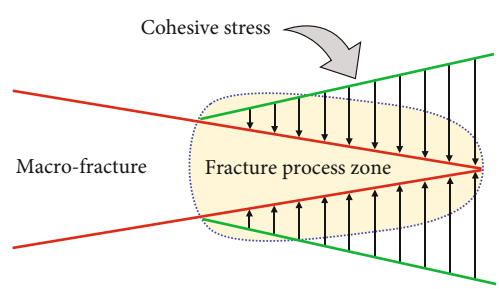

Figure 10: The fracture process zone ahead of the fracture.

$$r = \frac{\mathrm{Cov}(B_1, F_d)}{\sqrt{\mathrm{Var}[B_1]\mathrm{Var}[F_d]}}, \tag{7}$$

$$r_{\max} = f\left(\alpha_{\mathrm{opt}}, \beta_{\mathrm{opt}}, \gamma_{\mathrm{opt}}\right), \tag{8}$$

$$B_4 = B_{1m} + kF_d, \tag{9}$$

$$B_4 = 91.04\% - 49190E_d^{-2.77}\nu_d^{2.65}, \tag{10}$$

where r is the correlation coefficient of B_1 and F_d; α_{opt}, β_{opt}, and γ_{opt} are the optimized solutions of the corresponding parameters; B_4 is the calculated value of brittleness based

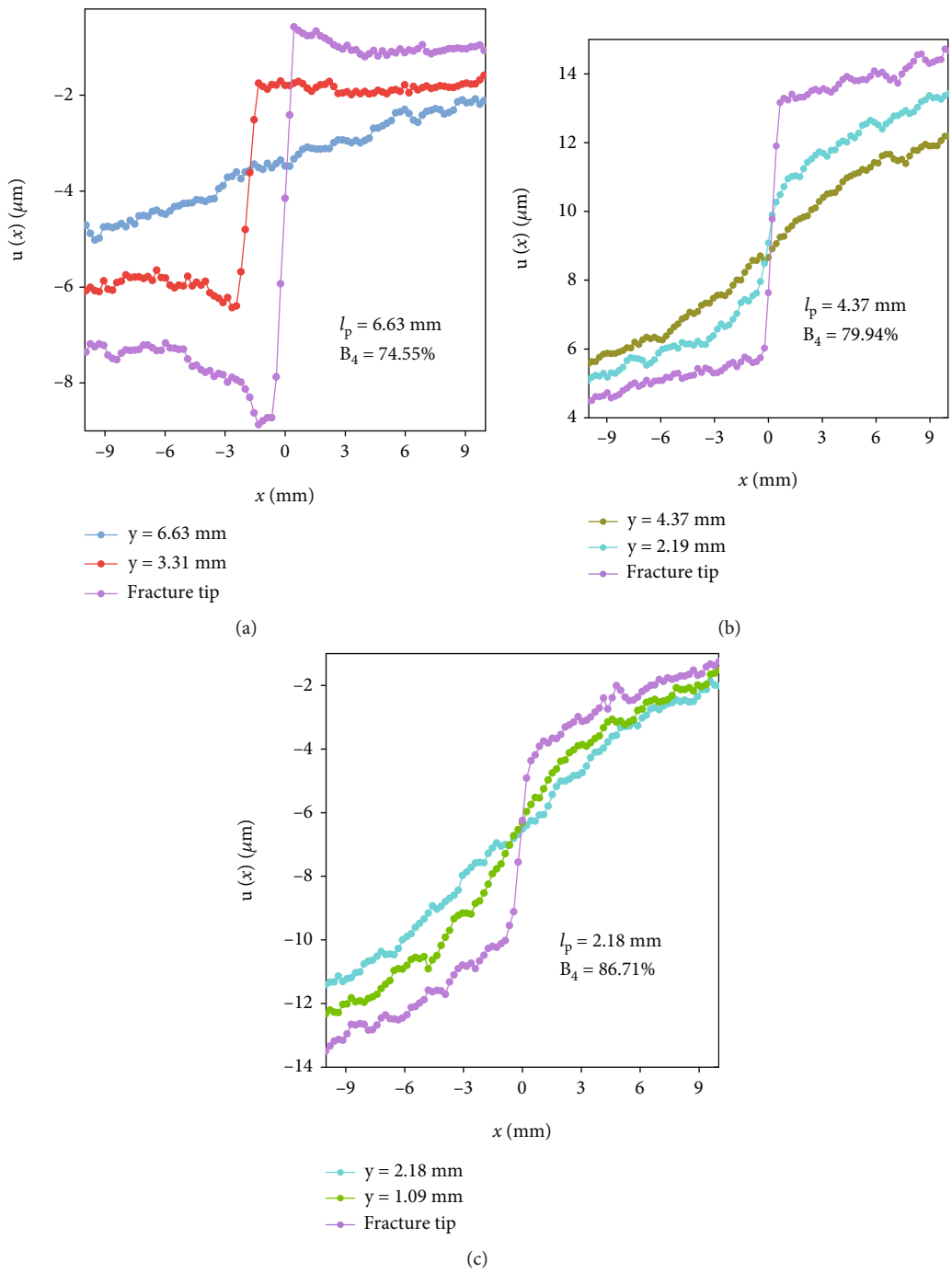

Figure 11: Characterization of the length of fracture process zone in different brittle rocks.

on the improved brittleness evaluation model; k is the linear fitting slope of B_1 and F_d; and B_{1m} is the extreme value of energy method (when α is positive, B_{1m} is the minimum value; when α is negative, B_{1m} is the maximum value).

Figure 5 shows the three-dimensional function relationship of B_4, E_d, and ν_d, drawn by the improved brittleness evaluation model based on dynamic elastic properties. It could be found that the brittleness index would increase when the elastic modulus increases and the Poisson's ratio decreases, consistent with the previous opinions. However, the influence of elastic properties on brittleness is nonlinear. In this paper, we discover the effects of the dynamic elastic properties on the brittleness index intuitively from the improved model.

Figure 6 is the relationship between B_4 calculated by the improved brittleness evaluation model and B_1 calculated by the energy method, where a significant linear correlation relationship could be found, with a correlation coefficient of 0.85, indicating the reliability of the improved brittleness evaluation model based on dynamic elastic properties.

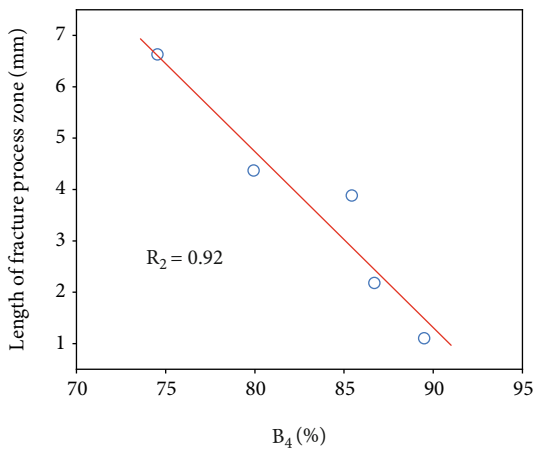

Figure 12: The relationship between B_4 and the length of the fracture process zone in Lucaogou Formation.

3.3. Application of the Brittleness Evaluation Model. In the previous section, an improved brittleness evaluation model based on dynamic elastic properties is proposed, providing a basis to evaluate the continuous brittleness distribution of reservoirs through acoustic logging data. Taking two wells in the Jimusar Sag as examples, we evaluated the continuous brittleness of shale oil in the Lucaogou Formation. When calculating the dynamic elastic properties of reservoirs, the relationship between the P-wave and the S-wave needs to be determined since the acoustic wave measured by acoustic logging is mainly P-wave. In this paper, through the indoor acoustic test, it is found that there is a significant linear relationship between the P-wave and the S-wave in the Lucaogou Formation. The relationships in the upper and lower sweet spots are shown in Equations (11) and (12), where r^2 are 0.83 and 0.82, respectively.

$$V_s = 0.5246V_p + 217.3816, \tag{11}$$

$$V_s = 0.5072V_p + 294.9584. \tag{12}$$

Well J10014 and well J251 were selected to analyze the longitudinal brittleness of the upper and lower sweet spots in the Lucaogou Formation. The dynamic elastic properties were calculated continuously based on the acoustic logging data, and then, the brittleness distribution of well J10014 and well J251 in different sweet spots could be obtained, as shown in Figure 7. By comparing the brittleness distribution of the upper and lower sweet spots, we could find that the vertical variation range of the brittleness index in the upper sweet spot is larger than that in the lower sweet spot.

4. Discussion

The improved brittleness evaluation model proposed in this paper could calculate the continuous brittleness of reservoirs through acoustic logging data. Compared with the conventional method of brittleness calculation based on elastic properties [38, 39], we found that the correlation coefficients between B_1 and B_2/B_3 were only 0.70 and 0.67, respectively, and the accuracy of the brittleness calculated by the improved model was improved by 21% and 27%, respectively. However, the reliability of the improved brittleness evaluation model still needs to be verified and discussed by mechanical experiments.

4.1. The Characteristics of Compression Fractures in Different Brittle Rocks. Conventional understanding believes that the brittleness index of rock would affect the complexity of the hydraulic fractures: the more brittle the rock is, the more complex the fractures are [10, 29]. To study the relationship between the fracture complexity and the brittleness index calculated by the improved model, we characterize the fracture complexity by the number of compression failure fractures in this paper. As in Figure 8, differences of compression fracture complexity exist in different brittle specimens of the Lucaogou Formation.

Based on the statistics of specimens, the number of compression failure fractures in the Lucaogou Formation is generally between 1 and 5. We calculated the average value of the brittleness index B_4 from core samples with the same number of compression failure fractures. As shown in Figure 9, there is a significant positive correlation between B_4 and the number of fractures. That is to say, the more brittle the rock is, the more complex the fractures are, verifying the reliability of the improved model in evaluating rock brittleness.

4.2. The Length of Fracture Process Zone in Different Brittle Rocks. The fracture process zone is a nonlinear development zone in front of the macrofracture, which could be regarded as a plastic zone roughly [42–45]. In the hydraulic fracturing of reservoirs, the fracture process zone will be generated ahead of the hydraulic fracture, as shown in Figure 10. There would be energy consumption in the development of the fracture process zone so that the energy consumption will increase with the length of the FPZ. The previous research indicates that the fracture process zone length is the inverse index of brittleness [46], and the longer the rock fracture process zone is, the lower the brittleness is. Although the monitoring and identification of the fracture process zone are complex, compared with other methods, the fracture process zone length could accurately reflect the brittleness of the rock.

In this paper, the reservoir cores with different brittleness indexes calculated by the optimization model were selected to carry out three-point bending fracture tests. The digital image correlation method was used to monitor the fracture process in real time, and the displacements of the specimens were calculated by an open-source program [47]. Based on the existing methods, the fracture process zone length of reservoir rocks was identified by the characteristics of horizontal displacement [48–50]. And the typical fracture process zone lengths of Lucaogou Formation rocks with different brittleness B_4 were characterized in Figure 11, where the length of the fracture process zone is larger when the rock brittleness evaluated by the improvement model is smaller.

A linear relation could be found from B_4 and the length of fracture process zone (Figure 12), providing a basis to evaluate the fully developed length of the fracture process zone of the Lucaogou Formation using acoustic logging, as in Equation (13). Previous studies show that the length of the fracture process zone is related to the fracture energy [46], indicating that more energy would be consumed in a longer process zone. The experimental results mean that B_4 is negatively correlated with the dissipated energy, verifying the reliability of the improved brittleness evaluation model based on dynamic elastic properties.

$$l_p = 32.16 - 34.27B_4\,(B_4 < 91.04\%). \tag{13}$$

5. Conclusion

In this paper, the reservoir cores of shale oil in the Lucaogou Formation, Jimusar Sag, were selected to carry out the triaxial compression, acoustic wave, and three-point bending tests. Based on the prepeak energy characteristics of the triaxial stress-strain curve, the brittleness index of different horizons in the upper and lower sweet spots was calculated. The improved model based on dynamic elastic properties was proposed to evaluate the continuous brittleness of reservoirs, verified by the compression fracture characteristics and the length of the fracture process zone, and the following conclusions are obtained.

(1) From the calculated results of rock brittleness, it is found that differences exist among horizons in the upper and lower sweet spots. The brittleness index of $P_2l_2^{2\text{-}2}$ is the largest in the upper sweet spot, which is 84.61%, and the brittleness index of $P_2l_1^{2\text{-}2}$ is the smallest in the lower, reaching 67.75%. The continuous brittleness in the Lucaogou Formation calculated by acoustic logging data shows that the vertical variation in the upper sweet spot is more significant than the lower

(2) A brittleness evaluation model based on dynamic elastic properties was proposed after the optimization of parameters. The linear correlation coefficient of the brittleness calculated by the improved model and the energy method is 0.85, which improves the accuracy of brittleness evaluation by 21% and 27%, respectively, compared with the results by the conventional evaluation methods from elastic properties

(3) The improved brittleness evaluation model was verified by the results of mechanical experiments, where the compression fractures would be more complex when the brittleness index is larger. The relationship between B_4 and the length of the fracture process zone obtained by experiments presents a linear negative correlation, indicating the reliability of the improved model

Data Availability

The data used to support the findings of this study are included within the article.

Conflicts of Interest

The authors declare that they have no conflicts of interest.

Acknowledgments

This study was supported by the Xinjiang Major Science and Technology Special Projects of China National Petroleum Corporation: Research and Application of Key Technologies in the Exploration and Development of Continental Medium and High Maturity Level Shale Oil (2019E-2607), Integration and Testing of Crucial Engineering Technologies in Horizontal Wells for the Efficient Development of Shale Oil in Jimusar, National Demonstration Area (2020F-50).

References

[1] Z. Kang, Z. Wang, Y. Lu, R. Cao, D. Huang, and Q. Meng, "Investigation on the effect of atmosphere on the pyrolysis behavior and oil quality of Jimusar oil shale," *Geofluids*, vol. 2022, Article ID 1408690, 9 pages, 2022.

[2] M. O. Eshkalak, S. D. Mohaghegh, and S. Esmaili, "Geomechanical properties of unconventional shale reservoirs," *Journal of Petroleum Engineering*, vol. 2014, 10 pages, 2014.

[3] B. Liu, A. Bechtel, R. F. Sachsenhofer, D. Gross, R. Gratzer, and X. Chen, "Depositional environment of oil shale within the second member of Permian Lucaogou Formation in the Santanghu Basin, Northwest China," *International Journal of Coal Geology*, vol. 175, pp. 10–25, 2017.

[4] B. Liu, H. Wang, X. Fu et al., "Lithofacies and depositional setting of a highly prospective lacustrine shale oil succession from the Upper Cretaceous Qingshankou Formation in the Gulong sag, northern Songliao Basin, Northeast China," *American Association of Petroleum Geologists Bulletin*, vol. 103, no. 2, pp. 405–432, 2019.

[5] Z. Z. Le, G. Q. Zhang, H. R. Dong, L. Z. Bin, and Y. X. Nie, "Creating a network of hydraulic fractures by cyclic pumping," *International Journal of Rock Mechanics and Mining Sciences*, vol. 97, no. 97, pp. 52–63, 2017.

[6] L. Chen, G. Zhang, Y. Lyu, Z. Li, and X. Zheng, "Visualization study of hydraulic fracture propagation in unconsolidated sandstones," in *53rd US rock mechanics/geomechanics symposium*, New York City, June 2019.

[7] D. Zhou, G. Zhang, Y. Wang, and Y. Xing, "Experimental investigation on fracture propagation modes in supercritical carbon dioxide fracturing using acoustic emission monitoring," *International Journal of Rock Mechanics and Mining Sciences*, vol. 110, pp. 111–119, 2018.

[8] J. Li, Y. Zou, S. Shi et al., "Experimental study on fracture propagation mechanism of shale oil reservoir of Lucaogou Formation in Jimusar," *Geofluids*, vol. 2022, Article ID 6598575, 11 pages, 2022.

[9] R. Rickman, M. Mullen, E. Petre, B. Grieser, and D. Kundert, "A practical use of shale petrophysics for stimulation design optimization: all shale plays are not clones of the Barnett Shale," in *SPE annual technical conference and exhibition*, vol. 2, pp. 840–850, Denver, Colorado, USA, Sep. 2008.

[10] S. Kahraman and R. Altindag, "A brittleness index to estimate fracture toughness," *International Journal of Rock Mechanics and Mining Sciences*, vol. 41, no. 2, pp. 343–348, 2004.

[11] K. K. Chong, W. V. Grieser, A. Passman, C. H. Tamayo, N. Modeland, and B. Burke, "A completions guide book to shale-play development: a review of successful approaches towards shale-play stimulation in the last two decades," in *Canadian unconventional resources and international petroleum conference*, Calgary, Alberta, Canada, October 2010.

[12] F. Meng, L. N. Y. Wong, and H. Zhou, "Rock brittleness indices and their applications to different fields of rock engineering: a review," *Journal of Rock Mechanics and Geotechnical Engineering*, vol. 13, no. 1, pp. 221–247, 2021.

[13] Y. Xia, H. Zhou, C. Zhang, S. He, Y. Gao, and P. Wang, "The evaluation of rock brittleness and its application: a review study," *European Journal of Environmental and Civil Engineering*, vol. 26, no. 1, pp. 239–279, 2022.

[14] B. Hou, Y. Zeng, M. Fan, and D. Li, "Brittleness evaluation of shale based on the Brazilian splitting test," *Geofluids*, vol. 2018, 11 pages, 2018.

[15] X. Jin, S. Shah, J. Truax, and J.-C. Roegiers, "A practical petrophysical approach for brittleness prediction from porosity and sonic logging in shale reservoirs," in *SPE annual technical conference and exhibition*, Amsterdam, The Netherlands, October 2014.

[16] M. Heidari, G. R. Khanlari, M. Torabi-Kaveh, S. Kargarian, and S. Saneie, "Effect of porosity on rock brittleness," *Rock Mechanics and Rock Engineering*, vol. 47, no. 2, pp. 785–790, 2014.

[17] D. M. Jarvie, R. J. Hill, T. E. Ruble, and R. M. Pollastro, "Unconventional shale-gas systems: the Mississippian Barnett Shale of North-Central Texas as one model for thermogenic shale-gas assessment," *American Association of Petroleum Geologists Bulletin*, vol. 91, no. 4, pp. 475–499, 2007.

[18] A. Hofmann, C. Rigollet, E. Portier, and S. Burns, "Gas shale characterization-results of the mineralogical, lithological and geochemical analysis of cuttings samples from radioactive Silurian Shales of a Palaeozoic Basin, SW Algeria," in *North Africa Technical Conference and Exhibition*, Cairo, Egypt, April 2013.

[19] B. Liu, S. Wang, X. Ke et al., "Mechanical characteristics and factors controlling brittleness of organic-rich continental shales," *Journal of Petroleum Science and Engineering*, vol. 194, article 107464, 2020.

[20] R. Sierra, M. H. Tran, Y. N. Abousleiman, and R. M. Slatt, "Woodford shale mechanical properties and the impacts of lithofacies," in *44th US rock mechanics symposium and 5th US-Canada rock mechanics symposium*, Salt Lake City, Utah, June 2010.

[21] D. Zhang, P. G. Ranjith, and M. S. A. Perera, "The brittleness indices used in rock mechanics and their application in shale hydraulic fracturing: a review," *Journal of Petroleum Science and Engineering*, vol. 143, pp. 158–170, 2016.

[22] B. Tarasov and Y. Potvin, "Universal criteria for rock brittleness estimation under triaxial compression," *International Journal of Rock Mechanics and Mining Sciences*, vol. 59, pp. 57–69, 2013.

[23] R. Nygård, M. Gutierrez, R. K. Bratli, and K. Høeg, "Brittle-ductile transition, shear failure and leakage in shales and mudrocks," *Marine and Petroleum Geology*, vol. 23, no. 2, pp. 201–212, 2006.

[24] S. Yagiz, "Assessment of brittleness using rock strength and density with punch penetration test," *Tunnelling and Underground Space Technology*, vol. 24, no. 1, pp. 66–74, 2009.

[25] C. Zhang, J. Cao, E. Li, Y. Wang, W. Xiao, and Y. Qin, "Revisiting controls on shale oil accumulation in saline lacustrine basins: the Permian Lucaogou Formation mixed rocks, Junggar Basin," *Geofluids*, vol. 2021, 25 pages, 2021.

[26] J. Lu, C. Zhang, J. Zeng, and H. Yuan, "Research on the oil-bearing difference of bedding fractures: a case study of Lucaogou Formation in Jimsar Sag," *Geofluids*, vol. 2021, 21 pages, 2021.

[27] L. Hou, X. Luo, Z. Zhao, and L. Zhang, "Identification of oil produced from shale and tight reservoirs in the Permian Lucaogou Shale sequence, Jimsar Sag, Junggar Basin, NW China," *ACS Omega*, vol. 6, no. 3, pp. 2127–2142, 2021.

[28] X. Wang, Y. Song, X. Guo et al., "Pore-throat structure characteristics of tight reservoirs of the Middle Permian Lucaogou formation in the Jimsar Sag, Junggar Basin, Northwest China," *Journal of Petroleum Science and Engineering*, vol. 208, p. 109245, 2022.

[29] H. Shimizu, T. Ito, T. Tamagawa, and K. Tezuka, "A study of the effect of brittleness on hydraulic fracture complexity using a flow-coupled discrete element method," *Journal of Petroleum Science and Engineering*, vol. 160, pp. 372–383, 2018.

[30] Y. Zhi, H. Lianhua, L. Senhu et al., "Geologic characteristics and exploration potential of tight oil and shale oil in Lucaogou Formation in Jimsar Sag," *China Petroleum Exploration*, vol. 23, no. 4, pp. 76–85, 2018.

[31] B. G. Tarasov, "Superbrittleness of rocks at high confining pressure," in *Proceedings of the Fifth International Seminar on Deep and High Stress Mining*, pp. 119–133, Perth, Australian, 2010.

[32] B. G. Tarasov and M. F. Randolph, "Superbrittleness of rocks and earthquake activity," *International Journal of Rock Mechanics and Mining Sciences*, vol. 48, no. 6, pp. 888–898, 2011.

[33] W. Jb and W. F. Brace, "A fracture criterion for brittle anisotropic rock," *Journal of Geophysical Research*, vol. 69, no. 16, pp. 3449–3456, 1964.

[34] W. R. Wawersik and C. H. Fairhurst, "A study of brittle rock fracture in laboratory compression experiments," *International Journal of Rock Mechanics and Mining Sciences & Geomechanics Abstracts*, vol. 7, no. 5, pp. 561–575, 1970.

[35] L. I. Baron, B. M. Loguntsov, and I. Z. Posin, *Determination of rock properties*, NTILGD. Published online, Moscow, 1962.

[36] V. Hucka and B. Das, "Brittleness determination of rocks by different methods," *International Journal of Rock Mechanics and Mining Sciences*, vol. 11, no. 10, pp. 389–392, 1974.

[37] W. Baocheng, L. Jianmin, W. Yuanyue, H. Le, Z. Tingfeng, and Z. Yushi, "Development practices of geology-engineering integration on upper sweet spots of Lucaogou Formation shale oil in Jimsar Sag, Junggar Basin," *China Petroleum Exploration*, vol. 24, no. 5, pp. 679–690, 2019.

[38] W. V. Grieser and J. M. Bray, "Identification of production potential in unconventional reservoirs," in *Production and Operations Symposium*, Oklahoma City, Oklahoma, U.S.A, March 2007.

[39] Z. Liu and Z. Sun, "New brittleness indexes and their application in shale/clay gas reservoir prediction," *Petroleum Exploration and Development*, vol. 42, no. 1, pp. 117–124, 2015.

[40] B. Liu, K. Liu, A. Abarghani et al., "1D mechanical earth modeling in the Permian Lucaogou Shale of the Santanghu Basin, Northwest China, from a complete set of laboratory data," *Interpretation*, vol. 9, no. 2, pp. T357–T372, 2021.

[41] N. A. Al-Shayea, "Effects of testing methods and conditions on the elastic properties of limestone rock," *Engineering Geology*, vol. 74, no. 1-2, pp. 139–156, 2004.

[42] L. Chen, G. Zhang, Z. Zou, Y. Guo, and X. Zheng, "The effect of fracture growth rate on fracture process zone development in quasi-brittle rock," *Engineering Fracture Mechanics*, vol. 258, p. 108086, 2021.

[43] L. Chen, G. Zhang, Z. Zou, Y. Guo, and X. Du, "Experimental observation of fracture process zone in sandstone from digital imaging," in *54th US Rock Mechanics/Geomechanics Symposium*, Golden, Colorado, USA, June 2020.

[44] Y. Xing, B. Huang, E. Ning, L. Zhao, and F. Jin, "Quasi-static loading rate effects on fracture process zone development of mixed-mode (I-II) fractures in rock-like materials," *Engineering Fracture Mechanics*, vol. 240, p. 107365, 2020.

[45] Y. Xing and B. Huang, "Injection rate-dependent deflecting propagation rule of hydraulic fracture: insights from the rate-dependent fracture process zone of mixed-mode (I-II) fracturing," *Geofluids*, vol. 2021, Article ID 8199095, 17 pages, 2021.

[46] M. Elices, G. V. Guinea, J. Gómez, and J. Planas, "The cohesive zone model: advantages, limitations and challenges," *Engineering Fracture Mechanics*, vol. 69, no. 2, pp. 137–163, 2002.

[47] J. Blaber, B. Adair, and A. Antoniou, "Ncorr: open-source 2D digital image correlation Matlab software," *Experimental Mechanics*, vol. 55, no. 6, pp. 1105–1122, 2015.

[48] Q. Lin and J. F. Labuz, "Fracture of sandstone characterized by digital image correlation," *International Journal of Rock Mechanics and Mining Sciences*, vol. 60, pp. 235–245, 2013.

[49] Y. Nie, G. Zhang, Y. Xing, and S. Li, "Influence of water-oil saturation on the fracture process zone: a modified Dugdale-Barenblatt model," *Energies*, vol. 11, no. 11, p. 2882, 2018.

[50] G. Zhang, Y. Xing, and L. Wang, "Comprehensive sandstone fracturing characterization: integration of fiber Bragg grating, digital imaging correlation and acoustic emission measurements," *Engineering Geology*, vol. 246, pp. 45–56, 2018.

Hindawi
Geofluids
Volume 2022, Article ID 4370907, 11 pages
https://doi.org/10.1155/2022/4370907

Research Article

Investigation on Hydration and Deformation Characteristics of Shale Using X-ray Computed Tomography

Yong-Ting Duan,[1,2] **Xiao Li**,[3,4] **Bo Zheng**,[3] **and Bai-Cun Yang**[5]

[1]*Key Laboratory of Ministry of Education on Safe Mining of Deep Metal Mines, School of Resources and Civil Engineering, Northeastern University, Shenyang 110819, China*
[2]*Key Laboratory of Liaoning Province on Deep Engineering and Intelligent Technology, Northeastern University, Shenyang 110819, China*
[3]*Key Laboratory of Shale Gas and Geoengineering, Institute of Geology and Geophysics, Chinese Academy of Sciences, Beijing 100029, China*
[4]*Institutions of Earth Science, Chinese Academy of Sciences, Beijing 100029, China*
[5]*School of Resources and Civil Engineering, Northeastern University, Shenyang 110819, China*

Correspondence should be addressed to Yong-Ting Duan; duanyongting@mail.neu.edu.cn

Received 24 February 2022; Revised 20 March 2022; Accepted 4 April 2022; Published 22 April 2022

Academic Editor: Bing Hou

The physical and mechanical properties of shale are significant for completion engineering and fracturing design for shale oil and gas production. To further study the water effect and the deformation characteristics of shale, some cylindrical specimens were soaked at three periods (0, 20, and 60 days), the in situ uniaxial compression tests were conducted, and the CT technique was used at different hydration and loading stages. Based on the CT results, the image gray variance value in each hydration specimen was extracted; the evolution results show that the water imbibition has a significant influence on the structure of shale in the early soaking stage, and the influence degree is more evident in the external region. Moreover, the water influence on the mechanical property of shale was analyzed by comparing the failure characteristics of specimens with and without hydration; the CT results show that the hydration treatment affects the failure mode of shale. In addition, a new method based on the CT image was proposed to calculate the lateral strain; the evolution of the axial stress-strain curve reveals that the expansion phenomena exist before failure, and the evolution process includes four stages. At last, the differences in the deformation degree were discussed by analyzing the volumetric strain at different CT scanning layers; the results reflect the expansion or compression degree along with the specimen height. Those conclusions can help us further understand the water effect and the deformation characteristics of shale oil and gas reservoirs.

1. Introduction

In 2018, China's dependency on foreign oil and natural gas had reached 69.8% and 45.3%. Exploring and developing complementary and replacement sources of conventional energy have become top priorities. Shale oil and gas, as unconventional energy, have attached attention and will play an essential role in ensuring China's oil and gas security and economic growth [1–3]. So far, hydraulic fracturing is a commonly used technique for recovery enhancement in shale oil and gas development. Shale's physical and mechanical properties are of great significance for completion engineering and fracturing design for shale oil and gas production [4, 5].

Previous studies [6, 7] have shown that the fraction of recovered flow backwater with an average of 10% or less after fracturing operation, and water absorption in shale often causes the swelling of rocks, leading to cracks and fractures. In order to find out how the remaining fracturing fluid affects the shale formation, some experimental studies about the water effect on shale have been made. Ma and Chen [8] investigated the mesodamage characteristics of shale

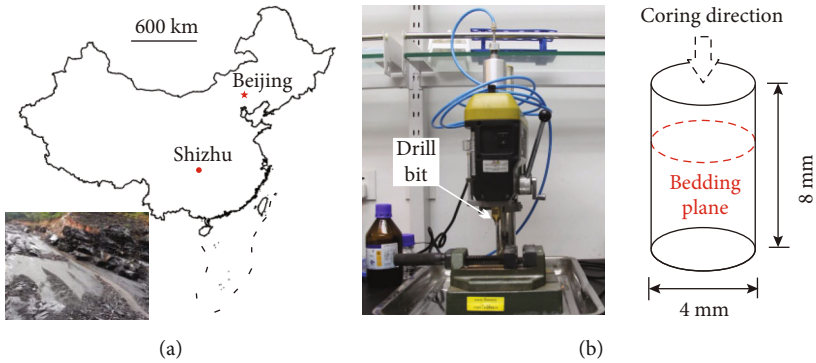

Figure 1: The location of sampling (a), the hand-operated electric drill and the diagram of a specimen (b).

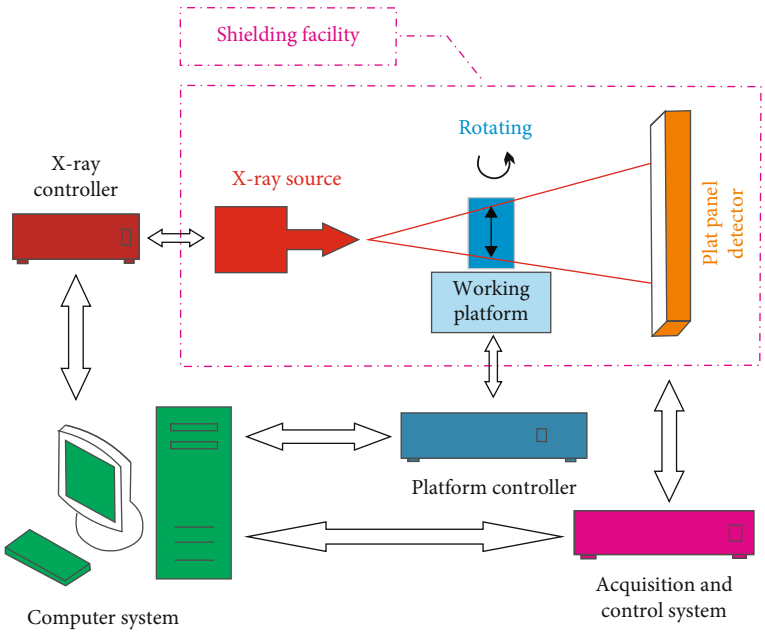

Figure 2: Schematic diagram of the industrial cone-beam X-ray system (modified after Ma [32]).

hydration and analyzed the relationships between damage variables and shale hydration under different stages based on the CT technique. Roshan et al. [9] performed a set of experiments on partially saturated shale samples and revealed that both capillary forces and surface-osmotic hydration control the water adsorption into partially saturated shale. Zhou et al. [10] qualitatively analyzed the effects of capillarity and osmosis diffusion on the imbibition process of shale. Liu et al. [11] researched the shale damage caused by hydration by immersion experiment and analyzed the mechanism of formation and propagation of cracks. Chakraborty et al. [12] presented an experimental study of water imbibition in shale and investigated the time-dependent permeability evolution. Zhang and Sheng [7] investigated the influence of hydration on permeability in shale, and generation fractures were observed by CT technique. The previous studies have clarified the effect of hydration on the internal structure of shale. However, how the remaining fracturing water affects the mechanical properties of shale formation is still not solved and needs further research.

In shale gas exploration, the remaining fracturing water and the production of shale gas will make the shale matrix shrink or swell, causing its strain. Thus, it is necessary to investigate the volumetric strain of shale induced by the combined effects of adsorption fluid and stress compression, especially the stress-volumetric strain curve, which is the sensitive indicator in the study of basic mechanical properties of shale [13, 14]. The earliest study that used the volumetric strain to analyze the deformation characteristics of rock was carried out by Brace et al. [15]. Later, many scholars have studied the volumetric strain characteristics of different rocks. For the sedimentary rocks, Jiang et al. [16], Hu et al. [17], and Lu and Liu [18] investigated the sandstone under uniaxial and triaxial compression tests. Gatelier et al. [19] researched the sandstone under two types of cyclic triaxial tests. Palchik and Hatzor [20] and Kelvis and Nordlund [21] analyzed the dolomite and limestone. Pellet and Fabre [22], He et al. [23], and Liang et al. [24] studied the argillaceous rocks, coal, and salt rocks, respectively. For the igneous rocks, Takarli et al. [25] and Liang et al. [26] analyzed the damage process of

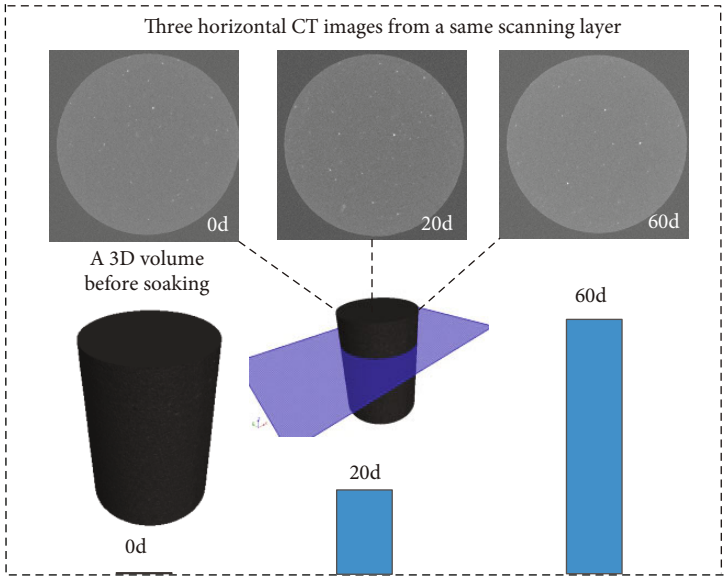

Figure 3: Scanning results of 3D volume before soaking and CT images after three hydration periods of S1.

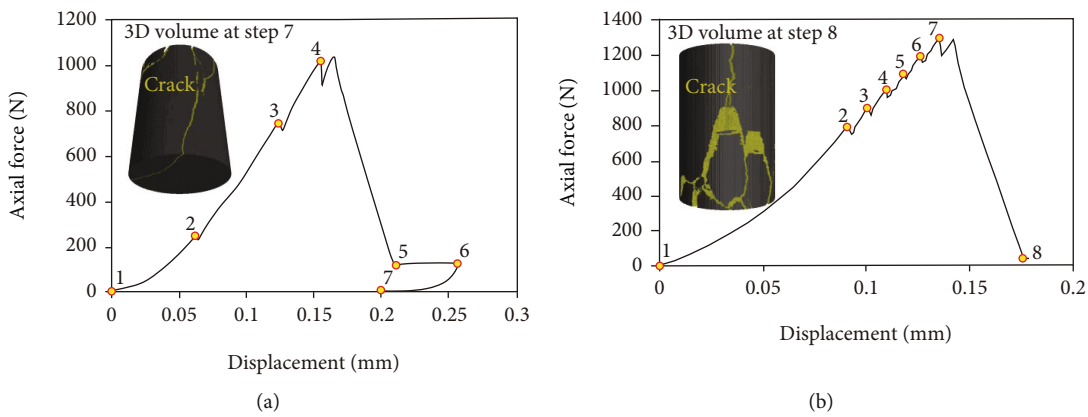

Figure 4: The axial force-displacement relationships and the reconstructed failure 3D volumes at the last scanning steps (the yellow areas are cracks) of S3 (a) and S4 (b).

granite. Pellet et al. [27] and Nicksiar and Martin [28] investigated the characteristics of gabbro and diorite, respectively. For the metamorphic rocks, Huang et al. [29] researched the stress-volumetric strain curves of marble at different loading strain rates. In all the experimental researches above, the deformation characteristics of rocks were described well using the volumetric strain. However, its value was calculated by using the directly measured axial strain and the lateral strain at a center portion of the tested specimen, which would cause the loss of information of the lateral strain in other locations and then the volumetric strain in the whole specimen.

To further study the water effect and the deformation characteristics of shale, some cylindrical specimens were soaked in water for a certain period of time, the in situ (loading and scanning at the same time) uniaxial compression tests were conducted, and the nondestructive CT technique was used for scanning at different hydration and loading stages. Based on the scanned CT results, the image gray variance value in each hydration specimen at different soaking periods was extracted, and the evolution characteristics were quantitatively analyzed. The differences of the crack morphology after uniaxial compression tests between shale specimens with and without hydration process were also analyzed. In addition, a new method based on the CT images was proposed to calculate the lateral strain, and the evolution of axial stress-strain (including the axial strain, lateral strain, and volumetric strain) curve was revealed. At last, the differences of the expansion/compression degree along with specimen height were discussed.

2. Tested Specimens and Equipment

All prepared specimens were cored from the same shale block, which was taken from the outcrop shale formation in Shizhu, Chongqing, China (Figure 1(a)). During the indoor sample preparation, this shale block was fixed under the drill bit of a hand-operated electric drill, and shale specimens with horizontal bedding planes were prepared

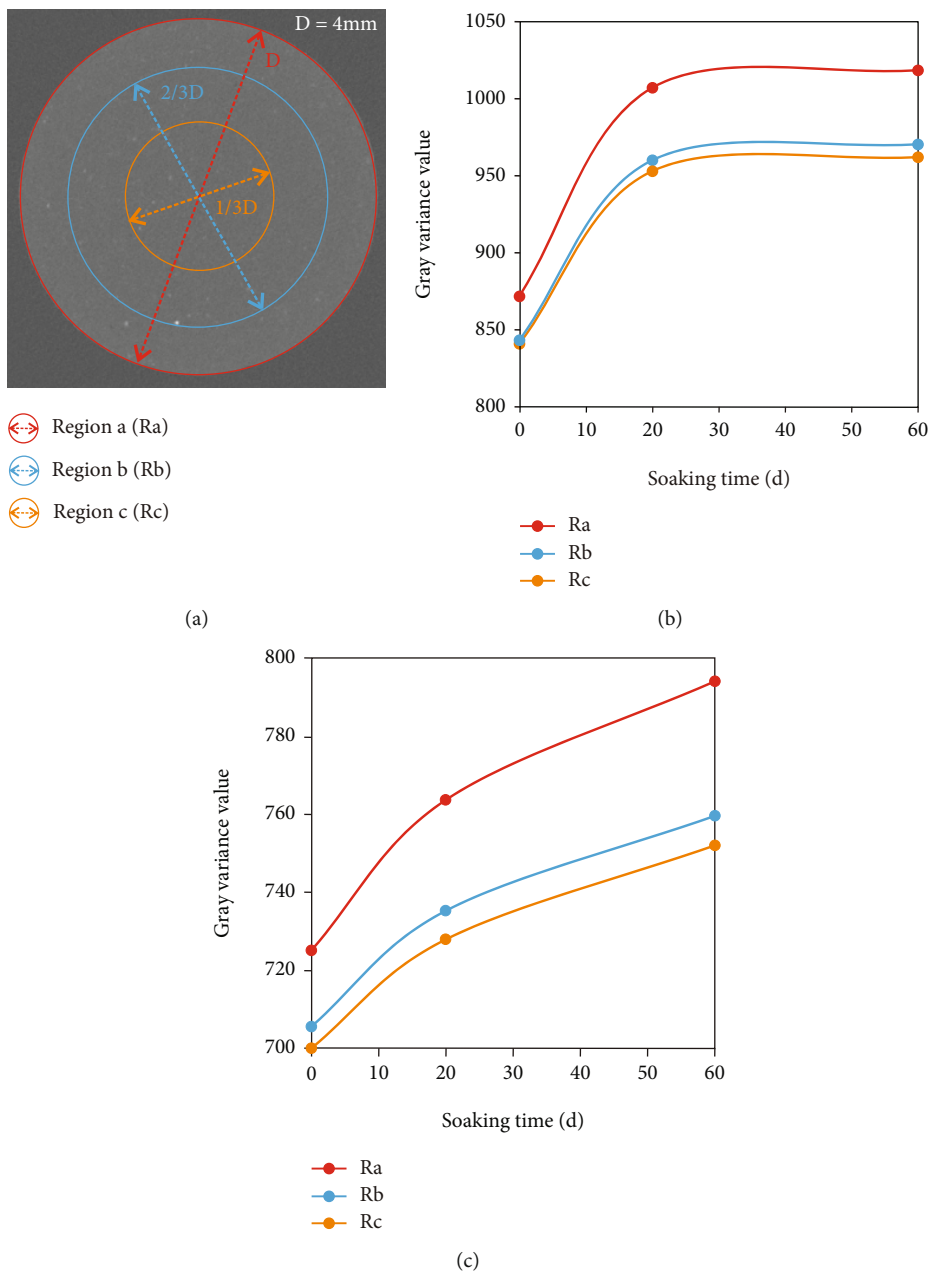

Figure 5: Diagram of statistical regions (a) and evolution curves of gray variance value in S1 (b) and S2 (c).

(Figure 1(b)). In order to obtain the parallel surfaces of samples for testing, a cutting-grinding machine was used to smooth the top and bottom of the drilling specimens. The size of each prepared specimen is with a diameter of 4 mm and a height of 8 mm (Figure 1(b)), and four specimens named S1, S2, S3, and S4 were prepared.

The micro-CT equipment available at the Institute of Geology and Geophysics, Chinese Academy of Sciences, Beijing, China, was used to scan the tested specimens' internal structures [30, 31]. Figure 2 shows the diagram of this device (ZEISS Xradia 520 Versa X-ray microscopy), which is mainly composed of an X-ray source (90 kV in voltage and 88.9 μA in current), working platform, X-ray detector (plat panel), mechanical scanning control system, and shielding facility. At each scanning step, the key workflows to obtain CT images include the following: (1) the X-ray source uses the cone-beam (cone angle of 5.11°), a full vertical projection can first be recorded on the detector after the X-ray had passed through the specimen; (2) the working platform was rotated with an angle of 0.2°, and the specimen was scanned again; (3) the rotating and scanning operations were repeated until the specimen completed a 360° rotating; and (4) those vertical projections were reconstructed to a three-dimensional (3D) volume, and then, the two-dimensional CT images in different directions can be segmented from 3D volume. In addition, for realizing the in situ uniaxial compression tests, a special loading apparatus (DEBEN Microtest CT5000) named the uniaxial

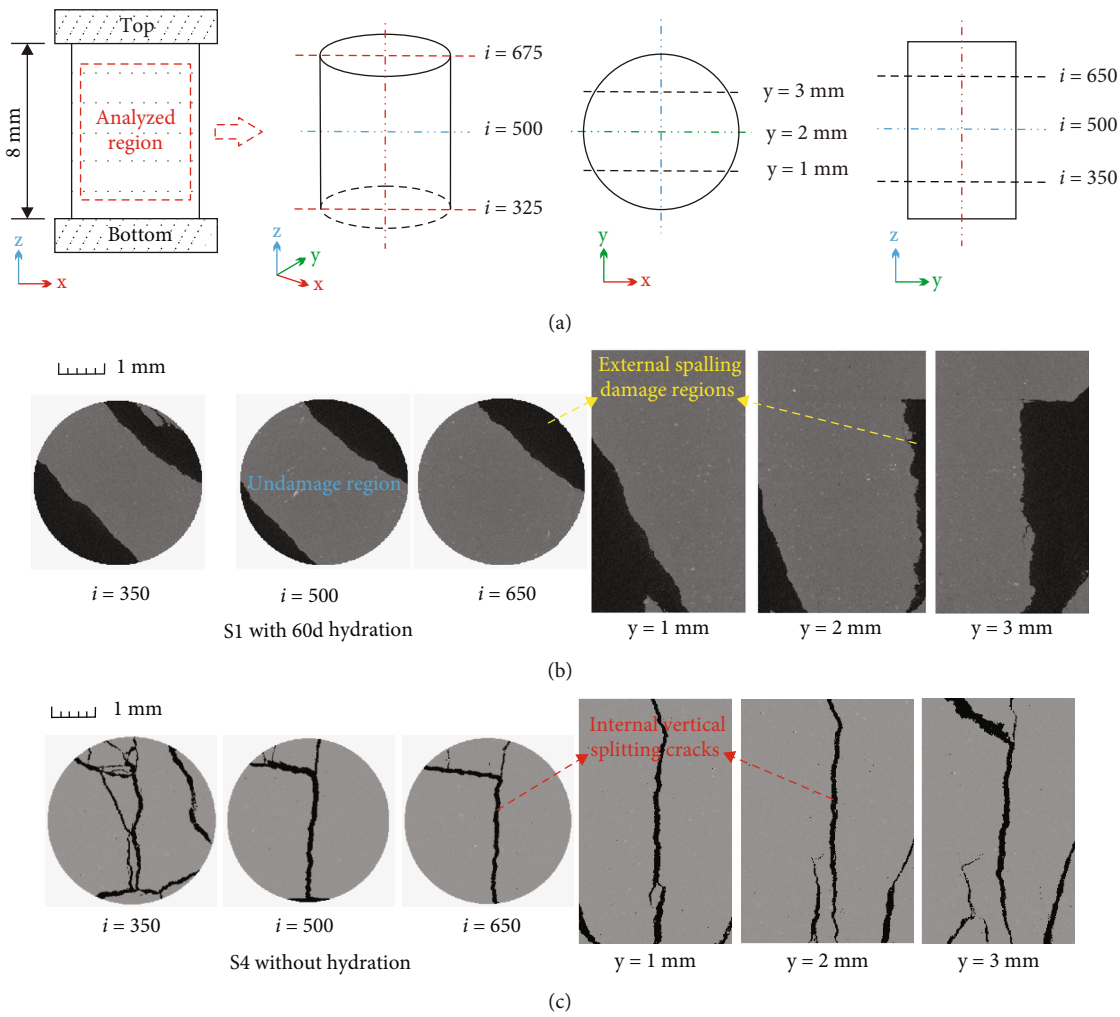

Figure 6: CT slice position (a) and results of failure S1 with 60d hydration (b) and S4 without hydration (c).

compression-tensile attachment was placed on the working platform, and the specimen can be scanned during loading. The maximum allowable pressure of this apparatus is 5 kN, the compression range is from 15 mm to 5 mm, and the adjustable displacement loading rate is 0.03-3 mm/min.

3. Experimental Process and Results

The prepared specimens, S1 and S2, were used for the hydration tests. Firstly, to obtain the internal structural characteristics of shale before soaking, the two specimens were scanned under the natural state using the high-resolution micro-CT equipment. Then, to compare the internal variation of shale after different water imbibition periods, some soaking tests and corresponding CT scanning tests were conducted. Each experimental specimen was first soaked into clean water at natural temperature (~20°C) and atmospheric pressure to begin the hydration. Then, the specimen was scanned after soaking for twenty days. After that, the specimen was put back into the water to continue the hydration for forty days, and then, the CT scanning operation was repeated after the hydration. Thus, the duration of a whole hydration experiment is sixty days and the three periods of CT scanning are 0, 20, and 60 days. The hydration process and results of one of the specimens are shown in Figure 3. The 3D volume is the reconstructed result of the specimen before soaking. The horizontal CT images are the scanning results from the same elevation of S1 after three hydration periods.

The uniaxial compression tests at the minimal constant displacement rate of 0.03 mm/min were conducted in the prepared specimens, S3 and S4 without hydration and the tested S1 with hydration. Meanwhile, some in situ CT scans were completed at some force levels during loading, which means that the loading was stopped at some given stress values, and the CT scanning was performed. Figure 4 shows the loading curves (the axial force-displacement relationships) and the CT scanning steps (the yellow points, each one indicates the scanning step i) of S3 and S4. The CT scans of S3 were mainly distributed near the characteristic stress points (the yellow points in Figure 4(a)), and the CT scans of S4 mainly appeared around the peak strength (the yellow points in Figure 4(b)). At each scanning step, a 3D volume of the loading specimen can be reconstructed, and then, some horizontal CT images (named as i^{th} layer from bottom to top successively) can be obtained [33, 34].

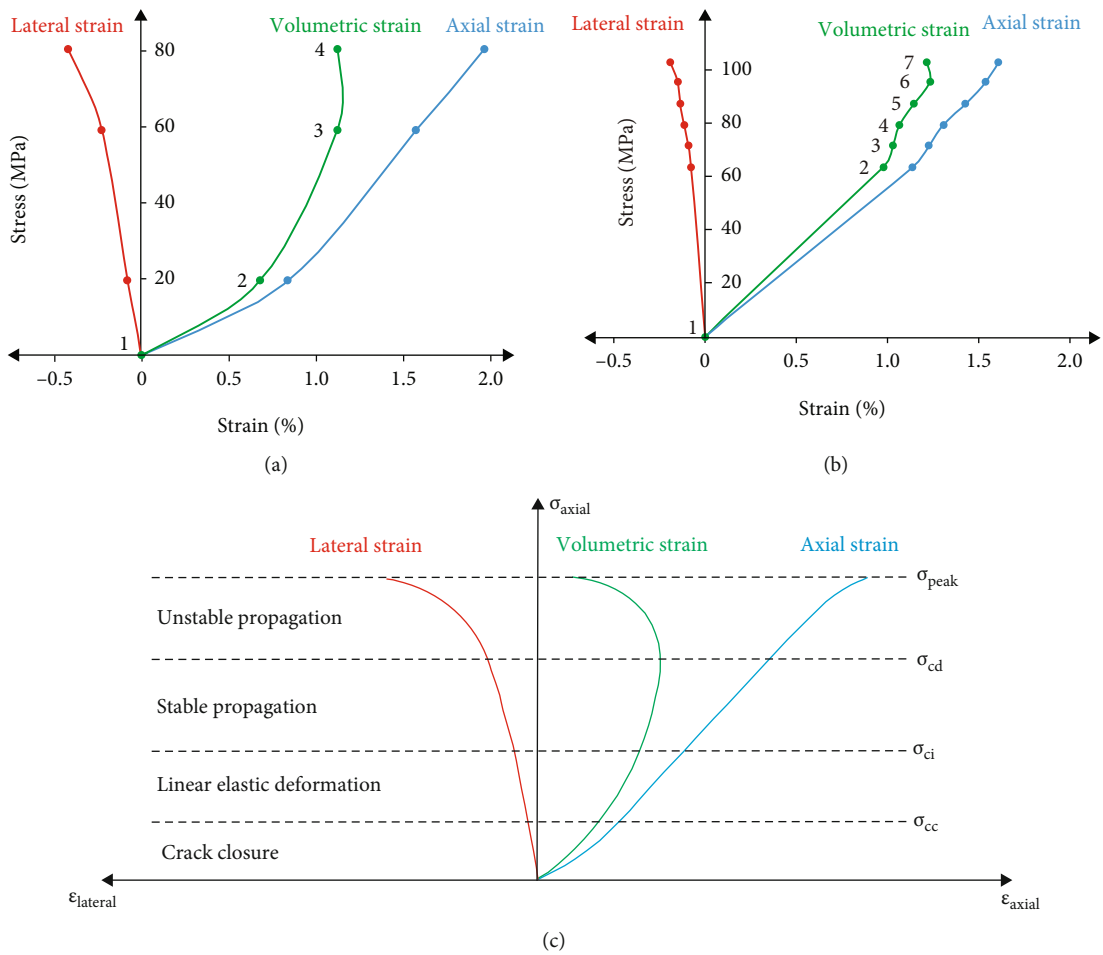

Figure 7: Uniaxial compression stress-strain curves of S3 (a), S4 (b), and Eberhardt et al. [40] (c).

4. Analysis of Hydration and Deformation Characteristics

4.1. Hydration Characteristics. In theory, a CT image is a digital image matrix, and the value of each pixel is presented by using the pixel gray level. The CT gray variance value of the collection points means the distance to the average value, which can reflect the density distribution characteristic of the internal structure of the scanned specimen from a CT image, and it can be used to quantitatively describe the difference of internal structures [35, 36]. Thereafter, based on the CT images scanned at three soaking periods, the CT gray variance values in S1 and S2 were extracted using the Mimics Research software. For the results of each scanning, some horizontal CT images from the center layers ($i^{th} = 325^{th}$ to 675th) were chosen for statistics, and for each image, there are three statistical regions A, B, and C (Ra, Rb, and Rc) were selected, as shown in Figure 5(a), the three regions are three concentric circles, and the diameters of them are equal to the specimen diameter (D, where $D = 4$ mm), two-thirds diameter (2/3 D), and one-third diameter (1/3 D).

The CT gray variance value of each statistical region at different layers can be obtained, and then, the average value can be calculated. The results of S1 and S2 are shown in Figures 5(b) and 5(c), respectively. The evolution curves reveal that the gray variance values of S1 and S2 show an increasing trend in the process of soaking. The growth trend is almost the same at different statistical regions (Ra, Rb, and Rc) of each specimen, and the values in Ra (the red points and curves) are the largest in both specimens. Those indicate that the water soaking can change the structural characteristics of shale, and the influence degree is more evident in the outer region than the internal region. Moreover, it was found that in the early stage of soaking (0-20d), the image gray variance values in the three statistical regions of S1 and S2 both increased rapidly, which indicates that water has a significant influence on the internal structure of shale in the early stage of soaking. In the later stage of soaking (20-60d), each statistical region's image gray variance curves in S1 gradually slowed down. In contrast, the three curves in S2 still showed a rapid rise, indicating that the water influence on S1 tended to be stable, and the effect on S2 continued.

4.2. Hydration Effect. As mentioned above, water soaking with different periods influences the evolution of the internal structure of shale. To further study the effect of water soaking on the mechanical property of shale, the S1 with 60d water imbibition was also subjected to a uniaxial compression test, and the failure specimen was observed using the micro-CT equipment. Then, the influence of hydration on

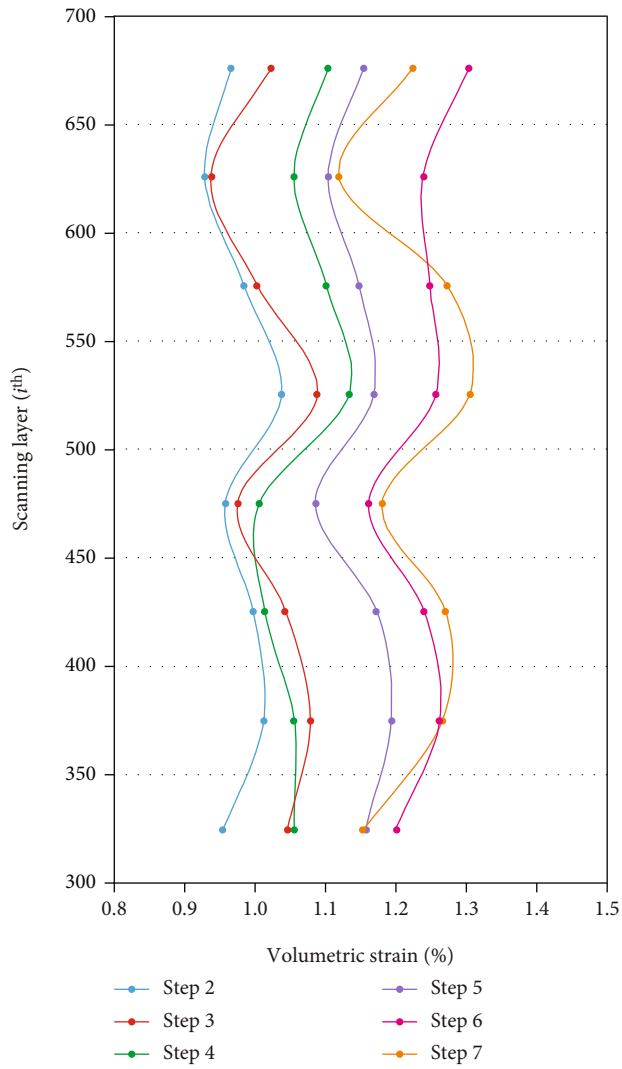

Figure 8: Volumetric strain distributions along with specimen height at different scanning steps for S4.

shale fracturing characteristics was analyzed by comparing the internal crack distribution of specimens with hydration and without hydration. Figure 6(a) shows the diagram of CT slice position for a 3D reconstructed CT volume, there are three horizontal CT slices ($i^{th} = 350^{th}$, 500th, and 650th) and three vertical CT slices ($y = 1$ mm, 2 mm, and 3 mm) of each specimen is selected. Figures 6(b) and 6(c) give the scanning results of failure S1 with 60d water imbibition and S4 without water imbibition.

It was found that the failure regions were distributed mainly in the external position of S1 from Figure 6(b) according to the basic principle of X-ray CT [31, 37]. The CT results show that the failure of the specimen is primarily the whole piece spalling in the outer region after the uniaxial compression test. Those phenomena indicate that the hydration degree in the peripheral area was high. It was consistent with the characterization results of gray variance (Figure 5), and it resulted in the crack morphology that the external spalling damage regions were dominant. In addition, the failure characteristics of S1 with hydration were compared with that of S4 without hydration. It was found that the outer area of S1 was severely damaged, and the damaged part presented as some whole irregular blocks (Figure 6(b)), and some vertical splitting cracks occurred in the internal position of S4 (Figure 6(c)) after the uniaxial compression test destroyed them. Those differences in the crack morphology indicate that the hydration treatment affects the failure mode of the specimen, especially the outer regions of shale.

4.3. Deformation Characteristics. As mentioned above, the deformation characteristics of rocks can be described quantitatively using the volumetric strain. In theory, the changing of the specimen volumes (the volumetric strain) can be directly calculated after obtaining the 3D reconstructed stereograms at some force levels during the loading process. However, to eliminate the influence of the end-effect, some CT images from the center layers ($i^{th} = 325^{th}$ to 675th) of specimens at each scanning step were chosen to analyze the deformation characteristics. The specific method and results are as follows.

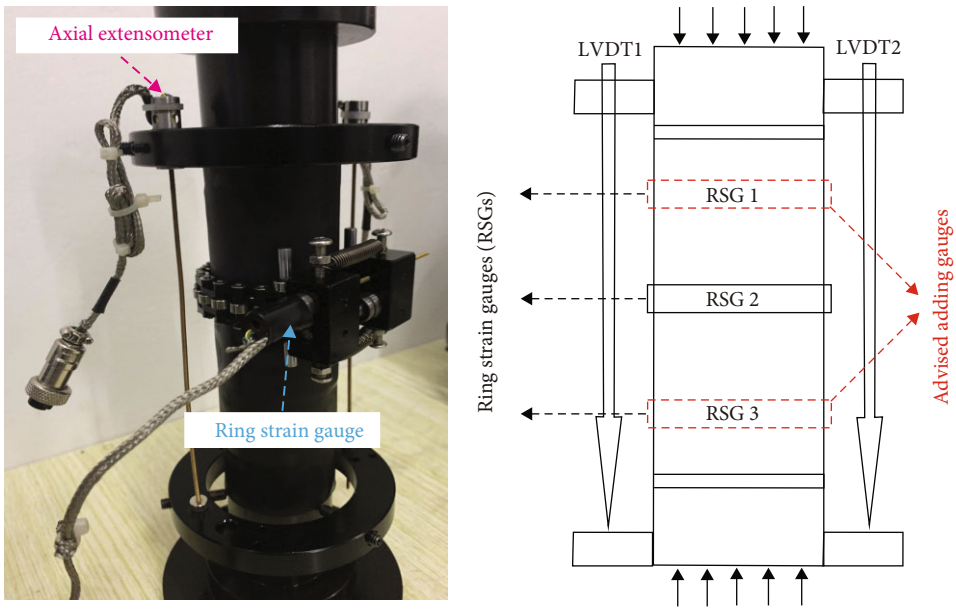

(a) (b)

Figure 9: The measuring method of the lateral strain before (a) and after (b) advised.

4.3.1. Calculating Method. According to the definition of elastic mechanics [31, 38], when compression is positive, the volumetric strain is defined as

$$\varepsilon_v = \frac{-(V - V_0)}{V_0} = \frac{-\Delta V}{V_0}. \quad (1)$$

For a cylindrical specimen, the formula is expressed as

$$\varepsilon_v = \frac{-\Delta V}{V_0} = \varepsilon_y + 2\varepsilon_x, \quad (2)$$

where V_0 and V are the specimen volumes before and after the deformation of rocks, ε_v, ε_x, and ε_y are the volumetric strain, lateral strain, and axial strain of a cylindrical specimen, respectively.

In the in situ uniaxial compression tests, the axial strain was calculated from the changing of the measuring displacement during loading. The lateral strain was not measured during testing, but it was calculated using a new method based on CT image, which is expressed as

$$\varepsilon_x = -\frac{(P_i - P_0)}{P_0}, \quad (3)$$

where P_0 is the perimeter of rock specimen before loading and P_i is the perimeter after loading to the scanning step i.

For each scanning specimen, a scanning layer corresponds to a value of perimeter. The specimen perimeters in CT images at different layers and scanning steps can be measured using the Image-Pro-Plus (IPP) software. Thus, the statistical perimeters from the same layer at different scanning steps can be plugged into Equation (3) successively, the lateral strain at different layers can be calculated; then, the lateral results and the calculated axial strain can be plugged into Equation (2), the volumetric strain along with the specimen height can be obtained.

4.3.2. Calculation Results. An average value of the volumetric strain from different scanning layers can be calculated considering the statistical height. Figure 7 shows the stress-strain curves (including the axial strain, lateral strain, and volumetric strain) before peak strength of the two specimens under in situ uniaxial compression conditions. For S3 (Figure 7(a)), although the axial strain curve changes almost in linear, the volumetric strain curve begins to deviate from linearity almost from scanning step 2, which means that the microcracks inside the rock are further developed, or the pore spaces are further deformed. From scanning step 3 to step 4, the deviation degree of the volumetric curve is even worse, and the back-bending phenomenon can be observed, which indicates the beginning of the crack instability expansion, and this corresponds to the phenomenon that there are existing cracks at step 3 from CT images [39]. For S4 (Figure 7(b)), although there are no obvious cracks existed in CT images before peak strength, the stress-volumetric strain curve has slightly deviated from linearity, which indicates the formation and the development of the internal microcracks. The evolution law of those stress-strain curves in this study corresponds to the result of Eberhardt et al. [40], which divided the evolution process into four stages (the crack closure, linear elastic deformation, stable propagation, and unstable propagation stages) according to the characteristics of stress-strain curves (Figure 7(c)). Here, the evolution stages in both in situ testing shale specimens are not specifically divided, but the expansion phenomena before compressive strength are indeed observed, and the overall trends are both consistent with the previous research.

5. Discussion

The average volumetric strain can reflect the evolution characteristics of deformation in the whole specimen, but it cannot reflect the deformation differences along with the specimen height. Figure 8 shows the volumetric strain distributions along with the specimen height at different scanning steps of S4. In the first six scanning steps, it is obvious that the values of the volumetric strain in the whole height direction all increase with the scanning steps, which indicates that the S4 was almost compressed. At the seventh scanning step, values of the volumetric strain at the top and bottom parts have a rebound, and the degree of enlargement in the middle part has decreased, which means the formation and development of damage from both ends. Additionally, it was found that the stain curve at each step looks like an upright sine curve, which indicates the different degrees of compression along with the specimen height and may be caused by the existence of the horizontal bedding planes of shale. Due to the differences in physical properties, the bedding plane's position is more easily deformed than the matrix's position, leading to an upright sine curve of volumetric strain and indicating the compression differences along with the specimen height.

From the volumetric strain results at different scanning layers and steps, the differences of the expansion or compression degrees along with the specimen height were observed, and the development of the internal damage along with the specimen height was reflected correspondingly. Those deformation differences cannot be obtained from the conventional rock mechanics tests, because the lateral strain was measured only in the middle position using the resistance strain gauge or the ring strain gauge (Figure 9 (a)). Thus, to obtain the strain characteristics along with the specimen height in laboratory tests, an improved measuring method of strain was advised. Another two groups of strain gauges can be used in positions at one-quarter height and three-quarters height of the specimen (Figure 9 (b)), considering the size of the strain gauge and the standard rock specimen. If the size of the rock specimen allowed more strain gauges to be installed, the numbers of the lateral strain gauges could be added accordingly. For the conventional tests, this advised method can resolve the measuring of the strain differences along with the specimen height easily by adding the standard strain equipment and does not cost much.

6. Conclusions

To further obtain the water effect and the deformation characteristics of shale, the cylindrical specimens were soaked in water for three periods, the uniaxial compression tests were conducted, and the CT technique was used for scanning at different hydration and loading stages. Based on the CT results, the evolution characteristics of image gray variance value in each hydration specimen and the differences of the hydration effect on failure characteristics were quantitatively analyzed. In addition, the evolution of axial stress-volumetric strain curves based on a new method was revealed, and the deformation degree along with the specimen height was discussed. The conclusions drawn from this study are as follows:

(1) The hydration specimens were scanned at three soaking periods of 0, 20, and 60 days, and the CT gray variance values at three soaking periods and three statistical regions of each specimen were analyzed. The evolution results show that the water imbibition can change the internal structure of shale, and it has a significant influence in the early stage of soaking. The influence degree is more evident in the external region in the entire soaking period

(2) The water influence on shale mechanical property was analyzed by comparing the failure characteristics of specimens with and without hydration. The CT results show that the outer part of the specimen with hydration was severely damaged, and some vertical splitting cracks occurred in the internal position of the specimen without hydration. Those differences indicate that the hydration treatment affects the failure mode of shale

(3) A new method based on the perimeter changing of specimens in CT image was proposed to calculate the lateral strain and the volumetric strain. The morphologies of stress-strain curves (including the axial strain, lateral strain, and volumetric strain) before peak strength show that the expansion phenomena exist before failure, and the overall evolution law is consistent with the previous research that divided the evolution process into four stages

(4) The values of volumetric strain from CT image at different scanning layers were discussed in detail, and the results reflect the differences in the expansion or compression degree along with the specimen height. To measure the strain differences along with the specimen height as more as possible, an improved measuring method of the lateral strain was advised by adding another two groups (or more) strain gauges in the conventional experiments

Data Availability

The data used to support the findings of this study are included within the article.

Conflicts of Interest

The authors declare no conflict of interest.

Acknowledgments

This work was funded by the National Natural Science Foundation of China (42102309, 42007243, and 41227901), the Fundamental Research Funds for the Central Universities (N2101032), and the China Postdoctoral Science Foundation (2021M690562).

References

[1] C. L. Ya, J. G. Deng, Y. F. Cheng, M. L. Li, Y. C. Feng, and X. R. Li, "Mechanical properties of gas shale during drilling operations," *Rock Mechanics and Rock Engineering*, vol. 50, no. 7, pp. 1753–1765, 2017.

[2] Z. J. Jin, Z. R. Bai, B. Gao, and M. W. Li, "Has China ushered in the shale oil and gas revolution?," *Oil and Gas Geology*, vol. 40, no. 3, pp. 451–458, 2019.

[3] J. Wang, Y. Wang, S. Li, and L. Yang, "Strength softening characteristics of shale clay mineral expansion," *Chemistry and Technology of Fuels and Oils*, vol. 56, no. 2, pp. 300–311, 2020.

[4] L. C. Jia, M. Chen, L. T. Sun et al., "Experimental study on propagation of hydraulic fracture in volcanic rocks using industrial CT technology," *Petroleum Exploration and Development*, vol. 40, no. 3, pp. 405–408, 2013.

[5] B. Hou, R. X. Zhang, Y. J. Zeng, W. N. Fu, Y. F. Muhadasi, and M. Chen, "Analysis of hydraulic fracture initiation and propagation in deep shale formation with high horizontal stress difference," *Journal of Petroleum Science and Engineering*, vol. 170, pp. 231–243, 2018.

[6] H. Singh, "A critical review of water uptake by shales," *Journal of Natural Gas Science and Engineering*, vol. 34, no. 2, pp. 751–766, 2016.

[7] S. F. Zhang and J. J. Sheng, "Effect of water imbibition on fracture generation in Mancos shale under isotropic and anisotropic stress conditions," *Journal of Geotechnical and Geoenvironmental Engineering*, vol. 144, no. 2, article 04017113, 2018.

[8] T. S. Ma and P. Chen, "Study of meso-damage characteristics of shale hydration based on CT scanning technology," *Petroleum Exploration and Development*, vol. 41, no. 2, pp. 249–256, 2014.

[9] H. Roshan, S. Ehsani, C. E. Marjo, M. S. Andersen, and R. I. Acworth, "Mechanisms of water adsorption into partially saturated fractured shales: an experimental study," *Fuel*, vol. 159, pp. 628–637, 2015.

[10] Z. Zhou, H. Abass, X. Li, D. Bearinger, and W. Frank, "Mechanisms of imbibition during hydraulic fracturing in shale formations," *Journal of Petroleum Science and Engineering*, vol. 141, pp. 125–132, 2016.

[11] X. J. Liu, W. Zeng, L. X. Liang, and J. Xiong, "Experimental study on hydration damage mechanism of shale from the Longmaxi Formation in southern Sichuan Basin, China," *Petroleum*, vol. 2, no. 1, pp. 54–60, 2016.

[12] N. Chakraborty, Z. T. Karpyn, S. Liu, and H. Yoon, "Permeability evolution of shale during spontaneous imbibition," *Journal of Natural Gas Science and Engineering*, vol. 38, pp. 590–596, 2017.

[13] S. L. Crouch, "Experimental determination of volumetric strains in failed rock," *International Journal of Rock Mechanics and Mining Sciences*, vol. 7, no. 6, pp. 589–603, 1970.

[14] W. Tian and H. Q. Liu, "Insight into the adsorption of methane on gas shales and the induced shale swelling," *American Chemical Society*, vol. 5, pp. 31508–31517, 2020.

[15] W. F. Brace, B. W. Paulding Jr., and C. Scholz, "Dilatancy in the fracture of crystalline rocks," *Journal of Geophysical Research*, vol. 71, no. 16, pp. 3939–3953, 1966.

[16] Y. D. Jiang, X. F. Xian, D. G. Xiong, and F. C. Zhou, "Study on creep behaviour of sandstone and its mechanical models," *Chinese Journal of Geotechnical Engineering*, vol. 27, no. 12, pp. 1479–1481, 2005.

[17] D. W. Hu, H. Zhou, F. Zhang, and J. F. Shao, "Evolution of poroelastic properties and permeability in damaged sandstone," *International Journal of Rock Mechanics and Mining Sciences*, vol. 47, no. 6, pp. 962–973, 2010.

[18] X. L. Lu and Q. S. Liu, "Experimental investigation of dilatancy-bulking behavior of weak sandstone," *Advanced Materials Research*, vol. 197-198, pp. 1420–1424, 2011.

[19] N. Gatelier, F. Pellet, and B. Loret, "Mechanical damage of an anisotropic porous rock in cyclic triaxial tests," *International Journal of Rock Mechanics and Mining Sciences*, vol. 39, no. 3, pp. 335–354, 2002.

[20] V. Palchik and Y. H. Hatzor, "Crack damage stress as a composite function of porosity and elastic matrix stiffness in dolomites and limestones," *Engineering Geology*, vol. 63, no. 3-4, pp. 233–245, 2002.

[21] P. H. Kelvis and E. Nordlund, "Comparison between stress and strain quantities of the failure-deformation process of Fennoscandian hard rocks using geological information," *Rock Mechanics and Rock Engineering*, vol. 46, no. 1, pp. 41–51, 2013.

[22] F. L. Pellet and G. Fabre, "Damage evaluation with p-wave velocity measurements during uniaxial compression tests on argillaceous rocks," *International Journal of Geomechanics*, vol. 7, no. 6, pp. 431–436, 2007.

[23] M. C. He, C. G. Wang, J. L. Feng, D. J. Li, and G. Y. Zhang, "Experimental investigations on gas desorption and transport in stressed coal under isothermal conditions," *International Journal of Coal Geology*, vol. 83, no. 4, pp. 377–386, 2010.

[24] W. G. Liang, Y. S. Zhao, S. G. Xu, and M. B. Dusseault, "Effect of strain rate on the mechanical properties of salt rock," *International Journal of Rock Mechanics and Mining Sciences*, vol. 48, no. 1, pp. 161–167, 2011.

[25] M. Takarli, W. Prince, and R. Siddique, "Damage in granite under heating/cooling cycles and water freeze-thaw condition," *International Journal of Rock Mechanics and Mining Sciences*, vol. 45, no. 7, pp. 1164–1175, 2008.

[26] C. Y. Liang, X. Li, S. X. Wang, S. D. Li, J. M. He, and C. F. Ma, "Experimental investigations on rate-dependent stress-strain characteristics and energy mechanism of rock under uniaxial compression," *Chinese Journal of Rock Mechanics and Engineering*, vol. 31, no. 3, pp. 1830–1838, 2012.

[27] F. L. Pellet, M. Keshavarz, and K. Amini-Hosseini, "Mechanical damage of a crystalline rock having experienced ultra high deviatoric stress up to 1.7 GPa," *International Journal of Rock Mechanics and Mining Sciences*, vol. 48, no. 8, pp. 1364–1368, 2011.

[28] M. Nicksiar and C. D. Martin, "Evaluation of methods for determining crack initiation in compression tests on low-porosity rocks," *Rock Mechanics and Rock Engineering*, vol. 45, no. 4, pp. 607–617, 2012.

[29] D. Huang, R. Q. Huang, and Y. X. Zhang, "Experimental investigations on static loading rate effects on mechnical properties and energy mechanism of coarse crystal grain marble under uniaxial compression," *Chinese Journal of Rock Mechanics and Engineering*, vol. 31, no. 2, pp. 245–255, 2012.

[30] B. C. Yang, L. Xue, Y. T. Duan, and M. M. Wang, "Correlation study between fracability and brittleness of shale-gas reservoir," *Geomechanics and Geophysics for Geo-Energy and Geo-Resources*, vol. 7, no. 2, p. 31, 2021.

[31] Y. T. Duan and B. C. Yang, "How does structure affect the evolution of cracking and the failure mode of anisotropic shale?," *Geomechanics and Geophysics for Geo-Energy and Geo-Resources*, vol. 8, no. 1, p. 25, 2022.

[32] J. F. Ma, *Research of 3D cone-beam CT image reconstruction accelerating technology*, Shandong University Master's Thesis, 2011.

[33] Y. T. Duan, X. Li, P. G. Ranjith, and Y. F. Wu, "An investigation of the evolution of the internal structures and failure modes of Longmaxi shale using novel X-ray microscopy," *Journal of Petroleum Science and Engineering*, vol. 184, article 106479, 2020.

[34] B. C. Yang, S. Q. Qin, L. Xue, and H. R. Chen, "The reasonable range limit of the shape parameter in the Weibull distribution for describing the brittle failure behavior of rocks," *Rock Mechanics and Rock Engineering*, vol. 50, no. 6, pp. 3359–3367, 2021.

[35] Y. T. Duan, X. Li, B. Zheng, J. M. He, and J. Hao, "Cracking evolution and failure characteristics of Longmaxi shale under uniaxial compression using real-time computed tomography scanning," *Rock Mechanics and Rock Engineering*, vol. 52, no. 9, pp. 3003–3015, 2019.

[36] Y. T. Duan, X. Li, J. M. He, S. D. Li, and R. Q. Zhou, "Quantitative analysis of meso-damage evolution for shale under in situ uniaxial compression conditions," *Environmental Earth Sciences*, vol. 77, no. 4, pp. 154–162, 2018.

[37] Y. Wang, H. N. Yang, J. Q. Han, and G. Zhu, "Effect of rock bridge length on fracture and damage modelling in granite containing hole and fissures under cyclic uniaxial increasing-amplitude decreasing-frequency (CUIADF) loads," *International Journal of Fatigue*, vol. 158, p. 106741, 2022.

[38] L. Y. Li, H. P. Xie, X. Ma, Y. Ju, T. W. Tang, and Q. J. Fang, "Experimental study on relationship between surface temperature and volumetric strain of rock under uniaxial compression," *Journal of China Coal Society*, vol. 37, no. 9, pp. 1511–1515, 2012.

[39] X. Li, Y. T. Duan, S. D. Li, and R. Q. Zhou, "Study on the progressive failure characteristics of Longmaxi shale under uniaxial compression conditions by X-ray micro-computed tomography," *Energies*, vol. 10, no. 3, p. 303, 2017.

[40] E. Eberhardt, D. Stead, B. Stimpson, and R. S. Read, "Identifying crack initiation and propagation thresholds in brittle rock," *Canadian Geotechnical Journal*, vol. 35, no. 2, pp. 222–233, 1998.

Hindawi
Geofluids
Volume 2022, Article ID 3553796, 16 pages
https://doi.org/10.1155/2022/3553796

Research Article

Cement Sheath Integrity in Anisotropic Shale Formations: A Numerical Investigation

Xiaorong Li,[1,2] **Yijin Zeng**,[1] **Zechen Ding**,[2] **Rengguang Liu**,[1] **and Hai Lin**[3]

[1]*State Key Laboratory of Shale Oil and Gas Enrichment Mechanisms and Effective Development, Beijing 100728, China*
[2]*College of Safety and Ocean Engineering, China University of Petroleum, Beijing 102249, China*
[3]*Tianjin Branch, China National Offshore Oil Corporation, Tianjin 300452, China*

Correspondence should be addressed to Xiaorong Li; xiaorongli@cup.edu.cn and Yijin Zeng; zengyj.sripe@sinopec.com

Received 5 November 2021; Revised 13 February 2022; Accepted 14 February 2022; Published 7 April 2022

Academic Editor: Chris Harris

Cement sheath should provide zonal isolation and structural support during the full life cycle of a well. However, achieving long-term cement sheath integrity under complex geological and operational conditions, especially in bedding shales characterized by strong anisotropy, is still a great challenge. Thus, to better understand the effects of the anisotropy of shales on cement sheath integrity, this paper developed a 3D coupled thermal-hydro-mechanical model of the formation-cement-casing system. Stress generation and evolution within cement sheath are also considered in the modeling. The model is validated against analytical solutions and physical experimental results. Then, sensitivity analyses were performed to investigate the initial stress of cement sheath and shale anisotropy on cement sheath integrity. The results show that the anisotropy of Young's modulus has a greater influence on cement sheath integrity compared to the anisotropy of Poisson's ratio. Debonding between the cement sheath and formation can be easily generated due to the shale's high anisotropy of Young's modulus. The aperture of the microannulus along the cement interface varies with the angle between the wellbore axis and the bedding plane. The minimum microannulus is developed where the wellbore is parallel to the shale's bedding planes. The results also indicate that initial stress generated in the cement sheath after its hardening is beneficial for the integrity of the cement-formation interface.

1. Introduction

The long-term integrity of a well structure is critical to ensure the safe and efficient development of oil and gas resources. A typical well structure consists of casing and cement sheath. Casing is lowered to the well, and an annulus is formed between the casing and formation after drilling to the desired depth. Then, cement slurry is pumped into the annulus and it gradually becomes a solid cement sheath with a complicated hydration reaction. Eventually, a wellbore structure with formation, cement sheath, and the casing is created, and the cement sheath is tightly bonded to the formation and casing.

The cement sheath is a key element in the well structure system, which not only provides mechanical support for the well but also prevents cross-flow of formation fluids along the well. However, cement sheath is a porous material and generally considered as a brittle elastic material; it is easy to fail under the complicated loading conditions of high pressure, high temperature, and high in situ stress anisotropy [1–7]. Meanwhile, the mechanical properties of cement sheath after a series of cementing operations also play a key role in cement sheath integrity. Thus, a comprehensive understanding of cement sheath integrity under complex geological and operational conditions is necessary to evaluate the long-term integrity of cement sheath.

Many studies assumed cement sheath as an elastic or elastic-plastic material [8, 9]. Wang et al. [10] analyzed the effects of cement sheath's elastic properties on the stress state of the casing-cement sheath-formation system by assuming cement sheath is an elastic material. The results show that the cement sheath with lower elastic modulus is harder to lose its integrity; the radial stress at the outer surface of the casing first increases and then decreases with the increase of Poisson's ratio of cement sheath. Wang et al. [11] developed a sealing capacity chart of cement sheath with a comparison of equivalent stress and yield strength based

on the assumption of elastic-plastic behavior of cement sheath. They reported that the range of elastic modulus from 6 GPa to 9.7 GPa is the optimal value for maintaining cement sheath integrity in their studied cases.

As mentioned earlier, in the real situation, the cement sheath is a poro-elasto-plastic material due to its natural micro defects. Thus, the pore pressure of the cement sheath should not be neglected in the analysis. Fourmaintraux et al. [12] introduced a new methodology to efficiently design cement sheath and highlighted the importance of pore pressure in his predictive cement-sheath modeling; the high pore pressure of cement sheath results in low radial effective stress, which might result in a high risk of cement sheath tensile failure. Nygaard et al. [13] assumed cement sheath as a poroelastic material and considered the pore pressure of cement sheath. Their parametric study revealed that the risk of debonding and tensile failure of cement sheath increases with Young's modulus and Poisson's ratio of the cement under dynamic-loading conditions.

However, even if high quality of primary cementing is achieved, variations in temperature and pressure within the cement sheath over its life cycle are likely to induce the failure of cement sheath integrity. Several studies [14, 15] have carried out to characterize the thermal stress within cement sheath with an assumption of thermal poro-elasto-plastic behavior. Gholami et al. [16] developed an analytical approach for evaluating cement sheath integrity based on the theory of thermo-poroelasticity. Meng et al. [17] proposed a transient thermo-poroelastic model for wellbore integrity analysis. Their results indicate that the pore pressure of cement sheath is a key factor, and well-temperature perturbations induce greater pore pressure changes than well-pressure perturbations.

The cement sheath integrity is also significantly influenced by the mechanical properties and stress state of formations, especially the layered shale formations. Fan et al. [18] studied the failure evolution of the casing/cement sheath interface during the multistage hydraulic fracturing in shales. Wang et al. [19] also studied the integrity of cement sheath during the hydraulic fracturing process in shales. These studies assumed the shales as an isotropic material. However, the layered shale formations represent transverse isotropy with an anisotropic property. Higgins et al. [20] and Wang et al. [21] pointed out that it is reasonable to assume layered shales as the transversely isotropic material by theoretical studies and laboratory experiments, respectively. Therefore, in this work, the shale formation is considered as transversely isotropic material and a coupled thermal-hydro-mechanical model is used to characterize the formation rock and the cement sheath.

Besides, the initial stresses of the cement sheath also play a critical role in the long-term integrity of the cement sheath. The stress state within cement sheath after cementing operation and before any additional loads is generally defined as "the initial stresses" of cement sheath; it represents how far the material is from the yield point and, as a consequence, how much loading it can be submitted to before being damaged [22]. The importance of the initial stresses of cement sheath has been widely discussed in existing publications. For example, some of them proposed that the value of the initial stress of cement sheath is equal to the hydrostatic pressure of cement slurry or it is directly assumed to be zero [9, 23–25]. However, others argue that the initial stress within the cement sheath is not equal to zero due to the generation of the hydration products which can support its gravity and isolate the hydrostatic pressure [26]. And the initial stress is also not equal to the hydrostatic pressure of the cement slurry since there is a weight loss of cement slurry during its hydration process [27, 28].

Drecq and Parcevaux [26] reported that the initial stress state within cement sheath can be described based on Terzaghi's law as $\sigma = \sigma' + u$, where σ is the total stress or the hydrostatic pressure of cement slurry before hardening, σ is the effective stress, and u is the pore pressure or hydrostatic pressure. At the beginning of the cement hydration, cement grains are fully dispersed in the cement slurry, and u is equal to σ with zero effective stress σ'. During the cement hardening process, the hydrostatic pressure or pore pressure (u) gradually transfers to the effective stress σ' while the total stress σ always remains constant. Furthermore, Haijin et al. [29] reported that the pressure drop in cement slurry is the same as its static gel strength, especially at the early stage of the cement hydration, which agrees with the viewpoint of Drecq and Parcevaux. In summary, these studies indicate that the initial stress of the cement sheath is approximately equal to the hydrostatic pressure of cement slurry before hardening subtracting the pore pressure in cement sheath at the end of the hardening process [13, 30–32].

Although it has been noted that the effective stress of cement sheath gradually increases with accumulation of hydration products during the hydration process, few studies focused on the effects of the initial stress on the integrity of the cement sheath. Sun et al. [30] developed a model to analyze the variations in temperature and pressure of cement sheath during the cementing operation in deep water wells. Cement temperature dramatically increases while cement pore pressure gradually decreases during the hydration reaction. Zhang et al. [32] developed a casing-cement-formation model to estimate the generation of microannulus along cement interfaces due to cycling pressures and temperatures. These studies provide strong evidence for the importance of the initial stress within cement sheath. However, a comprehensive study and discussion are still necessary for fully understanding the effects of the initial stress of cement sheath on its integrity, especially with the consideration of the entire loading history of the cement sheath.

Therefore, to comprehensively investigate the coupled effects of the variations in temperature/pressure, the anisotropy of the shale formations, and the entire loading history of cement sheath (especially its initial stress state), a 3D coupled thermal-hydro-mechanical model of cement sheath integrity in shales is developed. The accumulation or change of stress-strain state of the cement sheath during its life cycle is incorporated in the modeling. A parametric study of the in situ stress anisotropy, the formation property anisotropy, and the initial stress state of cement sheath was conducted using the proposed model.

2. Governing Equations

In this work, each part of the casing-cement sheath-formation system is separately defined with different material models as follows.

The casing is considered as an isotropic linear elastic material, which is defined with Young's modulus (E) and Poisson's ratio (ν).

The cement sheath is considered as an isotropic poro-elasto-plastic material, and the plastic behavior of the cement sheath is defined by the Mohr-Coulomb criterion:

$$H_m q - p \tan \beta - d = 0, \tag{1}$$

where H_m is the factor that controls the form of the yield surface in π plane:

$$H_m = -\frac{1}{\sqrt{3}\cos\varphi} \sin\left(\Theta + \frac{\pi}{3}\right) + \frac{1}{3}\cos\left(\Theta + \frac{\pi}{3}\right)\tan \varnothing, \tag{2}$$

where β is the friction angle of the cement sheath, d is the cohesion of the cement sheath, p is the equivalent pressure stress, q is the equivalent Mises stress, and Θ is the deviator polar angle. p, q, and Θ are defined as

$$\begin{aligned} p &= \frac{1}{3}\mathrm{trace}(\sigma), \\ q &= \sqrt{\frac{3}{2}(S:S)}, \\ \cos(3\Theta) &= \left(\frac{g}{q}\right)^3. \end{aligned} \tag{3}$$

Θ is the third invariant of deviatoric stress, defined as

$$g = \left(\frac{9}{2} S \cdot S : S\right)^{1/3}. \tag{4}$$

S is the deviatoric stress:

$$S = \sigma + pI, \tag{5}$$

where σ is the total stress tensor and I is the identity matrix.

The formation is assumed as a poro-elasto-plastic material with transverse isotropy. Since the Mohr-Coulomb criterion is not compatible with anisotropic material in the finite element code Abaqus used in this study, the plastic behavior of the formation is defined by the Drucker-Prager criterion (Figure 1):

$$\begin{aligned} F &= t^{D-P} - p\tan\beta - d = 0, \\ t^{D-P} &= \frac{1}{2} q\left[1 + \frac{1}{K^{D-P}} - \left(1 - \frac{1}{K^{D-P}}\right)\left(\frac{r}{q}\right)^3\right], \end{aligned} \tag{6}$$

where β is the slope of the linear yield surface in the $p-t$ plane, termed as the frictional angle. d is the cohesion of the materials. K^{D-P} is the yield stress ratio of the tensile stress and the compressive stress.

The plastic flow is material is defined as

$$G^{D-P} = t^{D-P} - p\tan\Psi, \tag{7}$$

where G^{D-P} is the flow potential and Ψ is the dilatancy angle on the $p-t$ plane.

The shale formation is assumed as a transversely isotropic material within the elastic range, and the stress-strain law of the transversely isotropic material can be defined as

$$\begin{aligned} \left\{\varepsilon'\right\} &= D^{-1}\left\{\sigma'\right\}, \\ D^{-1} &= \begin{bmatrix} \frac{1}{Ep} & \frac{-\nu p}{Ep} & \frac{-\nu tp}{Ep} & 0 & 0 & 0 \\ \frac{-\nu p}{Ep} & \frac{1}{Ep} & \frac{-\nu tp}{Ep} & 0 & 0 & 0 \\ \frac{-\nu pt}{Ep} & \frac{-\nu pt}{Ep} & \frac{1}{Et} & 0 & 0 & 0 \\ 0 & 0 & 0 & \frac{1}{Gp} & 0 & 0 \\ 0 & 0 & 0 & 0 & \frac{1}{Gt} & 0 \\ 0 & 0 & 0 & 0 & 0 & \frac{1}{Gt} \end{bmatrix}, \end{aligned} \tag{8}$$

where p stands for the lateral direction of the bedding plane, t stands for the direction perpendicular to the bedding plane, and vij stands for Poisson's ratio that characterizes the transverse strain in the j direction while the material is stressed in the i direction.

The cohesive interface model based on the traction-separation law is used to model the behavior of the casing/cement interface and cement/formation interface. The traction-separation law (Figure 2) consists of three stages: linear elastic stage, damage initiation stage, and damage evolution stage.

The cohesive interface model assumes the initial interface behavior obeys linear elastic law:

$$\mathbf{t} = \mathbf{K}\boldsymbol{\delta}, \tag{9}$$

where $\mathbf{t}$, $\mathbf{K}$, and $\boldsymbol{\delta}$ represent the nominal traction tensor, stiffness tensor, and displacement tensor of the interface, respectively.

With the increase of the traction at the interface, damage initiation will occur. In this paper, the damage initiation is defined by the maximum nominal stress criterion:

$$\max\left\{\frac{\langle t_n\rangle}{t_n^0}, \frac{t_s}{t_s^0}, \frac{t_t}{t_t^0}\right\} = 1, \tag{10}$$

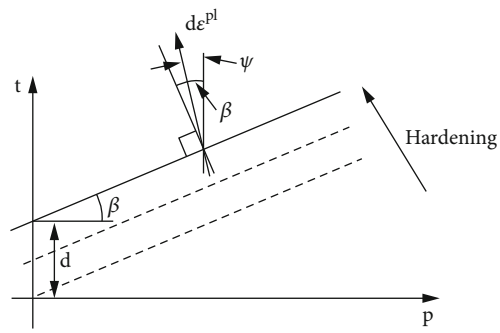

Figure 1: Linear Drucker-Prager model: yield surface and flow on the $p-t$ plane [33].

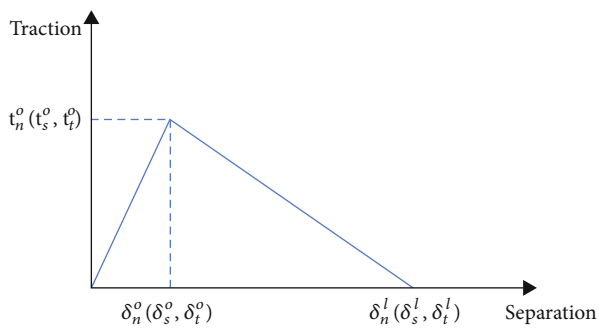

Figure 2: Typical traction-separation response.

where t_n^0, t_s^0, and t_t^0 represent the maximum traction in the normal and the two local shear directions, respectively. $\langle\rangle$ is the Macaulay symbol, representing the pureness compression displacement.

Once the stressed state of interface meets the condition of damage initiation, the interface enters to the stage of damage evolution. A scalar damage variable, D, represents the overall damage at the contact point. And the variable monotonically evolves from 0 to 1 with the further loading. The contact stress components are affected by the damage according to

$$t_n = \begin{cases} (1-D)\bar{t}_n, & \bar{t}_n \geq 0, \\ \bar{t}_n, & \text{otherwise(no damage to compressive stiffness)}, \end{cases}$$
$$t_s = (1-D)\bar{t}_s,$$
$$t_t = (1-D)\bar{t}_t, \tag{11}$$

where $\bar{t}_n$, $\bar{t}_s$, and $\bar{t}_t$ are the contact stress components predicted by the elastic traction-separation behavior for the current separations without damage.

And in this work, the damage evolution of the interface is defined by the Benzeggagh-Kenane fracture energy criterion [34]:

$$G^C = G_n^c + (G_s^c - G_n^c)\left(\frac{G_S}{G_T}\right)^{\eta}, \tag{12}$$

where $G_S = G_s + G_t$ and $G_T = G_n + G_s$. G_S and G_n represent the fracture energy in the shear direction and normal direction, respectively. G_T is the total fracture energy; G_n^c is the critical energy in the normal direction; G_s^c is the critical energy in the first shear direction; η is the viscosity coefficient.

The fluid flow in the cement sheath and formation is assumed to obey Darcy's law:

$$q_i = -\frac{k}{\mu}p_{,i}, \tag{13}$$

where q_i is the fluid flux; k is the permeability of the materials; $p_{,i}$ is the borehole pressure; μ is the viscosity of the fluid.

The fluid flow at the formation/cement sheath interface also obeys this law while assuming the seepage between cement sheath and formation is connected.

The heat conduction in the casing-cement-formation system is defined as

$$\frac{\rho c}{\lambda}\frac{\partial T}{\partial t} = \nabla^2 T, \tag{14}$$

where ρ, λ, c, and T represent the density, the thermal conductivity, the specific heat, and the temperature of the materials, respectively.

Considering the influence of microannulus (at formation/cement interface and the casing/cement interface) on heat conduction, the conductive heat transfer between the gap surfaces is defined by

$$q_{\text{cont}} = k(\theta_A - \theta_B), \tag{15}$$

where q_{cont} is the heat flux per unit area crossing the interface from point A on one surface to point B on the other; θ_A and θ_B are the temperature of the points on the surfaces; k is the gap conductance between points A and B. And point A is a node on the slave surface; point B is the location on the master surface contacting the slave node.

The heat flux between the inner surface of the casing and the wellbore fluid is governed by

$$q = -h(T_s - T_l), \tag{16}$$

where q is the heat flux; h is the reference film coefficient; T_s is the temperature on the surface which contacts with the fluid; T_l is the temperature of the fluid.

3. Model Construction

3.1. Model Geometry. In this work, the 3D coupled thermal-hydro-mechanical model was developed using Abaqus (a commercial finite element code). The 3D finite element model consists of a casing, cement sheath, and formation (Figure 3). The inner and outer diameters of the casing are 0.1005 m and 0.1143 m, respectively. The outer diameter of the cement sheath is 0.1543 m. And the formation size is 2 $\times 1 \times 0.1$ m, which is large enough to eliminate the boundary

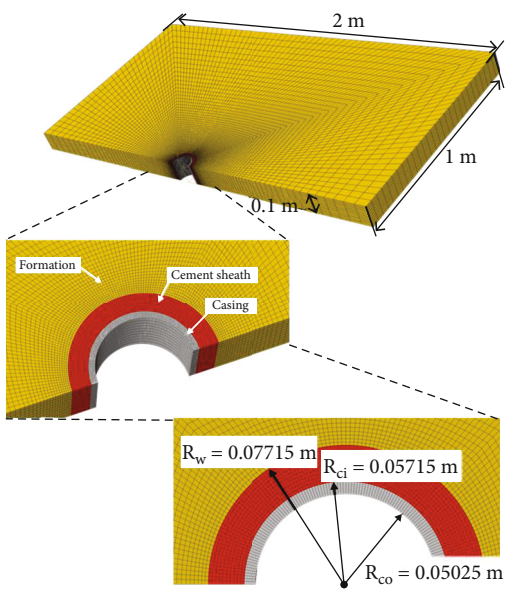

Figure 3: The geometry of the model consisting casing, cement sheath, and formation.

effect. To reduce the computing cost and guarantee the accuracy of the model, a denser mesh near the wellbore and a gradually coarser mesh away from the well are used.

The casing is discretized by 11200 elements. To take pore pressure degree of freedom into account, the cement sheath and formation are discretized by coupled pore pressure and displacement element (C3D8P), and the numbers of elements are 11200 and 83652, respectively. The pore pressure cohesive element (COH3D8P) was used to model the casing/cement interface and cement/formation interface.

3.2. Simulation Steps and Boundary Conditions. The simulation steps corresponding to the different operational stages during the life of a well are briefly described as follows.

Step 1 (initial equilibrium). The first step is an initial equilibrium calculation; it is the origin of the whole simulation. The virgin in situ stress, pore pressure, and the formation temperature are applied to the formation by "Predefined Field" in Abaqus. Considering the formation size is large enough compared with the wellbore size, the normal constraint conditions and the initial pore pressure and temperature are deployed on the outer boundary of formation. In this step, the parts of the casing and cement sheath are deactivated. The initial stress and pore pressure are shown in Table 1.

Step 2 (drilling). In the drilling process, the wellbore rock was destroyed and removed from the formation; the in situ stress state of the formation was perturbed. To keep the wellbore stability and prevent formation fluid blowout, the drilling mud was added into the wellbore to balance the pressure between the wellbore and formation. Thus, the hydrostatic pressure from drilling mud needs to be equal to or greater than the pore pressure of the formation. In this stage, the wellbore rock is removed via the "Model Change" function in Abaqus. Meanwhile, the drilling mud pressure is applied to the wellbore wall, and the value of hydrostatic pressure of drilling mud is equal to the formation pressure.

Table 1: Formation in situ stress in the base case.

Parameter	Values
Overburden pressure (MPa)	106
Maximum horizontal stress (MPa)	84
Minimum horizontal stress (MPa)	78
Pore pressure (MPa)	70

In the real situation, the drilling mud will permeate into the formation under the pressure difference between the wellbore and the formation. The solid grains and chemical composition within drilling mud will also migrate to the formation under the pressure difference, causing formation damage. Thus, the drilling mud should also be able to build impermeable filter cake over the surface of the wellbore to minimize the loss into the porous formations [35, 36]. Thus, considering the impermeable filter cake may isolate the wellbore pressure and formation pressure, in this work, the formation pressure is assumed constant during the simulations.

Step 3 (casing). The steel casing was run into the wellbore after drilling. In this stage, the casing elements are reactivated and the drilling mud pressure is applied on the inner/outer casing surfaces and the wellbore wall.

Step 4 (cementing). In the cementing stage, the cement slurry was pumped into the annulus between the casing and the formation. Therefore, the drilling mud pressure applied on the wellbore wall and the outer casing surface is replaced by the slurry pressure. By doing this, the effect of fluid pressure on the stress and strain state around the wellbore wall can be considered.

Step 5 (hardening). In the hardening stage, a series of hydration reactions of the cement slurry results in a solid cement sheath, which induces a complicated variation in stress state within the cement sheath. In this work, the pore pressure of the cement sheath gradually decreases while its initial stress increases with the hydration reaction. The sum of pore pressure and initial stress of cement sheath at any time during the hydration process is approximately equal to the hydrostatic pressure of the cement slurry. Thus, the maximum value of the initial stress is equal to the value of the hydrostatic pressure when the pore pressure of the cement sheath is lowered to zero. In this step, the elements of the cement sheath are reactivated, and the pressure deployed on the wellbore wall and the outer casing surface is removed. Moreover, the cement shrinkage is also considered in this stage by reducing the cement volume.

Step 6 (completion). In the completion stage, the pressure deployed on the inner surface of the casing is replaced by the hydrostatic pressure of the completion fluid.

Table 2: Material properties for the casing, cement, and formation (the parameters that have expression with $*$ are shown in Table 3).

Parameters	Casing	Cement	Rock
Density (kg/m^3)	7800	2350	3960
Modulus (GPa)	210	10	$*$
Poisson's ratio	0.30	0.25	$*$
Permeability (mD)	—	0.001	0.064
Friction angle (°)	—	27	30
Cohesion (MPa)	—	10	20
Thermal expansion coefficient (m/m/K)	$1.2e-5$	0.0005	$0.79e-5$
Specific heat (J/kg/K)	434	1600	1000
Thermal conductivity (W/m/K)	52	0.80	2.40

Step 7 (production). In the production stage, the pressure deployed on the inner surface of the casing is replaced by the hydrostatic pressure of the production fluid.

Step 8 (injection—loading). In the injection step, the high injection pressure is deployed on the inner surface of the casing, replacing the previous production pressure.

Step 9 (injection—unloading). After the loading stage, the casing pressure recovers to the production pressure.

3.3. Material Properties. As described in Section 2, the casing is considered an isotropic linear elastic material. The cement sheath is considered an isotropic poro-elasto-plastic material with Mohr-Coulomb plasticity. The formation is assumed as a poro-elasto-plastic material with transverse isotropy. The cement interfaces are modeled based on the traction-separation law.

In the base case, the formation properties are modified from Yang [35], which comes from deep shales in the Sichuan Basin, China. Tables 2 and 3 list the detailed values of the data used in the model.

Yin et al. [36] developed a coupled thermal-mechanical model for cement sheath and validated it against the physical experiment results [37]. The numerical results are in good agreement with the experiment results. Thus, the material properties of the interface (casing/cement interface and cement/formation interface) in Yin et al. [36] are adopted in this work, as shown in Table 4.

3.4. Model Validation. Although numerous analytical models have been carried out for efficiently estimating cement sheath integrity based on elastic-plastic theory [9, 38–42], they only focus on a particular stage without considering the stress-strain evolution of the well system during its full life cycle, which cannot be used to validate the complicated model in this work. Therefore, to validate the accuracy of the finite element model proposed in this work, the validation process is divided into two parts.

Part one: during the first four steps (initial equilibrium, drilling, casing, and pumping cement slurry), the solid cement sheath is not formed yet; the stress-strain change of the well is mainly induced by the hydrostatic pressure of drilling fluid or cementing slurry, which can be validated by the analytical models.

Table 3: Transversely isotropic elastic parameter for the shale formation.

Transversely isotropic parameters	Values
Young's modulus in horizontal direction (GPa)	35
Young's modulus in vertical direction (GPa)	25
Poisson's ratio in the horizontal direction	0.20
Poisson's ratio in the vertical direction	0.27

Table 4: Material properties for casing/cement interface and cement/formation interface [36].

	Casing/cement interface	Cement/formation interface
Tensile bond strength (MPa)	0.5	0.42
Shear bond strength (MPa)	2	0.42

Thus, the stresses and displacements around the wellbore immediately after the drilling are calculated from the numerical model, and the results are compared against the analytical solutions proposed by Salencon [43] (see Appendix). A similar validation method was also adopted by Wang and Sharma [44–46].

In Salencon's study, the plastic behavior of the formation was defined by the Mohr-Coulomb criterion; however, in the simulation, a Drucker-Prager model for the formation is used. Therefore, it is necessary to convert the parameters between these two models for validation purposes. Equations (17)–(19) can be used for the conversion. The parameters in Table 5 were used for the validation.

$$\tan\beta = \frac{6\sin\varnothing}{3-\sin\varnothing}, \tag{17}$$

$$k_f = \frac{3-\sin\varnothing}{3+\sin\varnothing}, \tag{18}$$

Table 5: Parameters used in the validation case [43].

Parameters	Values	Units
Young's modulus, E	6.778	GPa
Shear modulus, G	2.8	GPa
Poisson's ratio, υ	0.21	—
Cohesion strength, d	3.45	MPa
Friction angle, $\varnothing$	30	°
Dilation angle, ψ	30	°
In situ stresses, P_0	20	MPa
Wellbore pressure, P_i	0	MPa
Wellbore radius, a	0.07715	m
Wellbore pressure, P_i	0	MPa

$$\sigma_c = 2C\frac{\cos\varnothing}{1-\sin\varnothing}, \tag{19}$$

where β, k_f, and σ_c represent the friction angle, the flow stress ratio, and the yield stress in the Drucker-Prager model, respectively. $\varnothing$ is the cohesion of formation rock, in the Mohr-Coulomb model.

Figure 4 shows the comparison of the radial stress and tangential stress around the wellbore among the analytical solution, the numerical model with Mohr-Coulomb plasticity (M-C), and the numerical model with Drucker-Prager plasticity (D-P). And Figure 5 shows the results of the distribution of the radial displacement around the wellbore, from these three methods. The results show a good agreement, verifying the accuracy of the numerical model.

Part two: in this part, to further validate the accuracy of the model, physical test results of cement sheath leakage from Jackson et al. [37] are used to compare the numerical results from the proposed model in this work.

Firstly, a brief description of Jackson's work is necessary. In 1993, to reveal the influence of casing pressure on cement sheath sealing property, Jackson et al. set up an experimental research. As shown in Figure 6, the experimental equipment mainly consists of the inner pipe (to simulate the casing) and the outer pipe (to simulate the effort of formation).

During the cement sheath curing process, the cement slurry was poured into the annulus between the inner pipe and the outer pipe, and then, the cement sheath was formed. Then, a source of 0.69 MPa air was injected into the bottom of the annulus, which created a differential pressure across the cement sheath in the annulus [37], and the casing pressure can be changed in the experiment. Once the gas channel occurs in the cement sheath, the real-time monitoring system can detect the gas at the top of the cement sheath and record the casing pressure at that moment. In the two tests, the casing pressure descended from 69 MPa and 55 MPa to less than 6.9 MPa, respectively. Gas was detected at the top of the cement sheath when the casing pressure dropped to 3.3 MPa and 1.4 MPa, respectively.

These experimental results are used to validate the model proposed in this work; the geometry and material properties

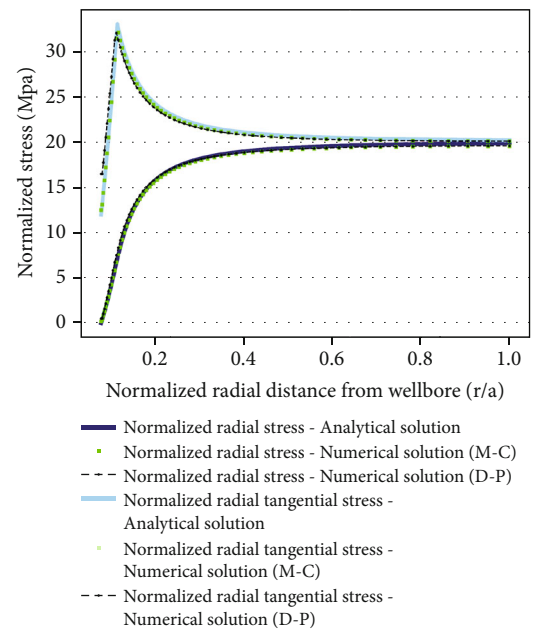

Figure 4: Comparison of radial and tangential stresses (normalized with P_0) between the analytical solution and numerical models.

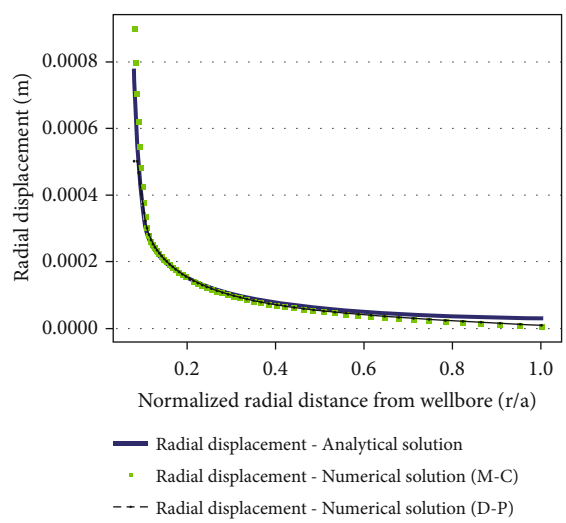

Figure 5: Comparison of radial displacement along with the normalized radial distance between the analytical solution and numerical models.

of the model are adjusted to the test samples in Jackson's experiments, as shown in Table 6.

The outer pipe in the mentioned experiments is regarded as a formation with ultralow (near zero but not zero) permeability and fluid content. The cement sheath in the experiment is assumed to reach an ideal condition after curing, and the water is completely consumed. Therefore, in this work, to simulate Jackson's experimental work, the formation part in the model is assumed to be elastic behavior without considering fluid flow; the fluid content in the cement sheath is zero, and the permeability of the cement sheath is less than 1 mD [26].

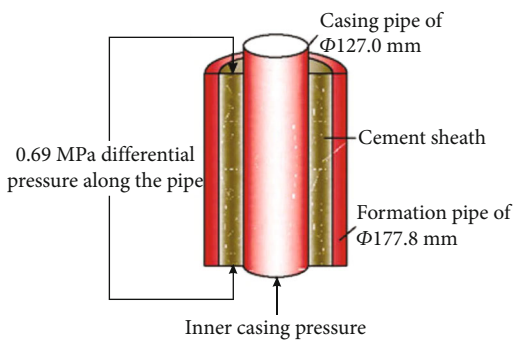

Figure 6: Schematics of Jackson's experiment research [39].

Table 6: Parameters of Jackson's experiment [39].

	Inner casing	Cement	Outer casing
Young's modulus (GPa)	210	13.8	210
Poisson's ratio	0.3	0.25	0.3
Friction angle (°)	—	27	—
Cohesion strength (MPa)	—	5.77	—
Inner diameter (mm)	108.6	127	154.78
Outer diameter (mm)	127	154.78	177.8

The validation work simulates the changes of casing pressure from 69 MPa and 55 MPa to 0 MPa, respectively. The radial displacement of the casing outer surface and cement sheath inner surface is analyzed. As shown in Figure 7, the debonding occurs at the casing-cement sheath interface (i.e., similar to the gas channels occurring in Jackson's experimental work: 3.3 MPa and 1.4 MPa) when the casing pressure is 3.65 MPa and 1.8 MPa. The main reason for the result differences between the numerical and experimental work is the different failure criteria of the casing-cement interface in these two methods. In the simulation work, as shown in Figure 7, the debonding can be estimated directly by the displacements of the cement sheath interfaces. However, in the experiment, the debonding is determined by observing the gas leakage at the top of the cement sheath. Meanwhile, the precision of the test equipment and the properties of the casing-cement sheath interface also have a considerable influence on the test results. Overall, although the casing pressure at the debonding initiation obtained from the numerical simulation is a little bit different from the casing pressure when there is a gas leakage in Jackson's experiment, this difference is acceptable. Thus, the accuracy of the complicated model proposed in this work is further validated by Jackson's physical experiment.

4. Sensitivity Analysis

4.1. Horizontal Stress Anisotropy. High horizontal stress anisotropy is one of the main characteristics of deep shales. For example, in the southern Sichuan Basin in China, the maximum horizontal stress difference can reach up to 25 MPa [47–50]. In this section, the behaviors of the cement

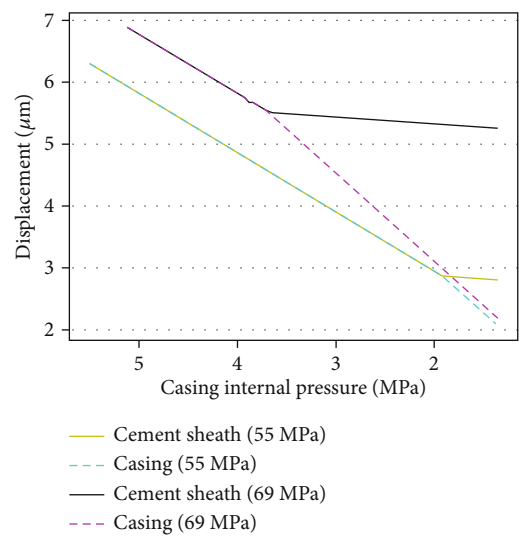

Figure 7: Radial displacement evolution at the casing-cement sheath interface during the unloading process of casing pressure.

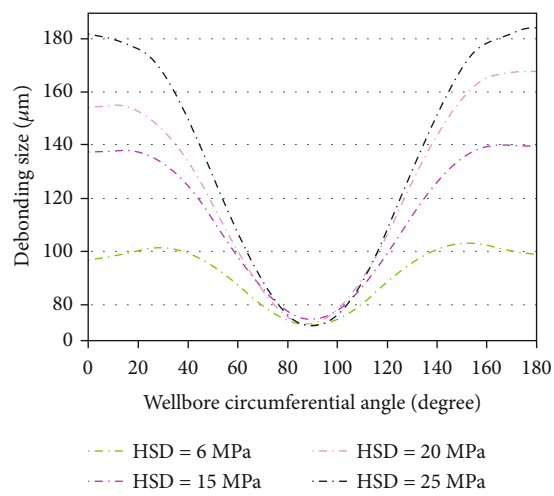

Figure 8: Debonding size of the cement/formation interface with different horizontal stress diffidence (HSD).

sheath under different horizontal stress anisotropies (6 MPa, 15 MPa, 20 MPa, and 25 MPa) are analyzed. In the simulations, the value of minimum horizontal stress is changed while maintaining the maximum horizontal stress as a constant to adjust the horizontal stress anisotropy.

Figure 8 shows that the debonding size for all cases at 0° and 180° direction (the direction of the minimum horizontal stress) is larger than the debonding size at 90° direction (the direction of the maximum horizontal stress). This is because the maximum displacement towards the wellbore before cement hardening occurs at 90° direction as shown in Figure 9, and the shrinkage of cement is uniform along the well circumference; the combined effect results in the minimum debonding size at 90° direction. With the horizontal stress difference increasing from 6 MPa to 25 MPa, the debonding size of the cement sheath gradually increases,

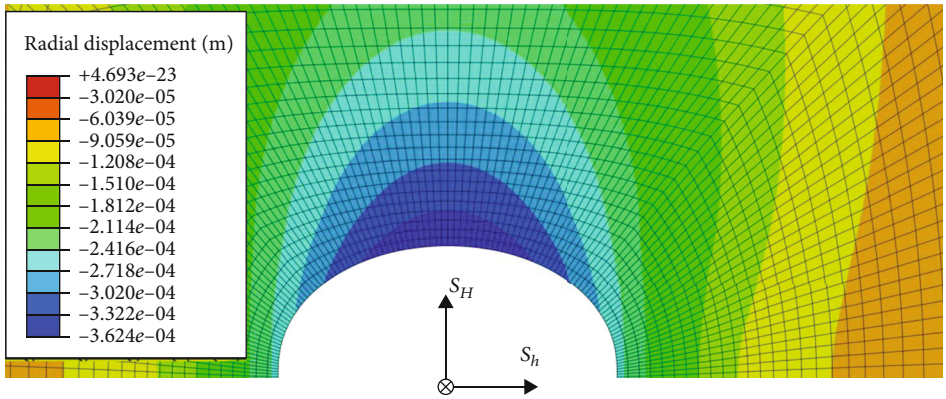

Figure 9: The deformation in the radial direction around the wellbore before cement hardening. The negative value means the deformation is towards the center of the wellbore.

especially at the direction of the minimum horizontal stress direction, as shown in Figure 8.

4.2. Transverse Isotropy

4.2.1. Elastic Parameters. As aforementioned, the shale formation has different elastic parameters in the directions parallel and perpendicular to the bedding planes. In this paper, the ratio of $R_e = E_{\text{horz}}/E_{\text{vert}}$ and $R_\nu = \nu_{\text{horz}}/\nu_{\text{vert}}$ is used to stand for the degree of anisotropy of Young's modulus and Poisson's ratio, respectively. E_{horz} and ν_{horz} stand for Young's modulus and Poisson's ratio in the horizontal direction, respectively; E_{vert} and ν_{vert} stand for Young's modulus and Poisson's ratio in the vertical direction, respectively.

Figure 10 shows the debonding size of the cement/formation interface with different R_e. In the elastic deformation stage of the material, the stress under linear stress state divided by the strain in that direction is Young's modulus. The modulus of elasticity is a measure of the size of the object's ability to resist elastic deformation; the larger the modulus of elasticity, the greater the material's ability to resist deformation. When the formation has a higher Young's modulus in the parallel direction (the value of R_e is higher), this direction has greater resistance to deformation. As a result, the radial deformation is smaller and the debonding size is larger, as shown in Figure 10.

Figure 11 shows the debonding size of the cement/formation interface with different R_ν. Poisson's ratio refers to the ratio of the absolute value of the transverse positive strain to the axial positive strain when the material is subjected to unidirectional tension or compression, which is the elastic constant reflecting the transverse deformation of the material. The debonding size is smaller with a higher value of R_ν.

The anisotropy of Young's modulus has a relatively larger influence on the interface debonding size than Poisson's ratio. The debonding size increases by 176% when the value of R_e increases by 96% (from 0.714 to 1.4), while the debonding size decreases by 26% when R_ν increases by 98.8% (from 0.704 to 1.4). The debonding size is almost zero when $R_e = 0.714$, which means the cement sheath is well

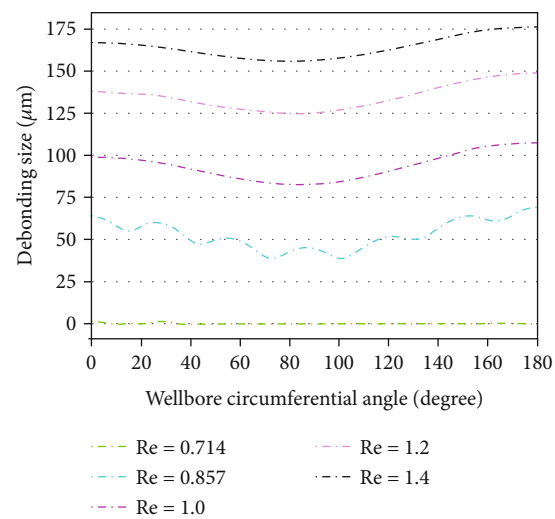

Figure 10: The debonding size of cement/formation interface with different R_e.

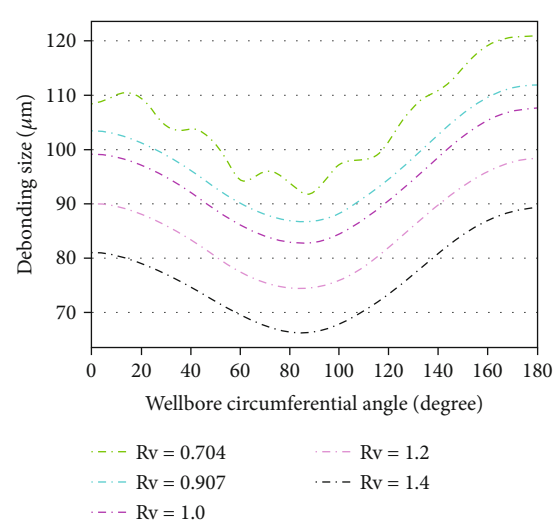

Figure 11: The debonding size of cement/formation interface with different R_ν.

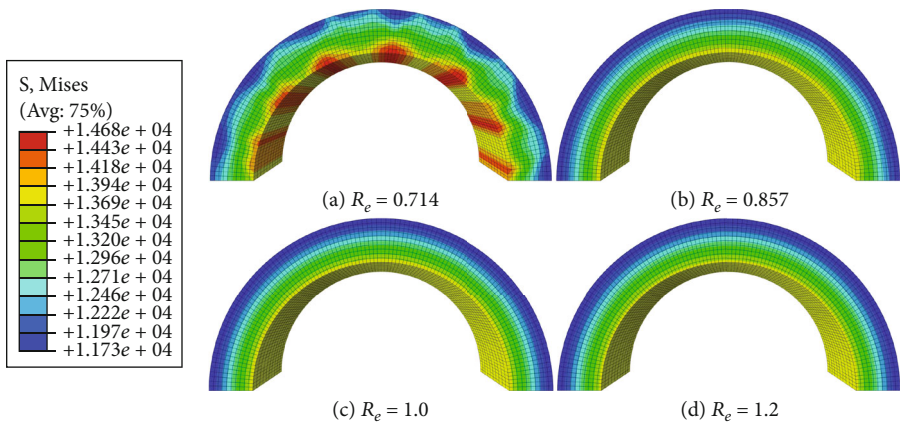

Figure 12: Mises stress distribution in cement sheath with different R_e.

bonded with the formation, and the stress from formation can be exerted to the cement sheath better. This is the reason that the stress distribution has a remarkable difference compared with the other cases, as shown in Figure 12. The results imply that for shales with a higher value of R_e, cement slurry with more expanding agents should be selected for cementing to reduce the risk of interface debonding between the cement sheath and the formation.

4.2.2. Bedding Dip. Directional wells are widely used in oil and gas development in shale formations. The wellbore axis is not always perpendicular to the bedding plane of shales. The effects of the angle between the wellbore axis and bedding plane (defined as angle "α" as shown in Figure 13) on the cement sheath integrity were analyzed in this section ($\alpha = 0^o, 30^o, 60^o, 90^o$). In this work, the range of α is 0~90°. Specifically, $\alpha = 0^o$ means the well is parallel to the bedding plane, while $\alpha = 90^o$ means the well is perpendicular to the bedding plane.

Figure 14 shows the vertical cross section of the radial displacements around the wellbore with different α. It indicates that the distribution of radial displacement around the wellbore is closely related to the angle α. In the analyzed formation interval, the radial displacement distributions along the well axis in case (b) and case (c) are strongly nonuniform. Drilling a well parallel to the bedding plane in case (d) has the largest radial displacement towards the wellbore center among all cases. On the contrary, the radial displacement in case (a) when the well is perpendicular to the bedding plane is the minimum. The main reason is that Young's modulus in the bedding plane is larger than the one in the perpendicular direction, as given in Table 3. For example, in case (d), Young's modulus in the horizontal plane and vertical bedding plane is $E_{\text{horz}} = 25$ MPa and $E_{vert} = 35$ MPa, respectively. Thus, with an increase in the angle α from 0° to 90°, the wellbore radial displacement gradually increases.

To further analyze the effects of bedding dip on cement sheath integrity, the distribution of debonding size at cement/formation interface with different α is illustrated in Figure 15. To reduce the boundary effects of the model due

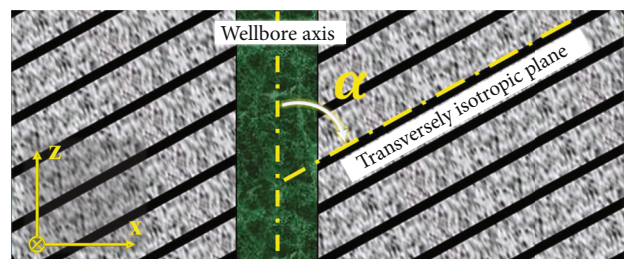

Figure 13: The angle between the wellbore axis and transversely bedding planes.

to the different angles between well axis and bedding planes, the debonding size around the well circumference is extracted from the middle plane that is perpendicular to the well axis in the model. The results show that the bedding dip has a significant influence on the distribution of the debonding size at the cement/formation interface around the well circumference. With the increase of α, the debonding size at the cement/formation interface generally increases. The results also show that drilling perpendicular to the bedding plane ($\alpha = 90^o$) causes the largest debonding size in the studied cases because of the relatively smaller radial displacement, as shown in Figure 14.

4.3. Initial Stresses of the Cement Sheath. In this work, the analyses of the initial stress states of cement sheath were divided into two sets. In the first set of cases, as shown in Table 7, the effect of stress states of cement sheath at different cure time, during the hardening process, was analyzed.

Although the cement sheath is a porous medium, the pore fluid is trapped during the hydration reactions, and there are very few channels connecting the pores. Thus, the permeability of cement sheath is extremely low; the cement sheath can be a reliable barrier that provides zonal isolation. This study assumes that the pore pressure system between the cement sheath and formation is independent. In the following analyses, the nomenclature "S" means the initial stress and "P" means pore pressure. For example, "S60P10"

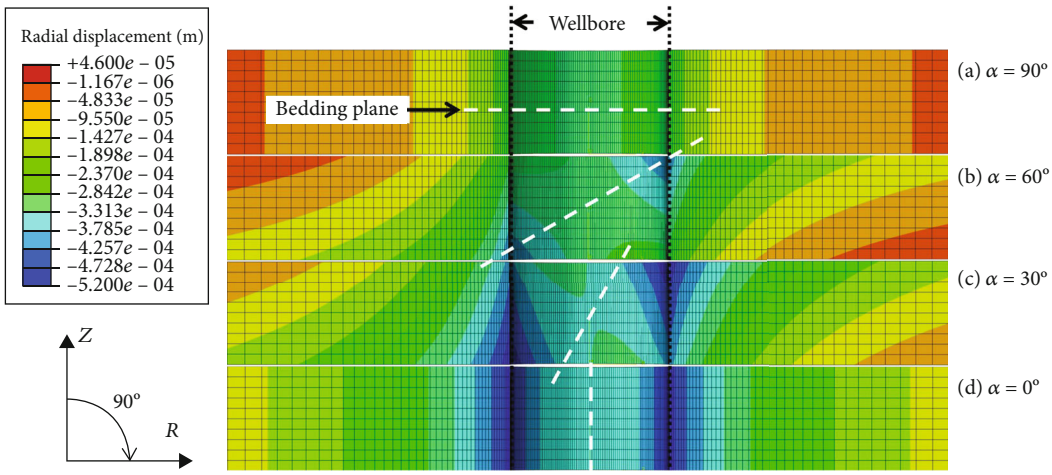

Figure 14: Radial displacements around wellbore wall with different angle α after injection stage.

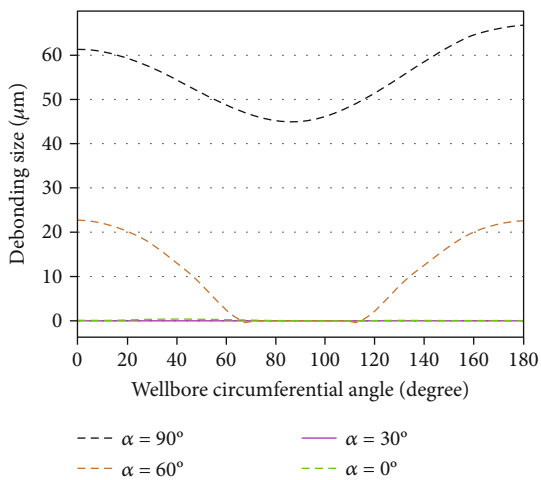

Figure 15: Debonding size at cement/formation interface with different bedding dip, α.

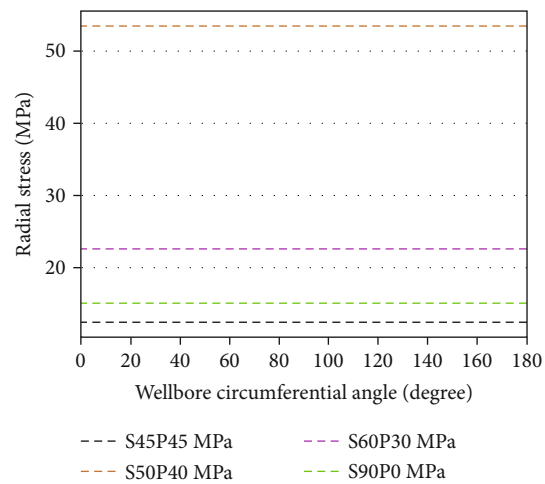

Figure 16: The distribution of radial stress at the interface between formation and cement sheath with different initial stress states.

Table 7: Initial stress and pore pressure of the cement sheath in case group 1.

Case no.	Initial stress (MPa)	Pore pressure (MPa)
1	90	0
2	60	30
3	50	40
4	45	45

means the initial stress is 60 MPa; in the meantime, the pore pressure is 10 MPa.

Figure 16 shows radial stress distribution at the cement sheath-formation interface at the end of the unloading stage. The radial stress increases gradually with the transfer of pore pressure to initial stress; as a result, the debonding size gradually decreases (Figure 17). The negative value of the contact pressure means the gap is generated between the formation and cement sheath, and the positive value means the

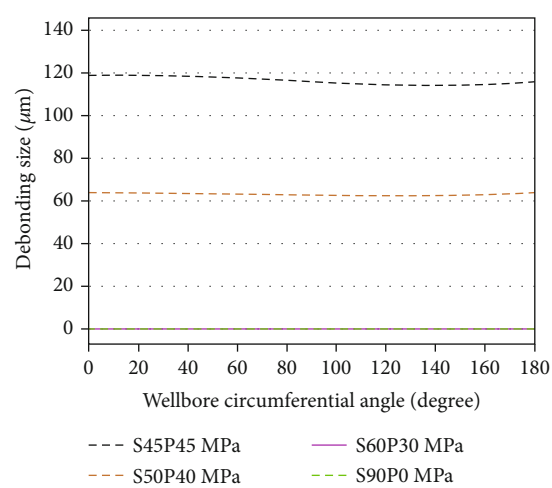

Figure 17: The distribution of debonding size around the interface between formation and cement sheath with different initial stress states.

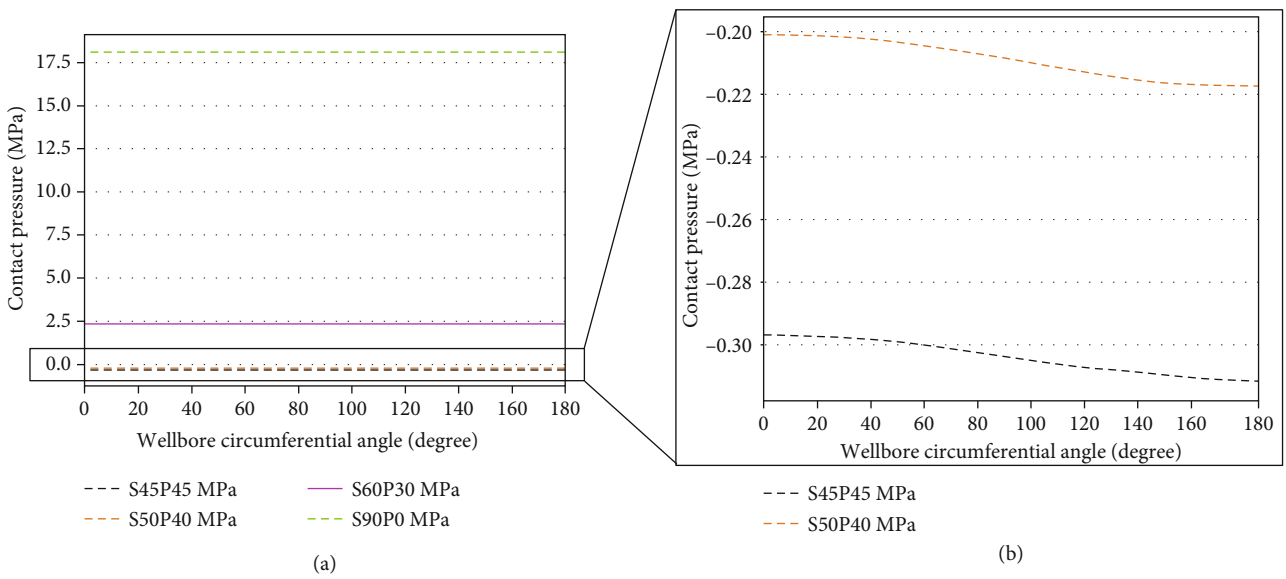

Figure 18: The distribution of contact pressure at the interface between formation and cement sheath with different initial stress states.

Table 8: Initial stress and pore pressure of the cement sheath in case group 2.

	Initial stress (MPa)	Pore pressure (MPa)	Total stress (MPa)
Case A	50	30	80
Case B	50	40	90
Case C	50	50	100
Case D	40	40	80
Case E	30	40	90

interface has a good contact (Figure 18). There is no significant debonding (the debonding size is only 1 μm) when the cement sheath is subjected to compressive stresses. The results correspond well to real practices. The more portion of the pore pressure transfers to initial stress with the hydration reactions, the failure of the cement sheath integrity is less likely to occur.

During the hardening process, both the initial stress and the pore pressure change with time. This changed stress state has a significant effect on the integrity of the cement sheath. The results from the cases of group 1 are for the conversion between pore pressure and initial stress. In order to study the respective effects of the initial stress and the pore pressure, the second group of cases was designed, as shown in Table 8.

The radial stress on the outer surface of the cement sheath increases with the increase of initial stress and the decrease of pore pressure (Figure 19), which results in a better bond between the cement sheath and the formation. The negative value of contact pressure means the interface is debonded (Figure 20). The larger the absolute value of contact pressure, the greater the debonding size between the formation and cement sheath (Figure 21).

The pore pressure has a stronger influence on the integrity of cement sheath than the initial stress. The radial stress increase by 50% when the pore pressure increases by 66.7% (from 30 MPa to 50 MPa, cases A~C), while the change of initial stress has a smaller influence (from 20 MPa to 50 MPa, cases B, D, and E).

Based on the results, the influences of initial cement sheath stress can be summarized as follows:

(1) Both the decrease of pore pressure and the increase of initial stress are beneficial to the integrity of cement sheath. The longer the cure time is, the more the pore pressure converts to the initial stress, and the less likely the failure of the cement sheath integrity

(2) There is a corresponding trend between the radial stress, the contact pressure, and the debonding size at the cement interface with the change of the stress state (initial stress and pore pressure) within the cement sheath during cementing stage. Thus, it may be possible to determine the optimal duration of wait on cement by evaluating the variation of radial stress

(3) The pore pressure greatly influences the integrity of the cement sheath. To improve the integrity of cement sheath, one can accelerate the consumption of free water in the cement slurry by adjusting the chemical compositions

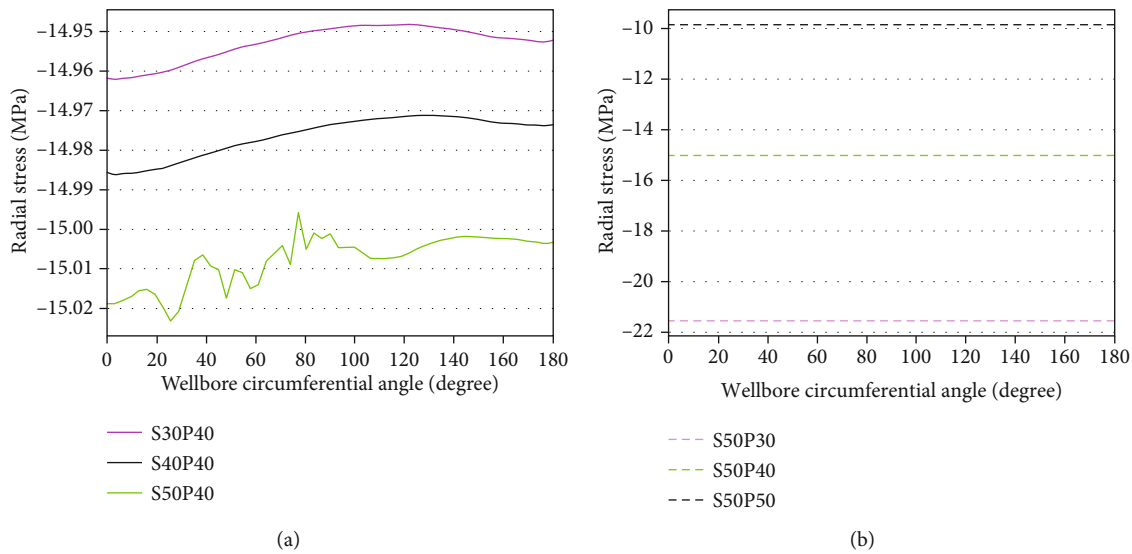

Figure 19: Distribution of radial stress at formation/cement interface with different initial stresses.

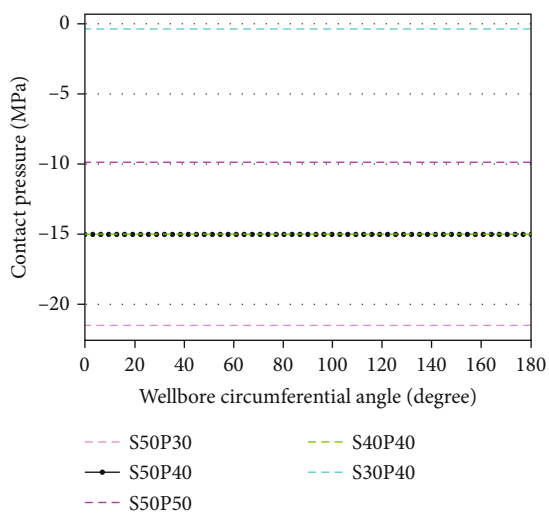

Figure 20: Distribution of contact pressure at formation/cement interface with different initial stresses.

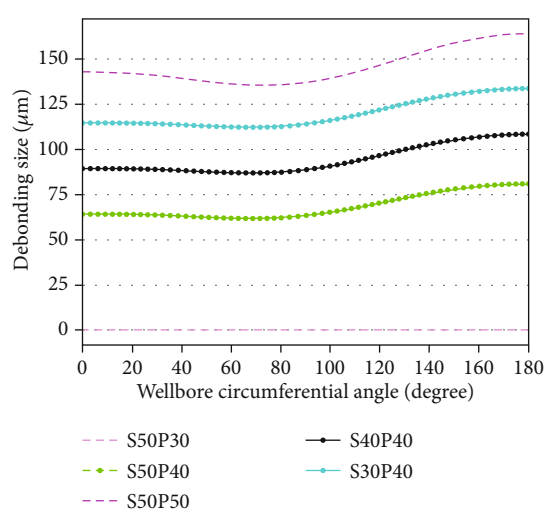

Figure 21: Distribution of contact pressure at formation/cement interface with different initial stresses.

5. Conclusions

In this work, a three-dimensional cement sheath system model was developed, which coupled thermal-hydraulic-mechanical and considered the accumulation of stress-strain states in each stage of the well life cycle. Sensitivity analysis of the anisotropy of deep shale formation and the variation of initial stress of the cement sheath on cement sheath integrity was performed. The results show that the anisotropy of horizontal stress and elastic parameters of the formation can significantly affect the stress-strain state of cement sheath. The angle between the wellbore axis and the bedding plane also has a considerable effect on the integrity of the cement sheath. The debonding size of the cement/formation interface is the minimum when the wellbore axis is parallel to the bedding plane, but the cement sheath may suffer a greater load at the outer surface compared with the case of a wellbore perpendicular to the bedding plane. A relatively high initial stress is beneficial to cement sheath integrity. Thus, to achieve the long-term integrity of cement sheath, the duration of wait-on-cement should be long enough for the pore pressure to transfer to initial stress or adjust the chemical compositions of the cement slurry to accelerate the consumption of free water in the slurry.

Appendix

Analytical solutions of the stress and displacement around the wellbore in an elastoplastic formation.

The radius of the plastic zone, R_o:

$$R_o = a\left(\frac{2}{K_p+1}\frac{P_o+\left(q/\left(K_p-1\right)\right)}{P_i+\left(q/\left(K_p-1\right)\right)}\right)^{1/\left(K_p-1\right)},$$
$$K_p = \frac{1+\sin\varnothing}{1-\sin\varnothing}, \tag{A.1}$$
$$q = 2C\tan\left(45+\frac{\varnothing}{2}\right),$$

where a is the radius of the wellhole; P_o is the uniform initial in situ stress; P_i is the internal pressure.

The stresses in the plastic zone are

$$\sigma_r = -\frac{q}{K_p-1}+\left(P_i+\frac{q}{K_p-1}\right)\bullet\left(\frac{r}{a}\right)^{K_p-1}$$
$$\sigma_\theta = -\frac{q}{K_p-1}+K_p\left(P_i+\frac{q}{K_p-1}\right)\bullet\left(\frac{r}{a}\right)^{K_p-1} \tag{A.2}$$

where r is the distance to the center of the wellhole; σ_r is the radial stress; σ_θ is the tangential stress.

The displacements in the plastic zone are

$$u_r = \frac{r}{2G}\chi,$$
$$\chi = (2\upsilon-1)\left(P_o+\frac{q}{K_p-1}\right)+A_1+A_2,$$
$$A_1 = \frac{(1-\upsilon)\left(K_p^2-1\right)}{K_p+K_{ps}}\times\left(P_i+\frac{q}{K_p-1}\right)\left(\frac{R_o}{a}\right)^{K_p-1}\left(\frac{R_o}{r}\right)^{K_{pS}-1},$$
$$A_2 = \left[(1-\upsilon)\frac{\left(K_pK_{ps}+1\right)}{K_p+K_{ps}}-\upsilon\right]\times\left(P_i+\frac{q}{K_p-1}\right)\left(\frac{r}{a}\right)^{K_p-1},$$
$$K_{ps} = \frac{1+\sin\Psi}{1-\sin\Psi}, \tag{A.3}$$

where υ, Ψ, and G represent Poisson's ratio, the dilation angle, and the shear modulus.

The stresses and displacements in the elastic zone are

$$\sigma_r = P_o-(P_o-\sigma_{re})\left(\frac{R_o}{r}\right)^2,$$
$$\sigma_\theta = P_o+(P_o-\sigma_{re})\left(\frac{R_o}{r}\right)^2, \tag{A.4}$$
$$u_r = \left(P_o-\frac{2P_o-q}{K_p+1}\right)\left(\frac{R_o}{2G}\right)\left(\frac{R_o}{r}\right),$$

where σ_{re} is the radial stress at the elastic/plastic interface:

$$\sigma_{re} = \frac{2P_o-q}{K_p+1}. \tag{A.5}$$

Data Availability

The data used to support the findings of this study are included within the article.

Conflicts of Interest

The authors declare that they have no conflicts of interest.

Acknowledgments

The work was financially supported by the Basic Research Program on Deep Petroleum Resource Accumulation and Key Engineering Technologies (U19B6003) and State Key Laboratory of Shale Oil and Gas Enrichment Mechanisms and Effective Development (25800000-20-ZC0607-0029) and National Natural Science Foundation Project of China (52004298).

References

[1] Z. Chen, D. Xiang, F. Zhang, M. An, Z. Yin, and Z. Jiang, "Fault slip and casing deformation caused by hydraulic

fracturing in Changning-Weiyuan Blocks, Sichuan: mechanism and prevention strategy," *Petroleum Science Bulletin*, vol. 4, pp. 364–377, 2019.

[2] Y. Chunhe and L. Jianjun, "Petroleum rock mechanics: an area worthy of focus in geo-energy research," *Advances in Geo-Energy Research*, vol. 5, no. 4, pp. 351-352, 2021.

[3] B. Hou, Y. Dai, C. Zhou, K. Zhang, and F. Liu, "Mechanism study on steering acid fracture initiation and propagation under different engineering geological conditions," *Geomechanics and Geophysics for Geo-Energy and Geo-Resources*, vol. 7, no. 3, p. 73, 2021.

[4] M. Faraji, A. Rezagholilou, M. Ghanavati, A. Kadkhodaie, and D. A. Wood, "Breakouts derived from image logs aid the estimation of maximum horizontal stress: a case study from Perth Basin, Western Australia," *Advances in Geo-Energy Research*, vol. 5, no. 1, pp. 8–24, 2021.

[5] F. Zhang, B. Damjanac, and S. Maxwell, "Investigating hydraulic fracturing complexity in naturally fractured rock masses using fully coupled multiscale numerical modeling," *Rock Mechanics and Rock Engineering*, vol. 52, no. 12, pp. 5137–5160, 2019.

[6] K. Zhang, B. Hou, M. Chen, C. Zhou, and F. Liu, "Fatigue acid fracturing: a method to stimulate highly deviated and horizontal wells in limestone formation," *Journal of Petroleum Science and Engineering*, vol. 208, article 109409, 2022.

[7] Q. Zhang, B. Hou, B. Lin, X. Liu, and Y. Gao, "Integration of discrete fracture reconstruction and dual porosity/dual permeability models for gas production analysis in a deformable fractured shale reservoir," *Journal of Natural Gas Science and Engineering*, vol. 93, article 104028, 2021.

[8] K. E. Gray, E. Podnos, and E. Becker, "Finite-element studies of near-wellbore region during cementing operations: part I," *SPE Drilling & Completion*, vol. 24, no. 1, pp. 127–136, 2009.

[9] M. J. Thiercelin, B. Dargaud, J. F. Baret, and W. J. Rodriquez, "Cement design based on cement mechanical response," *SPE Drilling & Completion*, vol. 13, no. 4, pp. 266–273, 1998.

[10] Y. Wang, D. Gao, and J. Fang, "Mechanical characteristics analysis of casing-cement ring-formation multilayer composite system," *Chinese Journal of Applied Mechanics*, vol. 31, no. 3, pp. 387–392, 2014.

[11] H. Wang, L. Shi, Y. Zheng, and C. Zhang, "Sealing capacity analysis of cement sheath based on combined mechanical model," *Journal of Northeastern University(Natural Science)*, vol. 41, 2020.

[12] D. M. Fourmaintraux, A.-P. Bois, C. Franco, B. Fraboulet, and P. Brossolllet, "Efficient wellbore cement sheath design using the SRC (system response curve)," in *SPE Europec/EAGE Annual Conference*, Madrid, Spain, 2005.

[13] R. Nygaard, S. Salehi, B. Weideman, and R. G. Lavoie, "Effect of dynamic loading on wellbore leakage for the Wabamun area CO_2-sequestration project," *Journal of Canadian Petroleum Technology*, vol. 53, no. 1, pp. 69–82, 2014.

[14] W. Li, M. Chen, Y. Jin et al., "The porothermoelastic response of a casing-cement- stratum system," in *52nd U.S. Rock Mechanics/Geomechanics Symposium*, Seattle, Washington, 2018.

[15] Z. Niu, J. Shen, L. Wang, and R. Yang, "Thermo-poroelastic modelling of cement sheath: pore pressure response, thermal effect and thermo-osmotic effect," *European Journal of Environmental and Civil Engineering*, vol. 26, pp. 657–682, 2022.

[16] R. Gholami, B. Aadnoy, and N. Fakhari, "A thermo-poroelastic analytical approach to evaluate cement sheath integrity in deep vertical wells," *Journal of Petroleum Science and Engineering*, vol. 147, pp. 536–546, 2016.

[17] M. Meng, L. Frash, J. W. Carey et al., "Predicting cement-sheath integrity with consideration of initial state of stress and thermoporoelastic effects," *SPE Journal*, vol. 26, no. 6, pp. 3505–3528, 2021.

[18] F. Mingtao and L. I. Li Shekun, "Numerical simulation of interface seal failure of cement sheath during multi-stage fracturing," *Science Technology and Engineering*, vol. 19, pp. 107–112, 2019.

[19] Y. Wang, D. Gao, and J. Fang, "Assessment on the cement mechanical properties of shale gas horizontal well in fracturing process," *Petroleum Tubular Goods & Instruments*, vol. 6, 2020.

[20] S. M. Higgins, S. A. Goodwin, A. Donald, T. R. Bratton, and G. W. Tracy, "Anisotropic stress models improve completion design in the Baxter Shale," in *SPE Annual Technical Conference and Exhibition*, Denver, Colorado, USA, 2008.

[21] Q. Wang, P. Wang, D. Xiang, and Y. Feng, "Anisotropic property of mechanical parameters of shale," *Natural Gas Industry*, vol. 32, pp. 62–65, 2012.

[22] J. Saint-Marc, A. Garnier, and A.-P. Bois, "Initial state of stress: the key to achieving long-term cement-sheath integrity," in *SPE Annual Technical Conference and Exhibition*, Denver, Colorado, USA, 2008.

[23] M. Bosma, K. Ravi, W. Van Driel, and G. J. Schreppers, "Design approach to sealant selection for the life of the well," in *SPE Annual Technical Conference and Exhibition*, Houston, Texas, 1999.

[24] M. De Simone, F. L. Pereira, and D. M. Roehl, "Analytical methodology for wellbore integrity assessment considering casing-cement-formation interaction," *International Journal of Rock Mechanics and Mining Sciences*, vol. 94, pp. 112–122, 2017.

[25] L. P. Frash and J. W. Carey, "Engineering prediction of axial wellbore shear failure caused by reservoir uplift and subsidence," *SPE Journal*, vol. 23, pp. 1039–1066, 2018.

[26] P. Drecq and P. A. Parcevaux, "A single technique solves gas migration problems across a wide range of conditions," in *International Meeting on Petroleum Engineering*, Tianjin, China, 1988.

[27] S. Guo, Y. Bu, and H. Liu, "Design of the experimental setup to measure the cement slurry weight loss under consideration of fluid loss," *Research and Exploration in Laboratory*, vol. 36, pp. 50–52, 2017.

[28] P. Lu, L. Sang, S. Xie, Y. Gao, J. Zhang, and X. Kang, "Analysis of the anti-gas channeling effect and weight loss law of styrene-acrylic latex cement slurry," *Petroleum Drilling Techniques*, vol. 47, pp. 52–58, 2019.

[29] Z. Haijin, L. Guangming, L. Aiping, X. Chengbin, and A. Shaohui, "Research on a new method to evaluate the hydrostatic pressure of cement slurries," in *IADC/SPE Asia Pacific Drilling Technology Conference and Exhibition*, Tianjin, China, 2012.

[30] B. Sun, X. Wang, Z. Wang, and Y. Gao, "Transient temperature calculation method for deep-water cementing based on hydration kinetics model," *Applied Thermal Engineering*, vol. 129, pp. 1426–1434, 2018.

[31] X. Wang, B. Sun, S. Liu et al., "A coupled model of temperature and pressure based on hydration kinetics during well cementing in deep water," *Petroleum Exploration and Development*, vol. 47, no. 4, pp. 867–876, 2020.

[32] W. Zhang, A. Eckert, and X. Liu, "Numerical simulation of micro-annuli generation by thermal cycling," in *51st U.S. Rock Mechanics/Geomechanics Symposium*, San Francisco, California, USA, 2017.

[33] SIMULIA, *Abaqus Version 2016 Analysis User's Guide*, Dassault Systèmes, Providence, RI, USA, 2016.

[34] M. L. Benzeggagh and M. Kenane, "Measurement of mixed-mode delamination fracture toughness of unidirectional glass/epoxy composites with mixed-mode bending apparatus," *Composites Science and Technology*, vol. 56, no. 4, pp. 439–449, 1996.

[35] Y. Yang, *Study on the Fracturing Optimum Design and Effect Evaluation of Deep Shale Gas*, China University of Petroleum, 2017.

[36] F. Yin, D. Hou, W. Liu, and Y. Deng, "Novel assessment and countermeasure for micro-annulus initiation of cement sheath during injection/fracturing," *Fuel*, vol. 252, pp. 157–163, 2019.

[37] P. B. Jackson and C. E. Murphey, "Effect of casing pressure on gas flow through a sheath of set cement," in *SPE/IADC Drilling Conference*, Amsterdam, Netherlands, 1993.

[38] Z. Chen and Y. Cai, "Study on casing load in a casing-stratum system by elastoplastic theory," *Petroleum Exploration and Development*, vol. 36, 2009.

[39] W. Chu, J. Shen, Y. Yang, Y. Li, and D. Gao, "Calculation of micro-annulus size in casing-cement sheath-formation system under continuous internal casing pressure change," *Petroleum Exploration and Development*, vol. 42, no. 3, pp. 414–421, 2015.

[40] J. Li, M. Chen, G. Liu, and H. Zhang, "Elastic-plastic analysis of casing-concrete sheath-rock combination," *Acta Petrolei Sinica*, vol. 26, 2005.

[41] Y. Yin, Y. Cai, Z. Chen, and J. Liu, "Theoretical solution of casing loading in non-uniform ground stress field," *Acta Petrolei Sinica*, vol. 27, no. 4, pp. 133–138, 2006.

[42] Y. Yin, Z. Chen, and P. Li, "Theoretical solutions of stress distribution in casing-cement and stratum system," *Chinese Journal of Theoretical and Applied Mechanics*, vol. 38, no. 6, pp. 835–842, 2006.

[43] J. Salencon, "Contraction quasi- statique d'une cavite a symetrie spherique ou cylindrique dans un milieu elasto-plastique," *Annales des Ponts et Chaussees*, vol. 139, pp. 231–236, 1969.

[44] X. Li, Y. Feng, and K. E. Gray, "A hydro-mechanical sand erosion model for sand production simulation," *Journal of Petroleum Science and Engineering*, vol. 166, pp. 208–224, 2018.

[45] H. Wang, P. Cardiff, and M. M. Sharma, "A 3-D poro-elasto-plastic model for sand production around open-hole and cased & perforated wellbores," in *50th U.S. Rock Mechanics/Geomechanics Symposium*, Houston, Texas, 2016.

[46] H. Wang and M. M. Sharma, "A fully 3-D, multi-phase, poro-elasto-plastic model for sand production," in *SPE Annual Technical Conference and Exhibition*, Dubai, UAE, 2016.

[47] M. Dong, W. Guo, L. Zhang et al., "Characteristics of paleotectonic stress field and fractures of Wufeng-Longmaxi formations in Luzhou area, southern Sichuan Basin," *Lithologic Reservoirs*, vol. 34, 2022.

[48] X. He, W. Li, L. Dang, and S. Huang, "Key technological challenges and research directions of deep shale gas development," *Natural Gas Industry*, vol. 41, pp. 1–7, 2021.

[49] Z. Li, Z. Zhang, P. Wu, T. Ma, and J. Fu, "Mechanical mechanisms of wellbore instability of deep anisotropic shale in southern Sichuan," *Journal of Southwest Petroleum University (Science & Technology Edition)*, vol. 43, 2021.

[50] J. Yan, X. Ye, Y. Fu, W. Li, N. Huang, and Y. Wang, "A breakthrough in the technical bottleneck of rotary steeting drilling for deep shale gas in southern Sichuan," *Mud Logging Engineering*, vol. 32, pp. 6–10, 2021.

Hindawi
Geofluids
Volume 2022, Article ID 4681189, 13 pages
https://doi.org/10.1155/2022/4681189

Research Article

Flow Field Simulation of Swirling Abrasive Jet Nozzle for Hard Rock Breaking

Zhang Dongqing,[1] Li Jingbin,[2] Hu Xiao,[2] Liu Xin,[2] and Cheng Kang[2]

[1]*State Key Laboratory of Shale Oil and Gas Enrichment Mechanisms and Effective Development, Beijing 102249, China*
[2]*China University of Petroleum Beijing, Beijing 102249, China*

Correspondence should be addressed to Li Jingbin; lijb@cup.edu.cn

Received 31 December 2021; Revised 25 January 2022; Accepted 14 February 2022; Published 9 March 2022

Academic Editor: Afshin Davarpanah

Radial jet drilling (RJD) technology has been proved to be an economical and efficient stimulation technology for oil and gas, geothermal, hydrate, etc. but conventional RJD technology adopts pure water jet to break rock and form laterals, which has low rock breaking efficiency and is unable to effectively break hard rock such as shale. Swirling abrasive jet is proposed to promote the development of RJD. Here, the characteristics of the flow field of the swirling abrasive jet nozzle and the influence of the key impeller parameters are studied by numerical simulation. The distribution and development of axial velocity, tangential velocity, and radial velocity of water and abrasive are analyzed. The results show that the swirling abrasive jet has no constant velocity core, has stronger diffusivity, and can form a larger impact area than the direct jet. Abrasive particles and water can acquire large tangential and radial velocity which can break rock under the action of shear and tensile stress efficiently. With the increase of the spinning angle, the axial velocity of the fluid decreases, and the tangential velocity increases gradually. With the increase of blade thickness, the axial velocity decreases, and the tangential velocity increases. With the increase of the number of blades, the axial velocity decreases, and the tangential velocity increases. The spinning direction almost has no effect on the flow field. Therefore, the spinning angle is recommended to be no less than 270°, blade thickness is 2.5 mm, and number of blades are 3. The research results provide theoretical guidance for the structural design of swirling abrasive jet nozzles.

1. Introduction

Radial jet drilling (RJD) technology can drill one or more horizontal laterals, whose diameter is about 30~50 mm and the maximum length is about 100 m, along the radial direction perpendicular to the main wellbore by hydraulic jetting. Multiple operations can form a three-dimensional well pattern structure of "multiple layers in one well and multiple branches in the same layer" [1–4]. RJD technology can increase the contact area with reservoir, establish high diversion channel, and efficiently exploit complex oil and gas reservoirs, which has achieved good application. Combined with reservoir simulation technologies such as hydraulic fracturing, full three-dimensional reconstruction can be realized to achieve the goal of enhanced oil recovery [5–13]. Recently, with more and more attention paid to clean energy, RJD technology is considered as an effective geothermal and hydrate resource development technique [14–17].

However, conventional RJD technology adopts pure water jet to break rock and form laterals. The high-pressure water jet technology is the key technology of RJD. Scholars have developed multiorifice nozzle [18, 19], swirling nozzle [20], and straight-swirling integrated nozzle [21] to achieve efficient rock breaking, but pure water jet has low rock breaking efficiency and is unable to effectively break granite, shale, carbonate, and other hard rocks. Therefore, it is necessary to develop new efficient rock breaking technology to promote the development and application of RJD technology.

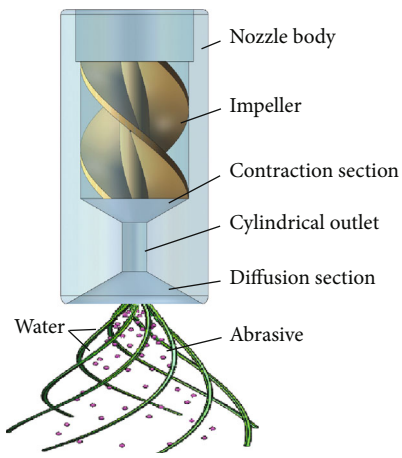

Figure 1: Structure diagram of swirling abrasive jet nozzle.

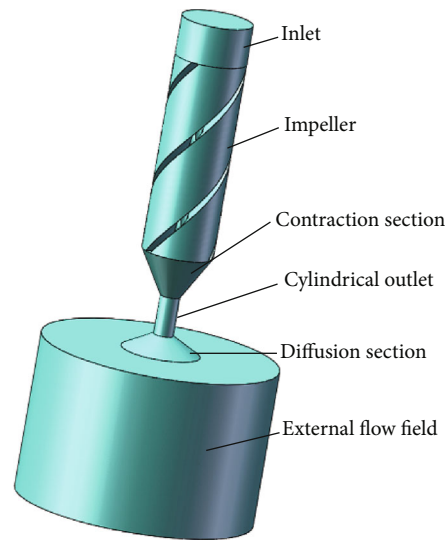

Figure 2: Physical model of swirling abrasive jet nozzle.

Abrasive water jet (AWJ) technology, which is a liquid-solid two-phase jet formed by adding solid particles (garnet or quartz sand, etc.) into high-speed flowing water, is used for a wide range of industrial applications, mainly for cutting and surface treatment [22]. Due to the impact and cutting action of abrasive particles, AWJ has much better rock-breaking performance [23]. AWJ is widely used in petroleum engineering, such as casing cutting, perforating, and hydraulic jet fracturing [24–27]. Huang et al. [28] verified that the abrasive jet has much higher rock-breaking ability. Niu et al. [29] optimized the jet parameters and abrasive parameters in the process of hydraulic jet fracturing through experimental methods. Under the experimental conditions, there is an optimal abrasive volume fraction (6%-8%) and an optimal abrasive particle size range (0.4-0.6 mm).

Although abrasive jet has strong rock breaking ability and high rock breaking efficiency, it has poor diffusivity and only forms small diameter rock-breaking hole, which cannot meet the demand of subsequent pipeline entering the formation. Therefore, Yang et al. [30] proposed swirling abrasive jet technology, which combined the characteristics of abrasive jet and swirling jet. A spiral impeller is added into the classic conical nozzle, so that the fluid and abrasive can obtain high radial and tangential velocity and then form a large impact diameter. Compared with the traditional direct jet, swirling abrasive jet shows complex and unique flow characteristics. Therefore, here, the flow field characteristics of swirling abrasive jet are studied by numerical simulation. Influence of impeller parameters on the flow field is analyzed. The research results can provide guidance for structural optimization design of swirling abrasive jet nozzle.

2. Structure and Principle of Swirling Abrasive Jet Nozzle

As shown in Figure 1, the swirling abrasive jet nozzle is mainly composed of the nozzle body, the impeller, the contraction section, the cylindrical outlet, and the diffusion section. High pressure water and abrasive are bumped to the nozzle by high-pressure plunger pump, through and swirl under the guidance of the impeller, obtain a higher velocity due to the decrease of the cross-sectional area of the contraction section, and then are jetted from the cylinder outlet. Under the protection of the diffusion section, a fully developed swirling abrasive jet is formed. The fluid acquires higher axial, tangential, and radial velocities, and the abrasive also achieves a higher three-dimensional velocity under the action of fluid carrying and acceleration. The rock breaking efficiency of abrasive jet is much higher than that of pure water jet [20]; so, the swirling abrasive jet can effectively break most rocks, even limestone, granite, etc. In addition, because the swirling abrasive jet has higher tangential and radial velocity, the fully developed swirling abrasive jet can form a large diameter hole. The swirling abrasive jet can efficiently break rocks and form large diameter radial branches, which is very suitable for RJD technology.

3. Numerical Simulation Model

3.1. Physical Model and Control Equation

3.1.1. Physical Model. The physical model of the swirling abrasive nozzle is shown as Figure 2. The main composition and basic parameters of the model are as follows: the nozzle inlet with 18 mm diameter, the impeller with 50 mm length, the contraction section with 60° angle, the cylinder outlet with 5 mm diameter and 10 mm length, the diffusion section with 120°angle, and the impact external flow field which is a cylinder with 40 mm height and 60 mm diameter.

3.1.2. Governing Equation. The turbulent viscosity model will directly affect the accuracy of the calculation results. The standard k-epsilon model is a two-equation model in the typical RANS vortex viscosity model. This model is a widely used turbulence model at present. It has a relatively simple calculation format, and better results can be obtained.

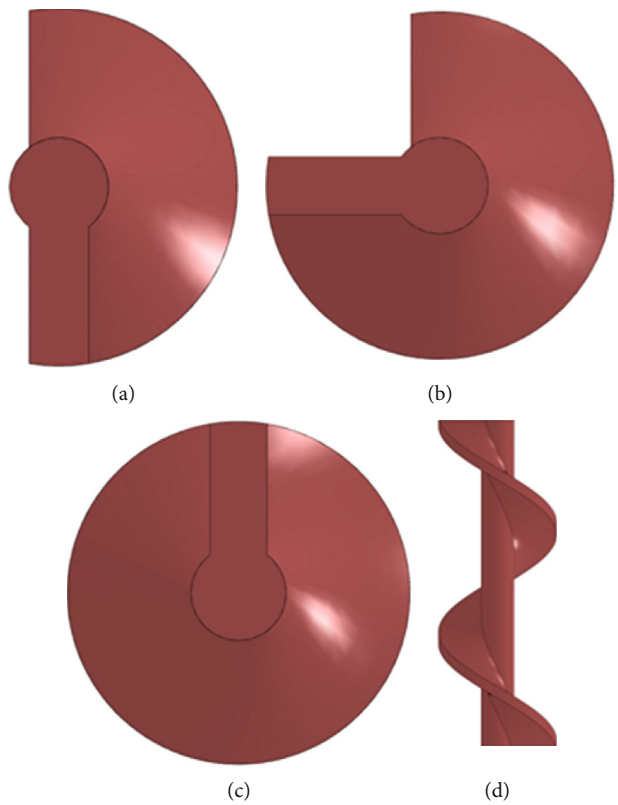

Figure 3: Diagram of impeller with different rotation angles.

The governing equation of the standard k-epsilon model can be expressed in the following general form:

$$\frac{\partial(\rho\phi)}{\partial t}+\frac{\partial(\rho u\phi)}{\partial x}+\frac{\partial(\rho v\phi)}{\partial y}+\frac{\partial(\rho\omega\phi)}{\partial z}=\frac{\partial}{\partial x}\left(\Gamma\frac{\partial\phi}{\partial x}\right)+\frac{\partial}{\partial y}\left(\Gamma\frac{\partial\phi}{\partial y}\right)+\frac{\partial}{\partial z}\left(\Gamma\frac{\partial\phi}{\partial z}\right)+S, \quad (1)$$

where ϕ denotes dependent variable, such as u, v, and ω, Γdenotes the diffusion coefficient, and S denotes the source term of the equation.

In the standard k-epsilon model, the turbulent kinetic energy k and the dissipation rate ε are two basic unknowns, and the corresponding transport equations are as follows:

$$\begin{aligned}\frac{\partial(\rho k)}{\partial t}+\frac{\partial(\rho k u_i)}{\partial x_i}&=\frac{\partial}{\partial x_j}\left[\left(\mu+\frac{\mu_l}{\sigma_k}\right)\frac{\partial k}{\partial x_j}\right]\\&\quad+G_k+G_b-\rho\varepsilon-Y_M+S_k\frac{\partial(\rho\varepsilon)}{\partial t}+\frac{\partial(\rho\varepsilon u_i)}{\partial x_i}\\&=\frac{\partial}{\partial x_j}\left[\left(\mu+\frac{\mu_l}{\sigma_k}\right)\frac{\partial k}{\partial x_j}\right]\\&\quad+C_{1\varepsilon}\frac{\varepsilon}{k}(G_k+C_{3\varepsilon}G_b)-C_{2\varepsilon}\rho\frac{\varepsilon^2}{k}+S_\varepsilon,\end{aligned} \quad (2)$$

where G_k is the generation term of turbulent kinetic energy k caused by average velocity gradient, G_b is the generation term of turbulent kinetic energy k caused by buoyancy, Y_M denotes the contribution of fluctuating expansion in compressible turbulence, $C_{1\varepsilon}$, $C_{2\varepsilon}$, and $C_{3\varepsilon}$ are empirical constants, σ_k and σ_ε are the Prandtl numbers corresponding to the turbulent kinetic energy k and the dissipation rate ε, and S_k and S_ε are the source terms of the equation.

3.2. Boundary Condition. For different nozzles, it is difficult to ensure the same flow rate and pressure drop at the same time. Therefore, the same pressure drop conditions are generally selected for comparative analysis. The nozzle inlet is set as the pressure inlet. The experimental results show that under the condition of 30 MPa pressure difference, the abrasive jet can break most of the rock materials; so, the inlet pressure is set as 30 MPa. The side of the impact external flow field is arranged as a pressure outlet which is atmospheric pressure.

3.3. Discrete Phase Setting. Fluent software provides three multiphase flow models: VOF (volume of fluid) model, mixture model, and Euler model. The Euler model can simulate the multiphase flow of arbitrary composition, and it can also simulate the multiphase flow of interaction [31]. Therefore, the Euler model was selected to study the flow field characteristics of the swirling abrasive jet nozzle. The physical parameters of water can be directly transferred from the Fluent database. The abrasive is set as density 2600 kg/m^3, viscosity 0.0001 kg/m^{-1}, and grain spacing 0.0002. Set the basic phase 1 to water and the phase 2 to abrasive.

3.4. Experimental Project. The impeller is the key component of the swirling abrasive jet nozzle. As shown in Figure 3, its

Table 1: Design of structural parameters of the impeller.

Parameters	Length (mm)	Diameter (mm)	Swirling angle (°)	Blade thickness (mm)	Blade number	Spinning direction
Control group	50	18	360	2.5	3	Clockwise
Swirling angle	50	18	180/270/540	2.5	3	Clockwise
Blade thickness	50	18	360	2/3/3.5/4	3	Clockwise
Blade number	50	18	360	2.5	2/4/5	Clockwise
Swing direction	50	18	360	2.5	3	Counterclockwise

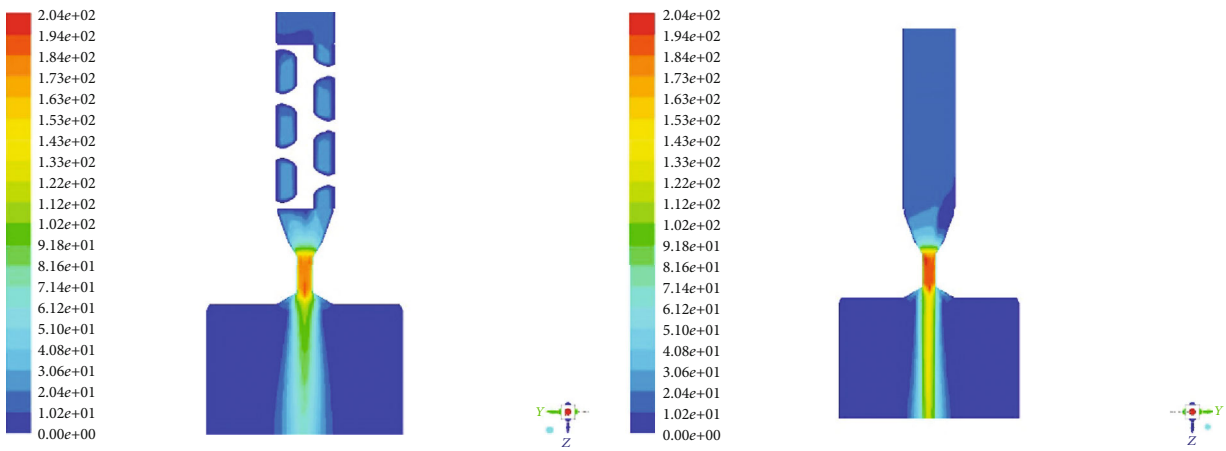

Figure 4: Cloud picture of velocity of swirling abrasive jet and direct jet.

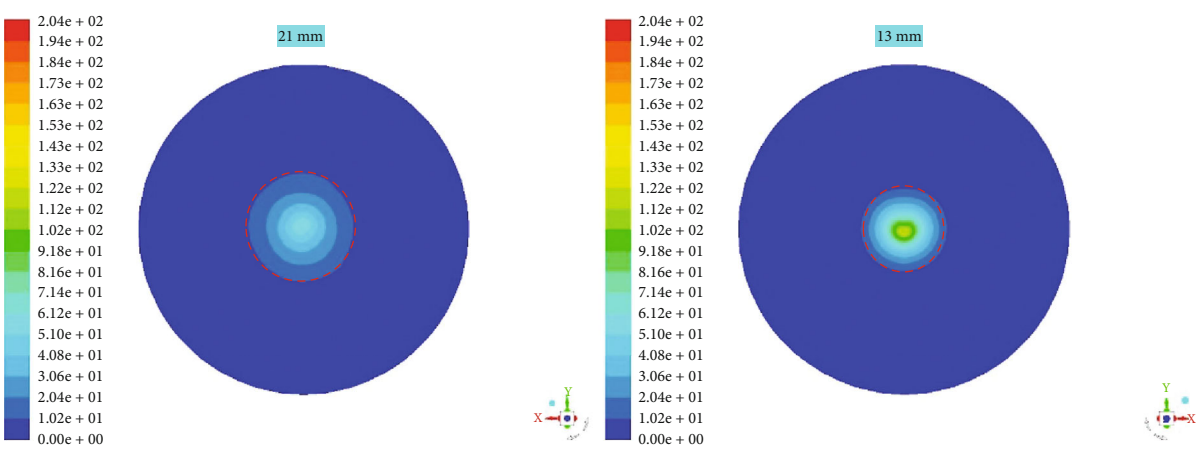

Figure 5: Cloud picture of bottom impact velocity of swirling abrasive jet and direct jet.

key parameters mainly include the following: blade thickness, blade number, blade swirling angle, and spinning direction. The effects of four parameters on the flow field characteristics of the swirling abrasive jet nozzle are studied. In the process of radial horizontal well, the nozzle needs to complete the steering under the steering effect of the deflector. In order to pass the deflector smoothly, the length of the nozzle is generally designed to be 30~50 mm, and the outer diameter is generally 20~30 mm [21, 32–34]. Therefore, the length of the impeller designed in this paper is no more than 50 mm, and the outer diameter is 18 mm. The blade thickness should ensure the strength without occupying too much space, the number of blades should be convenient for processing and occupy less space, and the rotation angle should be considered to cover a larger range during design so as to study its influence rules. The research project is shown in Table 1. Other structural parameters of the swirling abrasive nozzle remain the same.

4. Flow Field Characteristics of the Swirling Abrasive Jet Nozzle

The velocity distribution and impact pressure distribution of the fluid and abrasive particles in the nozzle flow field determine the rock-breaking effect. Specially, the tangential and radial velocity distribution of the swirling jet is of great significance for improving the rock breaking efficiency and forming a large area of rock breaking. In addition, the

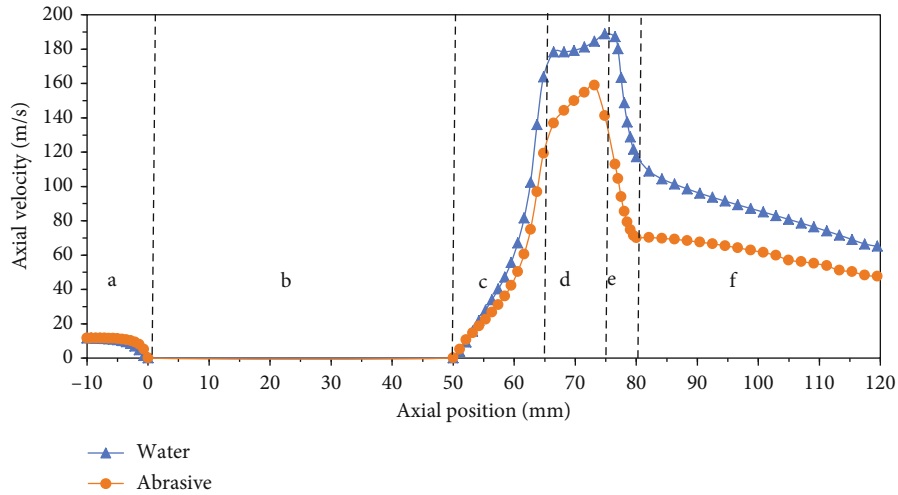

Figure 6: Axial velocity distribution of abrasive and water in swirling abrasive jet (a) inlet section, (b) swirling section, (c) contraction section, (d) cylindrical outlet section, (e) diffusion section, and (f) external flow field section.

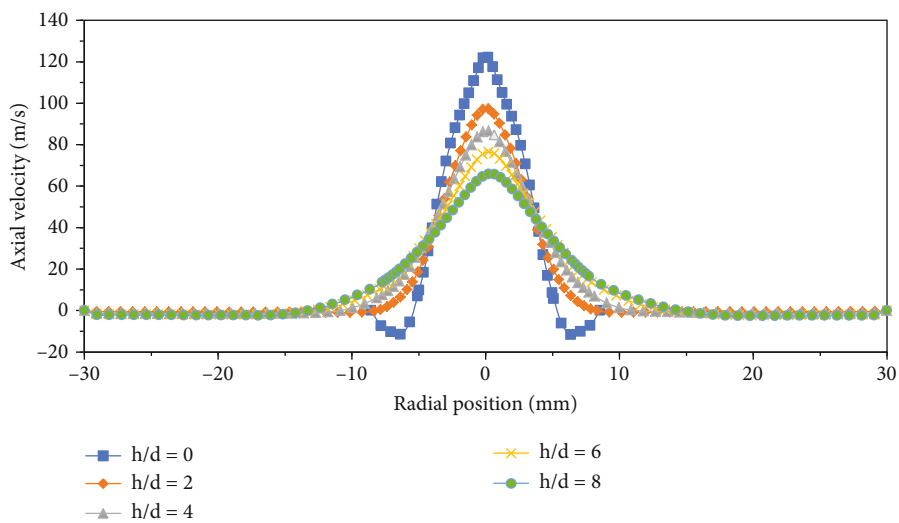

Figure 7: Development law of axial velocity of water.

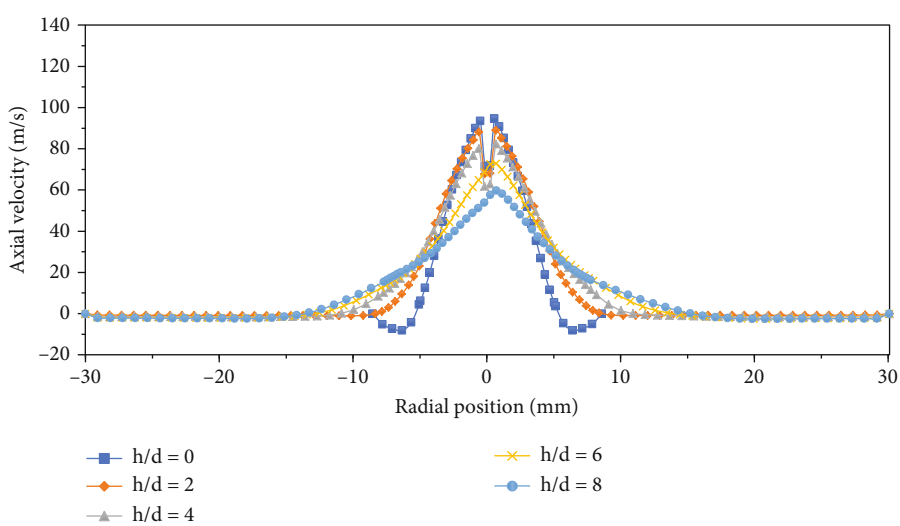

Figure 8: Development law of axial velocity of abrasive.

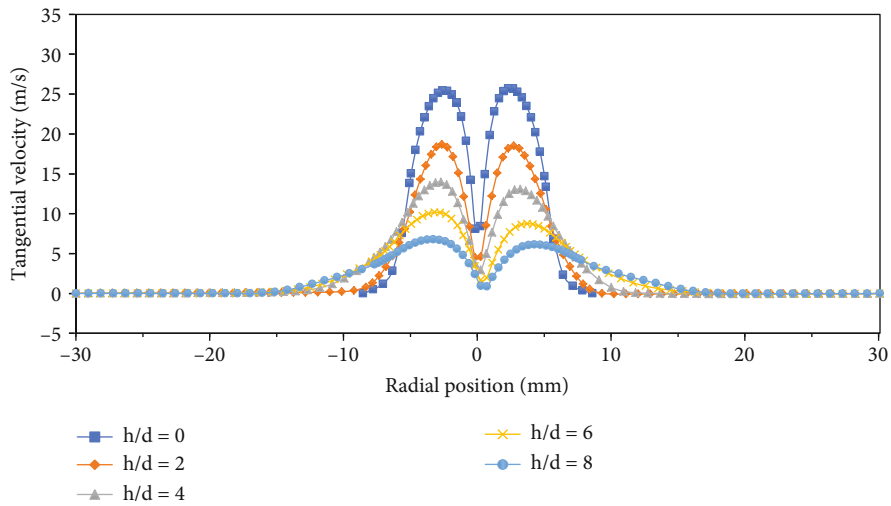

Figure 9: Development law of tangential velocity of water.

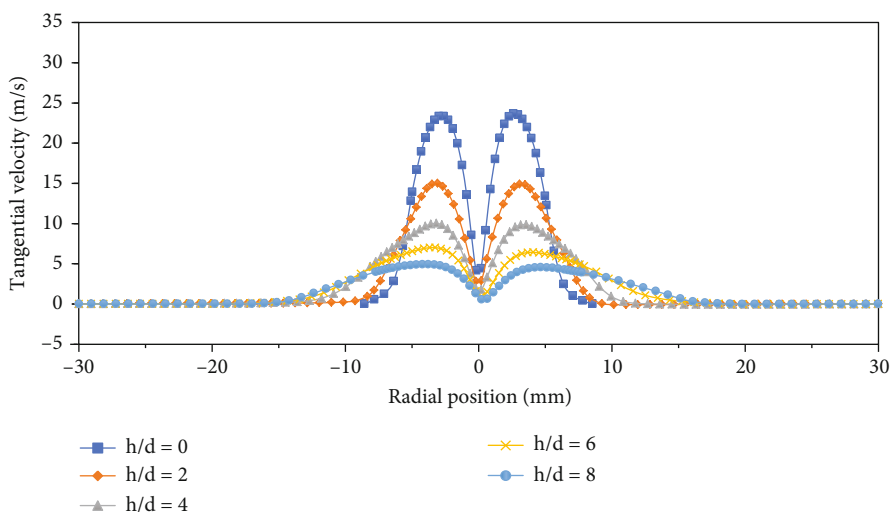

Figure 10: Development law of tangential velocity of abrasive.

rock-breaking ability of abrasive jet is strong, and the velocity distribution characteristics of abrasive particles need to be studied. The flow field of the classical conical nozzle with same equivalent diameter is carried out and compared.

4.1. Flow Field Characteristics of the Swirling Abrasive Jet. The velocity cloud images and jet impact pressure cloud images of the swirling abrasive jet and conical jet are shown in Figures 4 and 5. The flow field structure of swirling abrasive jet nozzle is similar to that of the conical jet, but the swirling abrasive jet has stronger diffusivity; that is, the impact area is larger. Accordingly, the velocity attenuation is fast, the impact pressure is low, and there is no potential core, which is consistent with the research results of Ahmed et al. [34]. It is well known that abrasive jet has high rock breaking efficiency. Therefore, the swirling abrasive jet can effectively break rock and form larger diameter laterals, which is very suitable for RJD technology.

4.2. Axial Velocity Distribution. The axial velocity determines the impact ability of the jet, specially the abrasive needs to obtain sufficient axial velocity to break the rock. The axial velocity of water and abrasive particles is shown in Figure 6. The flow field is divided into six sections from the nozzle inlet: the inlet section (a), the swirling section (b), the contraction section (c), the cylindrical outlet section (d), the diffusion section (e), and external flow field (f). Due to the existence of the impeller, the axial velocity is zero in the swirling section. In the contraction section, the velocity of water increases due to the reduction of the cross-sectional area. The abrasive accelerates under the drag force and pressure difference of water. In the cylindrical outlet section, the velocity of the water is gradually stable, but the velocity of the abrasive is always increasing. In the diffusion section, water and abrasive are ejected from the nozzle, the velocity decreases rapidly due to the loss of the nozzle constraint, and there is no potential core. At the section of the

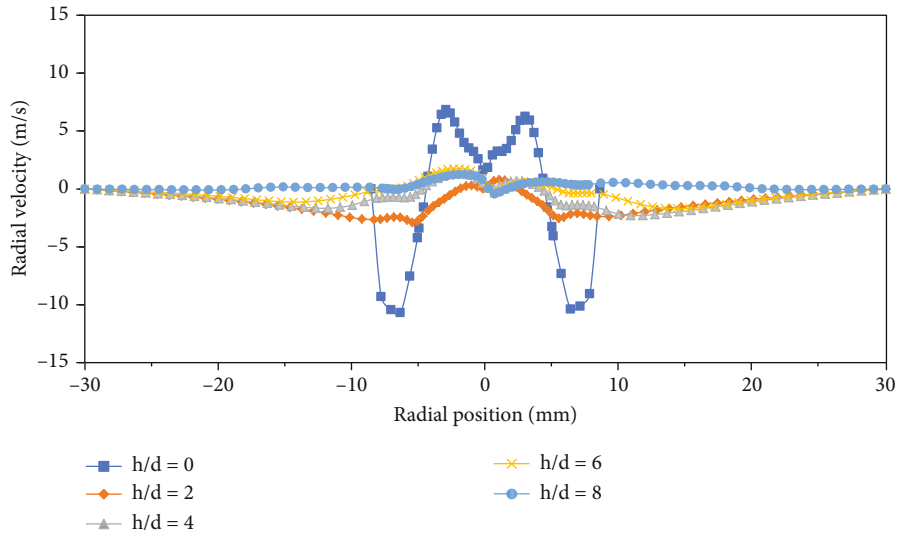

Figure 11: Development of radial velocity of water.

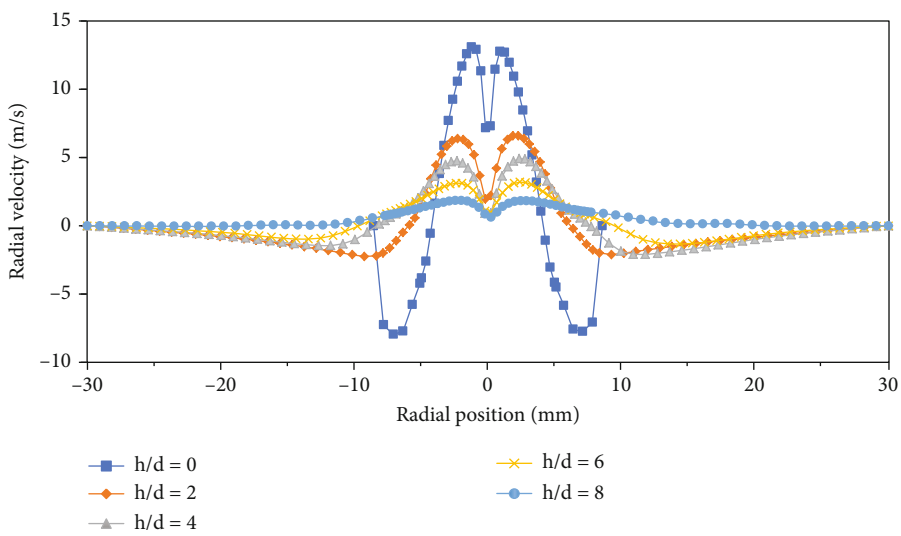

Figure 12: Development of radial velocity of abrasive.

external flow field, the axial velocity begins to decline, but for the speed of the abrasive is still lower than the speed of water, the axial velocity decreasing trend of the abrasive is slower than that of water. After the action of the nozzle, both water and abrasive obtain a higher axial velocity.

4.2.1. Development Law of Axial Velocity. The axial velocity distribution of water and abrasive under different standoff distance is shown in Figures 7 and 8. The zero of the abscissa is set as the center of the nozzle, while the ordinate is the axial velocity. The dimensionless standoff distance (the ratio of the standoff distance to the diameter of the nozzle outlet) is set as 0, 2, 4, 6, and 8. The axial velocity of the swirling abrasive jet obviously has the velocity distribution law of the normal jet, which means that the central velocity is the largest and gradually attenuates along both sides. When the standoff distance is zero, the velocity near the nozzle outlet is negative, which means that entrainment occurs. With the increase of the standoff distance, the jet gradually develops laterally and can form a larger impact area in a certain range. By comparing the axial velocity development curve of abrasive and water, it is found that the velocity of water at the central axis decreases greatly, while the energy loss of abrasive particles is small due to the existence of the speed difference. Therefore, the impact strength of the abrasive can be ensured.

4.3. Development Law of Tangential and Radial Velocity. As we all know, the shear and tensile strength of rock are much lower than its compressive strength, rock is easily broken under the action of shear and tensile stress. Swirling abrasive jet has higher tangential and radial velocity which can produce loads parallel to the surface of the rock, resulting in shear failure. It is necessary to study the development law of tangential velocity and radial velocity.

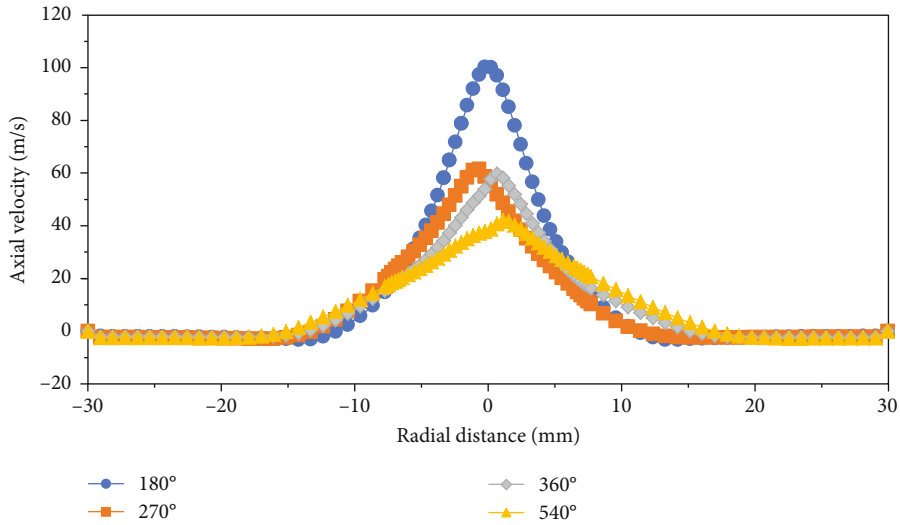

Figure 13: Axial velocity distribution of different spinning angles in $h/d = 8$.

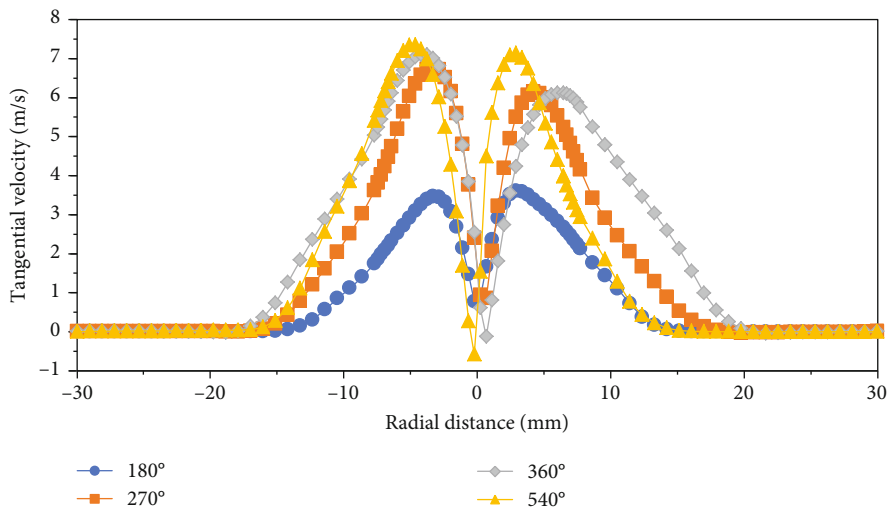

Figure 14: Tangential velocity distribution of different spinning angles in $h/d = 8$.

4.3.1. Distribution Law of Tangential Velocity of Abrasive Particles and Water. Figures 9 and 10 show the distribution of the tangential velocity of water and abrasive particles, the abscissa is the radial distance, and the ordinate is the tangential velocity. The dimensionless standoff distance is set as 0, 2, 4, 6, and 8. Water and abrasive particles do acquire large tangential velocities. The tangential velocity is almost zero along the axis and presents an M-shaped distribution. The maximum tangential velocity will appear at a certain radial radius. At the same time, with the increase of the standoff distance, the maximum tangential velocity gradually develops outward, but the peak value decreases. By comparison, it is found that there is little difference between the tangential velocity of abrasive and that of water, which can improve the efficiency of rock breaking.

4.3.2. Distribution Law of Radial Velocity of Abrasive Particles and Water. Figures 11 and 12 show the distribution of the radial velocity of water and abrasive, the abscissa is the radial radius, and the ordinate is the radial velocity. The dimensionless standoff distance is set as 0, 2, 4, 6, and 8. The radial velocity first increases and then decreases along the radius from the center and shows an symmetrical distribution, which is similar to that of the tangential velocity. When the standoff distance is small, the radial velocity appears negative value, which is due to the influence of entrainment effect. By comparing the radial velocity curve of abrasive and water, it is found that the radial velocity of abrasive particles is larger. However, the radial velocity has a small absolute value and fast attenuation rate. Therefore, radial velocity has little influence on rock breaking, but great influence on impact diameter. However, since the impact diameter can also be obtained from the radial distance where the axial velocity and tangential velocity close to zero, only the axial velocity and tangential velocity are used for analysis in the subsequent analysis.

As mentioned above, water and abrasive in swirling abrasive jet can obtain higher axial, tangential, and radial

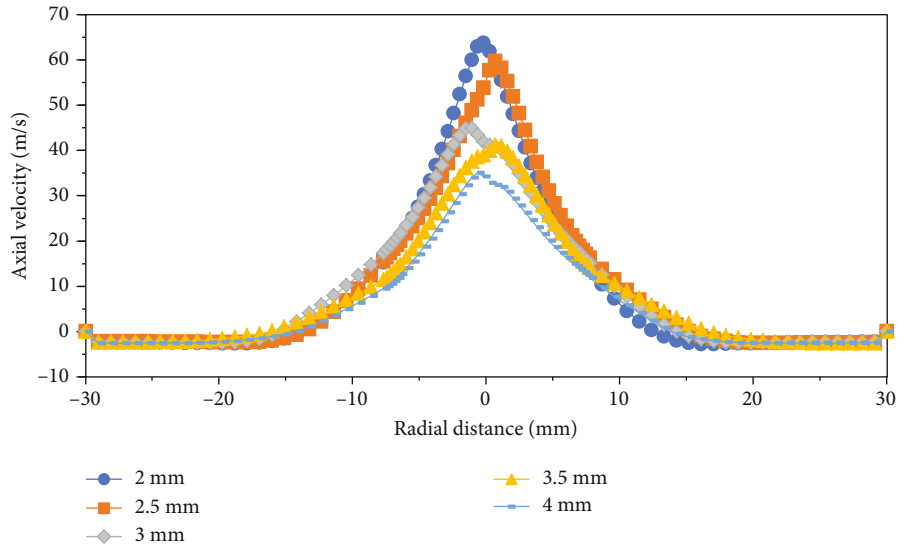

Figure 15: Axial velocity distribution of different blade thickness in $h/d = 8$.

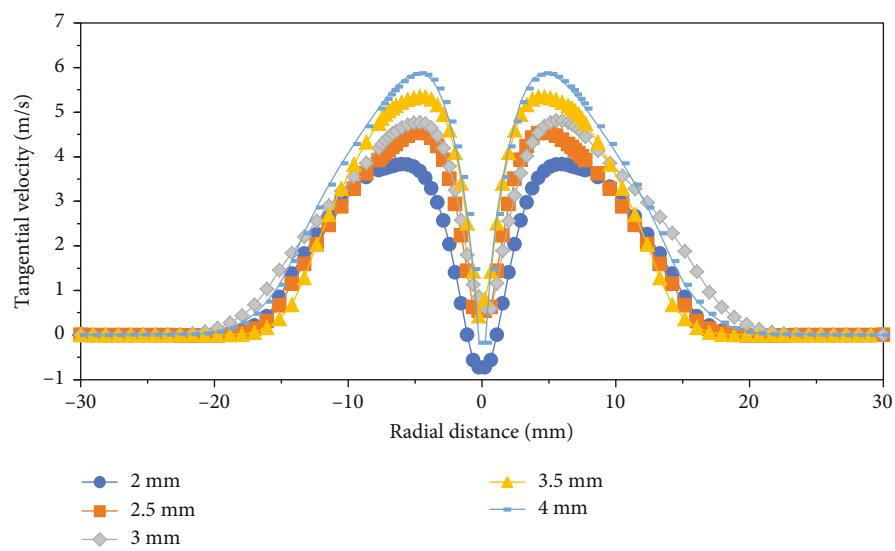

Figure 16: Tangential velocity distribution of different blade thicknesses in $h/d = 8$.

velocities under the guiding of swirling impeller. In other word, the swirling jet velocity is three-dimensional, and its rock breaking manner is mainly of slopping impact, which make it high rock breaking efficiency [35]. The tangential velocity presents an M-shaped distribution, and its maximum value appears on a ring at a certain distance from the jet center, which explains the phenomenon that rock fragmentation by swirling jet will form a circular region [36]. The radial velocity distribution shows the phenomenon of entrainment, but its absolute value is small and is not considered in the follow-up study.

5. Influence of Structural Parameters

In order to perform radial drilling well, the nozzle should simultaneously achieve high efficiency rock breaking and large diameter hole-forming [37]. According to the above analysis, the axial velocity and tangential velocity determines the rock-breaking efficiency. The core part of the swirling abrasive jet nozzle is the impeller. Therefore, the influence of various parameters of the impeller on the axial and tangential velocity is mainly analyzed.

5.1. Influence of Swirling Angle of Impeller. When the diameter and length of the impeller are constant, the swirling angle of the impeller determines the rotation of the fluid. The initial rotation angle is positioned at 180 degrees, followed by an increase of 90 degrees. In order to study the influence of a larger range of angles, the last group is positioned at 540°. To evaluate the impact effect, the axial and tangential velocities near the impact plane where the dimensionless standoff distance is equal to 8 are selected for analysis. As shown in Figures 13 and 14, with the increase of rotation angle, the axial velocity distribution becomes smoother, and the peak value

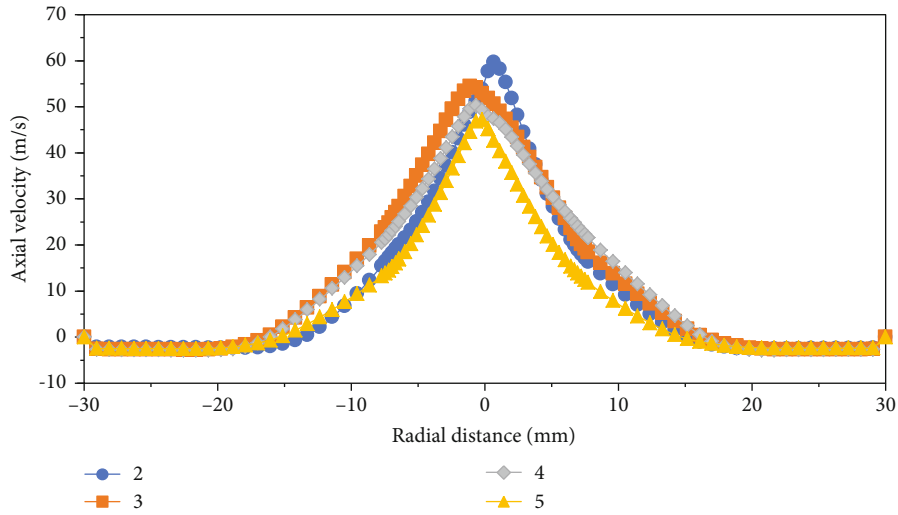

Figure 17: Axial velocity distribution of different blade thicknesses in $h/d = 8$.

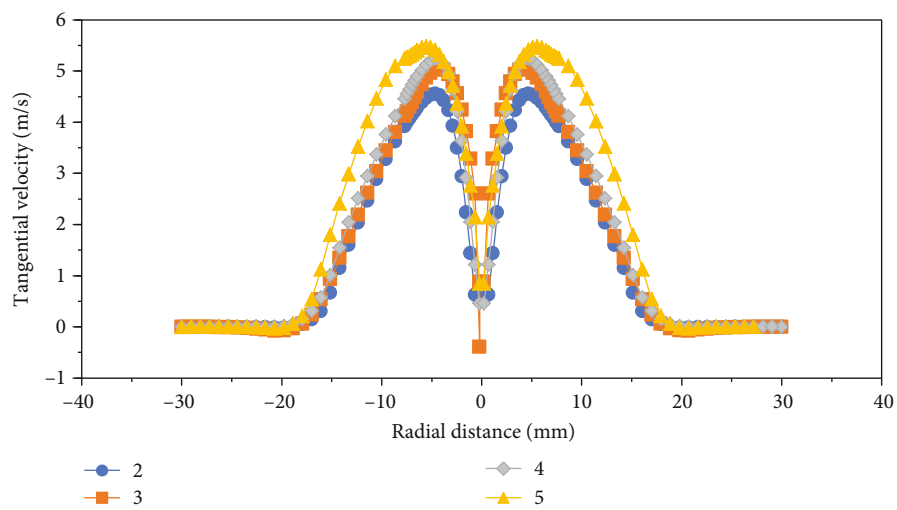

Figure 18: Tangential velocity distribution of different blade thicknesses in $h/d = 8$.

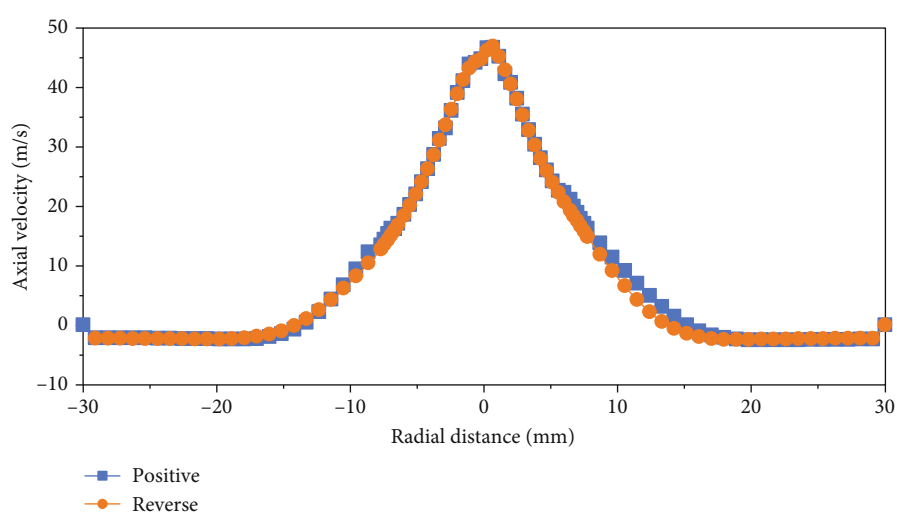

Figure 19: Axial velocity distribution of positive and reverse swirling in $h/d = 8$.

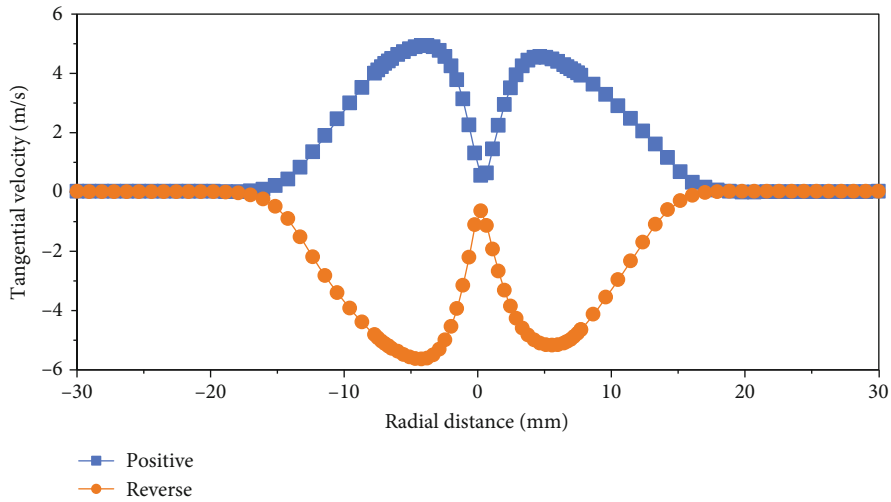

Figure 20: Tangential velocity distribution of positive and reverse swirling in $h/d = 8$.

decreases, while the peak tangential velocity gradually increases. It can be seen that with the increase of rotation angle, abrasive and fluid can obtain more tangential velocity, which can promote rock failure by shear action. When the rotation angle is greater than 270°, the influence of the rotation angle on the axial and tangential velocities decreases. Therefore, under the condition of this paper, the rotation angle is recommended to be no less than 270°.

5.2. Influence of Blade Thickness. When the other parameters of the impeller are constant, the impeller thickness affects the flow section and then the rotation capacity. The influence of the blade thickness on the abrasive flow field is carried out. Figures 15 and 16 show the axial and tangential velocity distributions of abrasive particles when the dimensionless standoff distance is 8 and the blade thickness is 2 mm, 2.5 mm, 3 mm, 3.5 mm, and 4 mm. It can be seen from Figure 16 that the tangential velocity of abrasive gradually increases with the increase of blade thickness, and the peak value of blade thickness 4 mm is the highest; so, it is recommended to increase blade thickness. Correspondingly, as shown in Figure 15, the axial velocity decreases with the increase of blade thickness. Although increasing the blade thickness can increase the tangential velocity, the increase is small and will lead to the increase of flow resistance. Therefore, 2.5 mm is recommended under the conditions of this paper.

5.3. Influence of Blade Number. The influence of the number of blades on the flow field of abrasive is carried out. Figures 17 and 18 show the axial and tangential velocity distributions of abrasive particles when the dimensionless standoff distance is 8 and the number of blades is 2, 3, 4, and 5. With the increase of the number of blades, the peak axial velocity decreases slightly while the tangential velocity increases. Generally, the number of blades has little effect. Considering axial velocity and tangential velocity, the recommended number of blades is 3.

5.4. Influence of the Spinning Direction. The influence of the swirling direction of impeller on the abrasive flow field is also studied. Figures 19 and 20 show the axial and tangential velocity distributions of abrasive particles when the dimensionless standoff distance is 8. It can be seen from Figures 18 and 19 that the axial velocities basically are the same while tangential velocities are mirrored, which means their absolute values, the development law, and expansion range are basically the same. Therefore, the spinning direction will not affect the flow field of the swirling abrasive jet.

6. Conclusion

Swirling abrasive jet technology can realize large diameter and efficient rock-breaking and hole-forming, which can greatly promote the development RJD technology. In order to better understand its working principle and improve its performance, the flow field characteristics and key impeller parameters of swirling abrasive jet nozzles are studied by numerical simulation, and the main conclusions are as follows:

(1) Compared with the direct jet, the flow field structure of the swirling abrasive jet is basically the same, but it has no constant velocity core, and its diffusivity is stronger, which can form a larger impact area; that is, the swirling abrasive jet nozzle can form a larger diameter rock-breaking

(2) Under the action of swirling impeller, abrasive particles can obtain larger axial and tangential velocities. The velocity of abrasive particles increases with the velocity of water, and when it comes out of the nozzle, the velocity of abrasive particles attenuates slowly. The tangential velocity shows an "M" distribution along the radial direction of the nozzle, which has a low central velocity and a high surrounding velocity. The radial velocity shows that there is an entrainment region. The combination of axial, tangential, and radial velocities can better break the rock by tensile shear, form a larger rock-breaking diameter, and improve the efficiency

(3) With the increase of the spinning angle, the axial velocity of the fluid decreases, and the tangential velocity increases gradually. With the increase of blade thickness, the axial velocity decreases, and the tangential velocity increases gradually. With the increase of the number of blades, the axial velocity decreases, and the tangential velocity increases gradually. The spinning direction almost has no effect on the flow field. Therefore, the spinning angle is recommended to be no less than 270°, blade thickness is 2.5 mm, and number of blades are 3

Data Availability

When data is required, the corresponding author can be contacted.

Conflicts of Interest

The authors declare that they have no conflicts of interest.

Acknowledgments

This support is gratefully acknowledged by the authors, who are also grateful to the reviewers of this paper for their detailed comments. This study was supported by the Foundation of State Key Laboratory of Shale Oil and Gas Enrichment Mechanisms and Effective Development (No. 35800000-20-ZC0609-0006), National Key Research and Development Program (2019YFB1504202), and Science Foundation of China University of Petroleum, Beijing (No. 2462021YJRC009).

References

[1] W. Dickinson and R. W. Dickinson, "Horizontal radial drilling system," in *The SPE California Regional Meeting, Conference*, pp. 27–29, Bakersfield, California, 1985.

[2] W. Dickinson, R. R. Anderson, and R. W. Dickinson, "The ultrashort-radius radial system," *SPE Drilling Engineering*, vol. 4, no. 3, pp. 247–254, 1989.

[3] LANDERS C W, *Method of and apparatus for horizontal well drilling: US Patent No. 5853056*, 1998.

[4] B. Marbun and S. Putra, "Review of ultrashort-radius radial system (URRS)," in *Proceedings of the international petroleum technology conference*, Bangkok, 2011.

[5] R. A. Cirigliano and J. F. T. Blacutt, "First experience in the application of radial perforation technology in deep wells," in *Latin American & Caribbean Petroleum Engineering Conference*, Buenos Aires, Argentina, 2007.

[6] M. K. Medetbekova, S. Salimzadeh, H. F. Christensen, and H. M. Nick, "Experimental and numerical study of the stability of radially jet drilled laterals in chalk reservoirs," in *80th EAGE conference and exhibition 2018*, Copenhagen, 2018.

[7] S. D. Cinelli and A. H. Kamel, "Novel technique to drill horizontal laterals revitalizes aging field," in *SPE/IADC Drilling Conference*, Amsterdam, The Netherlands, 2013.

[8] Q. Liu, S. Tian, G. Li et al., "An analytical model for fracture initiation from radial lateral borehole," *Journal of Petroleum Science and Engineering*, vol. 164, pp. 206–218, 2018.

[9] Y. Wang, B. Hou, W. Dong, and Z. Jia, "Features of fracture height propagation in cross-layer fracturing of shale oil reservoirs," *Petroleum Exploration and Development*, vol. 48, no. 2, pp. 469–479, 2021.

[10] B. Hou, Y. Dai, C. Zhou, K. Zhang, and F. Liu, "Mechanism study on steering acid fracture initiation and propagation under different engineering geological conditions," *Geomechanics and Geophysics for Geo-Energy and Geo-Resources*, vol. 7, no. 3, pp. 1–14, 2021.

[11] K. Zhang, B. Hou, M. Chen, C. Zhou, and F. Liu, "Fatigue acid fracturing: a method to stimulate highly deviated and horizontal wells in limestone formation," *Journal of petroleum science and engineering*, vol. 208, p. 109409, 2022.

[12] Q. Zhang, B. Hou, B. Lin, X. Liu, and Y. Gao, "Integration of discrete fracture reconstruction and dual porosity/dual permeability models for gas production analysis in a deformable fractured shale reservoir," *Journal of Natural Gas Science and Engineering*, vol. 93, p. 104028, 2021.

[13] X. Li and J. He, "Research and application of radial borehole fracturing based on numerical simulation," *Geofluids*, vol. 2019, 16 pages, 2019.

[14] T. Reinsch and D. Bruhn, "The SURE consortium (2016) Novel productivity enhancement concept for a sustainable utilization of a geothermal resource e the SURE project," in *In: Proceedings, European geothermal Congress 2016*, Strasbourg, 2016.

[15] Y. Shi, X. Song, G. Wang, J. Li, L. Geng, and X. Li, "Numerical study on heat extraction performance of a multilateral-well enhanced geothermal system considering complex hydraulic and natural fractures," *Renewable Energy*, vol. 141, pp. 950–963, 2019.

[16] Y. Q. Zhang, K. X. Zhao, X. Y. Wu et al., "An innovative experimental apparatus for the analysis of natural gas hydrate erosion process using cavitating jet," *The Review of Scientific Instruments*, vol. 91, no. 9, article 095107, 2020.

[17] Y. Zhang, X. Wu, X. Hu et al., "Visualization and investigation of the erosion process for natural gas hydrate using water jet through experiments and simulation," *Energy Reports*, vol. 8, pp. 202–216, 2022.

[18] Z. L. Ge, K. Deng, Z. Zhou, M. Yang, and C. Chai, "Fracture characteristics of coal jointly impacted by multiple jets," *Engineering Fracture Mechanics*, vol. 235, p. 107171, 2020.

[19] L. Jingbin, H. Zhongwei, Z. Guangqing, L. Xin, and L. Huan, "Rock breaking characteristics of the self-rotating multi-orifices nozzle applied to coalbed methane radial jet drilling," *International Journal of Rock Mechanics and Mining Sciences*, vol. 136, p. 104483, 2020.

[20] C. Dong, Y. Li, J. Long, Q. Zhang, D. Wang, and J. Wu, "Operation optimization of plugged screen cleanup by rotary water jetting," *Petroleum Science*, vol. 11, no. 1, pp. 122–130, 2014.

[21] H. Liao, D. Wu, L. Wang, and L. Zhu, "Comparisons of spraying structure and rock breakage characteristics of round straight, swirling, and straight-swirling integrated jets," *Atomization and Sprays*, vol. 23, no. 4, pp. 363–377, 2013.

[22] A. W. Momber and R. Kovacevic, "test parameter analysis in abrasive water jet cutting of rocklike materials," *International Journal of Rock Mechanics and Mining Sciences*, vol. 34, no. 1, pp. 17–25, 1997.

[23] Y. Liu, J. Zhang, T. Zhang, and H. D. Zhang, "Optimal nozzle structure for an abrasive gas jet for rock breakage," *GEOFLUIDS*, vol. 2018, 14 pages, 2018.

[24] W. Zuo, C. Huang, Y. Liu et al., "Analysis and modeling of particle velocities in premixed abrasive water jets," *GEOFLUIDS*, vol. 2020, 9 pages, 2020.

[25] J. B. Surjaatmadja, S. R. Grundmann, and B. McDaniel, "Hydrajet fracturing: an effective method for placing many fractures in openhole horizontal wells," Proceedings of, Society of Petroleum Engineers, 1998.

[26] L. I. Gensheng, H. U. A. N. G. Zhongwei, and T. I. A. N. Shouceng, "Research and application of water jet technology in well completion and stimulation in China," *Petroleum Science*, vol. 7, no. 2, pp. 239–244, 2010.

[27] Z. H. Zhu, T. Feng, Z. G. Yuan, D. H. Xie, and W. Chen, "Solid-gas coupling model for coal-rock mass deformation and pressure relief gas flow in protection layer mining," *Advances in Civil Engineering*, vol. 2018, 6 pages, 2018.

[28] Z. Huang, J. Niu, G. Li, X. Yuan, and Y. Liu, "Surface experiment of abrasive water jet perforation," *Petroleum Science & Technology*, vol. 26, no. 6, pp. 726–733, 2008.

[29] J. Niu, G. Li, and J. Song, "An experimental study on abrasive water jet perforation parameters," *PETROLEUM DRILLING TECHNIQUES*, vol. 31, no. 2, pp. 14–16, 2003.

[30] Y. Yang, Z. Shen, and R. Wang, "Experimental study on rotary abrasive jet drilling," *PETROLEUM DRILLING TECHNIQUES*, vol. 27, no. 4, pp. 4–6, 1999.

[31] B. Yuhuan, R. Wang, and Z. Weidong, "Study on the law of rock breaking and hole formation by rotating jet," *Journal of rock mechanics and engineering*, vol. 22, no. 4, pp. 664–668, 2004.

[32] Y. Liu, Q. Ba, L. He, K. Shen, and W. Xiong, "Study on the rock-breaking effect of water jets generated by self-rotatory multinozzle drilling bit," *Energy Science and Engineering*, vol. 8, no. 7, pp. 2457–2470, 2020.

[33] R. S. Balch, T. Ruan, and M. Savage, "Field testing and validation of a mechanical alternative to radial jet drilling for improving recovery in mature oil wells," Society of Petroleum Engineers, 2016.

[34] Z. U. Ahmed, Y. M. Al-Abdeli, and F. G. Guzzomi, "Impingement pressure characteristics of swirling and non-swirling turbulent jets," *Experimental Thermal and Fluid Science*, vol. 68, pp. 722–732, 2015.

[35] N. Hongjian and R. Wang, "A study of the rock breaking mechanism during swirling water jet drilling," *Petroleum Science*, vol. 1, no. 1, pp. 39–44, 2004.

[36] R. Wang and N. Hongjian, "Numerical analysis on rock-breaking mechanism using swirling water jet," *Journal of the University of Petroleum China*, vol. 27, no. 1, pp. 33–35, 2003.

[37] J. Li, J. Dai, Z. Huang, G. Zhang, X. Liu, and H. Li, "Rock breaking characteristics of the self-rotating multi-orifice nozzle for sandstone radial jet drilling," *Rock Mechanics and Rock Engineering*, vol. 54, no. 11, pp. 5603–5615, 2021.

Hindawi
Geofluids
Volume 2022, Article ID 6130848, 11 pages
https://doi.org/10.1155/2022/6130848

Research Article

Study on Effect of Perforation Orientation on Hydraulic Fracturing of Shale

Jian Li,[1] Dong Wang,[1] Hongjian Wang,[1,2] Fei Zhao,[2] Qingqing Ma,[1] Qi Qiao,[1] and Zhiyang Yao[1]

[1]*Sinopec Zhongyuan Oilfield Branch, Puyang, 457001 Henan, China*
[2]*North China University of Water Resources and Electric Power, Zhengzhou, 450045 Henan, China*

Correspondence should be addressed to Hongjian Wang; 493508184@qq.com and Fei Zhao; zhaofei_183@126.com

Received 8 November 2021; Accepted 16 February 2022; Published 3 March 2022

Academic Editor: Bing Hou

The core technology to realize the development of unconventional oil and gas resources is the large-scale volume transformation of shale reservoirs, but volume fracturing is a complex physical and mechanical process, and its mechanism remains to be further studied. In this paper, starting from the current research status of shale volumetric fracturing, the perforation orientation of volumetric fracturing is numerically simulated by using the finite element software. The following conclusions are drawn: ① when the ground stress conditions are equal, with the increase of perforation angle, the maximum principal stress at the front of perforation decreases gradually; that is, when the perforation is along the horizontal minimum principal stress, the maximum principal stress at the front of perforation is the largest, which is most conducive to fracturing of shale reservoirs. ② When the perforation is along the direction of the horizontal minimum principal stress and the horizontal stress difference is zero, the smaller the horizontal stress, the greater the maximum principal stress at the front of the perforation. Therefore, the smaller the horizontal stress, the more conducive to the rupture of shale reservoirs. ③ When the perforation is along the horizontal minimum principal stress, the maximum principal stress at the front of the perforation increases with the increase of the horizontal stress difference. Therefore, the larger the horizontal stress difference, the more favorable for the fracture of shale reservoirs.

1. Introduction

1.1. Research Status of Hydraulic Fracturing. Large-scale hydraulic fracturing technology is the core technology to realize the development of unconventional oil and gas resources. Foreign fracturing technology mainly includes [1–4] the following: nitrogen foam fracturing technology, the technology first began in January 1968, in the United States and Canada on the extensive use of foam fracturing technology, and foam fracturing is particularly suitable for low pressure and low permeability water sensitive formation [5]; water fracturing technology, which uses water to add appropriate drag reduction agent as fracturing fluid, can save 30% of the cost without reducing production and has achieved good application results in the transformation of low permeability reservoirs [6]; and synchronous fracturing technology is the latest fracturing technology which has been successfully applied in the development of Barnett shale gas in Vosburg Basin in recent years. It is the fracturing of two wells (or more than two wells) at the same time [7]. Repeated fracturing technology, which can reconstruct the linear seepage from reservoir to wellbore, restore or increase productivity, increase the final recovery rate by 8% ~10%, and increase the recoverable reserves by 60%, is a low-cost production increase method. Hydrojet fracturing is a hydraulic fracturing technology integrating hydraulic perforation, fracturing, and isolation. The biggest advantage of this technology is that it maintains low wellbore pressure without using sealing elements and can quickly and accurately open multiple fractures, which successfully solves the problem of hydraulic fracturing in open hole completion. Horizontal well-staged fracturing technology can effectively generate fracture network, improve ultimate recovery factor as much as possible, and save costs. The Tipton-1H-23 well

located in the Woodford shale gas accumulation belt of the Akoma Basin in the United States has been transformed by 7 hydraulic fracturing measures. The shale gas production is as high as 14.16×10^4 m^3/d [8].

The core technology of unconventional oil and gas resources development is large-scale volume fracturing of ultralow permeability reservoirs. As the core technology of commercial exploitation of shale gas, the application of volume fracturing theory and method has attracted the attention of engineers and peer scholars at home and abroad and has done a lot of scientific research in theory and experiment.

As early as 1981, Professor Huang Rongzun, a famous oil and gas geology expert in China, applied the linear elastic fracture mechanic theory to put forward the initiation criteria of vertical and horizontal fractures and various factors affecting the fracture propagation direction [9]. Chen et al. (2000) [10] used the large-scale true triaxial simulation test system to simulate the formation conditions, carried out the indoor simulation experiment of crack propagation on natural rocks and artificial models, realized the monitoring of the actual physical process of crack propagation, and discussed the influence of geostress, fracture toughness, joints, and natural fracture on crack propagation. Fisher et al. (2002) [11, 12] began to discuss the creation of large pressure fracture network in Barnett shale development area and initially proposed the influence of reservoir reconstruction scale size, fracture network size, and shape on shale gas production. Through field microseismic monitoring technology, it is preliminarily confirmed that the size of pressure fracture network is closely related to the volume of the reconstructed reservoir. Mayerhofer et al. (2008) [13] first proposed the concept of stimulated reservoir volume (SRV) when studying the microseismic technology and fracturing fracture changes of Barnett shale. The main factors affecting SRV include shale thickness, direction and size of ground stress field, natural fracture development, fracturing resistance, rock brittleness, and geological characteristics, such as faults and karst topography. The calculation formula for evaluating the total fracturing length of SRV is put forward:

$$L_{f\text{total}} = \frac{4x_f x_n}{\Delta x_s} + 2x_f + x_n, \tag{1}$$

which $L_{f\text{total}}$ is the total reservoir fracturing length, x_f is the half length of fracture network, x_n is the width of fracture network, and Δx_s is the fracture spacing. Domestic scholar Wu et al. [14] proposed the basic definition of "volume transformation" and the new concept of crack initiation and propagation based on the existing research abroad. The proposal of volume fracturing is based on the new modern theory of volume stimulation. It refers to the continuous expansion of natural fractures and the shear slip of brittle rocks in the process of hydraulic fracturing, forming a fracture network in which natural fractures and artificial fractures intersect, thereby increasing the stimulation volume and improving the initial production and final recovery. Xie et al. [15] realized the fine description of oil and gas storage and transportation in shale by fractal reconstruction and made shale embrittlement and high body fracture by using high energy thermal coupling gas. On this basis, pneumatic fracturing technology and polymer hollow thermal expansion support technology were proposed, which were different from conventional shale reservoir reconstruction methods.

1.2. Research Status of Numerical Simulation of Hydraulic Fracturing. Computer technology has played a vital role in scientific research and industrial development. The application of numerical simulation technology in the process of shale gas exploitation to achieve the visualization of large-scale volume fracturing process is helpful to further study the mechanism of volume fracturing and optimize the fracturing design. The representative research at home and abroad mainly includes the following: Al-Busaidi et al. [16] used the discrete element software PFC2 D to simulate the initiation mechanism and acoustic emission distribution characteristics of hydraulic fracturing cracks. The results show that the temporal and spatial expansion characteristics of cracks are closely related to the properties of rock samples and natural cracks. The tensile failure mainly occurs in the specimens, and only a small part of the shear slip occurs. Adachi et al. (2007) [17] summarized and discussed the standard method and propagation mechanism for controlling the hydraulic fracturing process, introduced the mathematical equation and boundary conditions for controlling the fracturing propagation, and systematically introduced the fracture propagation path and its control factors in the numerical calculation process, including time function, coupling equation, and time step program. Domestic scholar Zhu et al. [18] used the finite element method to simulate the three-dimensional fracture dynamic propagation of hydraulic fracturing in low permeability reservoirs, realized the dynamic description of the three-dimensional fracture formation process of low permeability reservoirs, and simulated the Zhao 38-271 well. Some scientists investigate the fracture modes using XFEM and acoustic emissions [19, 20]. Hamidi et al. (2013) [21] used three-dimensional discrete element software 3DEC to simulate the initiation and propagation of volume fracturing fractures. The results show that the successful volume fracturing depends not only on the characteristics of fracturing fluid and injection rate but also on the in situ stress state, the size and direction of principal stress, and rock mechanical properties that are not controlled by human factors. Ahn et al. (2014) [22] established an improved and effective numerical model to simulate the initiation and propagation characteristics of hydraulic fracturing cracks in shale reservoirs with natural fractures and studied the hydraulic fracturing process under natural joints, fracturing fluid filtration, and fluid flow, so as to further optimize the field fracturing design.

Most of the previous numerical simulation of hydraulic fracturing are the condition of two-dimensional plane and rarely reproduce the fracture initiation and propagation path in three-dimensional space [23–38]. In the future, the numerical analysis and research should be combined with

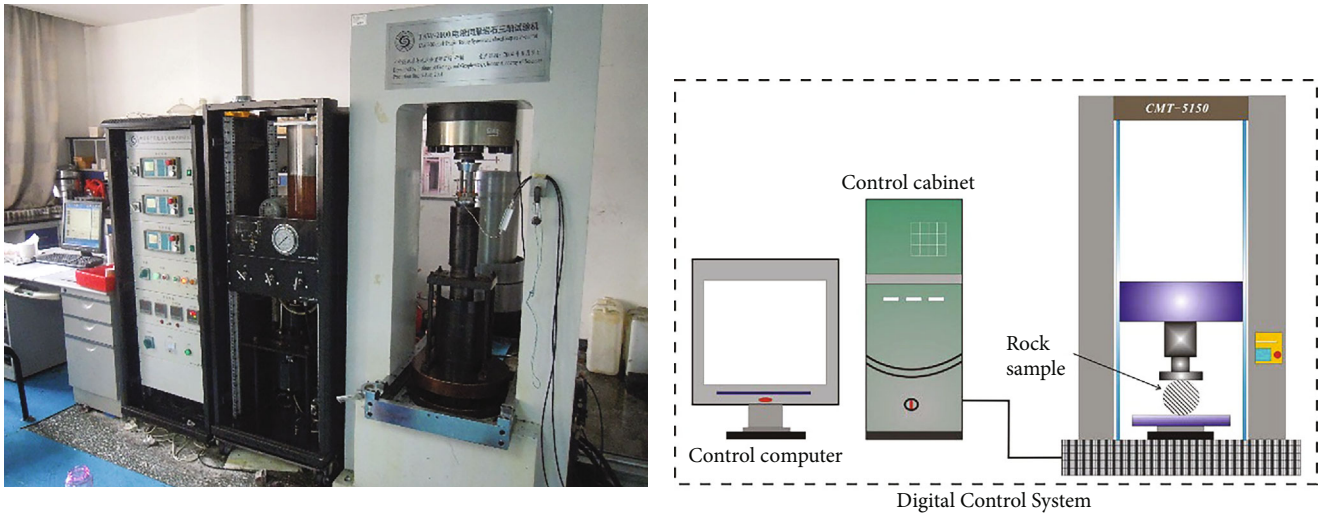

(a) TAW-2000

(b) CMT-5150

Figure 1: Rock mechanic test system.

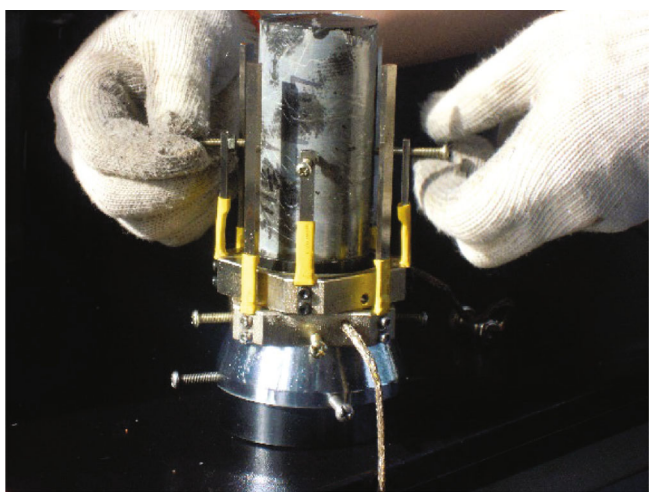

Figure 2: Uniaxial compression test of shale rock.

the actual geological engineering conditions to establish a more realistic three-dimensional numerical model, fully consider the various factors affecting the fracturing effect in the real situation, provide reliable data support for large-scale volume fracturing, and optimize the fracturing design.

2. Establishment of the Finite Element Model for Volume Fracturing Numerical Calculation

At present, the finite element method (FEM) has received high attention and has been widely used in scientific research and practical engineering. It is because the FEM has higher reliability and accuracy compared with other methods [39–42].

The main purpose of this section is to extend the conclusions obtained from the indoor volumetric fracturing test and numerical simulation to shale reservoir. Through numerical simulation of hydraulic fracturing process of shale reservoir, the influence of different factors on hydraulic fracturing process of shale reservoir is studied. This paper mainly studies the effect of perforation angle on fracturing. According to geological survey data and indoor physical and mechanical experiment (Figures 1–3), the relevant data of black carbonaceous shale formation in the dragon stream formation are as follows: the buried depth in the middle of the reservoir is about 2500 m, the mean elastic modulus is 35 GPa, the mean Poisson's ratio is 0.25, the internal friction angle is 33.86, the cohesion is 8.98 MPa, the permeability coefficient is 2×10^{-9} m/s, the initial pore pressure is 26.25 MPa, the horizontal minimum in situ stress is 46.25 MPa, and the horizontal maximum in situ stress is 52.5 MPa. The stress of overlying strata is 50 MPa. At the beginning of hydraulic fracturing site construction, about 1 m^3/min of fracturing fluid is injected, and the formation is fractured with the displacement of 2-5 m^3/min. After that, the displacement is increased to 10-15 m^3/min

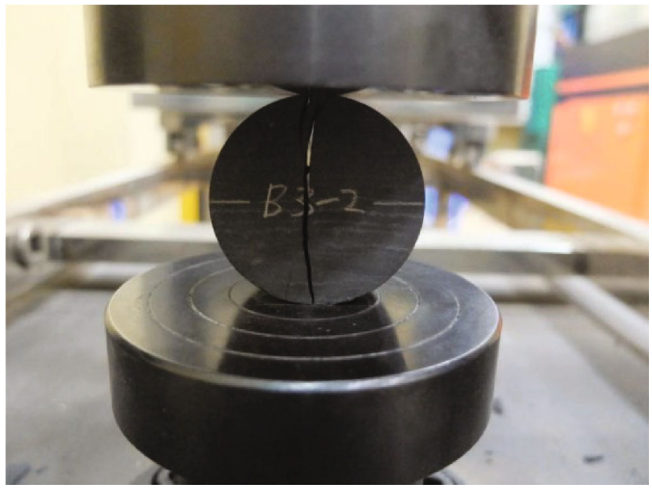

Figure 3: Brazilian splitting test of shale rock.

to increase the scale of fracture network. The pumping time is about 200 min, the fracturing fluid volume is 2000 m^3, and the length of a single hydraulic fracture is about 250 m. The Morh-Coulomb model is used in this simulation, and the simulation is carried out according to the above parameters.

First, enter the Part module to establish the reservoir model. The length, width, and height of the simulated shale reservoir are 6 m × 6 m × 0.5 m, respectively, and the model is named "Shale Reservoir," 3D variable shape, and solid type. Use the extrusion function to create a 6 m × 6 m × 0.5 m cuboid. The diameter of the well is 1 m, a circle with radius of 0.5 m is drawn on the upper surface of the model by partition command, and then a cylinder with diameter of 1 m and height of 0.5 m is cut out at the center of the model by partition cell: extrude edge command and name this cylinder as a collection "Well." The perforation radius is 0.5 in (12.7 mm), and the perforation length is 120 mm. In this simulation, the x direction is taken as the horizontal minimum principal stress direction, the y direction is taken as the horizontal maximum principal stress direction, and the z direction is taken as the vertical principal stress direction. This paper mainly studies the effect of angle change between perforation direction and horizontal minimum principal stress on hydraulic fracturing in shale reservoir, and the θ takes 0, 15, 30, 45, 60, 75, and 90, respectively. When establishing the perforation model, the direction with a certain angle with the x axis can be set, then the perforation cross-section can be stretched along this direction to form perforation of different angles, and the perforation part can be named as the collection "Perforation."

Enter the Property module, create material attributes, and input various parameters: elastic modulus is 35 GPa, Poisson's ratio is 0.25, mole Coulomb model, internal friction angle is 33.86, cohesion 8.98 MPa, and permeability coefficient is 2×10^{-9} m/s. After creating the material, set up defined cross-section attributes, and type is entity isotropy. Finally, cross-section attributes are assigned to the model. Next, enter the Assembly module and assemble the model. The assembled model is shown in Figure 4.

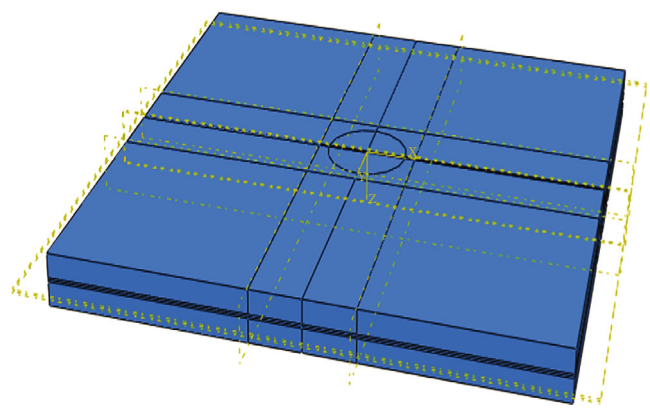

Figure 4: The assembled finite element model.

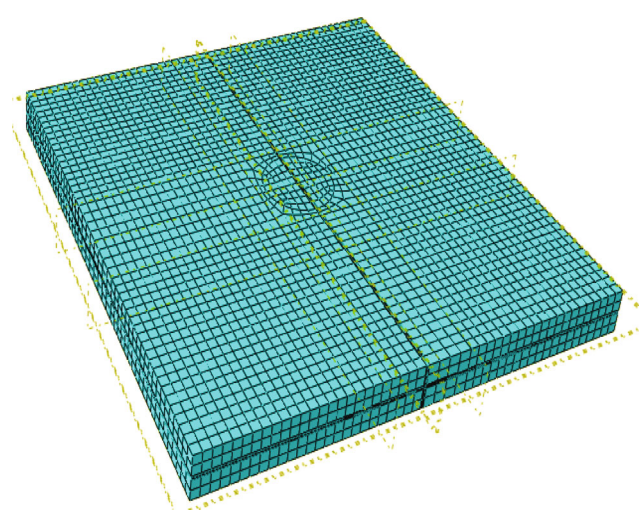

Figure 5: Finite element model after meshing.

Enter the Step module to establish the analysis step. This simulation needs two-step analysis. First, the in situ stress is balanced, and then the well digging and perforation are

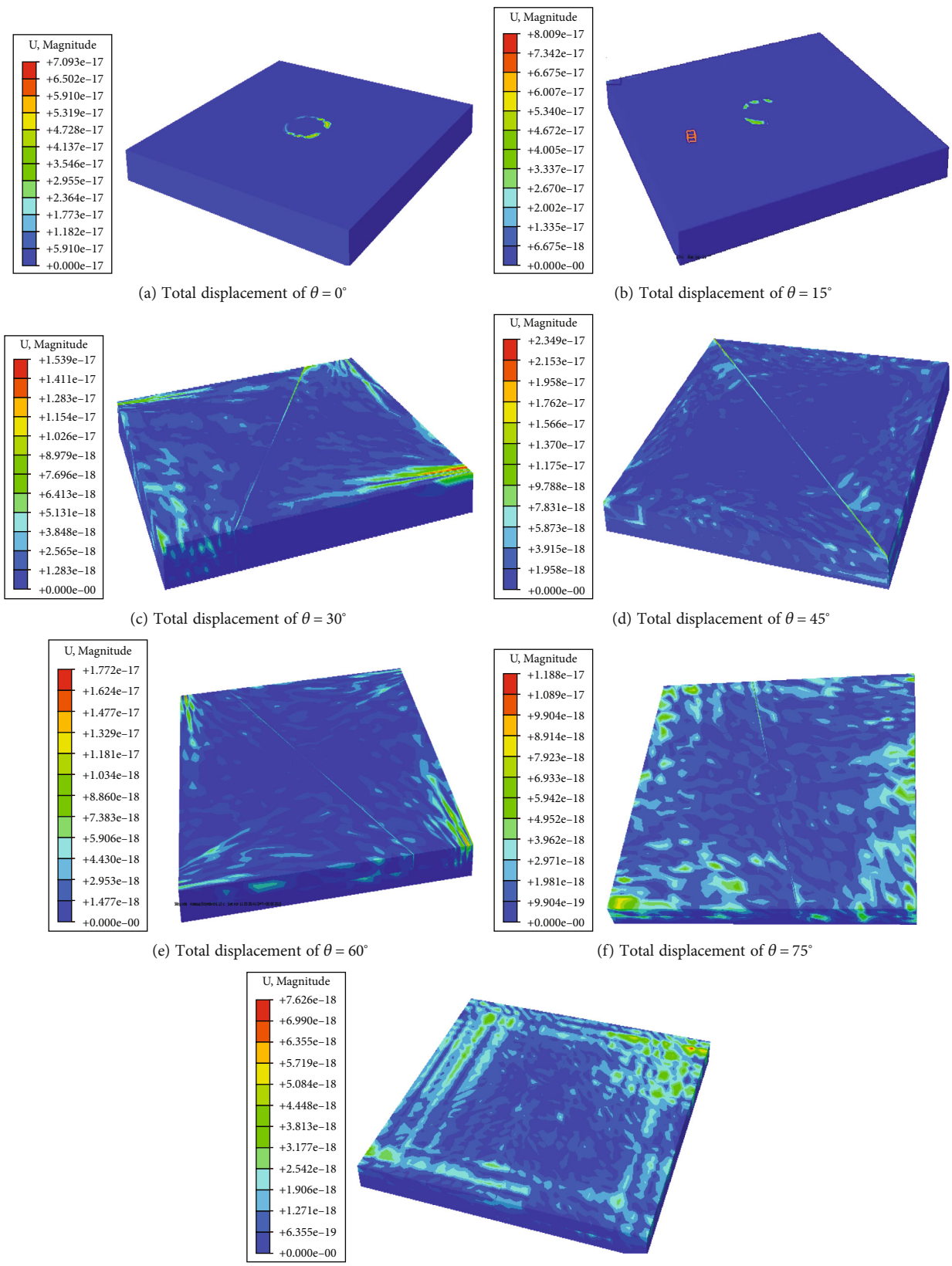

(a) Total displacement of $\theta = 0^{\circ}$

(b) Total displacement of $\theta = 15^{\circ}$

(c) Total displacement of $\theta = 30^{\circ}$

(d) Total displacement of $\theta = 45^{\circ}$

(e) Total displacement of $\theta = 60^{\circ}$

(f) Total displacement of $\theta = 75^{\circ}$

(g) Total displacement of $\theta = 90^{\circ}$

Figure 6: Displacement nephogram of the model under different perforation angles after in situ stress balance.

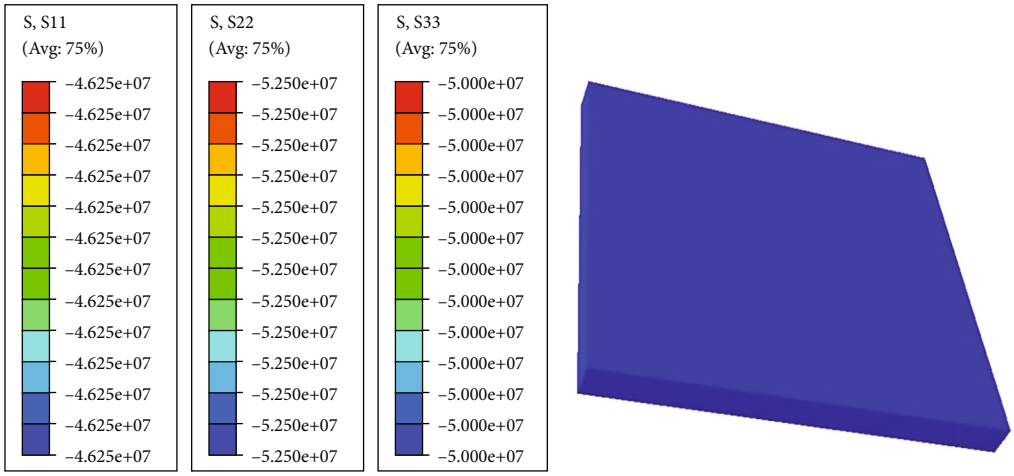

Figure 7: Stress nephograms in all directions (S11, S22, S33) after in situ equilibrium.

carried out after balance. Then, the pore water pressure is added to the perforation surface for fluid-solid coupling analysis. Perform the calculation of the first analysis step first and perform the calculation of the second analysis step after the calculation is successful. Therefore, the ground stress balance analysis step is established first, and the fluid-structure coupling analysis step will not be established temporarily. If the results obtained from the ground stress balance analysis step meet the requirements, the fluid-structure coupling analysis step is added. The order of displacement of soil should be less than 10^{-6} after ground stress balance. Create the geostatic analysis step and turn on the nonlinear button.

Boundary conditions and forces need to be applied to the model. Constrain the Z direction displacement of the underside and the X and Y displacements of the sides. Due to the thin thickness of the reservoir, gravity is much less than other loads; so, the effect of gravity can be ignored. Enter the Mesh module to mesh the model. Before the division, it is necessary to cut the model for some parts of the model are not regular enough. The reference surface method is mainly used to cut the rules of each part of the model to divide the grid. The global grid density is 0.12, the unit shape is hexahedral, and the structured grid division technology is adopted. The linear reduced integral element is more accurate in solving the displacement; so, the distortion of the grid has little effect on the analysis accuracy. For fluid-solid coupling analysis, the element used should have one more freedom than the conventional element; so, the linear reduced integral pore pressure element is used (C3D8RP). The grid is shown in Figure 5.

Define all nodes of the model as ALLNODES and all units of the model as ALLELE. Set the initial stress state and initial pore pressure in the keyword as follows: "∗initial conditions, type=pore pressure", "Shale Reservoir -1.ALLNODES,26250000", "∗initial conditions, type=stress", and "Shale Reservoir -1.ALLELE,-46250000., -52500000.,-50000000.,0.0,0.0,0.0".

Then, the task submission calculation is established to balance the ground stress. If the order of magnitude of displacement is 10^{-6} after ground stress balance, it meets the requirements, and the calculation of the second analysis step can be carried out. Enter the Step module again, create fluid-structure coupling analysis step (soil), select the steady flow, set the initial analysis step to 0.01, and use asymmetric solver. Then, set the output requirements of field variables, open the dialog box for editing output requirements of field variables, and add PEEQ (equivalent plastic strain) and FLVEL (seepage velocity) on the basis of the original output variables.

In order to conform to the actual situation, rigid body constraint is added on the surface of the well hole. Enter the interaction module, starting with a reference point at any point on the borehole surface, then click the create Constraints button, select the rigid body, select all the well surface with the mouse, and attach the rigid constraints to the well surface. In the fluid-structure interaction step, pore water pressure needs to be applied to the perforated surface. Firstly, enter the Mesh module and name the nodes on the perforating surface TUNNELNODES. Then, enter the Load module and apply pore water pressure of 60 MPa on TUNNELNODES. The whole analysis process is firstly the balance of ground stress, then the excavation of wells and perforation, and finally the fluid-solid coupling. So, the unit life and death function of ABAQUS is used to remove the unit of well and perforation part to complete the simulation of well and perforation excavation. Add the following statement to the keywords: "∗Model change, remove", "Shale Reservoir-1.Well", "∗Model change, remove", "Shale Reservoir-1. Perforation".

At this point, the whole process is completed, and the task can be submitted after the establishment of the operation.

3. Numerical Simulation of Fracturing Characteristics in Different Perforation Directions

In this section, the influence of the angle between the perforation direction and the direction of the minimum principal

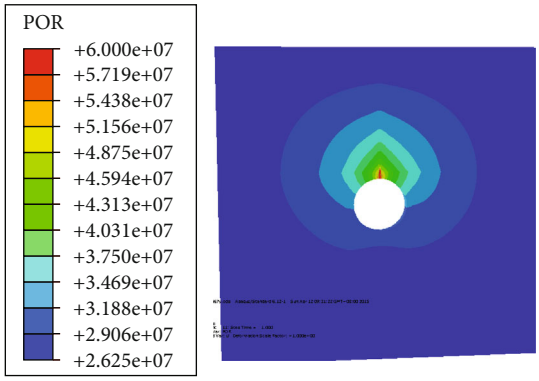

(a) Total displacement of $\theta = 0°$

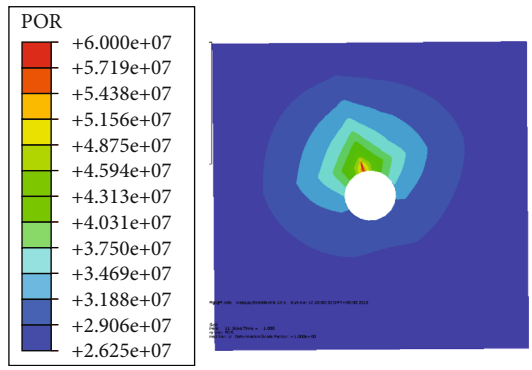

(b) Total displacement of $\theta = 15°$

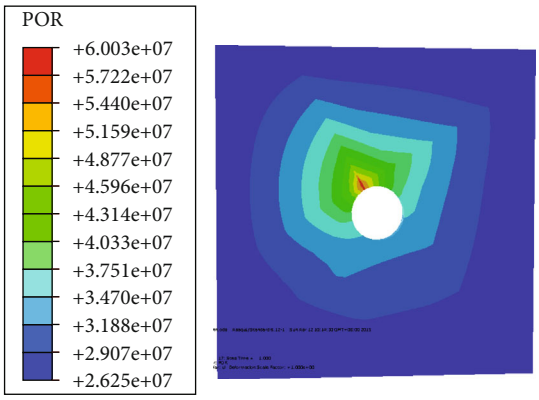

(c) Total displacement of $\theta = 30°$

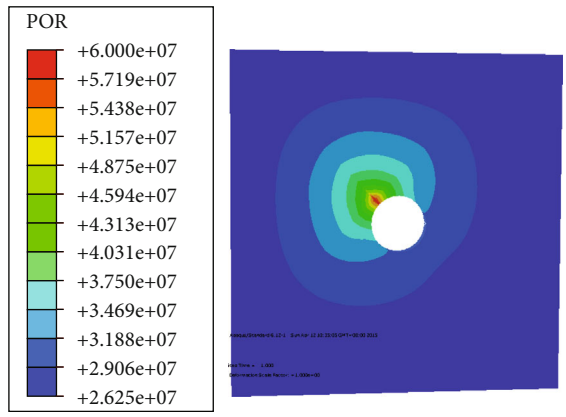

(d) Total displacement of $\theta = 45°$

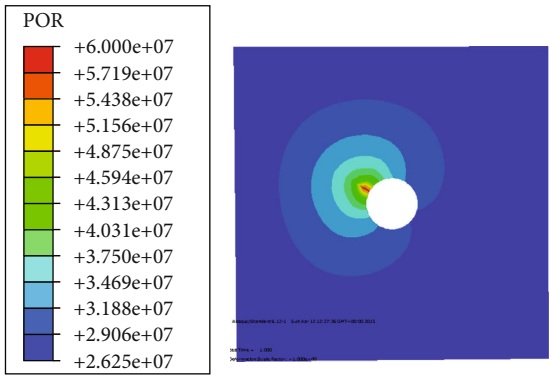

(e) Total displacement of $\theta = 60°$

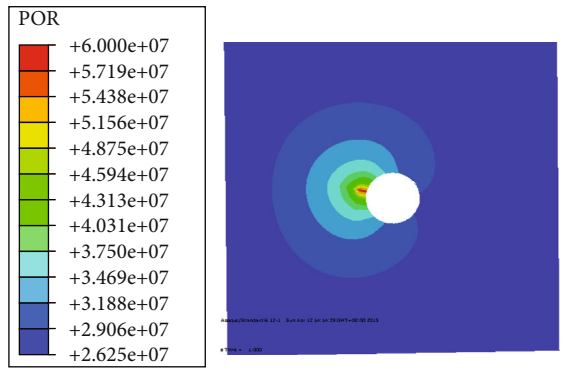

(f) Total displacement of $\theta = 75°$

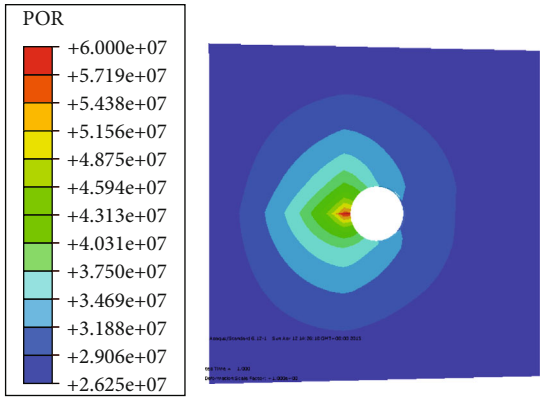

(g) Total displacement of $\theta = 90°$

Figure 8: Pore pressure nephogram under different perforation angles.

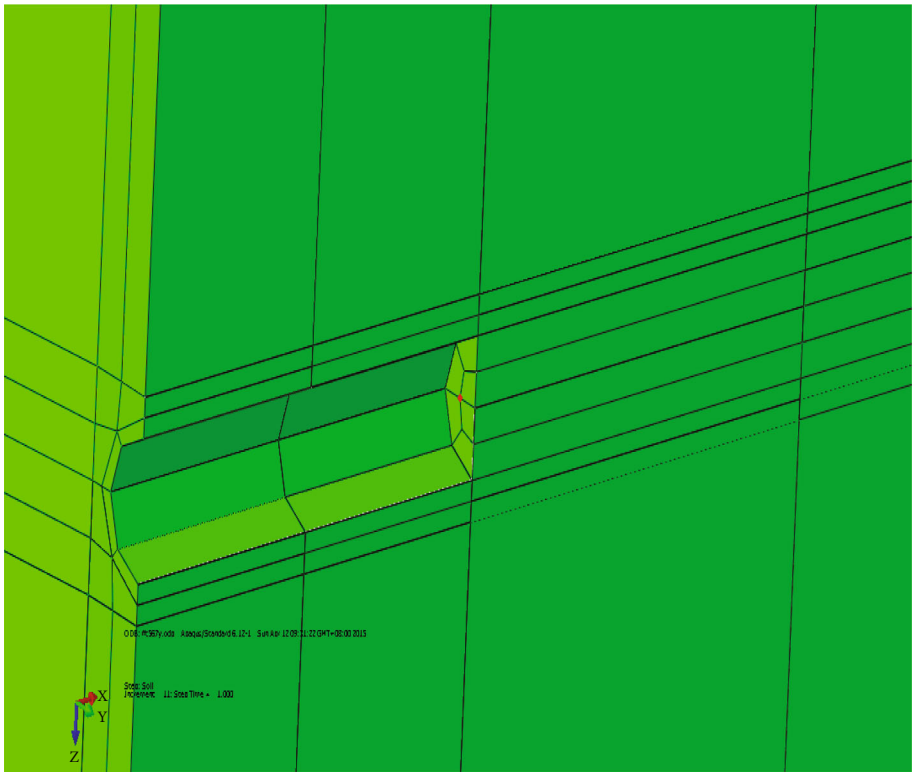

Figure 9: Location of test points.

stress on the hydraulic fracturing effect is studied. The values of $\theta = 0^\circ$ are 0°, 15°, 30°, 45°, 60°, 75°, and 90°, respectively. The geostress conditions are as follows: the horizontal minimum principal stress is 46.25 MPa in the x direction, the horizontal maximum principal stress is 52.5 MPa in the y direction, and 50 MPa in the z direction. According to the steps described in the above section, the material properties are defined, the analysis steps are set, the load and boundary conditions are applied, and the grid is divided and calculated. The ground stress equilibrium displacement results of each perforation angle are shown in Figure 6.

The displacement magnitude of each perforation angle model after stress balance is 10^{-17}, far less than 10^{-6} and close to zero, and then the stress balance meets the requirements. The cloud images of S11, S22, and S33 each perforation angle model after geostress balance are consistent with the initial geostress conditions, as shown in Figure 7.

Through the above displacement and stress results in all directions, it is known that the calculation of stress equilibrium step is correct. Then, the excavation hole and perforation are carried out, and finally, the fluid-solid coupling analysis step is calculated. The resulting pore pressure distribution is shown in Figure 8. To facilitate observation of the pore water pressure and perforation angle at the perforation location, the model is cut in a plane perpendicular to the z-axis and in the middle of the reservoir thickness.

It can be seen from the pore pressure distribution cloud map of perforation from the above angles that the pore water pressure at the perforation is 60 MPa and then gradually decreases from the perforation to the surrounding area, which is 26.25 MPa at the edge of the model. For the process of hydraulic fracturing of shale reservoirs, we mainly explore the fracture propagation at the front end of perforation. Therefore, the points at the same position at the front end of perforation are selected for each perforation model, and the maximum principal stress values of these points are compared to determine which perforation angle is most likely to crack the rock mass. The location of the selected observation point is shown in Figure 9.

Import the maximum principal stress data of this position point of each angle model into Excel and draw the curve of the maximum principal stress of each point with time as shown in Figure 10.

Through the curve in Figure 10, we can see that the maximum principal stress in the front of the perforation is the largest when the perforation is along the direction of the horizontal minimum principal stress, and when the maximum principal stress exceeds the tensile strength of the shale, cracks will occur and expand. When perforating along the direction of maximum principal stress, the maximum principal stress at the front of perforating is minimum. It can also be seen from Figure 10 that with the increase of perforation angle, the maximum principal stress at the front end of perforation gradually decreases. Therefore, when the perforation is along the direction of the horizontal minimum principal stress, the rock mass is most likely to rupture. In practical engineering, the perforation direction should be along the direction of the horizontal

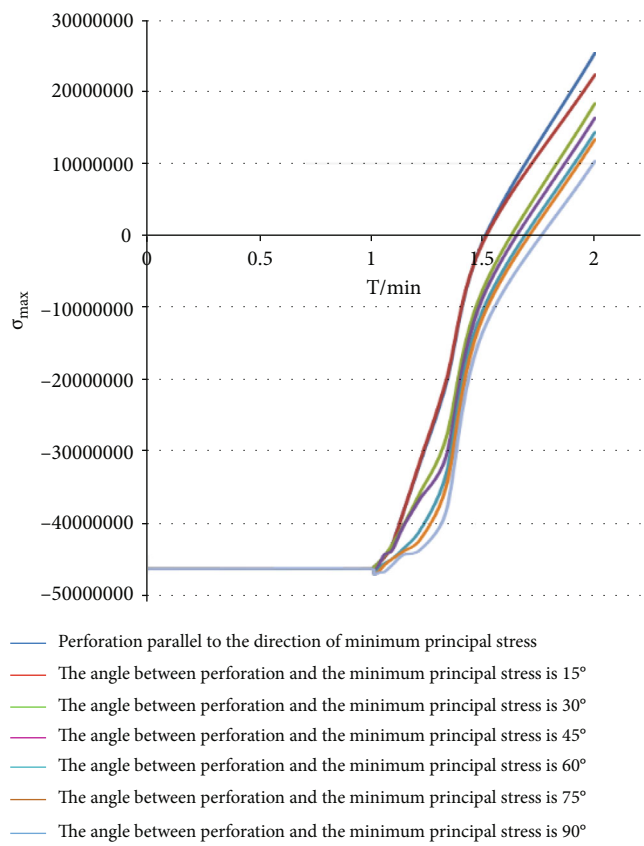

Figure 10: Curves of maximum principal stress changing with time in front of perforation at different angles.

minimum principal stress, so that hydraulic fracturing can achieve the best effect.

4. Conclusion

Low porosity and low permeability reservoirs, such as shale reservoir and tight sandstone reservoir, need fracturing to obtain production capacity. The selection of perforating parameters directly affects the fracturing effect and success rate of low porosity and low permeability reservoir. The perforation orientation affects the fracture pressure, fracture turning, and fracture morphology, which determines the success or failure of the volume fracturing. The conclusions are revealed through numerical research:

(1) When the ground stress conditions are equal, with the increase of perforation angle, the maximum principal stress at the front of perforation decreases gradually; that is, when the perforation is along the horizontal minimum principal stress, the maximum principal stress at the front of perforation is the largest; so, it is most conducive to the fracturing of shale reservoirs

(2) When the perforation is along the direction of the horizontal minimum principal stress and the horizontal stress difference is zero, the smaller the horizontal stress, the greater the maximum principal stress at the front of the perforation. Therefore, the smaller the horizontal stress, the more conducive to the fracture of shale reservoirs

(3) When the perforation is along the horizontal minimum principal stress, the maximum principal stress at the front end of the perforation increases with the increase of the horizontal stress difference. Therefore, the greater the horizontal stress difference, the more conducive to the rupture of shale reservoirs

Data Availability

The data used to support the findings of this study are included within the article.

Conflicts of Interest

The authors declare that they have no conflicts of interest.

Acknowledgments

This work was financially supported by the National Natural Science Foundation of China (41807254), China Postdoctoral Science Foundation (2020M682372), Young Talent Support Project of Henan Province (2021HYTP013), the Key Research & Development and Promotion Projects of Henan Province (No. 212102310374), and Key Engineering Technology for Exploration and Development of Tight Gas in Northeastern Sichuan Basin of China (P21115).

References

[1] H. L. Matthews, G. W. Schein, and M. R. Malone, "Stimulation of gas shales: they're all the same—right," in *Paper presented at the SPE Hydraulic Fracturing Technology Conference*, College Station, Texas, USA, 2007.

[2] J. Omkar, B. Grieser, K. K. Chong, and A. Passman, "A completions roadmap to shale-play development: a review of successful approaches toward shale-play stimulation in the last two decades," in *Paper presented at the International Oil and Gas Conference and Exhibition in China*, Beijing, China, 2010.

[3] P. N. Mutalik and R. W. Gibson, "Case history of sequential and simultaneous fracturing of the Barnett shale in parker county," in *Paper presented at the SPE Annual Technical Conference and Exhibition*, Denver, Colorado, USA, 2008.

[4] Y. Z. Wang, B. Hou, D. Wang, and Z. H. Jia, "Features of fracture height propagation in cross-layer fracturing of shale oil reservoirs," *Petroleum Exploration and Development*, vol. 48, no. 2, pp. 469–479, 2021.

[5] W. John and R. Roger, "The shale shaker: an investor's guide to shale gas," *Oil and Gas Investor*, vol. 1, pp. 2–9, 2007.

[6] G. D. Vassilellis, C. Li, R. Seager, and D. Moos, "Investigating the expected long-term production performance of shale reservoirs," in *Paper presented at the Canadian Unconventional Resources and International Petroleum Conference*, Calgary, Alberta, Canada, 2010.

[7] S. C. Maxwell, T. I. Urbancic, N. Steinsberger, and R. Zinno, "Microseismic imaging of hydraulic fracture complexity in

the barnett shal," in *Paper presented at the SPE Annual Technical Conference and Exhibition*, p. 77440, San Antonio, Texas, 2002.

[8] J. M. Zhang and X. F. Liang, "Impact of the shale gas revolution on the United States and the world," *Petrochemical Technology and Economy*, vol. 29, no. 4, pp. 8–14, 2013.

[9] R. Z. Huang, "Crack initiation and propagation by hydraulic fracturing," *Petroleum Exploration and Development*, vol. 5, 1981.

[10] J. Zhou, M. Chen, Y. Jin, and G. Q. Zhang, "Analysis of fracture propagation behavior and fracture geometry using a tri- axial fracturing system in naturally fractured reservoirs," *International Journal of Rock Mechanics and Mining Sciences*, vol. 45, no. 7, pp. 1143–1152, 2008.

[11] M. K. Fisher, B. M. Davidson, A. K. Goodwin, E. O. Fielder, and W. S. Buckler, "Integrating fracture mapping technologies to optimize stimulations in the Barnett Shale," in *Paper SPE 77411 presented at the SPE Annual Technical Conference and Exhibition*, San Antonio, Texas, 2002.

[12] S. C. Maxwell, T. I. Urbancik, and N. P. Steinsberger, "Microseismic imaging of hydraulic fracture complexity in the Barnett Shale," in *Paper SPE 77440 presented at the SPE Annual Technical Conference and Exhibition*, San Antonio, Texas, 2002.

[13] M. J. Mayerhofer, E. Lolon, N. R. Warpinski, C. L. L. Cipolla, D. Walser, and C. M. M. Rightmire, "What is stimulated reservoir volume?," *SPE Production & Operations*, vol. 25, no. 1, pp. 89–98, 2010.

[14] Q. Wu, Y. Xu, Y. Z. Liu, Y. H. Ding, X. Q. Wang, and T. F. Wang, "The status quo of shale gas volume modification technology in the United States and its enlightenment to China," *Petroleum Drilling and Production Technology*, vol. 33, no. 2, pp. 1–7, 2011.

[15] H. P. Xie, F. Gao, Y. Ju, Q. Fu, and F. B. Zhou, "The unconventional theory and technical conception of shale reservoir fracturing," *Journal of Sichuan University (Engineering Science Edition)*, vol. 6, no. 44, pp. 1–6, 2012.

[16] A. Al-Busaidi, J. F. Hazzard, and R. P. Young, "Distinct element modeling of hydraulically fractured Lac du Bonnet granite," *Ornal of Geophysical Research: Solid Earth*, vol. 110, no. B6, pp. 1978–2012, 2005.

[17] J. Adachi, E. Siebrits, A. Peirce, and J. Desroches, "Computer simulation of hydraulic fractures," *International Journal of Rock Mechanics and Mining Sciences*, vol. 44, no. 5, pp. 739–757, 2005.

[18] J. Zhu, P. Ye, S. L. Wang, D. F. Xiao, and H. Wang, "Numerical simulation of three-dimensional dynamic fracture propagation in hydraulic fracturing of low permeability reservoirs," *Journal of Petroleum*, vol. 31, no. 1, pp. 119–123, 2010.

[19] M. Haddad and K. Sepehrnoori, "XFEM-Based CZM for the simulation of 3D multiple-cluster hydraulic fracturing in quasi-brittle shale formations," *Rock Mechanics and Rock Engineering*, vol. 49, no. 12, pp. 4731–4748, 2016.

[20] H. J. Wang, D. A. Liu, Z. D. Cui, C. Cheng, and Z. Jian, "Investigation of the fracture modes of red sandstone using XFEM and acoustic emissions," *Theoretical and Applied Fracture Mechanics*, vol. 85, pp. 283–293, 2016.

[21] F. Hamidi and A. Mortazavi, "A new three dimensional approach to numerically model hydraulic fracturing process," *Journal of Petroleum Science and Engineering*, vol. 124, pp. 451–467, 2014.

[22] C. H. Ahn, R. Dilmore, and J. Y. Wang, "Development of innovative and efficient hydraulic fracturing numerical simulation model and parametric studies in unconventional naturally fractured reservoirs," *Journal of Unconventional Oil and Gas Resources*, vol. 8, pp. 25–45, 2014.

[23] S. L. Montgomery, D. M. Jarvie, K. A. Bowker, and R. M. Pollastro, "Mississippian Barnett Shale, Fort Worth basin, north-central Texas: gas-shale play with multi–trillion cubic foot potential," *AAPG Bulletin*, vol. 89, no. 2, pp. 155–175, 2005.

[24] J. S. Yoon, G. Zimmermann, and A. Zang, "Numerical investigation on stress shadowing in fluid injection-induced fracture propagation in naturally fractured geothermal reservoirs," *Rock Mechanics and Rock Engineering*, vol. 48, no. 4, pp. 1439–1454, 2015.

[25] H. J. Wang, F. Zhao, Z. Q. Huang, Y. Yao, and G. Yuan, "Experimental study of mode-I fracture toughness for layered shale based on two ISRM-suggested methods," *Rock Mechanics and Rock Engineering*, vol. 50, no. 7, pp. 1933–1939, 2017.

[26] K. Wu and J. E. Olson, "Numerical investigation of complex hydraulic-fracture development in naturally fractured reservoirs," *SPE Production & Operations*, vol. 31, no. 4, pp. 300–309, 2016.

[27] A. Kissinger, R. Helmig, A. Ebigbo et al., "Hydraulic fracturing in unconventional gas reservoirs: risks in the geological system, part 2," *Environmental Earth Sciences*, vol. 70, no. 8, pp. 3855–3873, 2013.

[28] J. Li, C. Wang, Wang, and H. Y. Tian, "Environmental concerns in shale gas development," *Environmental Protection in Oil and Gas Fields*, vol. 22, no. 6, pp. 42-43, 2012.

[29] R. W. Howarth, R. Santoro, and A. Ingraffea, "Methane and the greenhouse-gas footprint of natural gas from shale formations," *Climatic Change*, vol. 106, no. 4, pp. 679–690, 2011.

[30] A. Burnham, J. Han, C. E. Clark, M. Wang, J. B. Dunn, and I. Palou-Rivera, "Life-cycle greenhouse gas emissions of shale gas, natural gas, coal, and petroleum," *Environmental Science and Technology*, vol. 46, no. 2, pp. 619–627, 2011.

[31] A. Mazzoldi, A. P. Rinaldi, A. Borgia, and J. Rutqvist, "Induced seismicity within geological carbon sequestration projects: Maximum earthquake magnitude and leakage potential from undetected faults," *Green house Gas Control*, vol. 10, pp. 434–442, 2012.

[32] J. W. Teng and Y. S. Liu, "Chinese shale gas accumulation and potential productivity and environmental pollution analysis," *Chinese Geology*, vol. 40, no. 1, 2013.

[33] M. Zoback, S. Kitasei, and B. Copithorne, *Addressing the environmental risks from shale gas development*, World Watch Institute, 2010.

[34] T. Coons and R. Walker, *Community Health Risk Analysis of Oil and Gas Industry in Garfield County. Grand Junction*, Saccommano Research Institute, CO, 2008.

[35] Q. X. Zhang, B. Hou, B. T. Lin, X. Liu, and Y. Gao, "Integration of discrete fracture reconstruction and dual porosity/dual permeability models for gas production analysis in a deformable fractured shale reservoir," *Journal of Natural Gas Science and Engineering*, vol. 93, article 104028, 2021.

[36] Z. J. Zhao, H. J. Wang, Z. D. Cui et al., "Experimental study on mode-I fracture toughness using chevron straight-notched semi-circular bend (CSNSCB) method," *Theoretical and Applied Fracture Mechanics*, vol. 116, article 103093, 2021.

[37] S. H. Fallahzadeh, V. Rasouli, and M. Sarmadivaleh, "An investigation of hydraulic fracturing initiation and near-wellbore propagation from perforated boreholes in tight formations," *Rock Mechanics and Rock Engineering*, vol. 48, no. 2, pp. 573–584, 2021.

[38] L. M. McKenzie, R. Z. Witter, L. S. Newman, and J. L. Adgate, "Human health risk assessment of air emissions from development of unconventional natural gas resources," *Science of the Total Environment*, vol. 424, pp. 79–87, 2012.

[39] H. J. Wang, J. Li, F. Zhao, J. Dong, Y. Cui, and W. Gong, "Experimental study of volumetric fracturing properties for shale under different stress states," *Geofluids*, vol. 2021, Article ID 6650710, 16 pages, 2021.

[40] X. C. Wang, *Finite Element Method*, Tsinghua University Press, Beijing, 2003.

[41] K. Fei and J. W. Zhang, *Application of Abaqus in geotechnical engineering*, China Hydroelectric Press, Beijing, 2009.

[42] J. C. Wang and Y. Chen, *Application of Abaqus in civil engineering*, Zhejiang Zhejiang University Press, 2006.

Hindawi
Geofluids
Volume 2022, Article ID 9470952, 8 pages
https://doi.org/10.1155/2022/9470952

Research Article

Effective Stress Factor Analysis of Proppant for Multi-stage Fracturing in Horizontal Wells

Bo Cai,[1,2] Rui Gao,[1,2] Chunming He,[1,2] Jin Chen,[3] Ning Cheng,[3] Tiancheng Liang,[1,2] Guifu Duan,[1,2] Chuanyou Meng,[1,2] Haifeng Fu,[1,2] and Haoyu Zhang[1,2]

[1]*PetroChina Research Institute of Petroleum Exploration & Development, Beijing 100083, China*
[2]*CNPC Key Laboratory of Oil & Gas Reservoir Stimulation, Langfang, Hebei 065007, China*
[3]*PetroChina Xinjiang Oilfield Company, Karamay 834000, Xinjiang, China*

Correspondence should be addressed to Bo Cai; caibo69@petrochina.com.cn

Received 28 October 2021; Accepted 10 January 2022; Published 23 February 2022

Academic Editor: Bing Hou

In order to determine the effective stress factor of proppants during the multi-stage hydraulic fracturing operation in horizontal wells and select the appropriate proppant type, the analysis of the effective stress characteristics of proppants is carried out. This analysis considers the geomechanics and long-term production characteristics of multi-stage fractured horizontal wells in reservoirs like Xinjiang Mahu shale oil and Southwest China shale gas. The analysis of influencing factors is also carried out. The results show that, during the multi-stage hydraulic fracturing operation in horizontal wells, the stress on proppants is not only related to geological factors such as reservoir closure stress, but also closely related to total injection volume, cluster spacing, liquid type, injection displacement and post fracture management. First, increasing injection intensity, reducing fracture spacing, using low viscosity fracturing fluid, adopting high injection displacement and utilizing reasonable flowback system can effectively supplement reservoir energy, postpone the effective stress peak of proppants, and increase the effective conductivity of proppants. Second, the production performance analysis results of nearly 300 horizontal wells (from Xinjiang oil field, Erdos tight oil reservoir, Sichuan shale gas reservoir, etc.) shows that: the effective stress of proppants in horizontal wells is only 50–60% of that in vertical wells, which results in a different proppant selection criterion in the volume stimulation of horizontal wells and provides the geomechanics basis of replacing ceramsite proppant with quartz sand to reduce cost and increase efficiency. Based on the above conclusions, the field test of replacing ceramsite proppant with quartz sand was carried out. The proportion of quartz sand increased from less than 30% in 2014 to 69% in 2019. Without any impact on production, the annual investment cost was decreased by more than 1 billion yuan, which set a great example for the promoted low-cost development of unconventional oil and gas reservoirs under low oil price background.

1. Introduction

Common reservoir stimulation techniques include matrix acidizing, acid fracturing [1, 2] and hydraulic fracturing. In hydraulic fracturing, proppant is one of the most important materials. Since the North American shale oil and gas revolution featured by large-scale deployment of multi-stage fracturing in horizontal wells, the amount of proppant consumption has doubled and its cost consists about 20% of the total cost of well construction [3–6]. In 2019, the number of horizontal wells being fractured in the United States were nearly 25,000, which is 2.5 times more than that in 2014. In China the number has reached ~2,000, a new high in the history [7, 8]. With the increasing scale of fracturing operations year by year, the amount of material used, including proppant, has also increased significantly. In North America, the average amount of proppant used in a single well rose from 2500 tons in 2015 to 10,000 tons in 2018, with the cost proportion of proppant increasing from less than 10% to 19% meanwhile. Since 2014, due to the impact of low oil prices, North American oil and gas companies have replaced most of ceramic they used to use by sand. Now they even

strive to use locally-produced sand, and/or run a sand mill by themselves, achieving significant economic benefits in shale business. The cost of natural sand is as low as 200 US dollars/ton compared to that of artificial ceramic (about 700 US dollars/ton). The average single well cost of proppant in horizontal wells can be reduced by 7 million Yuan because of the huge amount consumed. Therefore, in the past five years, sand has gradually become the mainstream proppant. By the end of 2018, 100 million tons of sand had been used in the United States, accounting for more than 95% of the total proppant consumption, with the cost reduced by more than hundreds of millions of Yuan. Taking Permian Basin in the United States as an example, the amount of locally-produced sand consumed in the basin in 2018 was 28 million tons, saving about 2.2 billion US dollars in proppant cost [9]. Inspired by the low-cost development of unconventional oil and gas in North America, technical feasibility justification and pilot tests on fracturing with sand were carried out in the tight fields in Changqing, Xinjiang, and Southwest China in 2016. The proportion of sand as proppant increased from less than 30% to 69%, with 2.75 million tons of sand consumed. There is basically a consensus on the use of sand in stimulation of reservoirs not deeper than 2000 m. For Mahu oilfield in Xinjiang ceramic has been largely replaced by sand [10] in reservoirs not deeper than 3500 m, with significant results achieved. However, due to the difference in low-cost operation approach in North America and the "Practice first, theory second" philosophy in unconventional resource development, there is less research on the theoretical basis of sand application. In this context, some research work on this issue has been carried out domestically, and especially in the last five years, the research has been getting more and more in-depth. In 2016, Shaoyan andYong [11] reviewed the evolving history of proppants and summarized the advantages, disadvantages and evolving trends of commonly used proppants such as ceramic and sand. In 2017, Hongli et al. [12] further summarized the evolving history of proppants both at home and abroad in recent years, and elaborated the characteristics of several conventional proppants. In 2018, Lifeng et al. [13] and Xinping et al. [14] described the experimental research on fracturing conductivity upon replacement of ceramic by sand in shale gas reservoirs, and predicted the economic potential and the effect of field application of sand in shale gas development. In 2019, Jiaxiang et al. [15] analyzed the transport and distribution of proppants in circuitous micro-fractures. In 2020, Linhu et al. [16] devised an experimental facility which can be used to evaluate the diversion and transport of proppants during multi-stage fracturing of horizontal wells where complex fracture network can be generated, and revealed the law governing the diversion. The aforementioned research work preliminarily put forward the correlation between sand characteristics and fracture conductivity for shale reservoirs, and proposed the proppant transport law in the complex fracture system. All the work together laid a foundation for studying the stress on the proppant and selection of proppant in shale reservoir development, and further confirmed the necessity of research on low-cost sand application. However, for multi-stage fracturing in horizontal wells in unconventional reservoirs, the effective stress acting on the proppant is still not thoroughly understood. At present, the selection of proppant is still mainly based on the formation closure pressure, which hinders cost reduction in development of unconventional reservoirs. Especially under the influence of the persistent low oil price, the research and application of low-cost materials has become an important focus of the business. For this reason, the characteristics and influential factors of the effective stress acting on the proppant during massive fracturing of horizontal wells in unconventional reservoirs were analyzed in this paper, in combination with the tracking of long-term production performance of horizontal wells in Xinjiang tight oil and Southwest shale gas fields.

2. Characteristics of the Stress on the Proppant

The stress on proppants has always been a hot research topic. It is generally believed that the stress on proppants is related to the in-situ stress and pore pressure in formations. If the main fracture is, as usual, perpendicular to the direction of the minimum principal stress, the effective stress on the proppant in the main fracture during the early production phase is the differential between the closure pressure (which at this time is theoretically equal to the minimum principal stress) and the pore pressure. As the production goes on, the pore pressure gradually decreases, and thus the stress on proppants increases [17]. In this paper the equation for calculating the stress proposed by Wilson [18] was compared with that by Yang [13], indicating that the equations are pretty similar to each other. Hence the equation proposed by Yang was used for our analysis in this paper, shown as equation (1) here.

$$\sigma_e(t) = \sigma_c + \frac{\nu}{1-\nu}\left[\sigma_{\text{now}}(t) - p_o\right] - p_{\text{now}}(t), \tag{1}$$

where σ_e is the effective stress acting on proppants, MPa; σ_c is the original in-situ stress in the reservoir, MPa; ν is the Poisson's ratio of the rock, dimensionless; σ_{now} is the closure pressure in the artificial fracture, MPa; t is the production time, day; P_o is the original pore pressure, MPa; $P_{\text{now}}(t)$ is the pore pressure in the artificial fracture corresponding to time t, MPa.

Equation (1) shows that the effective stress on the proppant is related to the in-situ stress itself of the reservoir, which is in turn related to the burial depth of the reservoir, in-situ stress gradient, and tectonic stress. Generally speaking, the deeper the reservoir, the higher the in-situ stress, and accordingly the greater the stress on proppants [19]. The in-situ stress, Poisson's ratio and initial pore pressure are all uncontrollable (fixed) factors, but the stress on proppants and the fluid pressure within the fracture are closely related to fracturing operation. Analysis of the equation shows that the stress on proppants is negatively correlated to the volume of fracturing fluid injected, and the fluid pressure in the fracture is positively correlated to the volume injected. The higher the volume injected, the higher the fluid pressure in the fracture, and the lower the effective stress on the proppant. During fracturing in vertical wells in

the past, due to the small volume of fluid injected, the stress on the proppant was basically equivalent to the original in-situ stress, that is, the closure pressure. However, during massive stimulation of horizontal wells with huge volume injected, how the fluid volume, fluid type, fracture parameters, and interaction between the fractures affect the magnitude of the stress on proppants remains a question. In-depth understanding of all the issues will have important guiding significance to selection of proppants and optimization of fracturing operations.

3. Analysis of the Factors Influencing the Effective Stress

To further analyze the factors influencing the effective stress acting on proppants during multi-stage massive fracturing of horizontal wells, the reservoir properties and fracturing operation parameters of Mahu tight oil reservoir in Xinjiang [20] were used in this study. The reservoir properties included: average permeability (0.1 mD), average effective porosity (8.5%), reservoir thickness (30 m), burial depth (3800 m), oil saturation (55%), and reservoir pressure coefficient (1.1). The latter included: threshold injection pressure gradient (1.3 MPa/m), length of horizontal section (1500 m), length of each stage (60 m), number of perforation clusters in one stage (3, 6, or 12), spacing between clusters (5, 10, or 20 m), fracturing flowrate (5, 8, or 10 m^3/min), and injection intensity (10, 20, 30, 40 m^3/m). The fracturing fluid is slick water or guar gum fluid, with viscosity being 5 mPa·s or 35 mPa·s (0.25% concentration) respectively. The production performance data used in our study were all from production wells which had been producing for more than 600 days. Based on all the data collected, analysis of the factors influencing the effective stress on the proppant, such as fluid injection intensity, spacing between fractures, fluid type and post-fracturing production management, was conducted.

3.1. Fluid Injection Intensity. In order to effectively analyze the influence of injection intensity on the stress on proppants, four levels of injection intensity, 10, 20, 30, 40 m^3/m of horizontal section, were simulated to study the characteristics of pore pressure change. The results indicated that with the increase in the volume injected, the pore pressure in the formation increases significantly, so does the pressure within the fracture. When the injection intensity is 10, 20, 30, and 40 m^3/m, the average pore pressure in the formation increases by 1.1, 2.6, 3.2 and 3.6 MPa respectively, while the pressure within the fracture increases from 0 MPa to 3.4, 7.5, 14 and 21 MPa respectively (Figure 1). As shown in the figure, the average pore pressure near the fracture in the reservoir gradually increases with the increase in injection intensity. However, when the injection intensity reaches 30 m^3/m, the increase rate of pore pressure decreases as the injection intensity increases. To be more specific, the pore pressure increases from 3.2 MPa at 30 m^3/m to 3.6 MPa at 40 m^3/m. In contrast, the pressure increase rate in the artificial fractures increases as the injection intensity increases.

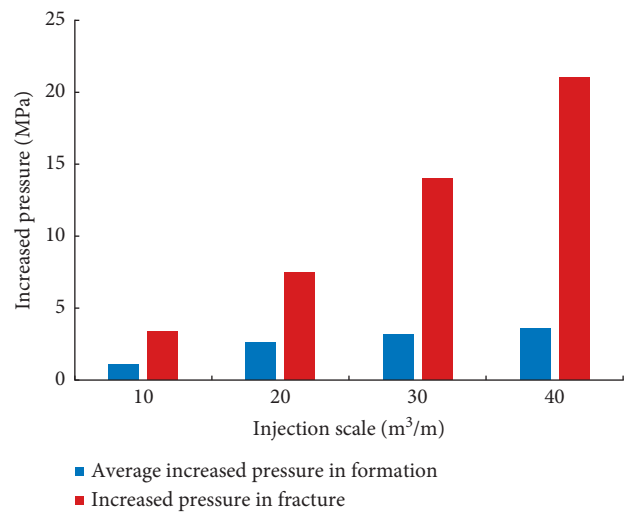

Figure 1: Average formation pressure and pressure increase in fractures under different injection scales.

Specifically, the fracture pressure increases from 14 MPa at 30 m^3/m to 21 MPa at 40 m^3/m. A large amount of fluid which cannot enter the pores remains in fractures instead. Combining reservoir numerical simulation results and equation (1), the conclusion can be drawn that the stress on proppants was basically the same in the early days for the three intensity levels of 20, 30, 40 m^3/m. As the pressure was released after fracturing operation and the fluid was flowed back gradually, the proportion of the fluid flowed-back increased rapidly for 30 m^3/m and 40 m^3/m intensity; upon back flowing for 120 days the pressure within the fracture was basically the same for the three injection intensity levels. The high injection intensity only increased the pressure in the fracture in the early days, but it did little for decreasing the stress later on. Consequently, the injection intensity of 30 m^3/m for Mahu tight oil is reasonable. The actual production data for 30 m^3/m intensity in horizontal wells and those of previous vertical wells was compared and the stress on proppants is calculated using equation (1) in each case. It was found that the stress on proppants increased from 5 MPa in the early days to 25 MPa after flowing back for 550 days for the horizontal well case while from 5 MPa to 45 MPa across the same time interval for the vertical case. For vertical wells, the proportion of flow-back fluid in 90 days is 100%. For horizontal wells, this number is only 13% in 90 days and 34% in 600 days. The large amount of retained fluid greatly decreases the stress on proppants. The stress on proppants in multi-stage fractured horizontal wells is only 50–60% of that in vertical wells (Figure 2), so the principle of selecting proppants based on closure stress in the past no longer works for horizontal wells. Therefore, it is more reasonable to use equation (1) to calculate the stress on proppants in horizontal wells. Based on the above analysis, more and more sand has been used instead of ceramic as proppants in Mahu oilfield in Xinjiang, China since 2017. The results of a pilot test in Block Ma-131 involving 25 wells show that, at the same proppant consumption (1.5 m^3/m), sand and ceramic resulted in average oil production of 18.1 t/

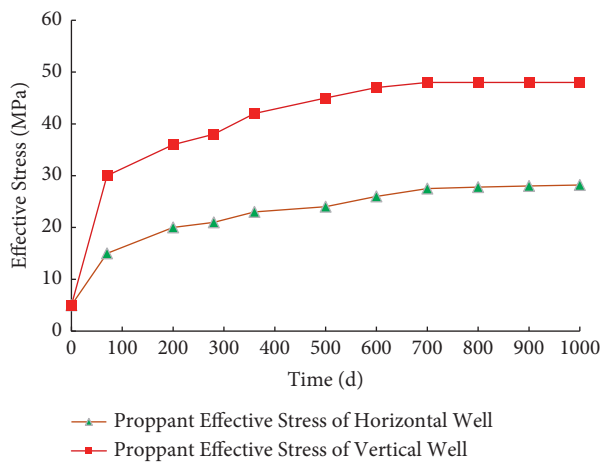

Figure 2: Changes in the effective stress of proppants in tight oil vertical and horizontal wells in Junggar Mahu.

d and 18.4 t/d in the initial 30 days, and 16.0 t/d and 15.3 t/d in the initial 360 days, respectively, with cumulative production being also roughly the same, which verified the feasibility of using sand as proppant. At the end of Dec. 2019, sand had been used in all reservoirs with burial depths less than 3500 m in Mahu oilfield, and the annual consumption of sand was 115,000 m^3, saving nearly 300 million Yuan in investment [21].

3.2. Spacing between Fractures. The influence of the number of perforation clusters on the stress on proppants was analyzed by simulating 3, 6, and 12 perforation clusters in one 60 m stage with spacing between clusters being 20 m, 10 m and 5 m, respectively. The characteristic parameters used in the simulation are also from Mahu oilfield. The simulation results show that, with all the other conditions being the same, pressure in the fracture was the highest for the 3-cluster scenario, but the pressure transmission was limited to a short range around the fracture. As the number of clusters increased to 6 and then to 12 (the spacing decreased in proportion), the pressure in the fracture successively decreased, but the pressure transmission extended to a larger range (Figure 3(a)). Production performance of 1 year after fracturing was analyzed. For the 3-cluster scenario, little oil was produced and most of the crude oil is remained in place because of the unfavorable reservoir properties and threshold pressure drawdown. Fluid flow from the formation to the artificial fractures was restricted, resulting in a significant pressure drop in the fractures. Most of the fracturing fluid flowed back, so the proppant suffered heavy effective stress in this case, and the loss of fracture conductivity was also substantial. For the 6-cluster scenario, the pressure transmission extended to a larger range, and the artificial fractures overcame the unfavorable reservoir properties and threshold pressure drawdown, resulting in a higher recovery rate. The pressure in and near the fractures increased, so did the reservoir energy. In this case the effective stress on proppants is lower, and the decrease of conductivity slows down. For the 12-cluster scenario, all the consequences become even more favorable (Figure 3(b)). The actual data of the first-year production in a block in Mahu further confirmed the above simulation results. Flowback volume for the three cases, 3, 6, and 12 clusters, was compared. The proportion of fluid flowing back was only 29% in the 6-cluster and 12-cluster cases, compared to 78% in the 3-cluster cases. The effective stress on the proppant was 24 MPa in the 6-cluster and 12-cluster cases and 33 MPa in the 3-cluster case, indicating a chance of using low-cost sand in the 6-cluster and 12-cluster cases. The average production also increased from 22.3 m^3/d in 3-cluster case to 31.4 m^3/d in 12-cluster case (Figure 4). The above analysis also confirmed the mechanism of outstanding achievements by decreasing the spacing between clusters (usually 5–10 m) and replacing ceramic with sand totally in North America [22]. It is also a strong support to conducting more pilot tests on multiple-cluster fracturing with sand in domestic shale gas and tight oil development. Taking well Chang-7 as an example, a horizontal well in a tight oil reservoir, the stage length was reduced from 110 m to 60 m, and the spacing between clusters was shortened from 30 m to 10 m. As a result, its single well production during well testing was 18.6 t/d, which was 8.3 t/d higher than that of offset wells.

3.3. Fluid Type and Injection Parameters. In order to effectively carry out single factor analysis, 10 core plugs (2.5 × 2 cm each) were cut from a 2.5 × 25 cm outcrop core sample corresponding to the target tight oil zone of well Chang-7. In this way the properties and other parameters of various plugs are basically the same, so deviation caused by the difference in sample properties can be ignored. The propagation characteristics of fracturing fluid, here slick water and low-concentration guar gum solution (0.25%), were analyzed under the same experimental conditions. Nuclear magnetic resonance CT was used in the experiments to study the hesitation time of the two fluids propagating through the core [23, 24]. The results showed that, compared with low-concentration guar gum solution, more slick water was retained in both the micro-pores (retention time 0.1–10 ms) and meso-pores (retention time 10–100 ms). High-speed centrifugation for dewatering showed that, at the same centrifugal speed, the flowback proportion of slick water was only about 50% of that of the guar gum solution, indicating that the slick water replaced the original liquid (mainly oil) in the pores through imbibition, and retained within the core, which increased the pore pressure and supported the core. Further observations of the core also confirmed that slick water is more likely to propagate along the pore throats evenly (the red circle in Figure 5 is the zone invaded by slick water), which helps to extract the oil in deep micro-pore throats, while the low-concentration guar gum solution is more likely to propagate unevenly and the propagation depth was only about 45% of the slick water. Therefore, use of slick water in unconventional reservoir fracturing is more conducive to increasing the fluid penetration depth and the pore pressure in the disturbed area (Figure 5). With the same amount of fluid injected, increasing the flow rate can also increase the penetration depth

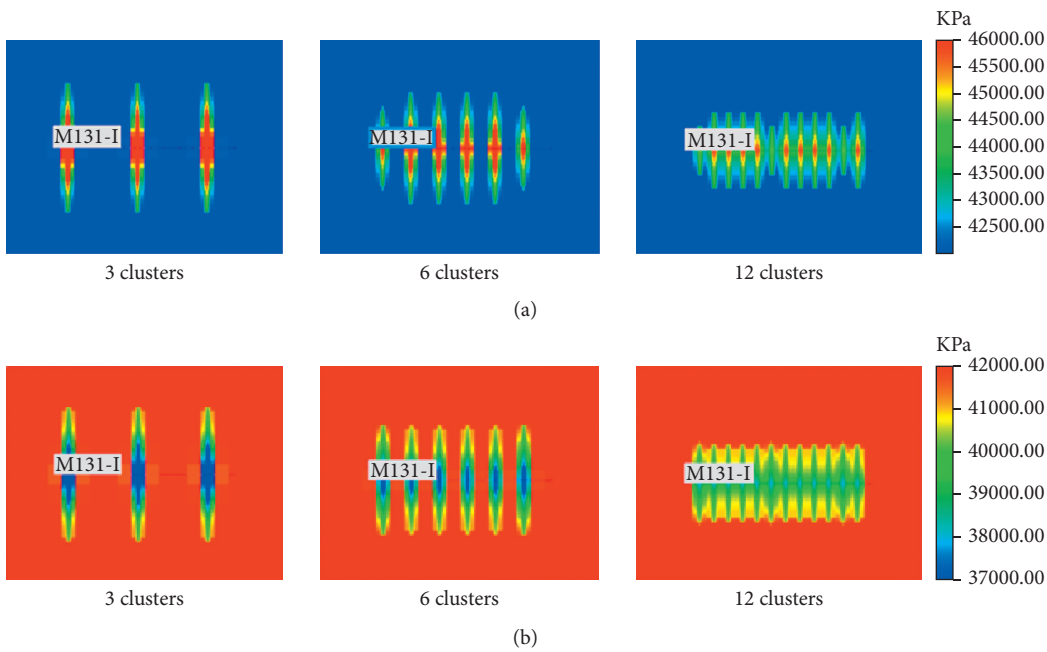

Figure 3: (a) Pressure change of the fracturing process when the number of perforation clusters in a single stage is 3, 6, and 12 clusters respectively. (b) Pressure change of the flowback process when the number of perforation clusters in a single stage is 3, 6, and 12 clusters respectively.

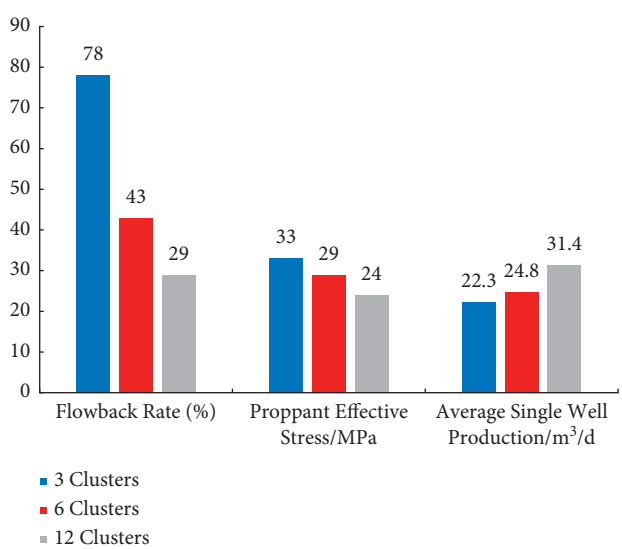

Figure 4: Flowback rate, proppant effective stress and daily production changes under different cluster numbers.

and pore pressure. This is why slick water accounts for more than 90% and 70% of fracturing fluid in unconventional resources abroad and domestically. High flow rate is more conducive to increase penetration depth, raise pore pressure, supplement energy, and reduce the effective stress acting on proppants, all favoring the use of low-cost sand as proppant.

3.4. Post-fracturing Production Management. In this section, how the production mode affects the stress on proppants and thus affects the fracture conductivity and production rate is studied. The conductivity was measured by lab experiments with sandstone core plates [25]. The experimental conditions were: temperature–90°C, fluid–2% KCl, proppant–20/40 mesh sand, and crevice (simulating the fracture) width–5 mm (Figure 6). When the effective stress rose to 70 MPa, the fracture conductivity dropped drastically, by as much as 70% because of compaction of the proppant packing and crushing of proppant grains. The effective stress was stabilized at 70 MPa for 72 h, and the conductivity dropped from 78 μm^2·cm to 29 μm^2·cm in this time interval, marking a 63% decrease. The dropping of conductivity was "fast first and then slow." At the end of the 72 hours, the effective stress was alternated between 65 MPa and 75 MPa, and the conductivity exhibited "step-like" dropping. After the alternation the conductivity at effective stress of 70 MPa was 11 μm^2·cm, with a drop of 60%. The result told us that frequent opening and shutting-in of wells during production would lead to a significant decrease in the conductivity of the proppant packing layer, which is unfavorable for use of sand instead of ceramic. Therefore, it is essential to avoid frequent choke replacement and downhole operations etc. that interrupt continuous production, and to rationally optimize the production mode.

4. Field Application of the Understandings

New understandings of the effective stress acting on the proppant in multi-stage fracturing of horizontal wells were gained in this research, which can be guidance for the design optimization of horizontal well stimulation in shale gas and tight oil development. The volume injected during multi-stage fracturing of horizontal wells is at least 5 times more

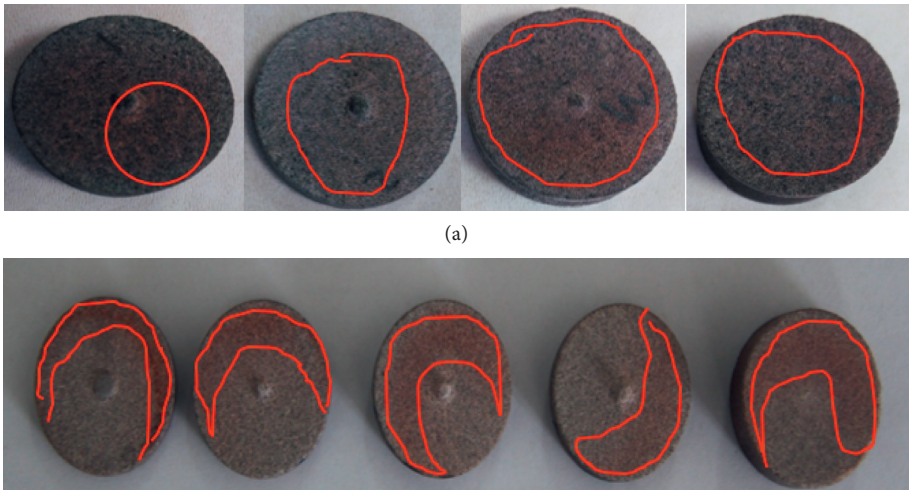

Figure 5: Comparison of the propagating of different fluids injected into tight oil cores. (a) Slick water injection and propagating. (b) Low-concentration guar gum solution injection and propagating.

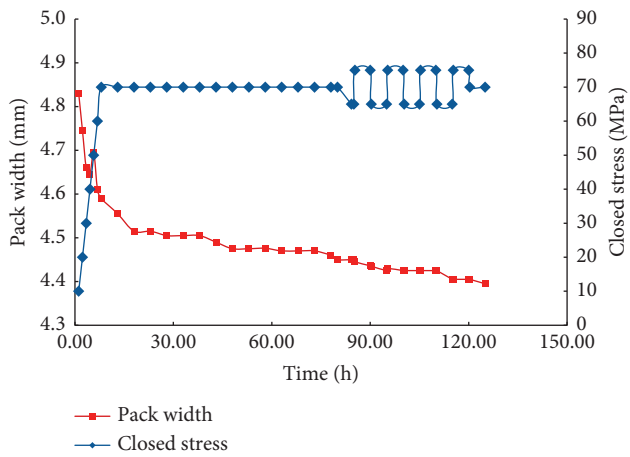

Figure 6: Proppant pack width change under different time and stress.

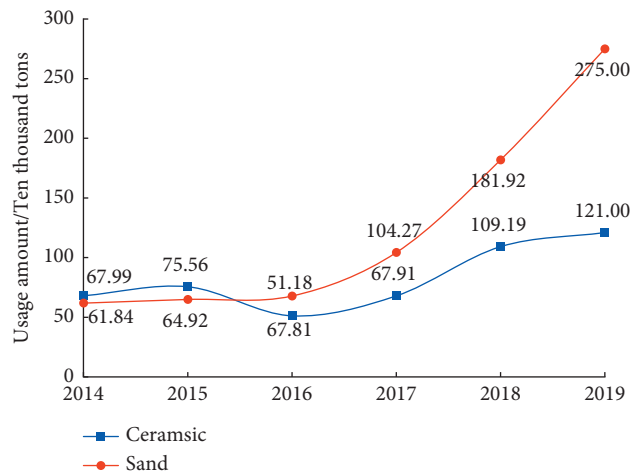

Figure 7: Consumption of ceramsic and sand in CNPC from 2014 to 2019.

than that during fracturing of vertical wells. The number of stages has been increased from 10 to more than 20; the number of clusters in one stage has been increased from 2 to 3 to 5–10; and the spacing between clusters has been reduced from 50–60 m to 10–30 m. Among all fracturing fluids, the proportion of low-viscosity slick water has increased from less than 30% to more than 60%. The combination of the above measures greatly decreases the stress on proppants. Analysis of production performance of nearly 300 horizontal wells in the tight oil fields in Xinjiang and Ordos, and shale gas fields in Sichuan showed that the effective stress on proppants during and after multi-stage fracturing of horizontal wells is only 50–60% of that for the vertical wells. This finding changed the criterion for selecting proppant for the multi-stage fracturing and provided a theoretical basis for promoting the use of low-cost sand as proppant. Since 2016, ceramic has been gradually replaced by sand in shale gas development in Sichuan, and tight oil development in Ordos, Xinjiang, and Songliao basins etc. The proportion of sand has increased from less than 30% in 2014 to 69% in 2019. As for the absolute volume, the consumption has increased from 680,000 tons in 2016 to 2.75 million tons in 2019 (Figure 7), with annual investment saved by more than 1 billion Yuan, which is a significant economic benefit. For example, a field test was implemented at Pad YS112H4 and Pad YS112H5 in Zhaotong shale gas reservoir to compare the cost and profit of 5, 7, and 11 clusters in one stage, with the spacing between clusters reduced from 20 m to 5–12 m. With the injection intensity being the same (30 m^3/m), the injected sand volume increased from 1.67 t/m to 3.18 t/m. The single well production increased from 100,000–200,000 m^3/d by conventional fracturing to 300,000–400,000 m^3/d, and the wellhead pressure remained at a relatively high level. The EUR per well is 120–160 million m^3, higher than the average 99 million m^3 in the same block. The replacement of ceramic by sand reduced the fracturing cost per well by 2 million Yuan.

5. Conclusions and Prospecting

With more and more applications of multi-stage massive stimulation of unconventional oil and gas horizontal wells, the scale of the stimulation gradually increases, causing a substantial cost increase in equipment, materials etc. The consumption of proppants has doubled, accounting for 20% of the cost of well construction. In this paper, analysis of the effective stress acting on proppants for the unconventional horizontal well fracturing, together with field tests, indicated that the stress is closely related to injection volume, cluster spacing, fluid type, injection flowrate and post-fracturing production management. Large injection volume, short cluster spacing, low-viscosity fluid and high flowrate are conducive to decreasing the effective stress on proppants. Analysis of production performance of nearly 300 horizontal wells in the tight oil fields in Xinjiang and Ordos, and shale gas fields in Sichuan showed that the effective stress on proppants for the multi-stage fractured horizontal wells was only 50–60% of that for the vertical wells. This finding changed the criterion for selecting proppants for the multi-stage fracturing operation, further explained the feasibility of replacing ceramic with sand in North America, and provided a theoretical basis for large-scale application of sand as proppant in China. The proportion of sand has increased from less than 30% in 2014 to 69% in 2019, with annual investment saved by more than 1 billion Yuan, showing a good prospect. Under the low oil price context, the conclusions are of pragmatic significance for reducing cost and increasing profit during the development of China's unconventional oil and gas in the future.

Data Availability

The test data used to support the findings of this study are available from the corresponding author upon request.

Conflicts of Interest

The authors declare that they have no conflicts of interest.

Acknowledgments

This work was funded by the National Science and Technology Major Project "Key Technology and Equipment of Reservoir Stimulation," China (Grant No. 2016ZX05023) and "Study on mechanism of complex fracture network and efficient hydraulic fracturing technology of shale oil reservoir" (project No.2021DJ1805).

References

[1] B. Hou, Y. Dai, C. Zhou, K. Zhang, and F. Liu, "Mechanism study on steering acid fracture initiation and propagation under different engineering geological conditions," *Geomechanics and Geophysics for Geo-Energy and Geo-Resources*, vol. 7, no. 3, pp. 1–14, 2021.

[2] K. Zhang, B. Hou, M. Chen, C. Zhou, and F. Liu, "Fatigue acid fracturing: a method to stimulate highly deviated and horizontal wells in limestone formation," *Journal of Petroleum Science and Engineering*, vol. 208, Article ID 109409, 2022.

[3] O. A. Jaripatke, I. Barman, J. G. Ndungu et al., "Review of Permian completion designs and results," in *Proceedings of the SPE Annual Technical Conference and Exhibition*, OnePetro, Astana, Kazakhstan, October 2018.

[4] J. Y. Kim, Z. Jing, and N. Morita, "Proppant transport studies using three types of fracture slot equipment," in *Proceedings of the 53rd US Rock Mechanics/Geomechanics Symposium*, OnePetro, New York, NY, USA, June 2019.

[5] W. Yizhao, H. Bing, W. Dong, and J. Zhenhua, "Features of fracture height propagation in cross-layer fracturing of shale oil reservoirs," *Petroleum Exploration and Development*, vol. 48, no. 2, pp. 469–479, 2021.

[6] Q. Zhang, B. Hou, B. Lin, X. Liu, and Y. Gao, "Integration of discrete fracture reconstruction and dual porosity/dual permeability models for gas production analysis in a deformable fractured shale reservoir," *Journal of Natural Gas Science and Engineering*, vol. 93, Article ID 104028, 2021.

[7] S. Uddin, J. Cox, N. Uddin, and R. Uddin, "Permian Basin's evolution of hydraulic fracturing techniques over the last decade: vertical to horizontal wells," in *Proceedings of the Abu Dhabi International Petroleum Exhibition & Conference*, OnePetro, Abu Dhabi, UAE, November 2018.

[8] X. Jiangwen, L. Jianmin, W. Yuanyue, D. Kun, and J. Hong, "Exploration and practice of volume fracturing technology in horizontal well of Mahu tight conglomerate reservoirs," *China Petroleum Exploration*, vol. 24, no. 2, p. 241, 2019.

[9] Z. Qingfan, J. Zhijun, Y. Guofeng, D. Ning, and S. Zhucheng, "Shale oil exploration and production in the US: status and outlook," *Oil & Gas Geology*, vol. 40, no. 3, pp. 469–477, 2019.

[10] L. Qun, G. Baoshan, C. Bo et al., "Technological progress and prospects of reservoir stimulation," *Petroleum Exploration and Development*, vol. 46, no. 3, pp. 605–613, 2019.

[11] M. Shaoyan and J. Yong, "Overview of fracturing proppants," *Chinese Journal of Engineering*, vol. 38, no. 12, pp. 1659–1666, 2016.

[12] D. Hongli, Z. Wei, M. Feng, and L. Chao, "Research progress of hydraulic fracturing proppants," *Bulletin of Chinese Ceramic Society*, vol. 36, no. 08, pp. 2625–2630, 2017.

[13] Y. Lifeng, T. Zhuhong, and Z. Zhongyi, "Economic adaptability of quartz sand for shale gas reservoir fracturing," *Natural Gas Industry*, vol. 38, no. 5, pp. 71–76, 2018.

[14] G. Xinping, P. Junliang, and P. Huan, "Experimental study on feasibility of replace ceramic with sand in shale fracturing," *Drilling & Production Technology*, vol. 41, no. 5, pp. 35–41, 2018.

[15] X. Jiaxiang, D. Yunhong, Y. Lifeng, L. Zhe, G. Rui, and W. Zhen, "Transportation and distribution laws of proppants in tortuous micro-fractures," *Acta Petrolei Sinica*, vol. 40, no. 8, p. 965, 2019.

[16] P. Linhua, Z. Ye, and W. Haibo, "Mechanism study on proppants division during shale complex fracturing of shale rock," *Journal of China University of Petroleum (Edition of Natural Science)*, vol. 44, no. 1, pp. 61–70, 2020.

[17] W. Renpu and L. Yingjun, *Production Technical Manual*, China Petroleum Industry Press, Beijing, China, 2nd edition, 1998.

[18] K. Wilson and R. R. Hanna Alla, "Efficient stress characterization for real-time drawdown management," in *Proceedings of the SPE/AAPG/SEG Unconventional Resources Technology Conference*, OnePetro, Austin, Texas, USA, July 2017.

[19] L. Mu, Z. Zhao, X. Li et al., "Fracturing technology of stimulated reservoir volume with subdivision cutting for shale

oil horizontal wells in Ordos Basin," *Oil & Gas Geology*, vol. 40, no. 3, 2019.

[20] S. Tao, H. Fuxi, W. Shaoyong et al., "Characteristics and exploration potential of Jurassic oil and gas reservoirs in Mahu sag of the Junggar Basin," *China Petroleum Exploration*, vol. 24, no. 3, p. 341, 2019.

[21] L. Jianmin, W. Baocheng, Z. Haiyan, C. Ning, and H. Jialing, "Adaptability of horizontal well volume fracturing to tight conglomerate reservoirs in Mahu oilfield," *China Petroleum Exploration*, vol. 24, no. 2, p. 250, 2019.

[22] R. Shelley, K. Shah, S. Sheludko, B. Davidson, and T. Palisch, "Is conductivity still important in unconventional reservoirs? A field data review," in *Proceedings of the Unconventional Resources Technology Conference*, pp. 2695–2706, Society of Exploration Geophysicists, American Association of Petroleum Geologists, Society of Petroleum Engineers, Houston, Texas, July 2018.

[23] D. Yixin, G. Hekun, and L. Haibo, "NMR experimental study of gas flooding of tight oil reservoir," *China Sciencepaper*, vol. 15, no. 01, pp. 105–111, 2019.

[24] B. Bin, Z. Rukai, W. Songtao et al., "Multi-scale method of Nano (Micro)-CT study on microscopic pore structure of tight sandstone of Yanchang Formation, Ordos Basin," *Petroleum Exploration and Development*, vol. 40, no. 3, pp. 354–358, 2013.

[25] Z. Yi, M. Xingqin, and J. Baojun, "Long-term fracture conductivity of fracturing propant," *Oil Drilling & Production Technology*, vol. 26, no. 1, pp. 59–61, 2004.

Hindawi
Geofluids
Volume 2022, Article ID 1518320, 13 pages
https://doi.org/10.1155/2022/1518320

Research Article

Experimental Study of Measuring Algorithm Accuracy of the Electromagnetic Distance Measurement Anticollision Tool

Cui Li,[1] Lei Li,[1] Yuzheng Zhao,[2] Ruichao Zhang,[1] and Yuanwei Sun[1]

[1]*College of Petroleum Engineering, Shandong Institute of Petroleum and Chemical Technology, Dongying 257061, China*
[2]*No. 5 Oil Production Plant Huabei Oilfield Company, PetroChina, Xinji 052360, China*

Correspondence should be addressed to Cui Li; licui1219@163.com

Received 8 September 2021; Revised 9 November 2021; Accepted 3 January 2022; Published 9 February 2022

Academic Editor: Bing Hou

In order to prevent collision of complex structure well, accurate measurement of the distance of adjacent wells must be required during the development of the unconventional reservoir. The precision of the traditional survey tools and scanning software is not accurate enough. Based on the electromagnetic anticollision measuring calculation method, the electromagnetic anticollision detection tool was designed and simulation experiments were carried out. The influence of different position relations between sensor and casing on magnetic field strength detected by the sensor was analyzed. When the sensor and the casing were parallel and the distance of them was 0.5 m~3 m, the tool could calculate accurately the distance and orientation of the adjoining well. When the angle between the sensor and the casing was within 50°, the calculation result was accurate. This research result validated the accuracy of the principle of the electromagnetic anticollision tool while drilling cluster well, and it could provide theoretical support for the development of electromagnetic detection tools.

1. Introduction

With the increasing difficulty of oil and gas resource exploration, the drilling technology of complex structure wells has become a key technology for the low-permeability, unconventional, and offshore oil reservoir [1,2]. The horizontal wells, infill wells, and cluster wells have been used to develop low-grade oil and gas resources. However, in order to prevent collisions between adjacent wells during drilling, the precise measurement of the distance between adjacent wells is required. The traditional inclinometer tools and offset well-scanning software are not enough [3,4].

At present, a series of relatively mature active magnetic detection tools have been invented, such as the MGT electromagnetic guidance tool, the RMRS rotating magnetic field measuring guidance system, and the SWG single cable guidance tool [5–8]. Although some electromagnetic detection tools can be used to measure the distance of adjacent wells accurately, these tools require additional equipment such as magnetic sources or probes to be run in the adjacent wells [9–11]. But this not only affects the normal production of the wells but also increases the cost [12–14]. Based on the principle of active anticollision ranging, cluster wells anticollision electromagnetic signal acquisition system was designed. The first reliable validation instrument could quickly handle weak electromagnetic MWD signals submerged in the strong noise environment [15]. A new antisymmetry electromagnets rotating magnetic ranging method was proposed [16]. A collision avoidance estimation was established based on magnetic difference signals [17]. The influence of several factors on magnetic difference signals was analyzed [18]. Based on the pseudo-analytical equation of electromagnetic log for layered formation, an optimal boundary match method was proposed to adaptively truncate the encountered formation structures [19–21]. The inverted results of field data demonstrated that the real-time interactive inversion method was capable of providing the accurate boundaries of layers around the wellbore from the LWD EM, and it will benefit the wellbore trajectory optimization and reservoir interpretation [22–24].

Therefore, it is necessary to develop an electromagnetic anticollision detection tool for adjacent wells. It should

realize measurement while drilling without magnetic sources or sensors in the adjacent wells, and it should also simultaneously monitor multiple surrounding wells that have been drilled. This tool of this research can reduce the risk of collisions between adjacent wells, and it can ensure the safety of drilling.

2. Experimental Principle

In order to realize the real-time measurement of the distance between adjacent wells to prevent collisions without affecting the normal production of surrounding production wells, a kind of active magnetization type electromagnetic detection tool was proposed [25]. A probe for the electromagnetic distance measurement was installed behind the downhole power drilling tool. A magnetic field sensor was placed in the middle of the probe. There was a magnetic source at each end of the probe. The magnetic source was placed symmetrically with respect to the magnetic field sensor. They were axially parallel, but the magnetic pole directions were opposite. As shown with the red line in Figure 1, the direction of magnetic field lines in the axial direction of the casing emitted by two magnetic sources was the same. When there was a casing around the probe, the casing was magnetized to generate a magnetic field along the axial direction of the casing, as shown with the green line in Figure 1. The magnetic induction intensity was related to the distance between the casing and the probe. Combined with the own attitude of the probe, the magnetic induction intensity could be detected by the probe. The relative distance between the positive well and the adjacent well could be calculated by the electromagnetic anticollision measuring and steering algorithm for adjacent wells while drilling.

The following assumptions were proposed. (1) The formation was uniform and isotropic. (2) The casing was infinitely long and isotropic. (3) The radius of the casing was smaller than the distance between the casing of the positive well and the adjacent well. (4) There were no ferromagnetic minerals with high magnetic permeability in the formation. The size of the magnetic source was much smaller than the distance between adjacent wells, so the magnetic source could be regarded as a magnetic dipole, as shown in Figure 2.

A Cartesian coordinate system was established. It is assumed that the origin C is the center of the magnetic source on the upper part of the probe, the y-axis is the axis of the probe, and the z-axis is the axis of the magnetic source. The distance OE which is from the center of the probe to the axis of the casing is d, m. The angle between the axis of the casing and the direction of the axis of the probe (the y-axis direction) is α. The distance between the two magnetic sources at both ends of the probe is $2h$. The angle between the line of any point P and point C on the casing and the z-axis is θ_1. The distance between P and C is r_1. Point D is another magnetic source. The angle between the line of any point P and point D on the casing and the z-axis is θ_2. The distance between P and D is r_2. Point A is the intersection of the extension of the magnetic source axis of point C and the casing axis AB. Point B is the intersection of the extension of the magnetic source axis of point D and the casing axis AB.

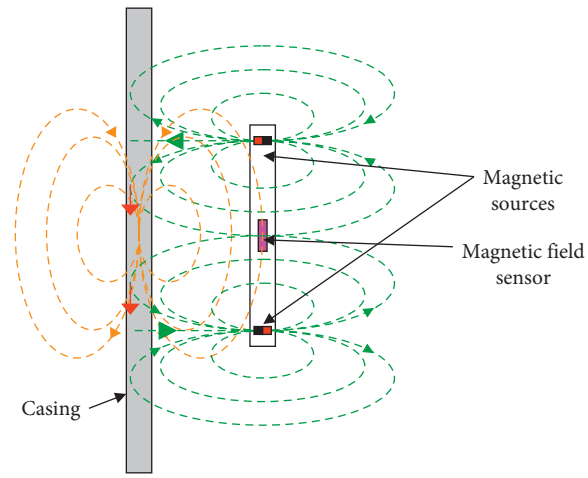

Figure 1: Distribution of magnetic line around probe with casing.

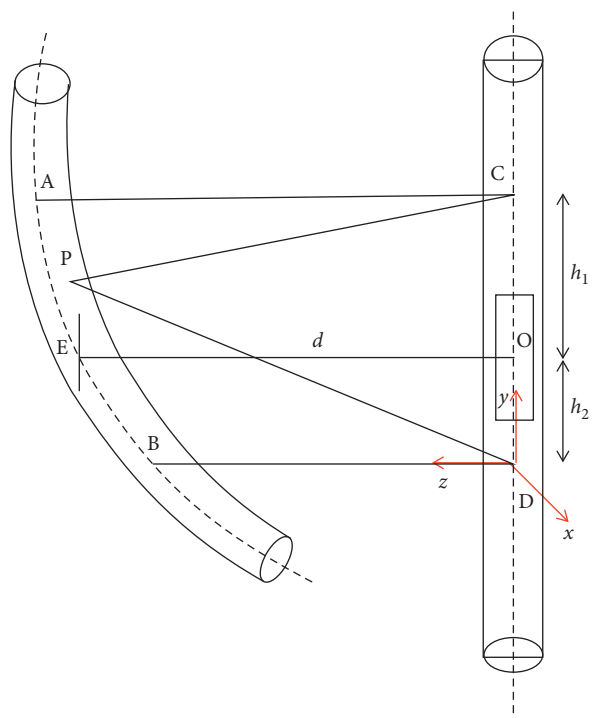

Figure 2: Calculation model of the magnetic intensity.

The casing is evenly divided into several microelements along the axis of the casing. For the microelement at point P of the casing, the total magnetizing magnetic field can be described as follows [26].

$$\begin{cases} B_{Px} = 0, \\ B_{Py} = \dfrac{3\mu_1 m}{8\pi}\left(\dfrac{\sin 2\theta_1}{r_1^3} - \dfrac{\sin 2\theta_2}{r_2^3}\right), \\ B_{Pz} = \dfrac{\mu_1 m}{2\pi}\left(\dfrac{1-(3/2)\sin^2\theta_1}{r_1^3} - \dfrac{1-(3/2)\sin^2\theta_2}{r_2^3}\right), \end{cases} \tag{1}$$

where B_{Px}, B_{Py}, and B_{Pz} are the triaxial magnetic induction components at point P, T. μ_1 is the surrounding space permeability, T·m/A. m is the magnetic moment when a magnetic source is used as a magnetic dipole, A·m^2. θ_1, θ_1 and θ_2 are the angles between any point of the casing and magnetic source axis, °. r_1, r_1 and r_2 are the distances between any point of the casing and magnetic source, m.

Assuming that the rectangular coordinates of point P are P(x, y, z), $x=0$, $z=d+y\tan\alpha$, then θ_1, r_1, θ_2, and r_2 in rectangular coordinates of point P are taken into formula (1). The magnetic induction intensity of the microelement casing at point P can be described as follows.

$$\begin{cases} B_{Px} = 0, \\ B_{Py} = \dfrac{3\mu_1 m}{4\pi}\left(\dfrac{(y-h)(d+y\tan\alpha)}{\left(\sqrt{(y-h)^2+(d+y\tan\alpha)^2}\right)^5} - \dfrac{(y+h)(d+y\tan\alpha)}{\left(\sqrt{(y+h)^2+(d+y\tan\alpha)^2}\right)^5}\right), \\ B_{Pz} = \dfrac{\mu_1 m}{2\pi}\left(\dfrac{1-\left(3(y-h)^2/2\left((y-h)^2+(d+y\tan\alpha)^2\right)\right)}{\left(\sqrt{(y-h)^2+(d+y\tan\alpha)^2}\right)^3} - \dfrac{1-\left(3(y+h)^2/2\left((y+h)^2+(d+y\tan\alpha)^2\right)\right)}{\left(\sqrt{(y+h)^2+(d+y\tan\alpha)^2}\right)^3}\right), \end{cases} \tag{2}$$

where h is the distance between the probe and magnetic source, m. d is the distance from the center of the probe to the axis of casing, m. α is the angle between casing axis direction and probe axis direction, °.

For the position of the magnetic field sensor at point O, according to the distribution of the magnetic field around the magnetic dipole [27,28], the magnetic induction intensity of the magnetic dipole at point P at the magnetic field sensor can be described as follows.

$$\begin{cases} B_x = 0, \\ B_y = -\dfrac{D^2\delta\chi_m\sqrt{B_{Py}^2+B_{Pz}^2}}{16\mu_1}\cdot\dfrac{3\mu y(d+y\tan\alpha)}{\left(\sqrt{y^2+(d+y\tan\alpha)^2}\right)^5}, \\ B_z = \dfrac{D^2\delta\chi_m\sqrt{B_{Py}^2+B_{Pz}^2}}{8\mu_1}\cdot\dfrac{\mu}{\left(\sqrt{y^2+(d+y\tan\alpha)^2}\right)^3}\left(1-\dfrac{3y^2}{2\left(y^2+(d+y\tan\alpha)^2\right)}\right), \end{cases} \tag{3}$$

where B_x, B_y, and B_z are the magnetic induction intensities of magnetic dipole at point P at the magnetic field sensor, T. D is the diameter of the element, m. δ is the length of the element, m. χ_m is the magnetic susceptibility of the casing.

The magnetic field sensor is taken as the center, and the simulation calculation is performed along the range of ±10 m in the y-axis direction. The range of ±10 m is divided into N equal parts, and each part has a length of δ. The magnetic induction intensity B_{Pi} of each point is calculated, and then the magnetic induction intensity B_{Oi} of each point at the position of the magnetic field sensor is calculated [29,30].

$$\begin{cases} B_{Ox} = 0, \\ B_{Oy} = \sum_{i=1}^{N} B_{Pyi}, \\ B_{Oz} = \sum_{i=1}^{N} B_{Pzi}, \end{cases} \tag{4}$$

where B_{Ox}, B_{Oy}, and B_{Oz} are the magnetic induction intensities of each point at the position of the magnetic field sensor, T.

Then, the total magnetic induction intensity detected by the magnetic field sensor can be obtained. All variables of formula (3) are known except for the variable y. The magnetic field of the magnetized casing has a definite relationship with the distance d between the probe and the

casing. The distance between the probe and the casing can be calculated with the magnetic induction intensity value which can be detected by the magnetic field sensor.

3. Design of Electromagnetic Anticollision System While Drilling

3.1. Structure Design. In order to measure the distance between adjacent wells while drilling, electromagnetic detection tools must be installed in downhole BHA. Theoretically, the smaller the distance between the tool and the bit is, the better the effect is. However, downhole power drilling tools need to be installed behind the bit during the actual directional well drilling process. The electromagnetic anticollision system while drilling in cluster wells needs mud pulse to transmit data to the ground. If it is installed directly behind the bit, it is difficult to connect with the mud pulse transmitter. Therefore, the best installation position of the probe is behind the downhole power drilling tool.

For the design of an electromagnetic detection system, the detection tube is directly connected with the power motor, and it is very similar to MWD. Therefore, the structural design of the system is based on the structure of MWD. Replace MWD probe with sensor nipple, and install magnetic source at both ends of probe shell. Mud flows through the gap between the magnetic source and the probe shell, and mud also flows through the gap between the sensor nipple and the probe shell. The overall structure of the probe is shown in Figure 3.

The probe is composed of the shell, the magnetic source, and the sensor nipple. All structures of the system should be designed according to the site standards. The 6 3/4″ drill collar is used for the probe shell, and the total length is 2000 mm. In order to ensure sufficient strength, the diameter of the hole in the middle of the probe is designed to be 71.4 mm, and the drilling fluid can flow to the bottom of the well through the hollow. In order to maximize the detection distance of the system, a total of 6 magnetic sources are placed at both ends of the probe, and the axes are parallel to each other. They are symmetrical about the center of the probe. The minimum distance between the two groups of magnetic sources is 1600 mm. The diameter of the magnetic source is 30 mm and the length is 150 mm. Permanent magnets or electromagnetic solenoids can be installed.

There is a spring circlip at both ends of the magnetic source. After the magnetic source is installed, both ends should be sealed with special high-temperature resistant resin glue to prevent leakage of the drilling fluid. The sensor joint is installed in the hollow of the probe. The length of the sensor joint is 750 mm and the outer diameter is 45 mm. There is a centralizer outside the sensor joint, and the sensor joint is installed in the hole in the middle of the probe. The center of the sensor must be located at the center point of the magnetic source at both ends of the probe during the installation.

The main function of the sensor joint is to collect three-axis magnetic field data and its own attitude data. The sensor joint processes the data and transmits it to the ground through mud pulse. The data is further processed and displayed by the ground system. The core of the sensor joint includes the three-axis magnetic field sensor, the three-axis accelerometer, and the signal processing circuit board.

The shell of the sensor joint is made of low-carbon high chromium manganese alloy steel which is of high strength and nonmagnetic. The outer diameter of the shell of the sensor nipple is 45 mm and the wall thickness is 5 mm, which is basically consistent with the MWD probe. There is an end cap seal head at both ends of the sensor joint to prevent the drilling fluid from entering the sensor joint. The upper and lower covers have the same size, and they are made of the high chromium manganese alloy steel with nonmagnetic low carbon. There are two O-ring grooves inside the upper and lower covers. The O-rings are installed during assembly to ensure good sealing after tightening. An outlet hole is reserved on the upper-end cover to output the processed data to the mud pulser through cable.

The sensor and signal processing circuit board inside the sensor joint are installed on a nonmagnetic aluminum support. The sensor is located in the hole under the support, and it is consistent with the axis of the sensor joint. The signal processing circuit board is installed above the support. The circuit board is in a long strip shape, and it is fixed on the support with copper columns and stainless steel screws.

3.2. Circuit Design. When the system works normally, the magnetic field sensor can collect not only the alternating signal but also the DC signal of the geomagnetic field. The alternating signal is superimposed on the DC signal of the geomagnetic field. The alternating signal of the magnetic field sensor is the key to calculating the distance and azimuth of adjacent wells. But it is very weak, and it may be in the order of 10^{-1} nT. Therefore, it is necessary to design a perfect amplification and filtering circuit to amplify the alternating signal. In this way, the signal with sufficient strength can be collected by the downhole processor.

In addition to the alternating signal of the magnetic field sensor, the geomagnetic signal of the magnetic field sensor also needs to be collected at the same time. The geomagnetic signal is used to calculate the well deviation, the azimuth, and the current rotation angle of the probe in combination with the acceleration sensor so that the azimuth of adjacent wells can be determined by the ground data analysis software.

The overall structure of the signal processing circuit board is shown in Figure 4. The DC component signal of the three-axis magnetic field sensor is directly analog-to-digital converted, and the AC component is processed by the AC amplification filter circuit before analog-to-digital conversion. The three-axis acceleration sensor collects data directly by the microprocessor. After the underground microprocessor reads the data, the final calculation result is obtained by the software. The results are sent to the mud pulse transmitter through the mud pulse interface, and the mud pulse transmitter sends the data to the ground.

3.3. Software Design. The electromagnetic anticollision system while drilling in cluster wells collects the triaxial alternating magnetic field data, the triaxial magnetic field

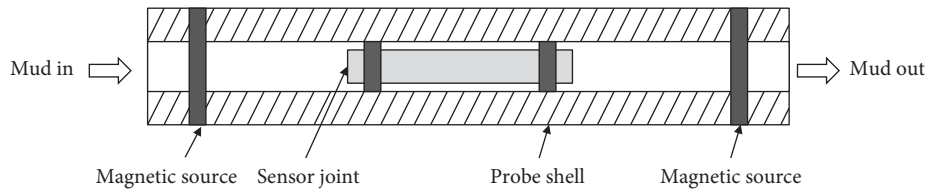

Figure 3: The overall structure of the probe.

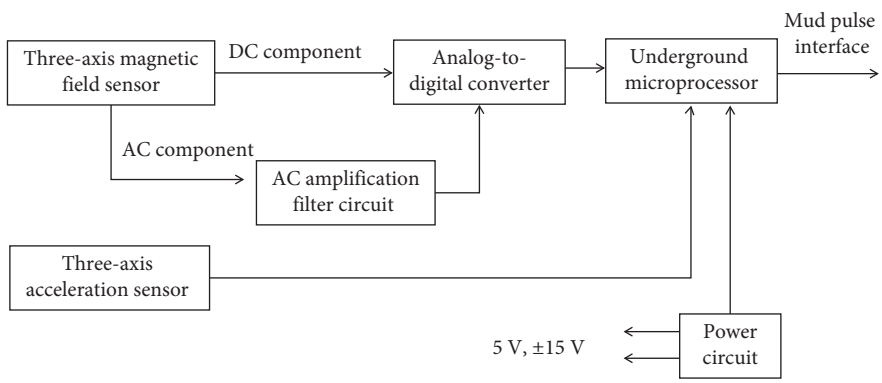

Figure 4: Overall structure diagram of signal processing circuit board.

DC component data, and the triaxial acceleration data during the drill string rotation. Because the acquisition rate is very high, and the mud pulse transmission rate is low. It is impossible to upload all collected data. This requires the downhole data to be processed to a certain extent. It should be simplified into some necessary data, and they can be transmitted to the surface system through mud pulse.

The electromagnetic anticollision system while drilling for cluster wells includes two kinds of software, which are the data processing software of downhole microprocessor and the surface data analysis software. The data processing software of the downhole microprocessor makes a preliminary analysis of the collected data, and the peak value and valley value of the collected signal can be calculated. Combining the collected peak and valley values with wellbore parameters, the surface data analysis software calculates the final distance and the azimuth of adjacent wells.

3.3.1. Data Processing Software Design of Downhole Microprocessor. The AD conversion chip of three-axis alternating magnetic field data acquisition is AD7712. The chip controls the start of AD conversion by writing the START bit of the control register. The write signal starts when the TFs signal is pulled low, and the TFS is pulled high after all bits are written. At this time, AD7712 starts AD conversion.

After the three-axis AD conversion is completed, the program reads the conversion results in the order of X, Y, and Z axes. The time difference of reading the conversion result program does not affect the time difference of three-axis data acquisition. Therefore, the conversion result of each chip can be read step by step. In order to meet the requirements of consistent acquisition values of three axes, the first acquisition value of the X-axis and the last acquisition value of the Z-axis can be discarded. Then, the average value point can be calculated again.

$$\begin{cases} V_X = \dfrac{1}{2}\left(\dfrac{1}{3}\displaystyle\sum_{3}^{n=1} V_{Xn} + \dfrac{1}{4}\displaystyle\sum_{7}^{n=4} V_{Xn}\right) = V_0 + \dfrac{15}{32}\left(V_1 - V_0\right), \\ V_Y = \dfrac{1}{8}\displaystyle\sum_{7}^{n=0} V_{Yn} = V_0 + \dfrac{15}{32}\left(V_1 - V_0\right), \\ V_Z = \dfrac{1}{2}\left(\dfrac{1}{4}\displaystyle\sum_{3}^{n=0} V_{Xn} + \dfrac{1}{3}\displaystyle\sum_{6}^{n=4} V_{Xn}\right) = V_0 + \dfrac{15}{32}\left(V_1 - V_0\right). \end{cases} \tag{5}$$

The recombined three-way acquisition outputs the same results, and the purpose of synchronous acquisition of X, Y, and Z axes is achieved. Similar to the alternating magnetic field, the X-, Y-, and Z-axis signal inputs are connected together during the test. A sinusoidal signal with the frequency of 1 Hz and amplitude of 5 V is input with a function generator. The three-axis AD conversion data is transferred directly to the computer test software. The test results are shown in Figure 5.

The magnitude and phase of the peaks of the three curves are consistent. It indicates that the consistency of the three-axis DC signal acquisition part is good, and the accuracy of the three-axis DC component data acquisition is high.

The three-axis acceleration sensor uses the MODEL544 microangle positioning sensor. It includes the three-axis fluxgate sensor, the three-axis acceleration sensor, and the temperature sensor. The interface uses TTL-level serial port. The communication parameters of MODEL544 are as follows: baud rate 19200, 8 data bits, 1 stop bit, and no parity. Based on the communication setting of MODEL544, the binary mode is used for output. The data output speed is

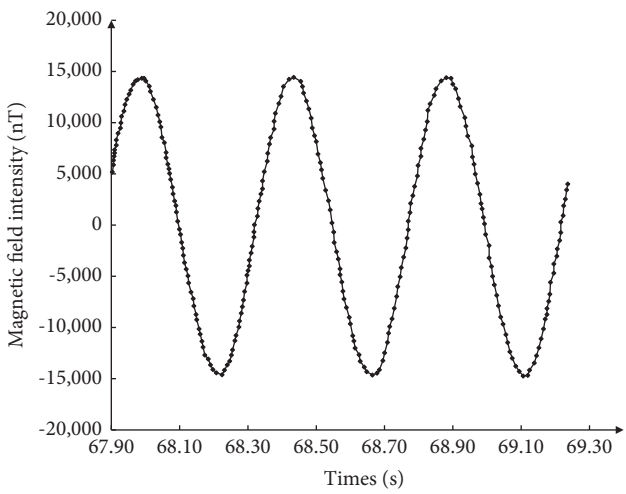

Figure 5: Data acquisition test result of three-axis DC component.

about 75 times/s, and the output data format is shown in Table 1.

In order to reduce the occupation of microprocessor time, the timeout receiving method is proposed in this research. The timeout receiving method uses the 3 ms data interval between frames. The specific process is shown in Figure 6.

After the actual test, the timeout receiving method generates an interrupt every 1 ms. The interrupt service program takes about 1~5 μs. It has little impact on other procedures. It solves the problem that serial port reception occupies microprocessor time. The main frequency of the microprocessor can be reduced to 48 MHz, which greatly reduces the power consumption of the system and improves the stability of the system.

The data acquisition program stores all data into a large array in the microprocessor memory, and the storage time is about 10 s. When the acquisition process is completed, the microprocessor will stop the acquisition, and it will process the data. For calculating the distance and relative orientation of adjacent wells, the parameters include the size of the peak value of the alternating magnetic field signal generated during one cycle of the probe rotation, and the rotation angle of the probe relative to the reference plane when the peak value is generated.

During the actual data acquisition process, the alternating magnetic field signal is placed in the alternating signal array, and the DC component data and the acceleration sensor data are placed in the DC component array. The two arrays correspond one by one depending on the acquisition time. The DC component data and acceleration sensor data stored in the DC component array are used to calculate the attitude of the probe itself, and then the rotation angle of the probe relative to the origin can be determined. The DC component array needs to be processed first to obtain the rotation angle value of the probe at each time point. And then when the alternating signal array is processed, the found signal peak can be corresponding to the angle.

The alternating signal array contains all the alternating magnetic field data, among which the useful data are the size of the signal peak and the time corresponding to the peak. If the process from the datum plane to the 360° rotation of the probe is regarded as a cycle, the alternating signal array should contain multiple cycles of data. During data processing, the angle and time correspondence array shall be generated according to the DC component array. Divide the data into multiple cycles and discard incomplete data cycles. Then, the peak and valley values of the data periodically can be calculated to obtain multiple groups of peak and valley data. These peak and valley data reflect the rotation angle of the probe when the peak and valley appear.

Table 1: Output date format of MODEL544.

Address offset	Data name	Remarks
0	START byte	Fixed to 0×10
1~2	Magnetic field X-axis data	High byte first
3~4	Acceleration X-axis data	High byte first
5~6	Magnetic field Y-axis data	High byte first
7~8	Acceleration Y-axis data	High byte first
9~10	Magnetic field z-axis data	High byte first
11~12	Acceleration z-axis data	High byte first
13~14	Temperature data	High byte first
15~16	Supply voltage data	High byte first
17~18	Check code	High byte first
19~20	End flag	Fixed to 0x7FFF

The final data processed by the microprocessor includes the peak value, the valley value, and the corresponding angle in a complete cycle. The actual transmission only needs to send these values, and the ground system data analysis software can complete the calculation. The format of data sent by the probe to the ground system is shown in Table 2.

When one well has been drilled near the well being drilled, there should be one peak value and one valley value. The data to be transmitted is 10 bytes in total, and the transmission time is about 80~90 s. Similarly, when 2 and 3 wells have been drilled near the well being drilled, the data to be sent are 18 bytes and 26 bytes, respectively, and the required transmission time is about 150 s ~ 160 s and 210 s~240 s, respectively. When it is ensured that there are no adjacent wells that may collide around the drilling well, the measurement may not be carried on. Frequent measurement is required only when there are adjacent wells close to each other.

3.3.2. Design of Ground Data Analysis Software. After the data collected and processed by the probe is transmitted to the ground through mud pulse, it is decoded by the ground receiving system, and the same group of peak and valley data sent by the probe is restored. After these data are input into the data analysis software, the relative distance and orientation of adjacent wells around the normal drilling can be calculated.

Based on the Boland C++ Builder 6.0 environment, the data analysis software of electromagnetic anticollision system while drilling for cluster wells is developed. The main function is to calculate the distance and azimuth of adjacent wells based on the signal peak and valley data uploaded by the probe. After entering the required parameters in the

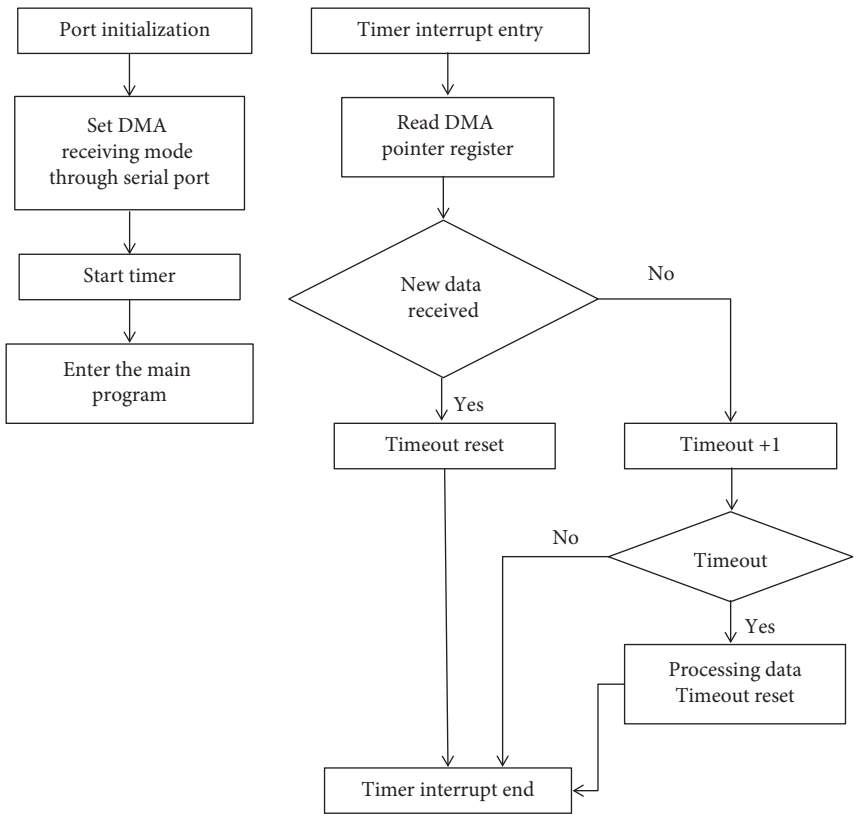

Figure 6: Flow of timeout reception method.

Table 2: Data sending format from the probe to the ground system.

Address offset	Data name	Remarks
0	Data quantity	For n groups of data, this byte is $0 \times 50 + n$
1~4	Peak or valley data 1	4 bytes and 1 group of data, respectively, high-order angle value, low-order angle value, high-order peak or valley value, and low-order peak or valley value
5~8	Peak or valley data 2	
...		
$n \times 4$–3~$n \times 4$	Peak or valley data n	
$n \times 4 + 1$	CRC check code	Verification of all previous bytes

software, click the "calculate" button to calculate the relative distance and the relative orientation of adjacent wells, and the figure will show on the right side of the software. The software also has the function of saving data. The input parameters, peak and valley data, and calculation results can be saved as an engineering file. It can be retransferred when necessary.

4. Experimental Equipment and Method

Based on the principle prototype of the electromagnetic distance measurement while drilling in adjacent wells, experiments were carried out. Although the electromagnetic anticollision measuring and steering algorithm of adjacent wells proposed in this paper has errors, it can realize the real-time monitoring of the distance and azimuth of adjacent wells.

4.1. Experimental Site. Due to the various magnetic fields in the real environment, the detection accuracy of electromagnetic detection tools will be affected. In order to minimize the influence of the surrounding environment on the measurement results of electromagnetic detection tools, this paper chose a farmyard in Shunyi District as the experiment site, which was far away from various buildings such as highways, high-voltage towers, and low-voltage wires. There were no metal cables and pipelines underground, and the environmental magnetic field was relatively stable. There were few stray interference signals. It was suitable as an experiment site for electromagnetic anticollision tools while drilling in cluster wells.

4.2. Experimental Equipment. As shown in Figure 7, the ground experimental equipment mainly included the casing, the experiment probe, the interface box, and the computer.

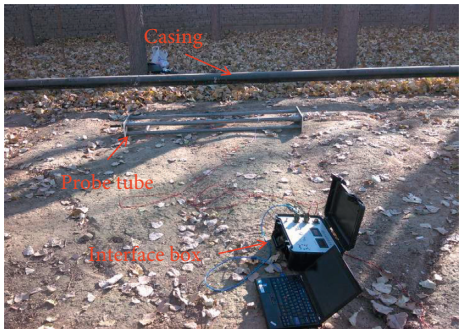

Figure 7: Diagram of simulated experimental instrument.

The experiment used three 5″ casings, and the casings were connected together. The total length is 28.47 m. The main structure of the experiment probe is made of nonmagnetic aluminum alloy. The diameter of the permanent magnet is 25 mm, and the length is 80 mm. The material is neodymium iron boron, and the surface magnetic field strength is 5000 Gs. The experiment probe is equipped with a three-axis fluxgate sensor and a three-axis acceleration sensor. Because it was a ground environment, there was no need to use mud pulses to transmit data, so the experiment probe sent data directly to a computer by a cable at a speed of up to 20 Kb/s. All alternating signal data and DC component data were directly transmitted to the computer, and it was convenient for the data analysis and processing. The two ends of the experiment probe were connected with the driving rod passing through the synchronization wheel and synchronization belt. Manually rotating the drive rod could drive the experiment probe to rotate around its axis to simulate the rotation of the drill string. The interface box was used to convert the signal collected by the experiment probe into a USB interface signal, and it provided 48 V power to the analog probe. The computer was equipped with the data acquisition software which could collect data.

4.3. Experimental Method

(1) Place the probe more than 20 m away from the casing to simulate that there is no drilled hole around the drilling well. Manually rotate the probe to simulate the rotation of the drill string. Record and save the data

(2) Align the probe to a position in the casing and place it parallel to the casing. The probe is 2 m away from the casing to simulate that there are drilled wells around the drilling well. Manually rotate the probe to simulate the rotation of the drill string. Record and save the data

(3) Align the probe with the same position in the casing and place it parallel to the casing. The probe is 0.5 m, 1 m, 2 m, 3 m, 4 m, and 5 m away from the casing, respectively, to simulate the situation of drilled wells around the drilling in progress. Manually rotate the probe to simulate the rotation of the drill string. Record and save the data

(4) Replace the position and repeat step (3)

(5) Change the position. Align the probe with the casing coupling, and repeat step (3)

(6) Place the probe and casing at angles of 10°, 20°, 30°, 40°, 50°, 60°, 70°, 80°, and 90°, respectively. The equipment is 1 m away from the casing to simulate that there are drilled wells around the drilling well. Manually rotate the probe to simulate the rotation of the drill string

(7) Change the distance between the probe and the casing to 2 m, and repeat step (6)

5. Experimental Results

5.1. Feasibility of Measuring Principle. The height of the casing was 0.35 m from the ground, and the axis of the probe was 0.25 m from the ground. When the rotation angle of the probe was 0°, the magnetic source axis at both ends of the probe was perpendicular to the ground, as shown in Figure 8. When the experiment probe was 21 m and 2 m away from the casing, respectively, the data obtained by the software was shown in Figure 9.

When the experiment probe was 21 m away from the casing, the magnetic field intensity changes little during the process of the probe rotating one circle, and there were no obvious wave crests and troughs. When the probe was 2 m away from the casing, although there were many data burrs during the process of the probe rotating one circle, it could be clearly seen that there was a peak and a trough in the magnetic field strength data. When the probe is 2 m away from the casing, the probe rotated to 96° and 276°, and the axis of the magnetic source just passed through the casing. In theory, the peak or trough should be detected at this time. The wave crests and wave troughs occurred exactly at the positions corresponding to these two angles. It proved the feasibility of the distance measurement principle of the electromagnetic anticollision tool while drilling in cluster wells.

5.2. Measuring Algorithm Accuracy Results

5.2.1. The Probe Was Placed Parallel to the Casing. Three points on the casing were selected as the measuring points. The position distribution of the three measuring points on the casing was shown in Figure 10. The measuring point 1 and measuring point 2 were different positions on the two casings, and measuring point 3 was the coupling position of the two casings.

After selecting the measuring points, the probe was placed in parallel with the casing. The probe was 0.5 m, 1 m, 2 m, 3 m, 4 m, and 5 m away from the casing. Six sets of data were measured, and the peak value, valley value, and the corresponding angle of the three measurement points were input into the data analysis software for calculation (Figures 11–13).

When the probe and the casing were placed in parallel, and the distance between the probe and the casing was 0.5~3 m, the calculation result was more accurate. The

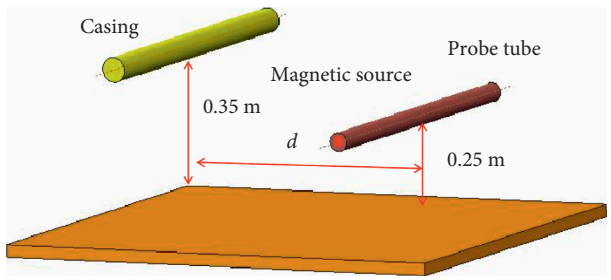

Figure 8: Position relationship between the probe and the casing.

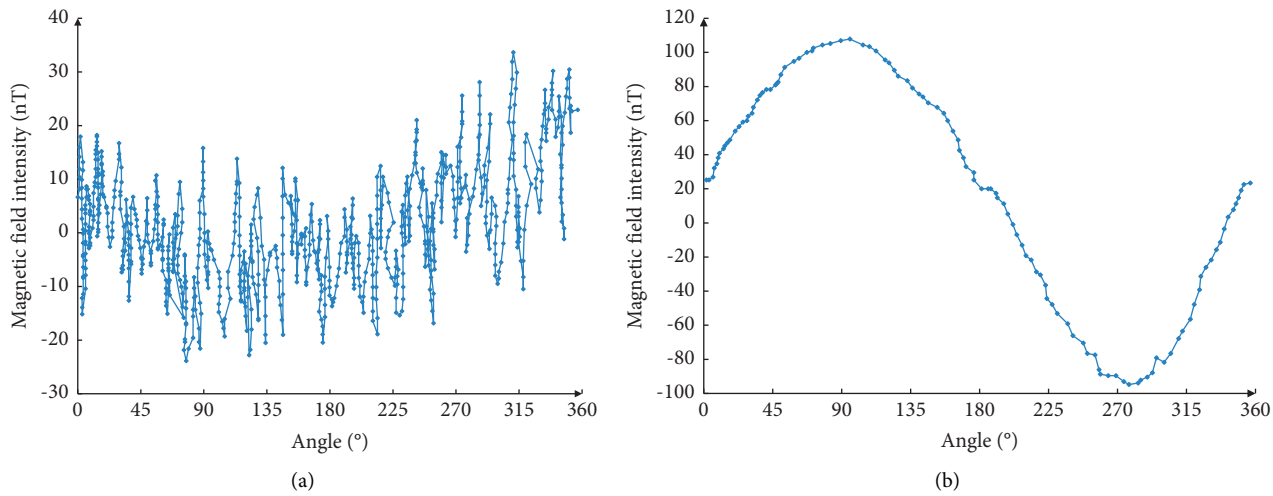

Figure 9: Simulation data when the distance from the probe to the casing is (a) $d = 21$ m and (b) $d = 2$ m.

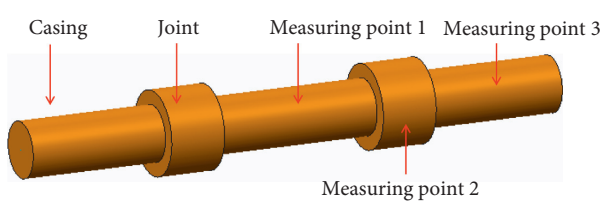

Figure 10: Selection of experiment position.

distance error and the angle error were both within 10%. When the distance between the probe and the casing exceeded 3 m, the error became larger and the signal became chaotic. The reason was that the tool currently only used two magnetic sources. When the distance was far away, the magnetic field strength signal was weak. At the same time, it was affected by the background noise of the circuit board, and the signal-to-noise ratio was low. The noise signal affected the peak magnetic field strength data, and it led to a larger calculation error.

Because the alternating magnetic field signals shielded the influence of the geomagnetic field and the remanence of the casing, different detection positions had relatively little influence on the measurement results of the magnetic field strength of the probe. However, due to the different diameters of the collar and casing, the existence of a step had a certain impact on the magnetic field strength measurement data. It may cause large deviations in the calculation results. Therefore, the position of the casing coupling should be avoided as far as possible during the actual measurement.

5.2.2. The Probe and the Casing Were Placed at a Certain Angle. The probe and the casing were placed at a certain angle, and the position of measuring point 1 was selected for the experiment. The distance between the probe and the casing was 1 m, and the peak value, valley value, and the corresponding angle of point 1 were input into the data analysis software for calculation. The calculation results were shown in Table 3.

When the distance between the probe and the casing was 2 m, the calculation results of different angles were shown in Table 4. Regardless of the distance, when the included angle between the normal drilling and the adjacent well was about 80°, the trend of the magnetic induction data detected by the probe had changed suddenly (Figure 14). When the included angle between the positive well and the adjacent well was large, the magnetic field generated by the magnetic source far away from the casing in the probe was too small. The direction of the magnetic pole of the magnetic source also pointed to the distance of the casing; it was equivalent to that only one magnetic source in the probe had magnetized the casing. The distribution of the magnetic field line had changed, and it resulted in a sudden change in the curve. When the included angle between the drilling well and the adjacent well changed from 0° to about 50°, the magnetic

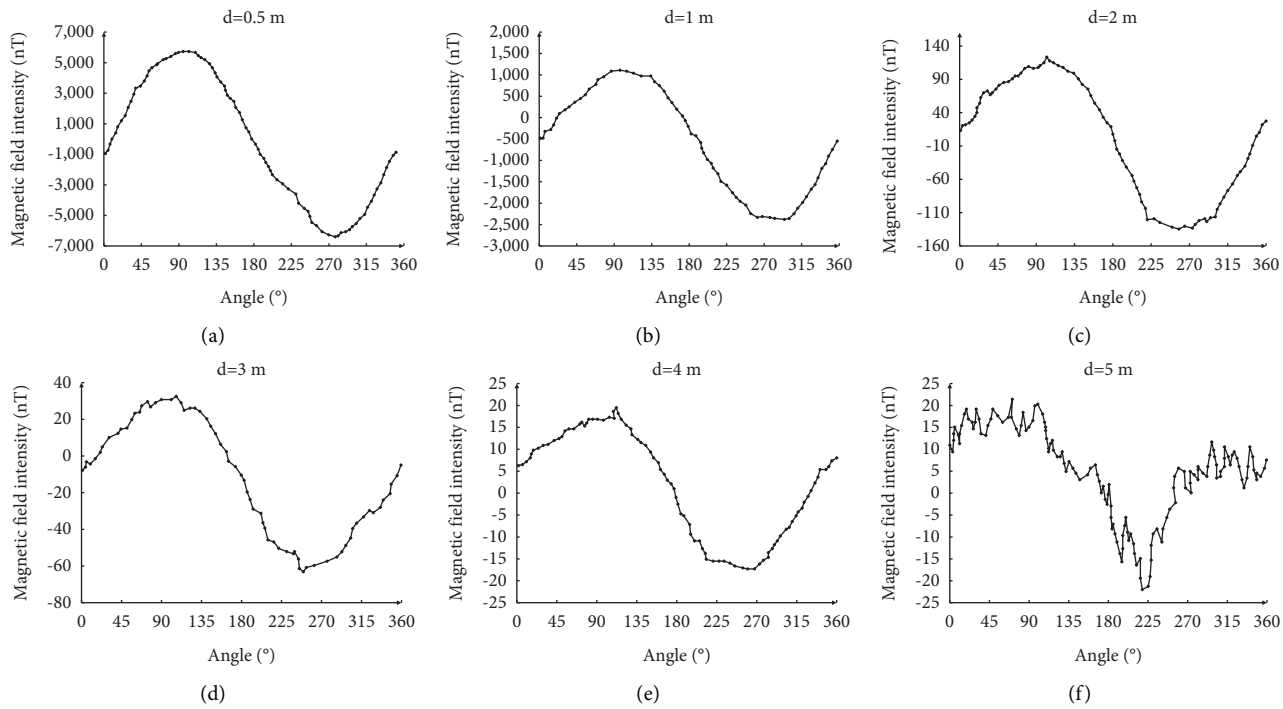

Figure 11: Calculation result of measuring point 1. (a) $d = 0.5$ m. (b) $d = 1$ m. (c) $d = 2$ m. (d) $d = 3$ m. (e) $d = 4$ m. (f) $d = 5$ m.

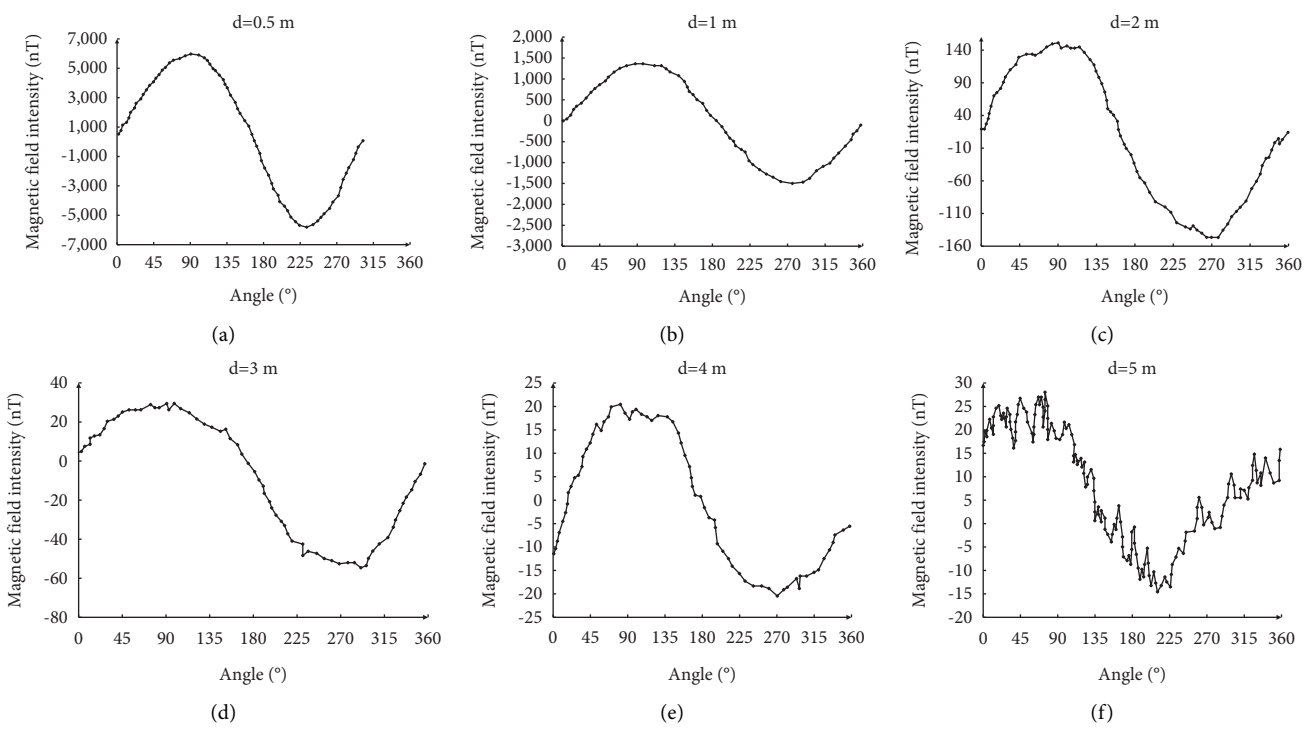

Figure 12: Calculation result of experiment point 2. (a) $d = 0.5$ m. (b) $d = 1$ m. (c) $d = 2$ m. (d) $d = 3$ m. (e) $d = 4$ m. (f) $d = 5$ m.

induction data detected by the probe had been basically reduced to half of the original. At this time, the collected signal had been relatively weak.

When the angle between the two magnetic sources exceeded 50°, the distribution of the magnetizing magnetic field generated by the two magnetic sources on the probe changed, so the error increased. Therefore, this tool was mainly suitable for the well section of which the angle between the two wells is within 50°. When the angle between the probe and the casing exceeded 50°, it was best to choose

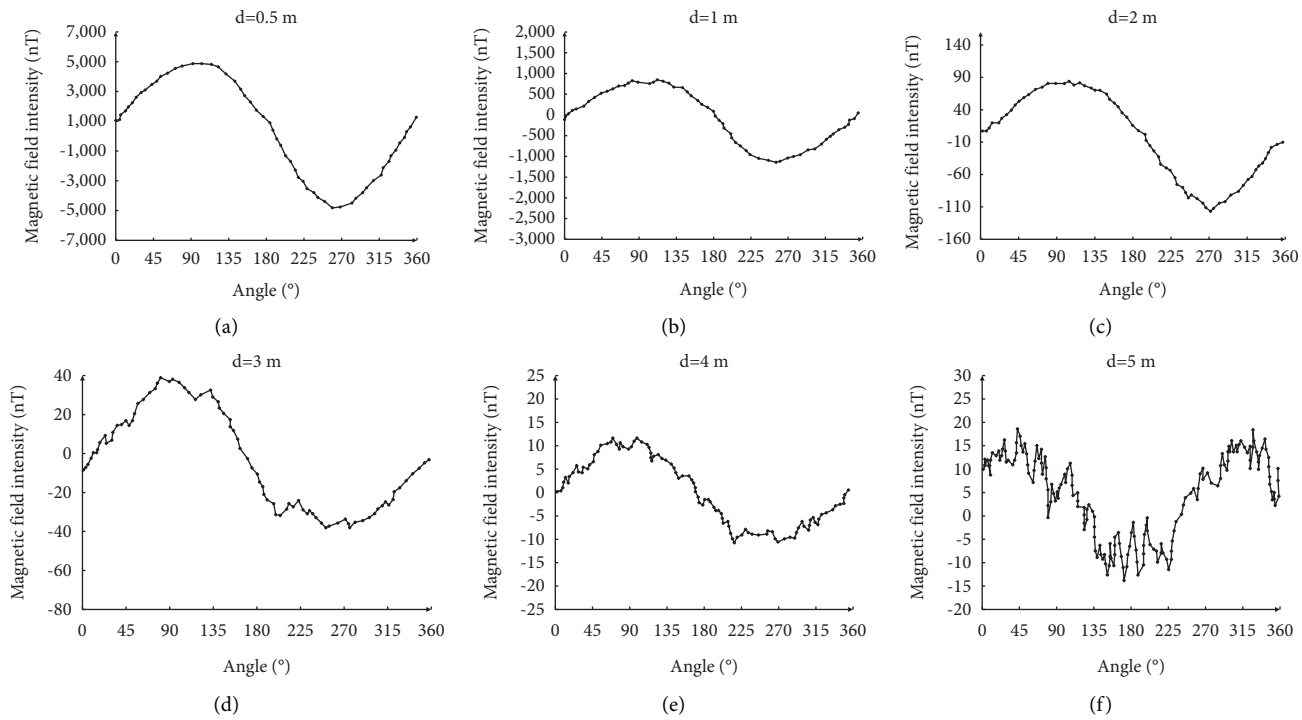

Figure 13: Calculation result of experiment point 3. (a) $d = 0.5$ m. (b) $d = 1$ m. (c) $d = 2$ m. (d) $d = 3$ m. (e) $d = 4$ m. (f) $d = 5$ m.

Table 3: Calculation result of different angles when the distance from sensor to casing is 1 m.

Angle (°)	Theory angle (°)	Peak (nT)	Peak angle (°)	Valley (nT)	Valley angle (°)	Calculation distance (m)	Calculation angle (°)	Distance error (%)	Angle error (°)
10	95	1292.1	97.3	−1033.4	271.2	0.92	97.5	8	2.5
20	95	1000.5	103.5	−1102	262	1.062	102.7	6.2	7.7
30	95	1025.2	103.7	−988.2	268.4	1.048	103.5	4.8	8.5
40	95	1005.4	104.8	−1010.2	270.5	0.958	103.2	4.2	8.2
50	95	998	104.2	−792.2	268.4	0.931	104.3	6.9	9.3
60	95	805.4	92.8	−810.1	273.9	0.822	92.9	17.8	2.1
70	95	538.2	110.4	−508.4	270.5	0.795	109.8	20.5	14.8
80	95	263.4	112.5	−336.2	281.3	0.788	110.2	21.2	15.2
90	95	383.5	134.2	−321.3	287.8	0.811	108.2	18.9	13.9

Table 4: Calculation result of different angles when the distance from sensor to casing is 2 m.

Angle (°)	Theory angle (°)	Peak (nT)	Peak angle (°)	Valley (nT)	Valley angle (°)	Calculation distance (m)	Calculation angle (°)	Distance error (%)	Angle error (°)
10	92	150.1	98.2	−146.8	268.1	2.151	98.8	7.6	6.8
20	92	120.5	101.4	−142.4	265.7	1.834	101.1	8.3	9.1
30	92	108.9	100.2	−108.7	264.2	1.91	99.5	9	7.5
40	92	101.5	99.6	−105.4	262.7	1.935	97.7	6.5	5.7
50	92	100.1	101.7	−78.9	269.1	1.822	101.2	8.9	9.2
60	92	72.7	85.7	−86.4	264.8	1.954	84.8	4.6	7.2
70	92	52.7	103.5	−50.1	271.3	1.809	102.8	19.1	10.8
80	92	48.9	105.8	−61.1	258.5	2.371	112.5	18.6	20.5
90	92	50.4	112.1	−55.6	281	1.929	111.2	7.1	19.2

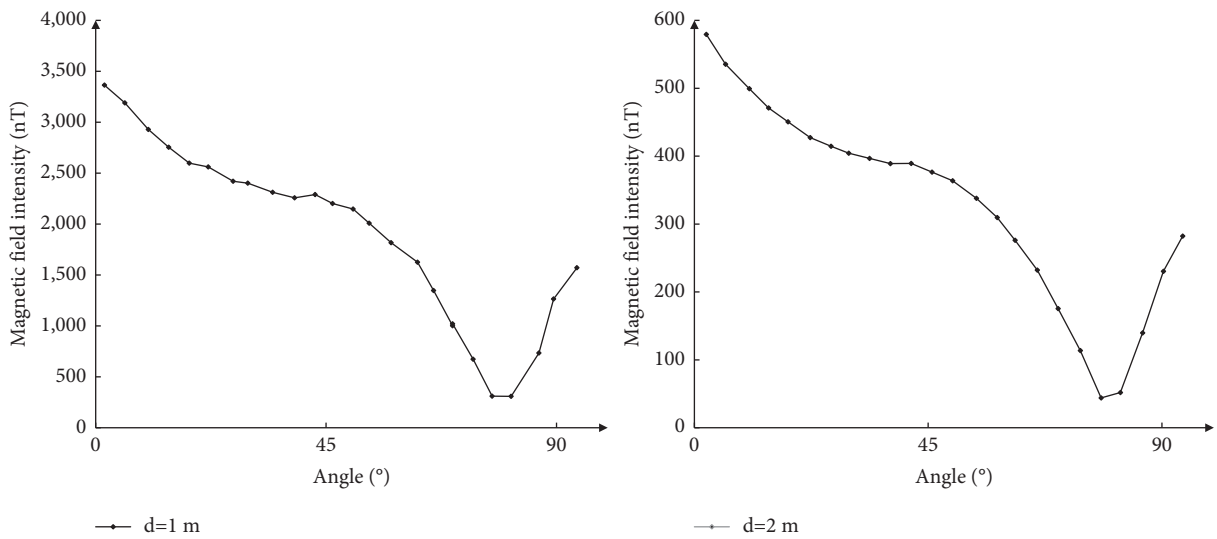

Figure 14: Effect of the angle between drilling well and adjacent well on measurement results.

other types of anticollision tools for the distance measurement and guidance.

6. Conclusion

To verify the accuracy of the electromagnetic anticollision measuring while drilling steering algorithms, a self-developed set of experimental prototypes of adjacent wells of electromagnetic measuring anticollision tools while drilling was used to conduct simulation experiments.

(1) When there was a casing around the probe, there was a peak and a trough in the data. The position of the peak and trough appeared at the moment when the axis of the magnetic source on the probe was directly opposite to the casing

(2) When the probe and the casing were placed in parallel, the distance between the probe and the casing was within 0.5~3 m, and the system could calculate the distance and azimuth information of the adjacent well more accurately. However, due to the weak magnetic field strength of the current magnetic source, the calculation result error increased when the distance exceeded 3 m

(3) Because the alternating magnetic field signal shielded the influence of the Earth's magnetic field and the remanence of the casing, different detection positions had relatively little influence on the measurement results of the probe. However, the casing coupling had a certain impact on the magnetic field, and it caused large deviations in the calculation results. Therefore, the position of the casing coupling should be avoided as far as possible during the actual measurement

Data Availability

The data used to support the findings of this study are available from the corresponding author upon request.

Conflicts of Interest

The authors declare that they have no conflicts of interest.

Acknowledgments

The work was supported by the Natural Science Foundation of China (NSFC, 52104014), the Dongying Science Development Fund (DJ2020005), and the team construction project of the Young Innovative Talents Inducing and Cultivating Program of Shandong Province (Research and Innovation Team of Complex Oil and Gas Well Drilling Engineering).

References

[1] M. Z. Lukawski, B. J. Anderson, C. Augustine et al., "Cost analysis of oil, gas, and geothermal well drilling," *Journal of Petroleum Science and Engineering*, vol. 118, pp. 1–14, 2014.

[2] O. E. Emmanuel, D. Adewale, and S. E. Iyuke, "Data on cost analysis of drilling mud displacement during drilling operation," *Data in Brief*, vol. 19, pp. 535–541, 2018.

[3] Y. Wang, B. Hou, D. Wang, and Z. Jia, "Features of fracture height propagation in cross-layer fracturing of shale oil reservoirs," *Petroleum Exploration and Development*, vol. 48, no. 2, pp. 469–479, 2021.

[4] H. Wang, Y. Xu, H. Zheng et al., "Monitoring and analysis of millisecond laser drilling process and performance with and without longitudinal magnetic assistance and/or assist gas," *Journal of Manufacturing Processes*, vol. 48, pp. 297–312, 2019.

[5] S. Zhang, B. Diao, and D. Gao, "Numerical simulation and sensitivity analysis of accurate ranging of adjacent wells while drilling," *Journal of Petroleum Science and Engineering*, vol. 195, Article ID 107536, 2020.

[6] B. Hou, Y. F. Dai, C. L. Zhou, K. P. Zhang, and F. Liu, "Mechanism study on steering acid fracture initiation and propagation under different engineering geological conditions," *Geomechanics and Geophysics for Geo-Energy and Geo-Resources*, vol. 7, no. 3, pp. 1–14, 2021.

[7] K. P. Zhang, B. Hou, M. Chen, C. L. Zhou, and F. Liu, "Fatigue acid fracturing: a method to stimulate highly deviated and horizontal wells in limestone formation," *Journal of Petroleum Science and Engineering*, vol. 208, Article ID 109409, 2022.

[8] D. Nyqvist, C. Durif, M. G. Johnsen, K. D. Jong, and L. D. Sivle, "Electric and magnetic senses in marine animals, and potential behavioral effects of electromagnetic surveys," *Marine Environmental Research*, vol. 155, Article ID 104888, 2020.

[9] Q. Zhang, B. Hou, B. Lin, X. Liu, and Y. Gao, "Integration of discrete fracture reconstruction and dual porosity/dual permeability models for gas production analysis in a deformable fractured shale reservoir," *Journal of Natural Gas Science and Engineering*, vol. 93, Article ID 104028, 2021.

[10] C. Chen and H. Sun, "Characteristic analysis and optimal survey area definition for semi-airborne transient electromagnetics," *Journal of Applied Geophysics*, vol. 180, Article ID 104134, 2020.

[11] Z. Wu, D. Gao, and B. Diao, "An investigation of electromagnetic anti-collision real-time measurement for drilling cluster wells," *Journal of Natural Gas Science and Engineering*, vol. 23, pp. 346–355, 2015.

[12] A. M. Al-Bahlani and T. Babadagli, "SAGD laboratory experimental and numerical simulation studies: a review of current status and future issues," *Journal of Petroleum Science and Engineering*, vol. 68, no. 3, pp. 135–150, 2009.

[13] B. B. Diao, D. L. Gao, and Z. Y. Wu, "Magnet ranging calculation method of twin parallel horizontal wells steerable drilling," *Journal of China University of Petroleum*, vol. 35, no. 6, pp. 71–75, 2011.

[14] D. Gao, B. Diao, Z. Wu, and Y. Zhu, "Research into magnetic guidance technology for directional drilling in SAGD horizontal wells," *Petroleum Science*, vol. 10, no. 4, pp. 500–506, 2013.

[15] Z. Guan, Y. Liu, Y. Shi et al., "Problems and developing direction of anti-collision technology in the dense well pattern area," *Procedia Engineering*, vol. 7, pp. 304–311, 2010.

[16] Z. Y. Guo, D. J. Liu, and Y. X. Luo, "Error analysis of magnetic field calculation using magnetic dipole based on circular current," *International Journal of Applied Mathematics & Stats*, vol. 51, no. 24, pp. 121–130, 2013.

[17] Z.-Y. Guo, D.-J. Liu, Q. Pan, and Y.-Y. Zhang, "Forward modeling of total magnetic anomaly over a pseudo-2D underground ferromagnetic pipeline," *Journal of Applied Geophysics*, vol. 113, pp. 14–30, 2015.

[18] K. M. Churchill, C. Link, and C. C. Youmans, "A comparison of the finite-element method and analytical method for modeling unexploded ordnance using magnetometryfinite-element method and analytical method for modeling unexploded ordnance using magnetometry," *IEEE Transactions on Geoscience and Remote Sensing*, vol. 50, no. 7, pp. 2720–2732, 2012.

[19] T. Liu and B. Wang, "Study of magnetic ranging technology in horizontal directional drilling," *Sensors and Actuators A: Physical*, vol. 171, no. 2, pp. 186–190, 2011.

[20] G. Liu, Q. Z. Yang, Z. X. Dong, B. S. He, and Z. L. Geng, "A drill bit vibration anti-collision monitoring system and field experiment," *Natural Gas Industry*, vol. 33, no. 6, pp. 66–70, 2013.

[21] G. P. Lousberg, J.-F. Fagnard, J. G. Noudem, M. Ausloos, B. Vanderheyden, and P. Vanderbemden, "Measurement of the magnetic field inside the holes of a drilled bulk high-Tcsuperconductorfield inside the holes of a drilled bulk high-Tc superconductor," *Superconductor Science and Technology*, vol. 22, no. 4, Article ID 045009, 2009.

[22] Y. C. Shi, D. Y. Jia, Z. C. Guan, and Y. Q. Xu, "A theoretical model of residual magnetic field around a pre-magnetized casing string," *Energies*, vol. 13, no. 16, Article ID 4226, 2020.

[23] M. Marchetti, V. Sapia, and A. Settimi, "Magnetic anomalies of steel drums: a review of the literature and research results of the INGV," *Annals of Geophysics*, vol. 56, no. 1, pp. 1–12, 2013.

[24] V. Sanchez, Y. G. Yaoguo Li, M. N. Nabighian, and D. L. Wright, "Numerical modeling of higher order magnetic moments in UXO discrimination," *IEEE Transactions on Geoscience and Remote Sensing*, vol. 46, no. 9, pp. 2568–2583, 2008.

[25] S. D. Billings, C. Pasion, S. Walker, and L. Beran, "Magnetic models of unexploded ordnance," *IEEE Transactions on Geoscience and Remote Sensing*, vol. 44, no. 8, pp. 2115–2124, 2006.

[26] B. Tu, D. S. Li, E. H. Lin, B. Luo, and Y. Z. Wang, "Analysis of drilling parallel horizontal twin wells rotating magnetic beacons magnetic field strength size in SAGD," in *Proceedings of the PIERS 2010 Cambridge - Progress in Electromagnetics Research Symposium*, vol. 7, pp. 5–8, Cambridge, MA, USA, July 2010.

[27] D. G. Wang and D. L. Gao, "Study of magnetic vector guide system in tubular magnet source space," *Acta Petrolei Sinica*, vol. 29, no. 4, pp. 608–611, 2008.

[28] W. A. Yang, C. Hu, M. Li, M. Q.-H. Meng, and S. Song, "A new tracking system for three magnetic objectives," *IEEE Transactions on Magnetics*, vol. 46, no. 12, pp. 4023–4029, 2010.

[29] Z. Y. Zhang, C. H. Xiao, J. J. Gao, and G. H. Zhou, "Experiment research of magnetic dipole model applicability for a magnetic object," *Yingyong Jichu yu Gongcheng Kexue Xuebao/Journal of Basic Science and Engineering*, vol. 18, no. 5, pp. 862–868, 2010.

[30] K. Wang, Y. Hu, K. Yang et al., "Experimental evaluation of rock disintegration detection in drilling by a new acoustic sensor method," *Journal of Petroleum Science and Engineering*, vol. 195, Article ID 107853, 2020.

Hindawi
Geofluids
Volume 2022, Article ID 2531181, 8 pages
https://doi.org/10.1155/2022/2531181

Research Article

Simulation and Experimental Study on Characteristics of Multiorifice Nozzle in Radial Jet Drilling

Tao Zhang,[1,2] Yumei Li,[1] Hui Lu,[3] and Jianing Jiang[2]

[1]*Beijing Key Laboratory of High Dynamic Navigation Technology, Beijing Information Science & Technology University, Beijing 100101, China*
[2]*High Dynamic Automation Technology Hejian Co., Ltd., Hejian 062450, China*
[3]*CNPC Tarim Oilfield Branch, Korla 841001, China*

Correspondence should be addressed to Yumei Li; liyumei3680238@163.com

Received 19 August 2021; Revised 23 November 2021; Accepted 8 December 2021; Published 10 January 2022

Academic Editor: Bing Hou

The radial jet drilling (RJD) is a key technology to improve the development efficiency of low-permeability oil and gas resources. In order to seek a reasonable hydraulic engineering parameter combination of hydraulic radial jet drilling, to obtain the optimal hydraulic energy distribution, a jet radial horizontal drilling simulation experiment system of the casing windowing is designed. A sequence of experimental investigations focused on engineering parameters of pump displacement, rotating speed, and frequency of high-pressure plunger pump is performed, and the operability and the feasibility of the experiment are verified. To evaluate the maximum drillable length and the self-propelled force of a jet nozzle, a 3D numerical model based on ANSYS-CFX is developed to evaluate the effects of the inlet flow displacement, the flow rates ratio K, and the angle ratio $F : B$ of the forward orifice and backward orifice of the jet nozzle on its maximum drillable length and self-propelled force by sensitivity analysis. Finally, the comparison of numerical simulation results (Ln), mathematical results (Lm), and experiment results (Le) of the maximum drillable length are presented. It is observed that the simulation results are consistent with the experiment results with an average accuracy of 97.07%. Therefore, the proposed numerical model has a good performance in predicting the maximum drillable length of the multiorifice nozzle. The research results can provide theoretical guidance for improving the rock breaking and drilling capability of radial jet drilling technology.

1. Introduction

Radial jet drilling (RJD) technology was imposed in the 1980s [1]. In the exploration of oil and gas wells, the application of radial jet drilling (RJD) technology can effectively reduce drilling costs for the unconventional oil and gas wells, abandoned renovation wells, and geothermal development wells, especially the exploration or development wells with poor fracturing effects [2–5]. Additionally, the RJD technology has been growing in applications aimed to increase the oil well drainage area and reduce the pore pressure of the reservoir for the low-permeability reservoirs and significantly increased reservoir production [6].

The hydraulic radial jet drilling technology mainly includes two processes: casing windowing and radial jet drilling. One of the cores is the casing windowing technology. Whether the radial jet drilling can be successfully completed depends on the casing windowing. The success of casing windowing directly affects the subsequent channel construction of radial horizontal wells. In the process of the casing windowing, it is necessary to use the blade bit to drill a microwellbore about 25 mm on the inside of the casing and then to connect the high-pressure hose with a coiled tubing. The high-pressure fluid is sprayed through the jet nozzle to penetrate the rock layer to form a tiny horizontal wellbore with a length of about 100 m and a diameter of

about 50 mm, whose radius of curvature is much smaller than that of conventional well [7, 8]. The radial oil and gas passages break through the near-well reservoir pollution zone and establish multiple diversion channels for the far-well zone, increasing well production. To obtain larger self-propelled force to pull the hose forward, the jet nozzle design is of great importance when selecting bottom-hole drilling tools. The casing window drilling tool assembly structure is shown in Figure 1.

In recent years, the application of the radial jet drilling (RJD) technology is increasingly investigated to stimulate low performing wells, such as geothermal wells and coalbed methane [9–11]. Chi et al. calculated the maximum drillable length of jet nozzle by theoretical analysis and experiments [12]. Li and Zhang developed a 3D numerical model based on ANSYS-CFX to investigate the self-propelled ability of a multiorifice nozzle, remarkably the effects of the physical parameters of the multiorifice nozzle on its self-propelled ability by sensitivity analysis [13]. Wang et al. conducted the experimental study of the NGH, and focusing on the effects of traverse jetting speed, jetting flow rate on rock breaking was studied [14]. Yang analyzed the effects of the jet velocity, distance, and saturation on the NGH sediment by experiment and simulation [15]. Wang et al. developed an engineering construction chart for solid fluidization well through jet experiments [16]. Liao et al. conducted the rock-breaking experiments of the self-propelled jetting efficiency and developed a numerical model of the self-propelled force of multiorifice nozzles [17]. For all the above studies, the optimization design of hydraulic parameters of radial horizontal wells and conventional drilling technologies are different in terms of optimization objectives and constraints. The existing hydraulic parameter design methods are not applicable to radial horizontal well technology.

In this paper, a jet radial horizontal drilling simulation experiment system of the casing windowing is designed, and the reasons for not opening window in the experiment are analyzed. To evaluate the maximum drillable length and the self-propelled force of a multiorifice nozzle, a 3D numerical model of the nozzle is established based on ANSYS-CFX. A sequence of simulations are develop to investigate the effects of the inlet flow displacement, the flow rates ratio K, and the angle ratio $F : B$ of the forward orifice and backward orifice of the jet nozzle on its maximum drillable length and self-propelled force by a series of sensitivity analysis. The design method of hydraulic parameters for radial horizontal drilling is proposed, which provides theoretical support for the application of radial horizontal well technology.

2. The Mathematical Model

2.1. Calculation of Self-Propelled Force. The recoil force that pushes the nozzle forward is obtained by the kinetic energy theorem of the nozzle outlet section [18].

$$F\Delta t = mv_2 - mv_1, \tag{1}$$

where F—the force on per unit volume, N;

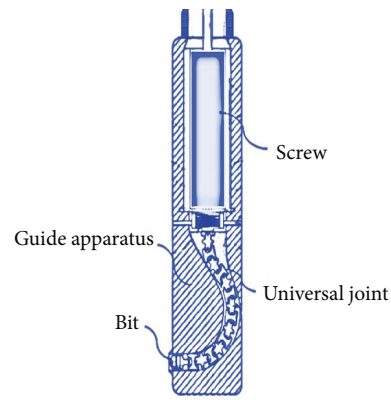

Figure 1: The casing window drilling tool assembly structure.

Δt—the time on per unit volume of fluid, s;

m—the mass of the fluid per unit volume, kg;

V_1—the average flow velocity in the nozzle outlet section, m/s;

V_2—the average flow velocity outside the nozzle outlet section, m/s.

According to the principle that the acting force is equal to the reaction force, F in the above formula is the jet recoil force F_z. It is known as $m/\Delta t = \rho d$, assuming that the flow path of jet nozzle is circular, according to the continuity equation between the outlet sections of jet nozzle, i.e., $A = \pi d^2/4$, it is obtained:

$$F_z = \rho q v_2 \left[1 - \left(\frac{d_2}{d_1}\right)^2\right], \tag{2}$$

where $(d_2/d_1)^4 \leq 1$

Simplified expression of jet velocity at jet nozzle outlet:

$$v = 44.77\sqrt{p}, \tag{3}$$

where P—the jet pressure, MPa;

V—the jet flow rate, m/s.

Substituting (3) into Equation (2), and finally,

$$F_z = 0.745q\sqrt{p}, \tag{4}$$

where F_z—the recoil force of water flow, N;

q—the jet flow, L/min.

Substituting the formula into Equation (4) yields another expression:

$$F_z = 1.56d^2p, \tag{5}$$

where d—the outlet diameter of the nozzle, mm.

The expression of recoil force is:

$$F_f = n_1 1.56 p {d_1}^2 \cos\theta_1, \tag{6}$$

where n_1—the number of backward orifices;
θ_1—the angle of the backward orifices, °;
d_1—the diameter of the backward orifices, mm.
The expression of rock breaking force is:

$$F_p = n_2 1.56 p d_2^2 \cos\theta_2, \tag{7}$$

where F_P—the breaking rock force, N;
n_2—the number of forward orifices;
θ_2—the angle of the forward orifices, °;
d_2—the diameter of the forward orifices, mm.
The self-propelled force of the multiorifice nozzle is expressed as:

$$F_t = F_z - F_p. \tag{8}$$

2.2. The Maximum Drillable Length. In the process of hydraulic jet rock breaking, the viscosity of the high-pressure hose wall is not considered. Assume that the friction force of the jet nozzle in the horizontal direction is F_w, the friction force at the radial borehole wall is F_f. The resultant force in the horizontal direction of radial jet drilling system is calculated as

$$F_{\text{pull}} = F_z - F_p - F_w - F_f, \tag{9}$$

where

$$F_f = \mu M g + \mu q_h g l. \tag{10}$$

In the above formula, μ is the sliding friction factor of the wellbore and wall; l is the penetration depth of the high-pressure hose, m; M is the mass of the jet nozzle, kg; q_h is the mass of the high-pressure hose line, kg/m; g is the gravitational acceleration, N/kg.

Assuming the jet nozzle is placed horizontally,

$$\frac{d}{dt}\left[(M + l q_n) v\right] = F_z - F_p - F_w - F_f, \tag{11}$$

where v is the drilling speed, m/s.

For convenience, define a length coordinate:

$$x = \frac{l + M}{q_h} = l + l_0, \tag{12}$$

where x is the extension length, m; l_0 is the equivalent length of the jet nozzle, m.

It is assumed that the frictional force F_w experienced by the high-pressure hose is a fixed value and can be determined experimentally. Since $F = F_f + F_p$, F can be written as:

$$F = \mu M g + \mu q_h g l + \eta(l + l_0). \tag{13}$$

According to formula (12),

$$F = \mu q_h g (M/q_h) + \eta(l + l_0) = (\mu q_h g + \eta) x. \tag{14}$$

In Equation (14), η is the coefficient of friction resistance, N/m.

$$\mu q_h g + \eta. \tag{15}$$

Assume Equation (14) can be simplified to:

$$F = kx, \tag{16}$$

where k is the combined friction coefficient, N/m.

In combination with Equations (11), (12), (14), and (15), we can obtain:

$$\frac{d}{dt}(q_h x v) = F_z - kx - 20, \tag{17}$$

$$\frac{q_h}{2}\frac{d}{dt}(xv)^2 = (F_z - kx - 20)x. \tag{18}$$

Initial conditions of a given jet nozzle: $x|_{t=0} = l_0, v|_{t=0} = v|_{x=l_0} = 0$.

Integrate Equation (18) to obtain the motion equation:

$$\frac{q_h}{2}(xv)^2 = (F_z - 20)\left(x^2 - l_0^2\right) - \frac{k}{3}\left(x^3 - l_0^3\right). \tag{19}$$

Equation (19) can be written:

$$\frac{q_h}{2}(xv)^2 = \left(n\rho Q_j v_j \cos\theta_j - m\rho Q_i v_i \cos\theta_i - \frac{\pi}{4} d_i^2 m p_{\text{out}} - 20\right) \cdot \left(x^2 - l_0^2\right) - \frac{k}{3}\left(x^3 - l_0^3\right), \tag{20}$$

where Q_i is the flow of the ith forward orifice, L/s, Q_j is the flow of the jth backward orifice, L/s; v_i is the jet velocity of the ith forward orifice, m/s, v_j is the jet velocity of the jth backward orifice, m/s; θ_i is the angle of forward orifice, °; and θ_j is the angle of backward orifice, °.

Assuming that the value of $k = 0.87$ N/m, we get:

$$\frac{\left(n\rho Q_j v_j \cos\theta_j - m\rho Q_i v_i \cos\theta_i - (\pi/4) d_i^2 m p_{\text{out}} - 20\right)\left(x^2 - 0.25\right) - 0.29\left(x^3 - 0.125\right)}{q_h x^2}. \tag{21}$$

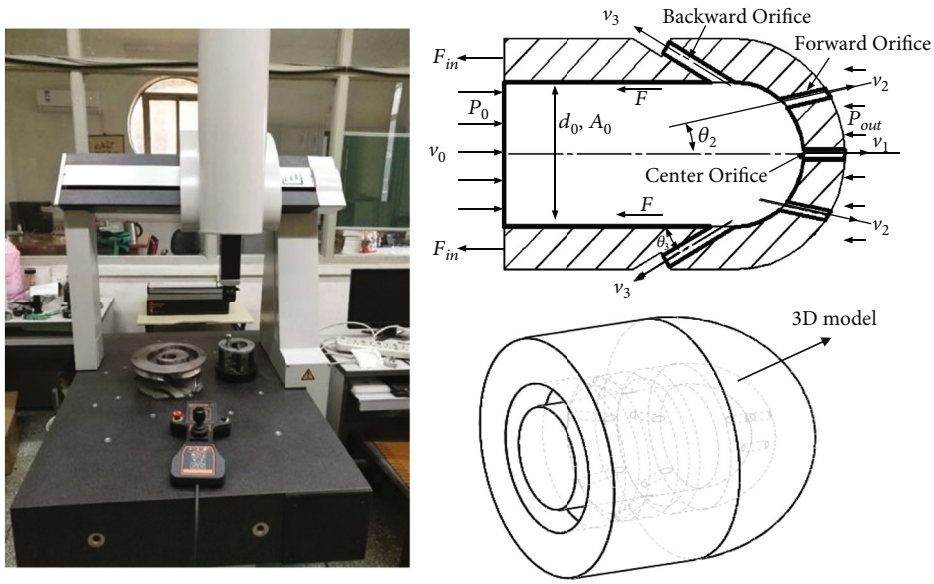

Figure 2: The 3D physical geometry model of the nozzle through three-coordinate measuring instrument.

When $v = 0$, the maximum drillable length can be expressed as follows:

$$X = \frac{n\rho Q_j v_j \cos\theta_j - m\rho Q_i v_i \cos\theta_i - (\pi/4) d_i^2 m p_{\text{out}} - 20}{0.29}. \tag{22}$$

3. Numerical Simulation

3.1. Geometry and Boundary. The multiorifice nozzle is the "core" of radial jet drilling (RJD) technology, especially the geometric design of the nozzle will have a greater impact on hydraulic parameters. The measuring instrument (CROMA, Hexagon, Sweden) is used to carry out the mapping design of the multiorifice nozzle. The 3D physical geometry model of the nozzle is shown in Figure 2 [9]. The diameter of the jet nozzle is 25 mm, the total length is 17.5 mm, the inner diameter is 8.6 mm, the outer diameter is 12.5 mm, the diameter of front orifice is 0.5 mm, the diameter of backward orifice is 0.7 mm; and the inlet ambient pressure $P = 30$ MPa, inlet flow rate Q_0. The flow field model of the jet nozzle is segmented by 3D modeling software, and then, the meshing model of multiorifice nozzles was established by ICEM (as shown in Figure 3). The boundary conditions of the inlet, outlet, and wall of the jet nozzle are set in the simulation of flow field characteristics. After setting the boundary conditions, the discrete format and relaxation factor are adjusted.

3.2. Sensitivity Analysis. In this simulation, the inlet flow rate Q_0 is set to 25 L/min, 35 L/min, 45 L/min, and 55 L/min, and multiple simulation models are established. Figure 4 shows the streamline diagram of velocity vector of jet nozzle. The jet velocity distribution diagram of forward orifice under different inlet displacement is shown in Figure 5. The jet velocity distribution diagram of backward orifice under different inlet flow displacement is shown in Figure 6. In the entire simulation, the maximum jet velocity is distributed near the forward orifices and backward orifices where there is a larger pressure difference.

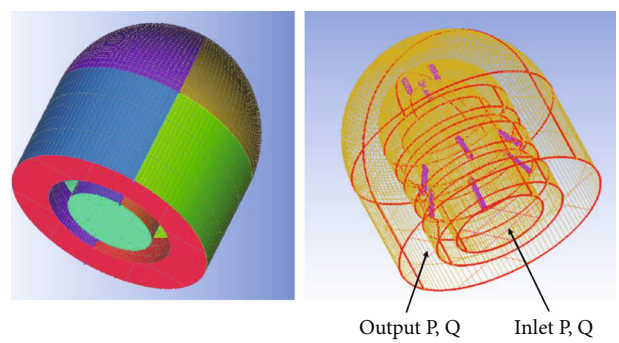

Figure 3: The meshing model of multiorifice nozzle.

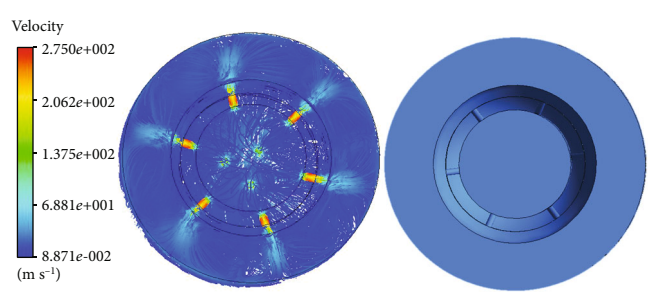

Figure 4: The streamline diagram of velocity vector of jet nozzle $(F + B)$: 3 + 5.

A series of simulations of the inlet flow displacement on the maximum flow rate of forward orifices and backward orifices of jet nozzle were investigated (as shown in Figure 7). When the inlet displacement $Q = 25$ L/min, the velocity of backward orifice is 162.4 m/s, the velocity of

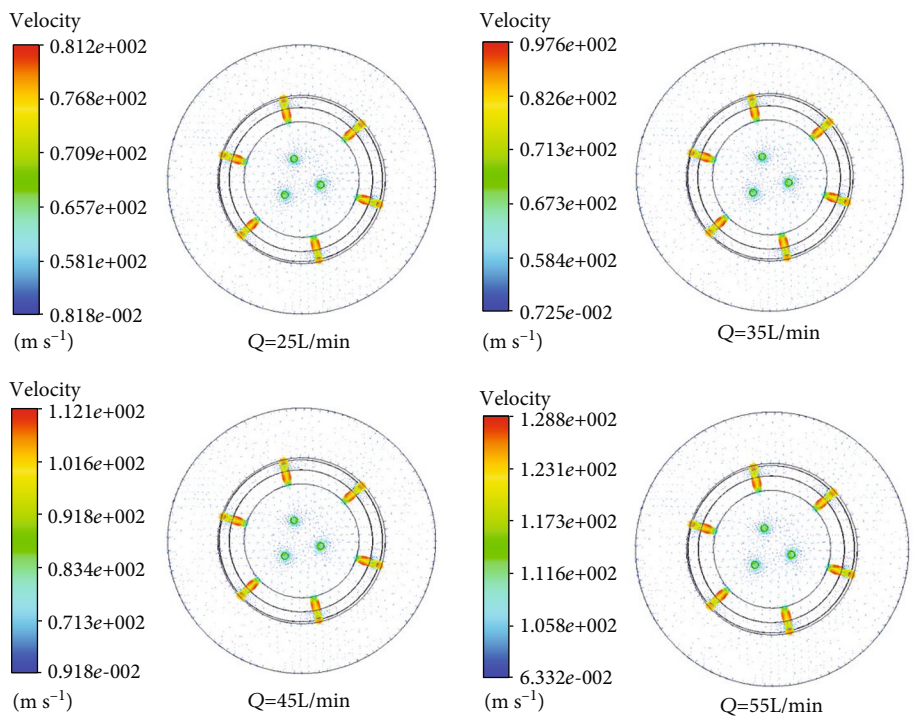

Figure 5: The jet velocity distributions of forward orifice under different inlet displacement.

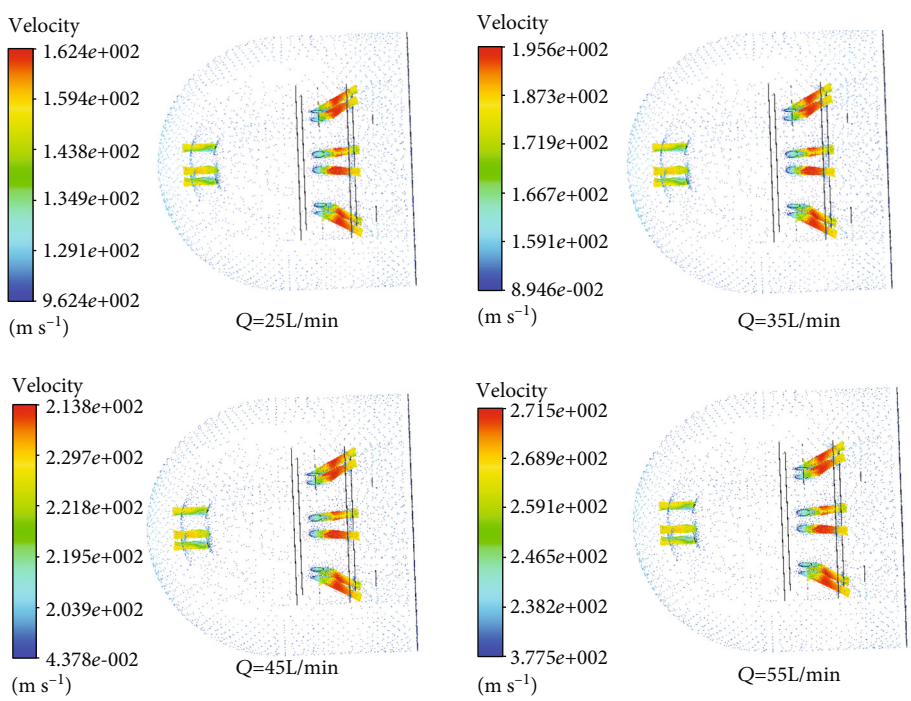

Figure 6: The jet velocity distributions of backward orifice under different inlet displacement.

forward orifice is 81.2 m/s, and the maximum flow rate is 199.8 m/s. It is observed that both the maximum flow rate of forward orifices and backward orifices increase as the inlet displacement increases. The flow rate of the backward orifices is greater than that of the forward orifices when the larger backward driving force can be obtained.

The ratio of the flow rates of the forward orifice to that of the backward orifice of the jet nozzle is defined as [8]:

$$K = \frac{n_2 Q_2}{n_1 Q_1} = \frac{n_2 d_2^2}{n_1 d_1^2}. \tag{23}$$

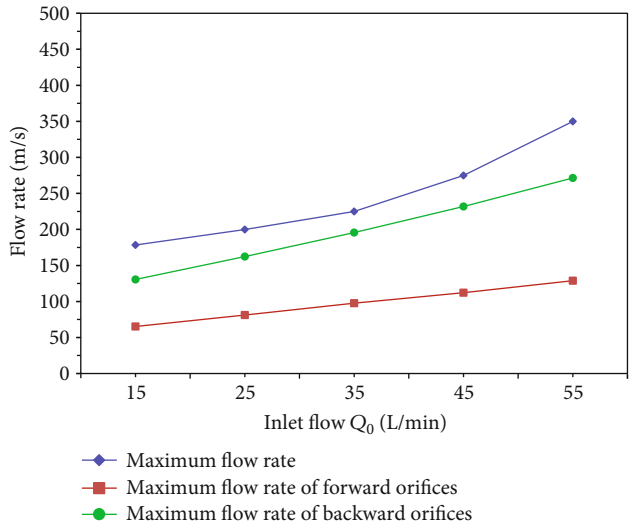

Figure 7: Comparison of the maximum speed of the injector under different inlet displacements.

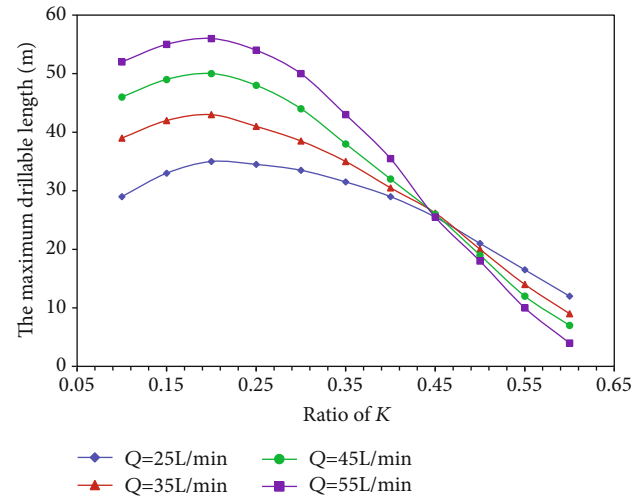

Figure 8: Effect of the ratio K on the maximum drillable length for representative values of Q.

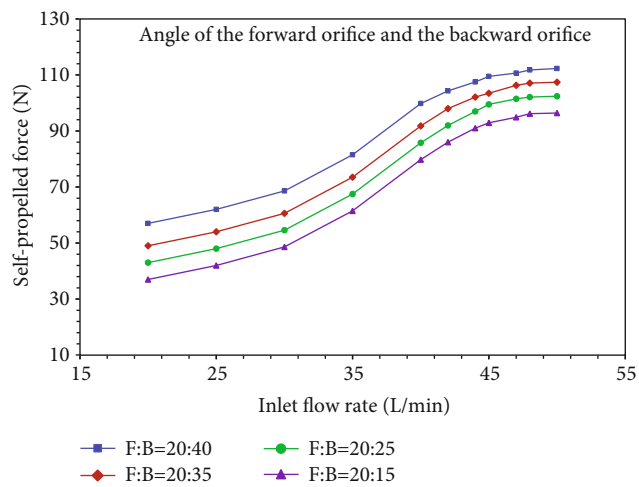

Figure 9: Effects of the inlet flow rate on the self-propelled force for representative values of $F : B$.

The key parameter will reflect the performance of the jet nozzle. Given the variation of the inlet displacement, the curves of the maximum drillable length versus the ratio K are plotted in Figure 8. As indicated from the comprehensive analysis, the maximum drillable length increases with the ratio K until $K = 0.2$, but a decreasing trend of the maximum drillable length is shown when $K > 0.2$. As demonstrated from the results, the larger inlet displacement value, the larger the maximum drillable length when $K < 0.45$; the larger inlet displacement value, the smaller the maximum drillable length when $K > 0.45$. This shows that the ratio K changes within a certain ratio range, and the inlet displacement has a greater impact on the maximum drillable length. The ratio of the flow rates of the forward orifice to that of the backward orifice of the jet nozzle might have an optimal value according to the curve trend when the effect of drilling hole is the best.

The calculated values of the self-propelled force with the inlet displacement are investigated from the simulation results for representative values of the angle ratio of the forward orifice and the backward orifice (as shown in Figure 9). It is obvious that the self-propelled force increases by a larger magnitude when the flow rate $Q < 40$ L/min, and the magnitude tends to decrease as the inlet flow rate when $Q > 40$ L/min. The simulations show that the self-propelled force is constantly increasing as the ratio $F : B$ decreasing under the same inlet displacement condition. This indicates that the recoil force increases with the increase of the inlet flow displacement, and the increasing trend is greater than that of the rock breaking force. Therefore, it is better to choose the larger inlet flow displacement to increase the recoil force, rock breaking force, and self-propelled force without considering other factors.

4. Field Experiment Description

In order to verify the simulation results of multiorifice nozzle, the field application experiment is conducted in well Nan XX-14, China. The field application apparatuses combination schematic of schematic of an RJD simulation experiment system with high-pressure water is shown in Figure 10.

The vertical depth of radial horizontal well is 2540 m; the inner diameter of the wellbore is 139.7 mm. The inner diameter of the multiorifice nozzle was 20.0 mm, and the outer diameter of the multiorifice nozzle was 12.2 mm. The number of the forward orifice is 3, and the number of the backward orifice was 6. The diameter of the forward orifice was $d_2 = 0.50$ mm, and the diameter of the backward orifice was $d_1 = 0.70$ mm. The angle of the forward orifice was $\theta_2 = 20°$, and the angle of the backward orifice was $\theta_1 = 30°$; the jetting azimuth is 90°. The working pipe string was the tubing with an outer diameter of 0.06 mm, and the steering gear was put into the predetermined position. The roughness of wellbore wall is 1 mm, and the friction coefficient is 0.3. The jetting fluid is clean water, the density is 988 kg/m^3, and the viscosity is 0.549 mPa·s. The treating pressure

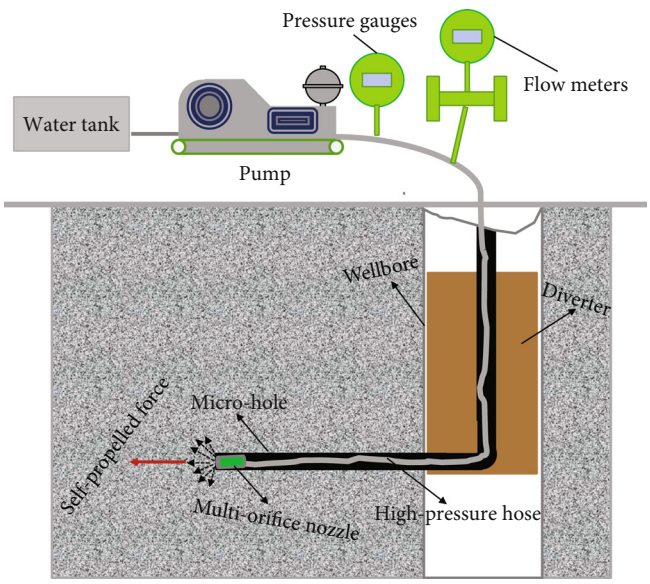

Figure 10: Schematic of an RJD system with high-pressure water.

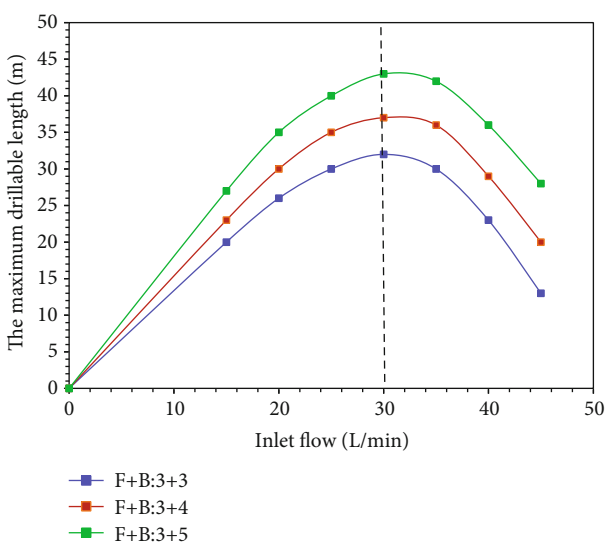

Figure 11: Effects of inlet flow on the maximum drillable length at $F + B$: 3 + 6, 4 + 6, and 5 + 6.

is 25~71 MPa, and the slurry proppant concentration is 35~115 kg/m^3.

In the experiment, it is found that the maximum drillable length of the jet nozzle has an increasing tendency and then decreasing with the increase of inlet flow displacement (as shown in Figure 11). This is because the backward jet flow rate increases as the inlet displacement increases, and the self-propelled force also increases. It is obvious that the self-propelled force is larger when the number of the backward orifices is larger, and then, the maximum drillable length can be obtained. Excessive flow will lead to increased circulating pressure loss of the system and lower pressure drop of jet nozzle, which is not conducive to rock breaking. The inlet flow displacement is controlled around 30 L/min,

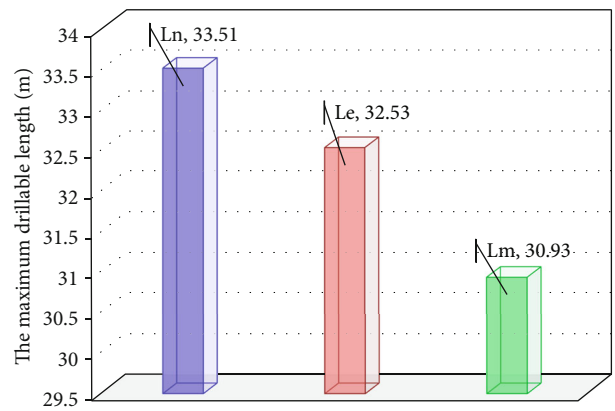

Figure 12: Comparison of simulation, calculation, and experiment results of the maximum drillable length.

the maximum drillable length 43.8 m of the jet nozzle can be obtained for representative values of $F + B$: 3 + 5. Therefore, it is more reasonable to choose the number of the backward orifices is $B = 5$.

Figure 12 shows the comparison of numerical simulation results (Ln), mathematical results (Lm), and experiment results (Le) of the maximum drillable length. It is obvious that the difference between the three results of Ln, Lm, and Le is very small, which proves that the simulation results are consistent with the experiment results with an average accuracy of 97.07%. Therefore, the proposed numerical model has a good performance in predicting the maximum drillable length of the microhole nozzle.

5. Conclusions

The research presented in this paper focused on the numerical simulation and experiment of a multiorifice nozzle in radial jet drilling. To evaluate the maximum drillable length and the self-propelled force, a 3D numerical model of multiorifice nozzles based on ANSYS-CFX is developed; the conclusions are summarized as follows:

(1) Multiple simulation models are established to investigate the effects of inlet flow displacement on the flow velocity of the forward orifices and backward orifices of the multiorifice nozzle. The numerical simulation results show that the maximum jet velocity are distributed near the forward orifices and backward orifices where there is a larger pressure difference. Both the maximum flow rate of forward orifices and backward orifices increase as the inlet displacement increases. The flow rate of the backward orifices is greater than that of the forward orifices when the larger backward driving force in rock breaking process can be obtained

(2) As indicated from the comprehensive analysis, the maximum drillable length increases until $K = 0.2$, but a decreasing trend of the maximum drillable length is shown when $K > 0.2$. When $K < 0.45$, the

larger inlet displacement value, the larger the maximum drillable length; when $K > 0.45$, the result is the opposite. This shows that the ratio of K changes within a certain ratio range, and the inlet displacement has a greater impact on the maximum drillable length

(3) The simulations show that the self-propelled force is constantly increasing as the ratio $F : B$ decreasing under the same inlet displacement condition. The self-propelled force increases by a larger magnitude when the flow rate $Q < 40$ L/min, and the magnitude tends to decrease as the inlet flow rate when $Q > 40$ L/min

(4) The comparison of numerical simulation results (Ln), mathematical results (Lm), and experiment results (Le) of the maximum drillable length are presented. The difference between Ln, Lm, and Le is very small, which proves that the simulation results are consistent with the experiment results with an average accuracy of 97.07%. Therefore, the proposed numerical model has a good performance in predicting the maximum drillable length of the multiorifice nozzles

Data Availability

All data generated or used during the study appearing in the submitted article are available from the corresponding author upon request.

Conflicts of Interest

The authors declare that there is no conflict of interest regarding the publication of this paper.

Acknowledgments

The authors gratefully acknowledge the financial support of the National Natural Science Foundation of China, grant/award numbers: 52104001 and 41802197; Beijing Municipal Education Commission "Science and Technology General Project", grant/award number: KM202111232004; Key Research Cultivation Program of Beijing Information Science & Technology University, grant/award number: 2121YJPY220; and the Strategic Cooperation Technology Projects of CNPC and CUPB grant/award number: ZLZX2020-03.

References

[1] W. Dickinson and R. W. Dickinson, "Horizontal radial drilling system," in *Presented at the SPE California Regional Meeting*, pp. 27–29, Bakersfield, California, 1985.

[2] G. Shu, H. L. Zhang, Q. Cao et al., "How to decide the well and the rock layer to be stimulated by radial hydraulic jet drilling," *Drilling and Production Technology*, vol. 40, no. 3, pp. 46–49, 2017.

[3] W. J. Cai, Z. H. Wu, Y. F. Nie, T. Han, J. J. Zhang, and P. Zhou, "Key technology and experimental study on water jet radial drilling," *Drilling and Production Technology*, vol. 39, no. 4, pp. 1–4, 2016.

[4] G. S. Li, Z. W. Huang, and J. B. Li, "Study of the key techniques in radial jet drilling," *Petroleum Drilling Technique*, vol. 45, no. 2, pp. 1–9, 2017.

[5] D. Yang, Q. Y. Gao, Y. J. Zhu, X. Q. Zhang, B. D. Zheng, and X. C. Wu, "Research and application of radial hydraulic jet drilling technology in oil and gas well," *Gas and Oil Well Testing*, vol. 26, no. 1, pp. 67–69, 2017.

[6] P. Buset, M. Riiber, and E. Arne, "Jet drilling tool: cost-effective lateral drilling technology for enhanced oil recovery," in *Paper SPE 68504 Presented at the SPE/ICoTA Coiled Tubing Roundtable*, Houston, Texas, USA, 2001.

[7] G. Bi, G. S. Li, Z. Qu et al., "Rock breaking efficiency of the self-propelled swirling jet bit," *Acta Petrolei Sinica*, vol. 37, no. 5, pp. 680–687, 2016.

[8] U. Stanislay, B. Alexander, and T. Eygeny, "First results of cyclic steam stimulations of vertical wells with radial horizontal bores in heavy oil carbonates," in *Paper SPE 115125 Presented at the 2008 Russian Oil and Gas Technical Conference and Exhibition*, pp. 28–30, Moscow, Russia, 2008.

[9] J. Li, G. Li, Z. Huang, X. Song, R. Yang, and K. Peng, "The self-propelled force model of a multi-orifice nozzle for radial jet drilling," *Journal of Natural Gas Science and Engineering*, vol. 24, pp. 441–448, 2015.

[10] L. Jingbin, H. Zhongwei, Z. Guangqing, L. Xin, and L. Huan, "Rock breaking characteristics of the self-rotating multi-orifices nozzle applied to coalbed methane radial jet drilling," *International Journal of Rock Mechanics and Mining Sciences*, vol. 136, article 104483, 2020.

[11] X. Song, Z. Lyu, L. Cui, G. Li, G. Ji, and Z. Pang, "Comparison of numerical analysis on the downhole flow field for multi-orifice hydrothermal jet drilling technology for geothermal wells," *Geothermics*, vol. 70, pp. 314–323, 2017.

[12] H. Chi, G. Li, Z. Huang, S. Tian, and X. Song, "Maximum drillable length of the radial horizontal micro-hole drilled with multiple high-pressure water jets," *Journal of Natural Gas Science and Engineering*, vol. 26, pp. 1042–1049, 2015.

[13] Y. Li and T. Zhang, "Investigation of the factors affecting the self-propelled force in a multi-orifice nozzle using a novel simulation method," *Energy Science & Engineering*, vol. 8, pp. 1–12, 2020.

[14] L. Wang, G. Wang, L. Mao, Q. Fu, and L. Zhong, "Experimental research on the breaking effect of natural gas hydrate sediment for water jet and engineering applications," *Journal of Petroleum Science and Engineering*, vol. 184, article 106553, 2020.

[15] L. Yang, *Study on the Breaking Process of Marine Hydrate Subjected to High Pressure Water Jet and the Production Increase of Marine Hydrate Reservoirs Reconstruction*, Jilin University, Changchun, 2018.

[16] G. Wang, L. Zhong, S. Zhou et al., "Jet breaking tools for natural gas hydrate exploitation and their support technologies," *Natural Gas Industry B*, vol. 5, no. 4, pp. 312–318, 2018.

[17] H. Liao, J. Niu, Y. Cheng, Z. Huang, and D. Ma, "Experiment study on water jet breaking rock by multi-orifice nozzle," *Journal of China Coal Society*, vol. 36, no. 11, pp. 1858–1862, 2011.

[18] P. Wu, "The parameters optimization that based on the finite element simulation of hydraulic injection radial drilling technology," *Advanced Materials Research*, vol. 616-618, pp. 944–947, 2012.

Hindawi
Geofluids
Volume 2021, Article ID 5827114, 11 pages
https://doi.org/10.1155/2021/5827114

Research Article

Drag Reduction Mechanism of Viscoelastic Slick-Water Fracturing Fluid in Tortuous and Rough Fractures

Zhiyu Liu,[1] Fan Fan,[2] Donghang Zhang,[3] Yang Li,[4] Yuan Li,[1] Kai Yang,[1] Hongkui Ge,[1] and Fujian Zhou[1]

[1]*The Unconventional Natural Gas Institute, China University of Petroleum, Beijing, China*
[2]*Beijing Utilities Engineering Design and Supervision Co., Ltd, Beijing, China*
[3]*No.1 Gas Production Plant, Sinopec Southwest Oil & Gas Company, Deyang, Sichuan 618000, China*
[4]*Deli Zhongcheng Petroleum Engineering Co., Ltd, Xinjiang, China*

Correspondence should be addressed to Fujian Zhou; zhoufj@cup.edu.cn

Received 1 September 2021; Accepted 11 November 2021; Published 6 December 2021

Academic Editor: Amer Syed

Slick-water can effectively reduce the flow drag of fracturing fluid. Many studies have focused on the drag reduction performance of slick-water in wellbore and perforation, but there has been little research on drag reduction characteristics in fracture flow. In this paper, a new visualization experiment system is used to simulate real fracture. The fracture surface is produced through actual triaxial hydraulic fracturing and is copied by a three-dimensional printer using resin material to maintain its shape feature. In comparing the experimental results, it was found that the main factors affecting drag reduction in a fracture are the relative molecular weight and the added concentration. Unlike the flow rule of the drag reducer in a pipeline, when the concentration is greater than 0.10%, a negative DR effect begins to appear. The influence of molecular weight is related to the flow stage; the increasing of molecular weight causes a reduction in DR effect when the flow rate is 0.24 m/s. However, the flow rate exceeds 0.5 m/s; drag reducers with higher molecular weight demonstrate better drag reduction performance. The drag reduction mechanism analysis in fractures was obtained from visualization observations, and the flow characteristics of fluid were characterized by using tracking particles. Drag reduction effect occurs mainly on the surface of the fractures in contrast to near the centre of the flow channel. This research can provide a reference for the experimental study on drag reduction in fractures and is of great significance to the optimization and improvement of drag reducing agent.

1. Introduction

Slick-water fracturing is a systemic method that increases production by injecting several million gallons of water into a formation to create a fracture network [1–4]. The fracturing slick-water is injected with proppant at a high pump rate to maintain the flow channel. Slick-water is commonly used in large-scale volume fracturing for its low flow drag, which is an advantage in creating more fractures and complex fracture networks to maximise the initial production rate, as consistently observed in the field [5–7]. Accurate estimation of fracturing flow drag is critical to fracturing design, and drag reduction performance is one of the most important technical indicator of slick-water fracturing fluid.

Drag reduction phenomenon is also called the "Toms" phenomenon. Only a small amount of additives can produce a significant pressure drop in turbulent flow, known as the drag reduction effect (DR effect) [8, 9]. There are three main types of drag reduction agents (bubbles, polymers, and surfactants) often used in slick-water. Polymer as the most commonly used type of slick-water additive is a kind of water-based fracturing fluid mixed with long-chain polymers such as polyacrylamide, polyethylene oxide, and guar derivatives [10–14]. Since the DR effect was discovered, many applications have been produced. However, the exact mechanism of drag reduction is still not reach a unified understanding and be widely accepted [15–17]. Previous drag reduction mechanism research has focused mostly on

wellbore flow drag. According to the results of previous study, the drag reduction performance of slick-water is dependent on the balance between the viscous modulus and the elastic modulus and is determined by the microstructure of the drag reducer. As a decisive factor in fracturing design, fracture flow drag requires research of flow patterns and drag reduction characteristics [18–20]. Although research on the pipeline flow has provided us with a foundation, the flow patterns and characteristics in the fractures need further thorough research.

The related research on the drag reduction mechanism of fluid in reservoirs did not concentrate on fractures but focused on microchannels or the microfractures in reservoirs. Some researchers advocated using the microfluidic chip to simulate the drag reduction flow in microfractures [21–23]. On contrast to the pipeline flow experiment, the fluid flow in microfracture is under laminar flow regime. The same drag reduction agents do not decrease the injection pressure but increased more than 50% [24]. Then, other researchers represented by Barrat further demonstrated that adsorption properties of surfactants are the main reason leading to drag reduction effect. They believe that the surfactants adsorbed on the wall of reservoir microchannels weaken the interaction between water molecules and therefore reduce the flow drag [25–28]. Generally, previous research studies the drag reduction mechanism in microscale, and the drag reduction agents used in the research are mainly surfactants. Few studies have investigated the flow characteristics of large-scale artificial fractures. What is more, most related research does not consider the roughness and tortuosity of the fractures. The representative results were published by Fengchen and Kawaguchi; experiments were executed using PIV method to test the quantitative characteristics of vortex structures and turbulent events in two-dimensional channel made of transparent acrylic resin [29]. The literature analyses the changes of turbulence structure but ignores the influence of real fracture parameters. So the drag reduction flow in large-scale artificial fractures has not been sufficiently studied through indoor experimental simulation. The drag reduction mechanism in fracture flow still not clear and cannot be universalized with the mechanism in pipeline flow.

In this study, a self-developed indoor drag testing cycle system considering fracture tortuous and roughness was constructed to test the flow drag in both pipeline and fracture. Essential experiments have been conducted to investigate the factors influencing the DR effect in fractures including concentration, temperature, molecular weight, and electrical characteristics. The experimental research in pipeline is mainly used as a reference to explore the drag reduction characteristic in fractures. As the DR mechanism has not been extended to fractures, considering the experimental differences between pipelines and fractures, a visualization fracture model is added. The flow characteristics of fluid are characterized by using tracking particles. Although the experiment is designed as complete as possible, there remain some limitations in this study. The accuracy of the test equipment can be guaranteed and is sufficient for drag reduction rate tests. However, the experimental conditions are not sufficient to confirm the value of R_e in fractures. Thus, further discussion on the relation between R_e and drag reduction characteristic is not presented.

2. Methodology

2.1. Research Equipment. The drag reduction performance of slick-water can be analysed using an indoor visualization drag testing cycle system [30]. A diagram of the experimental apparatus is shown in Figure 1. The testing system consists of five parts: (A) a liquid supply system including three plastic buckets; the one in the middle is the effluent water bucket and is the largest, with a volume of 70 L. Water and solution buckets with a volume of 50 L are on each side. The power output depends on a screw pump; its maximum pumping rate is 2.5 m^3/h. To better simulate flow conditions in the field, the solution buckets were equipped with a heater to test different fluid temperatures; (B) the pipeline testing system consisting of three pipelines. The pipeline diameters are 6 mm, 8 mm, and 10 mm; all pipelines are 3 m in length. With ball valves on both ends and a differential pressure transducer (0–0.5 MPa, ±0.02%) in the centre, to minimise the additional shear effect from the corners connected to each pipeline, pressure taps were set 0.25 m from each end to measure the 2.5 m pressure drop; (C) a visualization fracture testing system with a stainless steel frame (360 mm long, 140 mm high) with adjustable width for fitting the surface and visualization fracture model; (D) a data acquisition system consisting of a computer and a control system to control the equipment and collect flow rate, temperature, and pressure data; (E) a pressure sensing system with a differential pressure transducer (0–100 kPa, ±0.001%) to test the pressure drop between visual fractures with taps set 30 mm from each end to measure the 300 mm pressure drop. The system was designed to simultaneously measure pipeline and fracture flow drag and to precisely compare their differences in the same flow conditions.

2.2. Visualization Fracture Model. The visualization fracture model is showed in Figure 2, and the main body of the model is ASTM304 steel frame. Truly simulated fracture surface is made of resin material. There is an injection interface on one side and a flow out interface on the other side. Moreover, there is an injection connector on one side and a flow out connector on the other side. In order to introduce the model production process in specifically, the equipment manufacturing process is divided into three parts. The tortuous and rough fracture surface was created through large-scale actual triaxial hydraulic fracturing, as shown in Figure 3, and the rock size was 30 cm^3. A surface scanner was used to accurately describe the roughness and tortuosity of the fracture, which was copied by a three-dimensional printer using resin to maintain its clarity. The copied surface was assembled into a circumjacent and airtight stainless steel frame, and the size of the frame is 360 mm long and 140 mm high. The distance between this two surface can be adjusted to the fracture width from 1 to 8 mm. As shown in Figure 4, the visualization fracture model is connected with the loop testing system. A pressure transducer was installed (0–100 kPa,

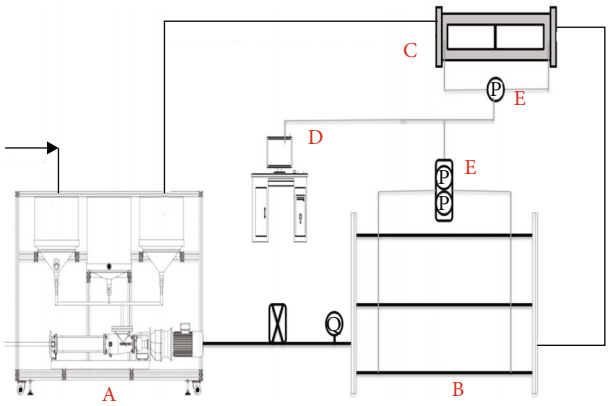

Figure 1: Diagram of experimental apparatus: (a) liquid supply system; (b) pipeline test system; (c) visualization fracture model; (d) data acquisition system; (e) pressure sensing system.

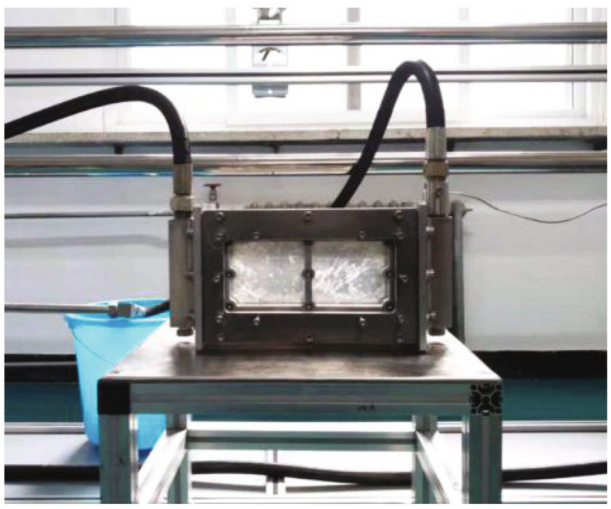

Figure 2: Visualization fracture model.

Figure 3: Large-scale actual triaxial hydraulic fracturing surface and copied fractures.

±0.01%) on each connector to monitor the changes of flow pressure, and the two pressure spots were set at a distance of 300 mm.

2.3. Selected Drag Reducer. Polyacrylamide polymer drag reducers are commonly used in hydraulic fracturing and can be generally categorised as cationic, anionic, or nonionic, according to their electrical characteristics after hydrolysis. Cationic drag reducers are relatively expensive.

Figure 4: Indoor visualization drag testing cycle system: (a) liquid supply system; (b) pipeline test system; (c) visualization fracture model.

Nonionic drag reducers require an amount approximately one order of magnitude greater to be added than cationic and anionic reducers for the same drag reduction effect. Thus, anionic drag reducers are usually used for fracturing [31]. The drag reducer used in this study is an emulsion form and water-soluble drag reducer and is synthesized from a mixture of acrylamide (AM), acrylic acid (AA), 2-acrylamido-2-methylpropanesulfonic acid (AMPS), and butyl acrylate (BA) in aqueous solution by the polymerization process. It is manufactured by Shengli Chemical Co., Ltd., commercially known as DR800. It is an anionic polyacrylamide with a high molecular weight of 8×10^6 and several long side groups. DR800 was mixed with tap water to synthesize slick-water, a commonly used fracturing fluid in unconventional reservoir development. The relationship between slick-water viscosity and drag reducer dosage was measured using a Ubbelohde viscometer at 25°C; the results are shown in Figure 5.

2.4. Data Processing. Drag reduction efficiency (DR%) is calculated as

$$\mathrm{DR\%} = \frac{C_{fD} - C_f}{C_{fD}} \times 100\%, \tag{1}$$

where C_{fD} is the Fanning friction factor of water and C_f is the Fanning friction factor of slick-water in the same flow conditions, defined as

$$C_f = \frac{2\tau_w}{\rho U_b^2}, \tag{2}$$

where τ_w is the wall shear stress, ρ is the density of the solvent, and U_b is the average flow velocity. Figure 6 shows a diagram of the fracture and pipeline.

For a fracture, Equation (2) can be deduced as

$$C_f = \frac{2\tau_w}{\rho U_b^2} = \frac{\Delta p H W}{\rho U_b^2 (H + W) L}, \tag{3}$$

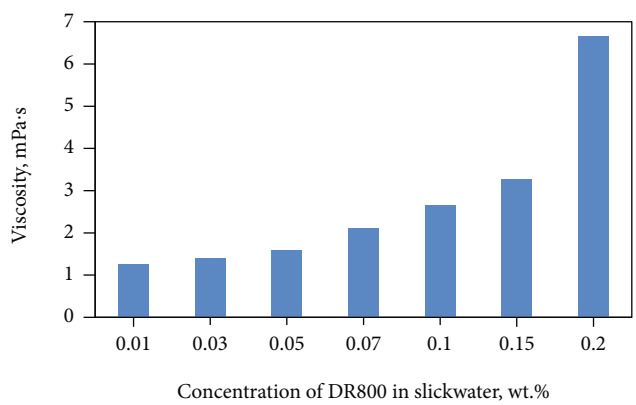

Figure 5: Relationship between slick-water viscosity and drag reducer concentration.

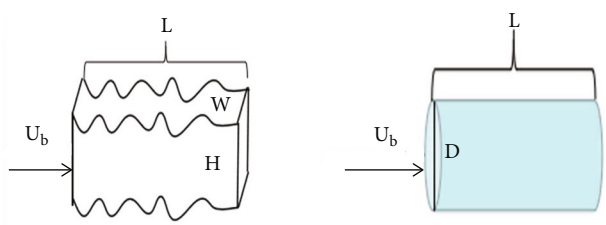

Figure 6: Diagram of fracture and pipeline.

where Δp is the pressure drop over the two pressure taps, L is the distance between the pressure taps, and H and W are the height and width of the fracture, respectively.

For a pipeline, Equation (2) can be deduced as

$$C_f = \frac{2\tau_w}{\rho U_b^2} = \frac{2D\Delta P}{\rho U_b^2 L}, \tag{4}$$

where D is the inner diameter of the pipeline.

The largest polymer dosage in our experiment was 0.15 wt.%; the density of the 0.15 wt.% solution was 997.043 kg/m^3, which is nearly the density of water. Thus, the displacement is the same. For each test section, Equation (1) can be reduced as

$$\mathrm{DR\%} = \frac{\Delta P_w - \Delta P_{\mathrm{DR}}}{\Delta P_w} \times 100\%, \tag{5}$$

where ΔP_w is the pressure drop of water.

The Reynolds number R_e is defined as

$$R_e = \frac{\rho U_b R}{\mu}, \tag{6}$$

where μ is the fluid viscosity and R is the hydraulic radius.

For a fracture, $R_f = HW/2(H + W)$; R_e can be deduced as

$$R_e = \frac{\rho U_b HW}{2\mu(H + W)}. \tag{7}$$

For a pipeline, $R_p = D/2$; R_e can be deduced as

$$R_e = \frac{\rho U_b D}{2\mu}. \tag{8}$$

In pipeline flow, the Reynolds number is an important parameter to distinguish laminar and turbulent flows but is not suitable for fractures. An explicit critical Reynolds number between laminar and turbulent flows has not been established for true complicated fracture flow.

2.5. Equipment Reliability. Equipment reliability was checked prior to the experiments. Considering that there are no mature empirical formulas or judgment bases for true complicated fracture flow drag, repeated experiments were performed to test the water flow drag in fractures under the same conditions. Figure 7 shows perfect repeatability, indicating high experimental device accuracy and providing strong evidence of drag reduction experiment reliability.

3. Results and Discussion

3.1. DR Performance. Generally, the DR concentration is approximately 0.05 wt.% to 0.15 wt.% in the field, considering both performance and economy [32]. In this study, the DR% of 0.05 wt.% DR800 solution with the same displacement in the fractures and pipeline are presented in Figure 7. As shown in Figure 8, in the same pumping displacement conditions, the maximum drag reduction rate in the pipeline flow exceeds 70%; the maximum drag reduction rate in the fracture flow does not exceed 7%, a difference of more than ten times. Thus, at the same displacement, the drag reduction flow characteristics in a pipeline and a fracture are completely different. This is a result of different flow channel cross-sectional shapes and many other factors. However, it is certain that the pump displacement parameters cannot be used as effective variables in the comprehensive evaluation of drag reduction in pipelines and fractures.

To better observe the DR performance in fractures, the variation regularity of the drag reduction rate was analysed with different average flow rates and Reynolds numbers. The experimental results are presented in Figure 9(a). For 0.05 wt.% DR800, the drag reduction rate increases with an increase in the average flow rate and Reynolds number. Under these two conditions, the variation regularity of the drag reduction rate is essentially the same. The actual Reynolds number of the fluid in tortuous and rough fractures is difficult to determine. It is more accurate to analyse the drag reduction performance in fractures in average flow rate conditions.

For comparison, the drag reduction performance of 0.05 wt.% DR800 in pipeline flow was also tested. The test results are presented in Figure 9(b). In pipeline flow conditions, the average flow rate reaches 2–18 m/s, greater than ten times the average flow rate in fracture flow. In pipeline flow, the Reynolds number at the minimum average flow rate must be greater than 15000 (the critical value for dividing laminar turbulent flow is 2100). However, in fracture flow, the Reynolds number is less than 2100, even at the

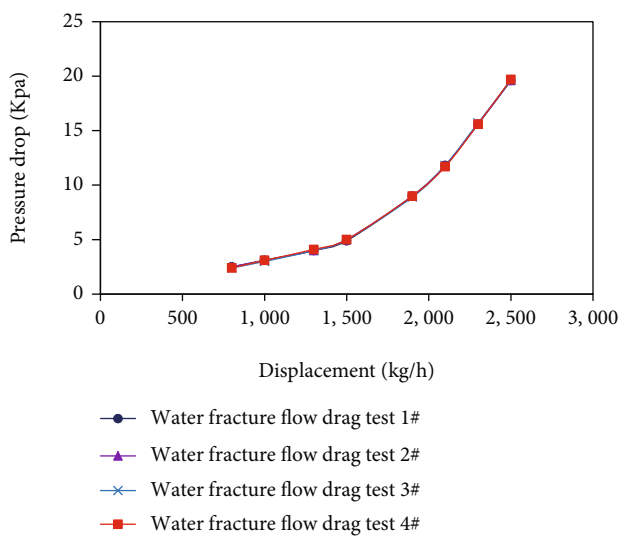

Figure 7: Results comparison in repeated experiments.

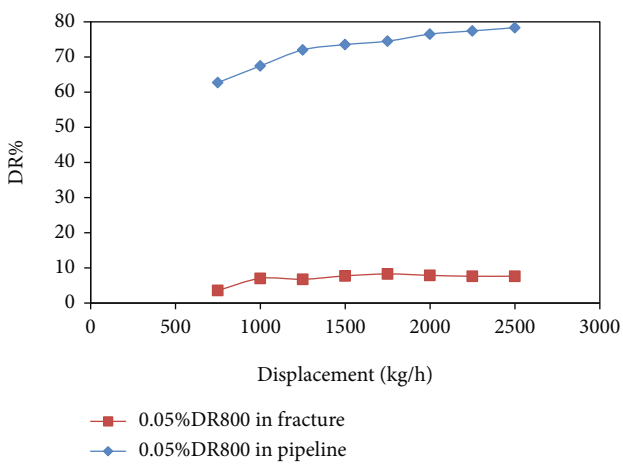

Figure 8: DR% of 0.05 wt.% DR800 with the same displacement in fracture and pipeline.

maximum average flow rate. Thus, the difference in the pipeline flow and fracture flow states is the main reason for the large difference in drag reduction performance. In different flow states, the drag reduction effect in pipeline flow occurs mainly in the centre of the flow channel where the turbulence is more concentrated; the drag reduction effect in fracture flow occurs mainly near the fracture surface.

Experiments were conducted to study the factors influencing DR% in fractures. To guarantee the accuracy of the experimental results, all experiments were repeated at least twice, and the results were averaged.

3.2. Factors Influencing the DR Effect

3.2.1. DRA Concentration. Eight concentration groups of DR800 were tested at 25°C with different flow rates. Figure 10 shows the influence of the DRA concentration on the DR effect in pipelines. At a low flow rate, an increase in additive concentration leads to an increase in viscosity, which increases the relative flow resistance and the drag reduction. The DR% of 0.01 wt.% DR800 decreases rapidly at 6 m/s, indicating that the liquid at this concentration has the greatest shearing resistance. When the flow velocity was increased, the DR% of 0.03 wt.% DR800 began to decrease slowly after reaching the peak value, indicating that its DR performance had reached its limit. With an increase in the flow rate, the DR% of 0.05 wt.% DR800 increased gradually, indicating that deformation or failure of the molecular structure may have occurred while achieving efficient drag reduction. The DR performance of 0.20 wt.% DR800 indicates that high viscosity is the greatest obstacle to drag reduction at low flow rates, which was further verified by the DR performance in the fracture.

Figure 11 shows the influence of DRA concentration on the DR effect in a 3 mm fracture, which is different from that in a pipeline; a higher concentration increases the DR effect. At high concentrations, the DRA cannot reduce the flow drag and increases the flow resistance compared with pure water. This phenomenon is referred to as a negative DR effect. At each concentration, the flow rate has a positive effect on the DR effect and an inhibiting effect on the negative DR effect. When the concentration is greater than 0.10%, a negative DR effect begins to appear. To further determine the critical concentration and to better analyse the change rule of the negative DR effect, additional high concentration drag reducer performance tests were conducted (0.09 wt.% DR800, 0.11 wt.% DR800, 0.13 wt.% DR800). As shown in Figure 12, 0.09 wt.% DR800 solution still reduces the flow drag, but 0.11 wt.% DR800 solution produces a negative drag reduction effect. This further proves that the critical concentration is 0.1 wt.%.

The results of experimental research on the influence of concentration indicated that drag reduction agents have the optimal concentration under relevant drag reduction flow conditions (both in pipeline flow and fracture flow). When pipeline flow is under low flow rate, concentration has an adverse effect on DR effect. But as the increases of flow rate, high concentrations of drag reducers begin to show benefit to their effect. In relation to fracture flow, increasing of drag reducer concentration causes reduction in drag reduction rate. The reason is mainly because the overall flow rate in the fracture is under lower level; high viscosity caused by concentration increases has a more significant negative impact on DR effect and leads to an increase in energy consumption, eventually caused a decrease in drag reduction effect.

3.2.2. Temperature. Five groups of 0.05 wt.% DR800 were tested at different flow rates at 25°C, 35°C, 45°C, 55°C, and 65°C in a circular pipeline. Within 45°C, temperature had a positive effect on drag reduction performance, as shown in Figure 13, indicating that a viscosity decrease accompanied by a temperature increase promotes drag reduction. The DR performance at 55°C began to decline at 12 m/s and rapidly declined at 65°C, indicating that the shearing resistance ability was significantly weakened by the joint action of high flow rate and high temperature.

Five groups of 0.05 wt.% DR800 were tested in fracture flow at different flow rates at 25°C, 35°C, 45°C, 55°C, and

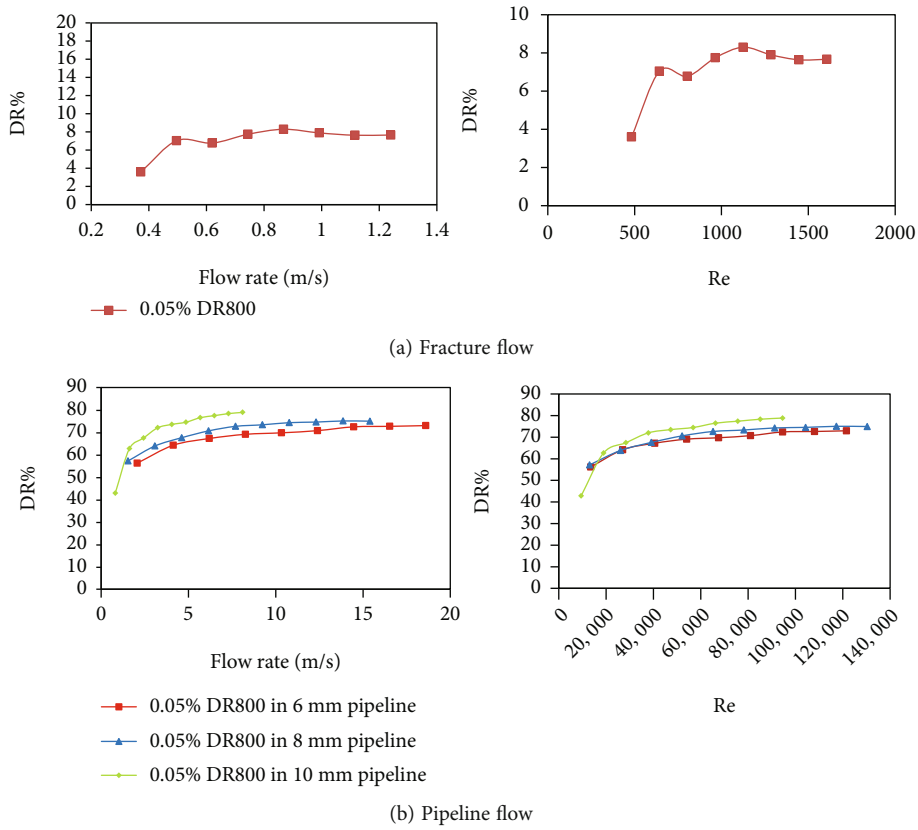

Figure 9: Relation of DR% with flow rate and Reynolds number.

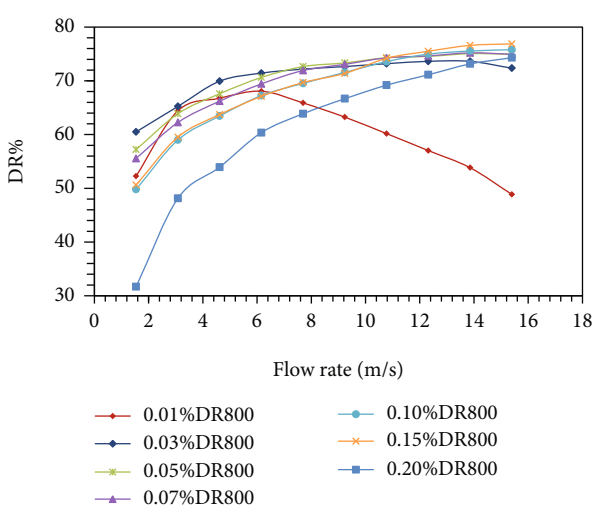

Figure 10: Influence of DRA concentration on DR effect in pipeline.

65°C. Within 45°C, temperature has a positive effect on drag reduction performance, as shown in Figure 14, because viscosity declines with increasing temperature, which is beneficial for the DR effect. At higher temperatures, the DR effect increased at low velocities and decreased at high velocities because excessive molecular thermal motion impedes the form of the DR structure; a small shear force can influence DR%.

3.2.3. Polymer Molecular Weight. The type of DRA was changed based on previous experiments. In this study, research was conducted on the influence of polymer molecular weight and polymer molecular structure on the DR effect as related to polymer-based drag reduction agents. Several anionic polymer DRA with different molecular weights at a given concentration were chosen for comparison and were named according to their molecular weight. DR800 was used as the reference. DR2000 and DR6000 are polymers with several long side groups, while DR1200 is a high polymer with many short side groups, as shown in Figure 15. From previous studies, it is generally acknowledged that the DR effect improves with increasing molecular weight under low flow rate conditions; short side groups are not conducive to the performance of drag reduction, and long side groups increase the drag reducing rate.

Figure 16 shows the DR% comparison for 0.05 wt.% DRA in pipelines. The influence of molecular weight on DR% is more obvious in the low flow rate section. At low flow rate (1.8 m/s), the DR effect is rising with an increase in molecular weight. But when the flow rate exceeded 8.0 m/s, the DR effect was tended to the same value. In comparison, DR1200 exhibited a better DR effect than the others at high velocity, indicating that a high flow rate can alleviate the disadvantageous effects of short side groups.

Figure 17 shows that 0.05 wt.% DRA in a 3 mm fracture is different than in a pipeline. Long side groups may not have had enough space for expansion; the increasing of molecular weight causes a reduction in DR effect. With

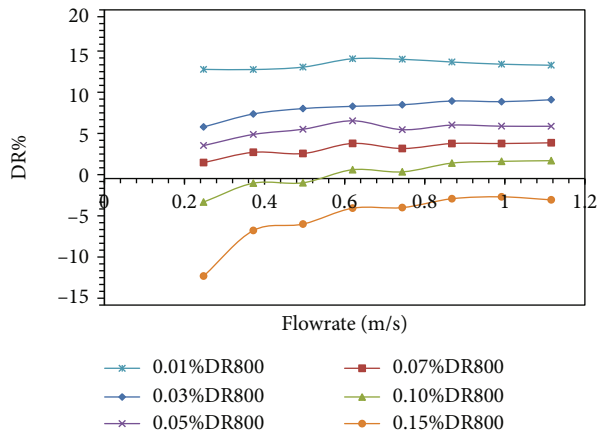

Figure 11: Influence of DRA concentration on DR effect in fracture.

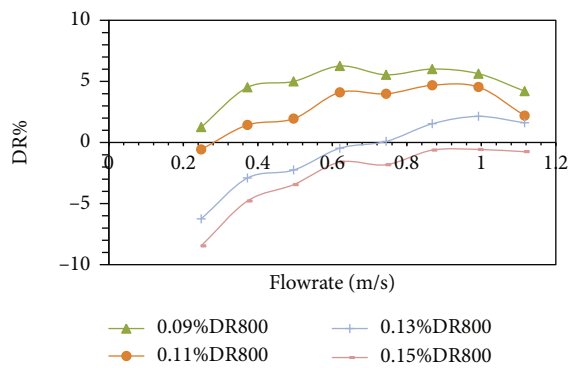

Figure 12: Influence of high DRA concentration on negative DR effect.

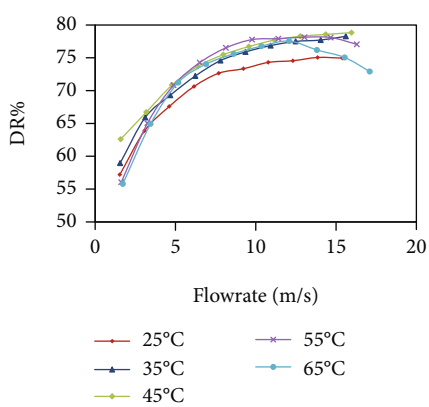

Figure 13: Relation of DR% and flow rate at different temperatures in pipelines with 0.05 wt.% DR800.

increasing of flow rate, the positive influence of molecular weight becomes apparent. As the influence of the tortuously and roughness of the fracture surface, the rule of polymer molecular weight affecting drag reduction performance has changed. When the flow rate is 0.24 m/s, the increase in molecular weight is not conducive to drag reduction performance in fracture flow. However, when the flow rate exceeds 0.5 m/s, drag reducers with higher molecular weight demon-

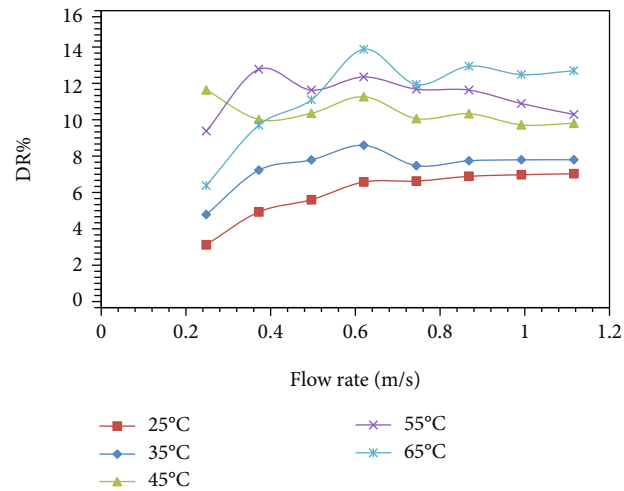

Figure 14: Relation of DR% and flow rate at different temperatures in fracture for 0.05% DR800.

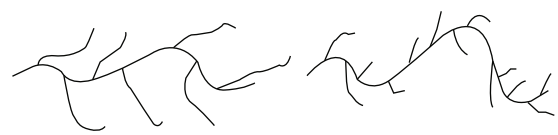

Figure 15: Two molecular DRA structures.

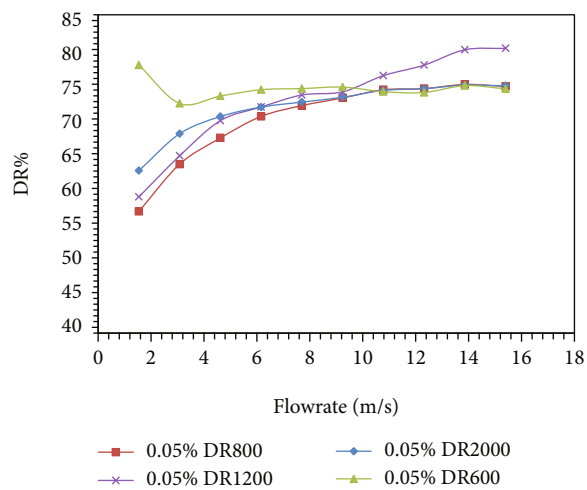

Figure 16: Comparison of 0.05% DRA in 8 mm pipeline.

strate better drag reduction performance. As stated above, the molecular weight has significant difference effects on drag reduction performance in pipelines and fractures. DR1200 exhibited a negative DR effect, indicating that the short side groups decrease the DR effect, especially in fracture flow.

3.2.4. Polymer Electrical Characteristics. Commonly used DRA in slick-water fracturing can be generally categorised as cationic, anionic, or nonionic according to their electrical characteristics after hydrolysis. Cationic, anionic, and nonionic DRA with the same molecular weight and molecular structure were chosen to study the influence of electrical

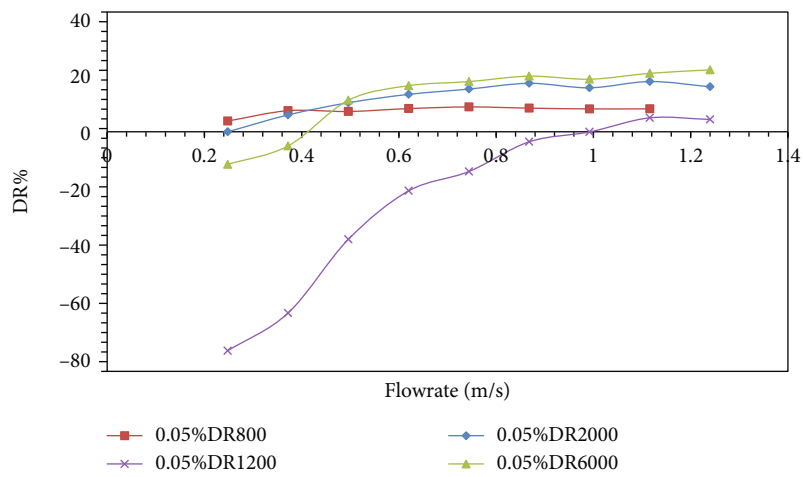

Figure 17: Comparison of 0.05% DRA in 3 mm fracture.

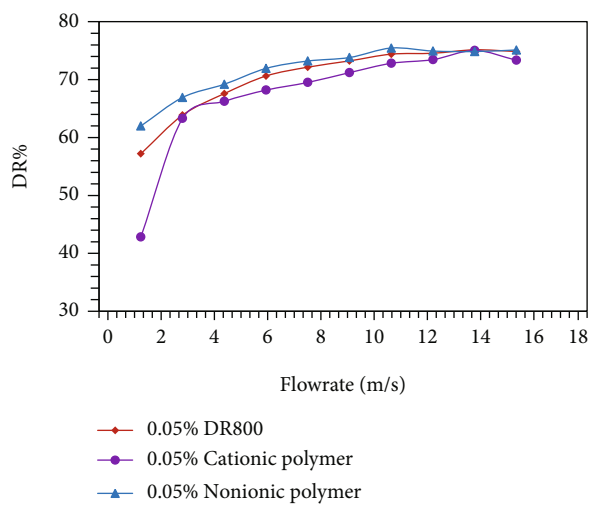

Figure 18: Results for three DRA types in 8 mm pipeline.

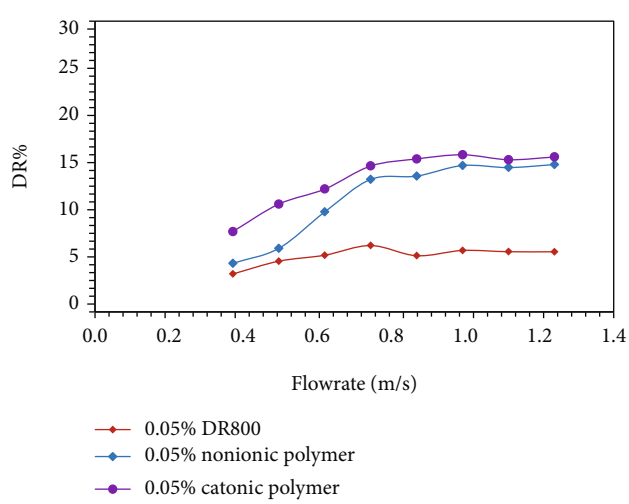

Figure 19: Results for three DRA types in 3 mm fracture.

characteristics on the DR effect. Figure 18 shows the DR% results for the three DRA types at 0.05 wt.% in an 8 mm pipeline. The DR effect for the three types can be ranked as follows: cationic type < anionic type < nonionic type. Figure 19 shows the DR% results for the three DRA types at 0.05% in a 3 mm fracture. In fractures, the DR effect can be ranked as follows: anionic type < nonionic type < cationic type. By comparing the results of electrical characteristics, cationic polymer shows the worst drag reduction performance in pipeline flow, in contrast to show the best effect in fracture flow. It indicated that the flow characteristics in the tortuous and rough fractures have an enhancement in the drag reduction effect of cationic polymers. The results may attribute to cationic polymer that has more active groups, which is more conducive to drag reduction effect under low flow rate.

3.3. DR Mechanism. Different from the calculation of flow drag in standard circular section pipelines, it is difficult to accurately calculate the internal flow drag of fractures with real tortuosity and roughness. Therefore, the visualization fracture model is used to observe the flow drag reduction characteristic in this study. Furthermore, the red tracer particles are added in the fluids, in order to get a more accurately description of the flow characteristic and analyse the drag reduction mechanism. The whole flow process in fractures can be divided into four stages, as shown in Figure 20.

(1) A circuitous surface can help the flow generate local vortexes as flow starts. Each recess has scale-matched vortexes that restrict the spanwise motions of turbulent vortexes, avoiding more perturbance as the surface is not regular, which increases the DR%. At a low flow rate, the convex area can induce interior flow and facilitate formation of the DR structure, which increases the DR%

(2) The scale-matched vortex balance is broken as the velocity increases; many vortexes in the concave area weaken the positive effect of scale-matched vortexes. However, the convex area is beneficial for the DR%

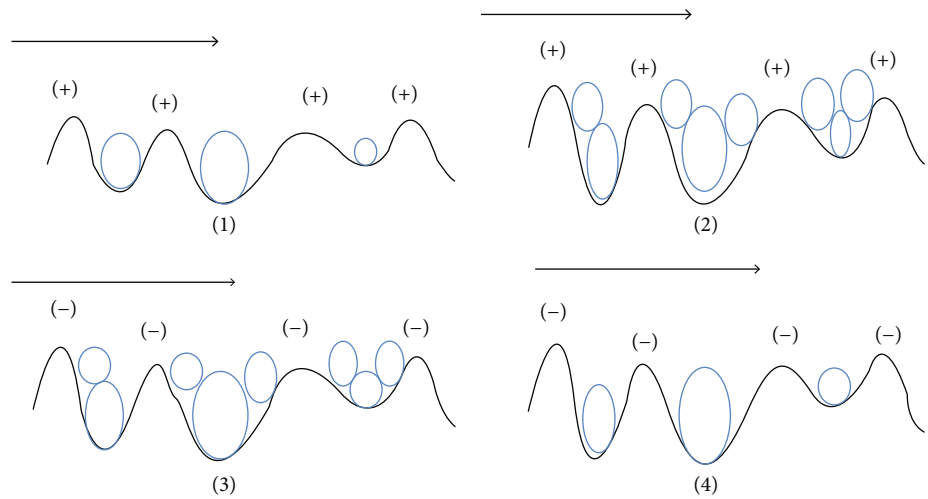

Figure 20: Images of DR mechanism.

(3) When the velocity reaches a critical value, the convex area tends to increase the shear force and facilitate formation of the DR structure, which helps increase turbulence and decrease the DR%. As the flow rate increases, the negative influence gradually becomes apparent

(4) As the flow rate increases, many small vertexes result from the shear force caused by the convex area, and the larger vortexes disappear. The negative effect of many smaller or larger vortexes in the concave area starts to diminish, reaching a balance with their counterparts

The division of the flow stages indicates a clearer mechanism for the change rule of the drag reduction performance. At low flow rates, turbulence is concentrated mainly on the fracture surface, especially in the recessed areas. At this time, the DR effect of the drag reducer is not obvious; as the flow rate increases, the turbulence increases, and the polymer starts to play a role in both the recessed and raised areas, producing an increase in the DR rate. As the flow rate is further increased, the turbulence is concentrated near the centre of the flow channel. In this stage, the DR effect occurs mainly in the middle of the fractured flow channel, similar to pipeline flow, and gradually reaches its greatest effect. The flow stage characteristics further reveal the rules of DR performance in fracture flow with changes in the flow rate.

4. Conclusions

In this study, a self-developed indoor visualization drag testing cycle system considering fracture roughness and tortuosity was constructed to simultaneously test pipeline flow drag and fracture flow drag. Multiple experiments were conducted to determine the factors influencing the DR effect in fractures including concentration, temperature, molecular weight, and electrical characteristics. Pipeline flow tests were used as a reference to explore the drag reduction characteristic in fracture flow. Based on the experimental differences between pipelines and fractures, the main conclusions are as follows:

(1) For the pipeline flow, as the flow rate increases, the drag reduction effect will get better and eventually reach the optimal drag reduction rate. Then, if the flow rate further increases, the drag reduction rate will decrease (the highest pipeline flow rate in experiment is 16 m/s). When it comes to fracture flow, the flow rate has a similar influence on the drag reduction rate. However, limited by experimental conditions, the highest flow rate in the fracture is only 1.2 m/s. For both pipeline flow and fracture flow, they all have an optimal drag reduction rate. Before reaching this rate, the flow rate has a positive correlation with DR effect

(2) The experimental results of concentration influence show that, in pipeline flow, concentration has an adverse effect on the drag reduction performance under low flow rate conditions because high viscosity has a more significant negative impact on DR effect and leads to an increase in energy consumption. However, as the flow rate further increases, the polymer has sufficient space for expansion, and the fully stretched chain structure is more conducive to drag reduction performance. As for fracture flow, there is a critical drag reduction concentration. When the concentration is greater than 0.10 wt.%, a negative DR effect begins to appear. The flow drag in fractures is rising with the growth in concentration of drag reducer

(3) The increase of temperature leads to the decrease of the viscosity of drag reducer solution, which is beneficial to the drag reduction effect under the low flow rate conditions. However, high temperature (greater than 55°C) makes the DRA more vulnerable to wall shear influence and finally causes reduction in drag reduction effect under high flow rate conditions

(4) In pipeline flow and fracture flow, the regular of drag reduction performance influenced by the molecular weight is opposite. Under low flow rate conditions, within a certain range of molecular weight increase, drag reduction effect is improved in pipeline flow but reduced in fracture flow. As for molecular structure, longer side groups can improve the form of structures to reserve more dissipated energy in the central of the pipeline flow. However, in fracture flow, excessive short side group is not conducive to the DR effect near the fracture surface

Data Availability

The experiment data used to support the findings of this study are available from the corresponding author upon request.

Conflicts of Interest

The authors declare no financial conflicts of interest regarding the publication of this paper.

Authors' Contributions

Professor Fujian Zhou, as the corresponding author of this paper, provided research ideas and funding. Professor Hongkui Ge provided guidance for experimental research methods and problems encountered in the experiment. Zhiyu Liu was the first author and responsible for experiment design and data analysis. Fan Fan as co-first author improved the experiments and added the test data. Donghang Zhang was the main experiment operator who finished the testing processes. Yang Li provided the test materials and was responsible for collecting and testing the parameters. Yuan Li and Kai Yang built and improved the experimental equipment and were responsible for drawing the flow chart of the experimental equipment. Fan Fan contributed equally to this work and co-first author.

Acknowledgments

This study is supported by the Shengli Oil Filed Luming Co., Ltd., "Research and Application of Temporary Plugging Technology in water fracture displacement of Beach-bar Sand Reservoir water fracture displacement" (LMKJ2021-05) and the Xinjiang Deli Zhongcheng Petroleum Engineering Co., Ltd., "Research on new drag reduction materials suitable for different fluid flow conditions" (ZC-20201209). The authors would like to acknowledge the financial support from the National Natural Science Foundation of China (No. 52174045).

References

[1] B. Yang, J. Z. Zhao, J. C. Mao, H. Tan, Y. Zhang, and Z. Song, "Review of friction reducers used in slickwater fracturing fluids for shale gas reservoirs," *Journal of Natural Gas Science and Engineering*, vol. 62, pp. 302–313, 2019.

[2] A. Muntasheri and G. A. Critical, "Review of hydraulic fracturing fluids over the last decade," in *SPE Western North American and Rocky Mountain Joint Meeting*, Denver, Colorado, 2014.

[3] R. Barati and J. Liang, "A review of fracturing fluid systems used for hydraulic fracturing of oil and gas wells," *Journal of Applied Polymer Science*, vol. 131, 2014.

[4] C. Robart, M. Ruegamer, and A. Yang, "Analysis of U.S. hydraulic fracturing design trends," in *Paper Presented at the SPE Hydraulic Fracturing Technology Conference*, The Woodlands, Texas, USA, 2013.

[5] H. D. Brannon and C. E. Bell, "Eliminating slickwater fracturing compromises for improved shale stimulation," in *SPE Annual Technical Conference and Exhibition*, Denver, Colorado, USA, 2011.

[6] G. Y. Gao, C. H. Wang, H. Zhou, and P. Wang, "Modified fracture mechanics approach for hydraulic fracturing stress measurements," *Geofluids*, vol. 2020, Article ID 8860163, 11 pages, 2020.

[7] Z. P. Sun, H. L. Zhang, Z. F. Wei et al., "Effects of slick water fracturing fluid on pore structure and adsorption characteristics of shale reservoir rocks," *Journal of Natural Gas Science and Engineering*, vol. 51, no. 2, pp. 27–36, 2018.

[8] H. Belyadi, E. Fathi, and F. Belyadi, "Chapter Five - Hydraulic Fracturing Fluid Systems," in *Hydraulic Fracturing in Unconventional Reservoirs (Second Edition)*, pp. 47–69, Gulf Professional Publishing, 2019.

[9] B. A. Toms, "Some observations on the flow of linear polymer solutions through straight pipelines at large Reynolds numbers," in *Proceedings of the 1st International Congress on Rheology*, pp. 135–141, Amsterdam, 1948.

[10] G. Sitaramaiah and C. L. Smith, "Turbulent drag reduction by polyacrylamide and other polymers," *Society of Petroleum Engineers Journal*, vol. 9, no. 2, pp. 183–188, 1969.

[11] Y. H. Li, G. R. Chesnut, R. D. Richmond, G. L. Beer, and V. P. Caldarera, "Laboratory tests and field implementation of gas-drag-reduction chemicals," *SPE production & facilities*, vol. 13, pp. 53–58, 1998.

[12] W. Brostow, "Drag reduction in flow: review of applications, mechanism and prediction," *Industrial and Engineering Chemistry*, vol. 14, no. 1, pp. 409–416, 2008.

[13] W. W. Li and R. K. Saini, "Polyacrylamide grafted polysaccharide as friction reducer for slickwater fracturing treatment," *Journal of Macromolecular Science, Part A*, vol. 58, no. 4, pp. 243–248, 2021.

[14] M. L. Luo, X. D. Si, M. Z. Li, X. H. Jia, Y. L. Yang, and Y. P. Zhan, "Experimental study on the drag reduction performance of clear fracturing fluid using wormlike surfactant micelles and magnetic nanoparticles under a magnetic field," *Nanomaterials*, vol. 11, no. 4, p. 885, 2021.

[15] Y. F. Zhang, F. B. Zhou, and J. H. Kang, "Flow and heat transfer in drag-reducing polymer solution flow through the corrugated tube and circular tube," *Applied Thermal Engineering*, vol. 174, pp. 115185–115185, 2020.

[16] N. le Brun, I. Zadrazil, L. Norman, A. Bismarck, and C. N. Markides, "On the drag reduction effect and shear stability of improved acrylamide copolymers for enhanced hydraulic fracturing," *Chemical Engineering Science*, vol. 146, pp. 135–143, 2016.

[17] J. GUO, Y. LI, and S. WANG, "Adsorption damage and control measures of slick-water fracturing fluid in shale

reservoirs," *Petroleum Exploration and Development*, vol. 45, no. 2, pp. 336–342, 2018.

[18] Z. Y. Liu, F. J. Zhou, H. Y. Qu, Z. Yang, Y. S. Zou, and D. B. Wang, "Impact of the microstructure of polymer drag reducer on slick-water fracturing," *Geofluids*, vol. 2017, Article ID 9080325, 8 pages, 2017.

[19] A. Abubakar, T. al-Wahaibi, Y. al-Wahaibi, A. R. al-Hashmi, and A. al-Ajmi, "Roles of drag reducing polymers in single- and multi-phase flows," *Chemical Engineering Research and Design*, vol. 92, no. 11, pp. 2153–2181, 2014.

[20] Z. Lufeng, Z. Fujian, Z. Shicheng, L. zhun, W. Jin, and W. Yuechun, "Evaluation of permeability damage caused by drilling and fracturing fluids in tight low permeability sandstone reservoirs," *Journal of Petroleum Science and Engineering*, vol. 175, pp. 1122–1135, 2019.

[21] D. Wang, S. Zlotnik, P. Díez, H. Ge, F. Zhou, and B. Yu, "A numerical study on hydraulic fracturing problems via the proper generalized decomposition method," *Computer Modeling in Engineering and Sciences*, vol. 122, no. 2, pp. 703–720, 2020.

[22] D. Wang, Y. Dong, D. Sun, and B. Yu, "A three-dimensional numerical study of hydraulic fracturing with degradable diverting materials via CZM-based FEM," *Engineering Fracture Mechanics*, vol. 237, p. 107251, 2020.

[23] X. Bo, Z. Shicheng, L. Xin, Z. Tong, Z. Bo, and C. Laijun, "Optimization and evaluation of drag reducer of slickwater fracturing in shale gas reservoir," *Oil and gas geology and recovery*, vol. 21, no. 2, pp. 102–105, 2014.

[24] K. Zhang, H. J. Choi, and C. H. Jang, "Turbulent drag reduction characteristics of poly (acrylamide-co-acrylic acid) in a rotating disk apparatus," *Colloid and Polymer Science*, vol. 289, no. 17-18, pp. 1821–1827, 2011.

[25] Y. M. Cheng, "Impact of water dynamics in fractures on the performance of hydraulically fractured wells in gas-shale reservoirs," *Journal of Canadian Petroleum Technology*, vol. 51, no. 2, pp. 143–151, 2012.

[26] N. Liu, Z. Zhang, Y. Zou, X. Ma, and Y. Zhang, "Propagation law of hydraulic fractures during multi-staged horizontal well fracturing in a tight reservoir," *Petroleum Exploration and Development*, vol. 45, no. 6, pp. 1129–1138, 2018.

[27] Y. P. Sun, Q. H. Wu, M. Z. Wei, B. Bai, and Y. Ma, "Experimental study of friction reducer flows in microfracture," *Fuel*, vol. 131, pp. 28–35, 2014.

[28] Z. J. Song, L. B. Liu, J. R. Hou, B. Bai, and W. Su, "Effect of polymer on gas flow behavior in microfractures of unconventional gas reservoirs," *Journal of Natural Gas Science and Engineering*, vol. 23, pp. 26–32, 2015.

[29] F. C. Li, Y. Kawaguchi, B. Yu, J. J. Wei, and K. Hishida, "Experimental study of drag-reduction mechanism for a dilute surfactant solution flow," *International Journal of Heat and Mass Transfer*, vol. 51, no. 3-4, pp. 835–843, 2008.

[30] F. Fan, F. Zhou, and Z. Liu, "Experimental and Numerical Study on Drag Reduction Performance of Slickwater in Turbulent Pipeflow," in *International Field Exploration and Development Conference*, pp. 471–484, Springer, 2018.

[31] J. Fink, "Chapter 12 - Drag Reducers," in *Petroleum Engineer's Guide to Oil Field Chemicals and Fluids (Third Edition)*, pp. 517–529, Gulf Professional Publishing, 2021.

[32] C. Zou, D. Dong, Y. Wang et al., "Shale gas in China: characteristics, challenges and prospects (II)," *Petroleum Exploration and Development*, vol. 43, no. 2, pp. 182–196, 2016.

Hindawi
Geofluids
Volume 2021, Article ID 9446293, 15 pages
https://doi.org/10.1155/2021/9446293

Research Article

Study on the Surge-Swab Pressure considering the Effect of the Cutting Plug in Shale Drilling

Tianyi Tan, Hui Zhang, Xusheng Ma, and Yufei Chen

College of Petroleum Engineering, China University of Petroleum-Beijing, 102249, China

Correspondence should be addressed to Hui Zhang; zhanghuicup@163.com

Received 7 September 2021; Accepted 5 November 2021; Published 26 November 2021

Academic Editor: Afshin Davarpanah

Wellbore instability is a frequent problem of shale drilling. Accurate calculation of surge-swab pressures in tripping processes is essential for wellbore pressure management to maintain wellbore stability. However, cutting plugs formed in shale horizontal wells have not been considered in previous surge-swab pressure models. In this paper, a surge-swab pressure model considering the effect of cutting plugs is established for both open pipe string and closed pipe string conditions; In this model, the osmotic pressure of a cutting plug is analyzed. The reduction of cutting plug porosity due to shale hydration expansion and dispersion is considered, ultimately resulting in an impermeable cutting plug. A case study is conducted to analyze swab pressures in a tripping out process. The results show that, in a closed pipe condition, the cutting plug significantly increases the swab pressures below it, which increase with the decrease of cutting plug porosity and the increase of cutting plug length. Under the give condition, the swab pressure at the bottom of the well increases from 3.60 MPa to 8.82 MPa due to the cutting plug, increasing by 244.9%. In an open pipe string condition, the cutting plug affects the flow rate in the pipes and the annulus, resulting in a higher swab pressure above the cutting plug compared to a no-cutting plug annulus. The difference increases with the decrease of the porosity and the increase of the length and the measured depth of the cutting plug. Consequently, the extra surge-swab pressures caused by cutting plugs could result in wellbore pressures out of safety mud density window, whereas are ignored by previous models. The model proposes a more accurate wellbore pressure prediction and guarantees the wellbore stability in shale drilling.

1. Introduction

As a fossil resource preserved in nanoscale pores in organic-rich shale, shale oil is now an essential part of the world energy market [1]. In 2018, the production of shale oil was 23.49×10^8 bbl in the U.S., accounting for 64.7% of the total petroleum output [2]. In 2040, the productivity is estimated as 94.6×10^5 bbl/d. In China, the technically recoverable shale oil is estimated as 55×10^8 t, making up 9.7% of the technically recoverable shale oil resource in the whole world [3], mainly distributed in Jilin, Daqing, and the northwest of China [4]. Due to the exhaustion of conventional oil and gas resources, shale oil has been considered as one of the most promising energy sources in the future [4]. However, along with the great prospect of shale oil, significant challenges still exist. The horizontal well drilling in a shale formation is the kernel technique to exploit shale oil. Due to the special trajectory of horizontal wells and the unique characteristics of shale formation, problems caused by wellbore instability are frequent in drilling engineering. Accidents like borehole collapse, loss of drilling fluid and pipe sticking result in vast nonproductive time, and tremendous economic losses.

Wellbore stability is the core of safe and efficient drilling. To guarantee wellbore stability in shale formations, the wellbore pressure should be kept in an allowable range (safety mud density window) during a drilling process [5]. In general, the upper limit of the allowable range is the formation fracture pressure. With the wellbore pressure higher than the formation fracture pressure, tensile failure occurs in the wellbore rock [6], and drilling fluid flows into the formation through these fractures. This harmful drilling fluid loss defined as lost circulation [7] entails various problems [8] like consumption of enormous drilling fluid, inefficient cutting transportation, and reservoir pollution. Especially for

shale drilling, the fluid loss aggravates the hydration of shale formation, resulting in further wellbore instability problems. The lower limit of the allowable range is determined by the larger one between the formation collapse pressure and the formation pore pressure. With the wellbore pressure lower than the formation collapse pressure, shear failure forms in the borehole rock and wellbore collapse occurs [6]. Wellbore collapse results in drilling problems like pipe sticking and borehole expansion. With the wellbore pressure lower than the formation pore pressure, formation fluid flows into the wellbore due to the hydraulic imbalance, defined as fluid influx. The fluid influx might induce serious drilling problems like well kick and blowout. Accidents caused by unsuccessful wellbore pressure management have resulted in enormous financial loss, nonproductive time, and even casualties [8, 9].

Most of the wellbore instability problems occur in tripping in/out processes, due to surge-swab pressures caused by pipe string movements. By definition, surge-swab pressures are the additional pressures generated by axial movements of the drilling string in the wellbore [10]. The research of surge-swab pressures has been started at an early time. Cannon [11] conducted tests to measure pressure changes with downhole pressure gauges when withdrawing pipes, regarding that the pipe withdrawing entails wellbore pressure reduction and might lead to blow-out accidents. Later, more experiments were conducted, and field data was investigated about surge-swab pressures [12–16], mostly for validation and improvement of theoretical models. Besides experimental work, theoretical studies are dedicated to establishing models of the surge-swab pressure, including steady-state models and dynamic (or transient) models. Clark [17] proposed semiempirical formulas of equivalent velocities for steady-state surge-swab pressure calculation. The pressure caused by fluid acceleration was also considered in his work. Burkhardt [18] established a surge-swab pressure model with theoretical studies, proposing the graph of mud clinging constant for convenient use. Fontenot and Clark [19] established a comprehensive steady surge-swab pressure model considering the drilling fluid property variation with depth. Subsequent work on steady-state surge-swab pressure has been dedicated to improving the model with various optimizations. Wang and Liu [20] established the steady-state surge-swab pressure model for Robertson-Stiff fluid, which is also a kind of yield-pseudoplastic fluid. In the work of Wang et al. [21], the effect of pipe eccentricity was considered on Newtonian drilling fluid. Crespo et al. [22] established a steady-state model taking account of fluid and formation compressibility and pipe elasticity for yield power-law (YPL) fluid. Later in 2013, a laboratory experiment was conducted, and a regression model of surge-swab pressures was developed for YPL fluid [23]. Tang et al. [24] established a steady-state model considering the effect of the drilling string velocity on the boundary condition. Ettehadi and Altun [25] established a steady-state model for Hershel-Bulkley (HB) fluid and applied in situ thermal rheological measurements to amend rheological parameters of drilling fluid. Krishna et al. [26] proposed explicit flow velocity equations for steady-state surge-swab pressure models of yield power law fluid to achieve more convenient calculation. The dynamic model (or transient model) is another route to deal with the issue of the surge-swab pressure [27–31]. Different from steady-state models, dynamic models take account of the elasticity of the pipes and the wellbore, the inertia and compressibility of drilling fluid, and the variation of tripping velocity [10]. Due to complexity of calculation, dynamic models are difficult to be applied in field drilling practice.

As noted above, scores of researches have been conducted on the surge-swab pressure in drilling engineering. However, in shale formation drilling, the effect of an influential phenomenon on the surge-swab pressure has not been considered in existing studies: the effect of a cutting plug. Due to the low permeability of the reservoirs, horizontal wells are essential in the development of shale oil. Wellbore uncleanness is a prominent problem of horizontal well drilling. Cutting particles are easy to accumulate in a horizontal wellbore, and cutting plugs might be formed when pump is stopped and tripping processes are conducted. Different from a cutting bed, a cutting plug fills the annulus at a certain length [32]. Fluid flow in tripping in and tripping out processes is affected by this particular accumulation of cutting particles. Excessive wellbore pressures under a cutting plug condition are not able to be predicted by previous models, resulting in the wellbore instability risk of shale drilling. In this article, a surge-swab model considering the effect of a cutting plug is established for both open pipe string and closed pipe string conditions. The porosity variety of the shale cutting plug is also considered. Finally, a case study is conducted to give a deeper insight.

2. Formation of Cutting Plugs

The cutting plug is a cutting particle cylinder in the annulus between the drilling string and the wellbore formed in three conditions (Figure 1): (1) the cuttings accumulated at a borehole-enlarged section slide down due to the disturbance of the tripping pipe string, (2) the cuttings in the vertical and small-inclination sections settle down and accumulate in the large-inclination and horizontal sections when circulation is stopped, and (3) the cuttings at the lower side of the wellbore as a cutting bed are pushed and accumulated by the large diameter tools in repetitive reaming or tripping processes like the bulldozer work.

3. Establishment of Model

3.1. Assumptions. To develop the model, following assumptions are made: (1) the drilling fluid is incompressible, (2) for the accurate description of drilling fluid rheological properties and the simplicity of expression [33], power-law flow pattern is considered for the drilling fluid, (3) the rheology of the drilling fluid is assumed constant, ignoring the effect of temperature and pressure, (4) the drilling string and the wellbore are rigid, (5) the drilling string is concentric in the wellbore, and (6) the effect of cutting particles out of the cutting plug is overlooked.

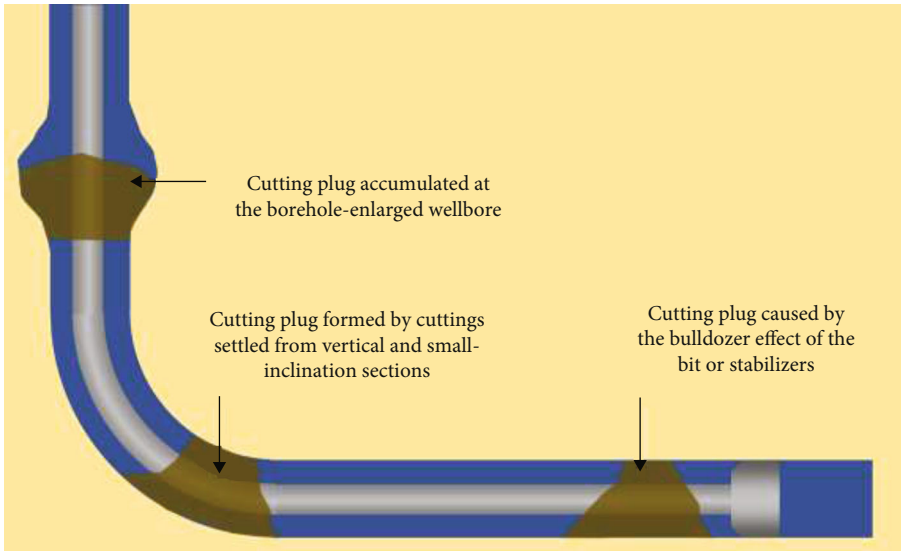

Figure 1: The sketch of cutting plugs formed in a shale horizontal well.

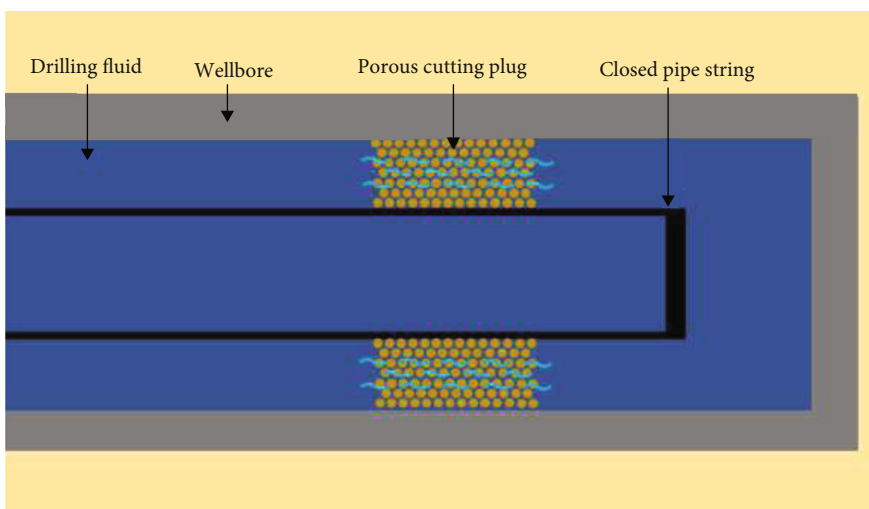

Figure 2: A closed pipe string with a porous cutting plug.

3.2. Closed Pipe String. A close pipe string features a blind end at the bottom, like a bit with blocked nozzles, a drilling pipe with a check valve, or a casing with a float collar. The close pipe string prevents the flow between the pipes and the annulus.

Two types of cutting plugs are considered in the model, namely, the porous cutting plug and the impermeable cutting plug. The porous cutting plug refers to an accumulated permeable cutting bulk (Figure 2), allowing the drilling fluid flow in the form of seepage. Further, due to the hydration expansion and dispersion of shale cutting particles, the pores in the cutting plug shrink and are blocked by fine dispersive particles. The porosity of the cutting plug reduced and finally an impermeable cutting plug is formed. Therefore, the impermeable cutting plug refers to an impermeable cutting bulk (Figure 3).

3.2.1. Porous Cutting Plug. The surge-swab pressure above a porous cutting plug is similar with that in a wellbore without a cutting plug, while the surge-swab pressure below the cutting plug equals the sum of two pressure losses: the frictional pressure loss along the annulus and the osmotic pressure loss at the porous cutting plug. The calculation of the frictional pressure loss in a steady-state model requires the effective velocity of drilling fluid, consisting of two components: the average velocity representing the flow rate of the drilling fluid and the cling velocity caused by pipe string axial motion.

The average velocity v_a of drilling fluid in the annulus can be obtained [10]:

$$v_a = \frac{4Q_a}{\pi\left(D_w^2 - D_{\mathrm{po}}^2\right)}, \tag{1}$$

in which, the flow rate in the annulus Q_a of a closed pipe string condition is expressed as

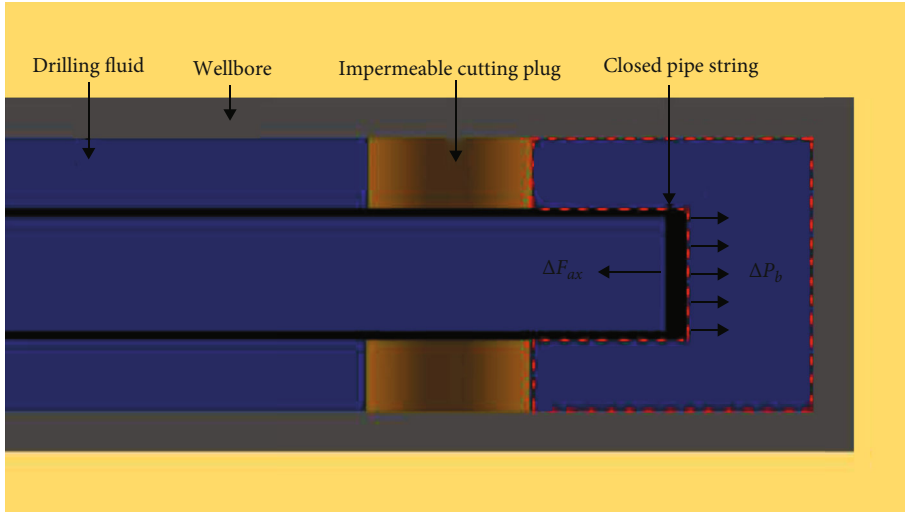

Figure 3: A closed pipe string with an impermeable cutting plug.

$$Q_a = -\frac{\pi D_{\mathrm{po}}^2 v_t}{4}. \tag{2}$$

The velocities from the well bottom to the ground in this paper are regarded positive. The clinging velocity of drilling fluid v_c in the annulus depends on the tripping velocity of the pipe string v_t:

$$v_c = -Cv_t, \tag{3}$$

in which, C is the mud clinging constant [10, 18]. Thus, the effective velocity of drilling fluid is expressed as

$$v_{ae} = v_a + v_c. \tag{4}$$

In this paper, the calculation method of frictional pressure in the annulus and pipes is referred to the literature of Fan [10] and Li et al. [5]. The frictional pressure loss in the annulus is obtained with the effective velocity v_{ae} (the positive or the negative sign of the frictional pressure loss is the same of that of the effective velocity):

$$\Delta p_a = \frac{2f_a L\rho v_{ae}^2}{D_w - D_{\mathrm{po}}}, \tag{5}$$

in which, the frictional factor f_a in the annulus is expressed as

$$f_a = \frac{a}{\mathrm{Re}^b}. \tag{6}$$

The constants a and b depends on the flow pattern of the drilling fluid. For laminar flow they are expressed as

$$\begin{cases} a = 24, \\ b = 1, \end{cases} \tag{7}$$

and for turbulent flow, they are

$$\begin{cases} a = \dfrac{\lg n + 3.93}{50}, \\ b = \dfrac{1.75 - \lg n}{7}. \end{cases} \tag{8}$$

The Reynolds number of the flow in the annulus is expressed as

$$\mathrm{Re} = \frac{12^{1-n}\rho\left(D_w - D_{po}\right)^n |v_a|^{2-n}}{K_c(2n + 1/3n)^n}. \tag{9}$$

The second part of the surge-swab pressure results from the osmotic pressure loss at the porous cutting plug, obtained with the flow rate through it and its physical properties like the porosity and the cutting plug length (in the flow direction). For the power law fluid, the osmotic pressure can be derived from the superficial velocity [34, 35] through a porous material:

$$\Delta p_o = \frac{2K_c\left(4Q_a/\left(D_w^2 - D_p^2\right)\pi\right)}{\phi^n(n/3n + 1)^n R_c^{1+n}} L_p, \tag{10}$$

in which, the capillary radius is obtained with the hydraulic radius [36]:

$$R_c = 2R_h, \tag{11}$$

and the hydraulic radius is obtained with the porosity [37]:

$$R_h = \frac{\phi D_c}{6(1-\phi) + (4D_c/D_w)}. \tag{12}$$

Therefore, the surge-swab pressure in the wellbore with a porous cutting plug is the sum of the frictional pressure loss and the osmotic pressure loss:

$$\Delta p_s = \Delta p_a + \Delta p_o. \tag{13}$$

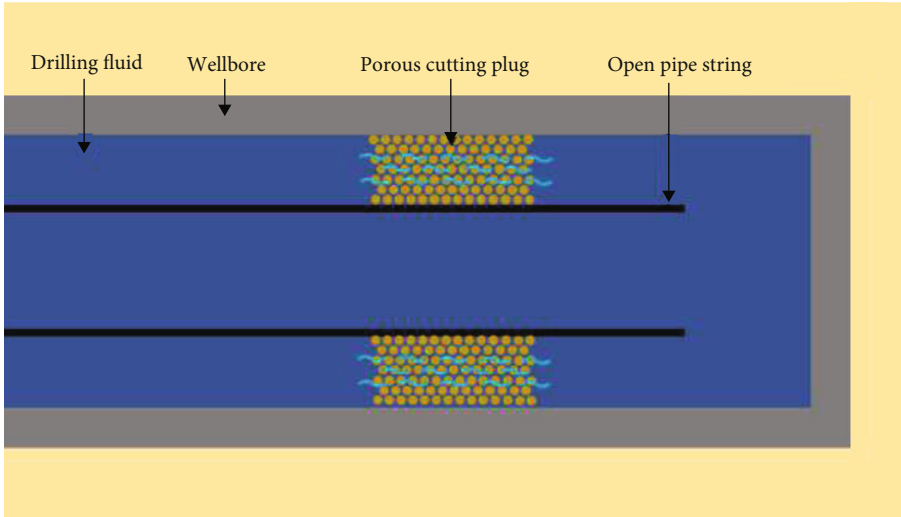

Figure 4: An open pipe string with a porous cutting plug.

The wellbore pressure at any given position in the annulus and below the pipe string can be obtained:

$$p_w = p_g + \Delta p_h + \Delta p_s. \tag{14}$$

3.2.2. Impermeable Cutting Plug. The condition with both an impermeable cutting plug and a closed pipe string is the most dangerous for wellbore stability. Shown as the area surrounded by red dotted lines in Figure 3, the impermeable cutting plug, the wellbore, and the closed pipe string form an enclosed space. Without mass transfer between the enclosed space and its outside, the surge-swab pressure is not controlled by the frictional pressure loss and osmotic pressure loss. Considering the assumed incompressibility of the drilling fluid, the additional axial force on the closed bottom of the pipe string in tripping in or tripping out processes is directedly balanced by the additional hydraulic pressure in the enclosed space:

$$\Delta F_{\mathrm{ax}} = \frac{\pi D_b^2 \Delta p_b}{4}. \tag{15}$$

3.3. Open Pipe String. An open pipe string allows drilling fluid to flow between the annulus and the pipes during tripping processes through the access at the end of it, such as nozzles of the bit. Both the porous cutting plug and the impermeable cutting plug are considered with the open pipe string.

3.3.1. Porous Cutting Plug. With the porous cutting plug in the annulus, the drilling fluid is still allowed to flow (Figure 4). Therefore, the surge-swab pressure above and below the cutting plug are composed the same as those under the closed pipe string condition, while the flow rates and velocities required for calculation are different due to the mass exchange with the inside of pipes.

For a condition with both a porous cutting plug and an open pipe string, the flow rates in the annulus and the pipes satisfy the conservation of mass [10]:

$$\frac{\pi\left(D_w^2 - D_{\mathrm{po}}^2\right)v_{\mathrm{ae}}}{4} + \frac{\pi\left(D_w^2 - D_{\mathrm{po}}^2\right)Cv_t}{4} + \frac{\pi\left(D_{\mathrm{po}}^2 - D_{\mathrm{pi}}^2\right)v_t}{4} + Q_p = 0. \tag{16}$$

Similar to the closed pipe condition, the calculation of frictional pressure loss in the annulus requires the effective fluid velocity:

$$v_{\mathrm{ae}} = -v_t\left(C + \frac{D_{\mathrm{po}}^2 - D_{\mathrm{pi}}^2}{D_w^2 - D_{\mathrm{po}}^2}\right) - \frac{4Q_p}{\pi\left(D_w^2 - D_{\mathrm{po}}^2\right)}. \tag{17}$$

Then, frictional pressure loss in annulus Δp_a can be obtained. The osmotic pressure can also be calculated with the method in the closed pipe string section, while the flow rate in the annulus Q_a is expressed as

$$Q_a = -\frac{\pi\left(D_{\mathrm{po}}^2 - D_{\mathrm{pi}}^2\right)v_t}{4} - Q_p. \tag{18}$$

As shown above, the effective fluid velocity and the flow rate in the annulus cannot be calculated explicitly due to the unknown Q_p. A trial-and-error calculation is required here to determined v_{ae} and Q_a. Q_p is adjusted to satisfy the pressure equality at the bottom of the pipe string [10]:

$$p_{p0} = p_{a0}, \tag{19}$$

which indicates the wellbore pressure at the bottom calculated with the flow in the pipes equals that with the flow in the annulus.

To calculate the wellbore pressure at the bottom with the flow in the pipes, the frictional pressure loss in pipes is necessary [10, 38]:

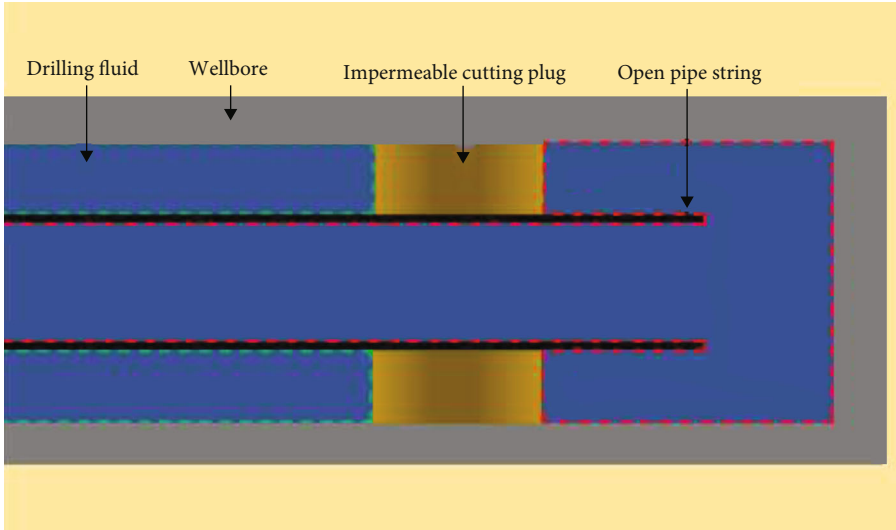

Figure 5: An open pipe string with an impermeable cutting plug.

$$\Delta p_p = \frac{2f_p L \rho v_{\mathrm{pe}}^2}{D_{\mathrm{pi}}}, \tag{20}$$

in which, the effective velocity of drilling fluid in pipes is the vector sum of the average velocity and the tripping velocity:

$$v_{\mathrm{pe}} = v_p - v_t, \tag{21}$$

and the average velocity of drilling fluid in pipes is expressed as

$$v_p = \frac{4Q_p}{\pi D_{\mathrm{pi}}^2}. \tag{22}$$

The friction factor for a pipe flow is similar to that in the annulus:

$$f_p = \frac{a}{\mathrm{Re}^b}, \tag{23}$$

while the constants for laminar flow are different:

$$\begin{cases} a = 16, \\ b = 1. \end{cases} \tag{24}$$

For turbulent flow, the calculation of constants a and b refers to Equation (8). The Reynolds number for the flow in pipes is expressed as

$$\mathrm{Re} = \frac{8^{1-n} \rho D_{\mathrm{pi}}^n v_{\mathrm{pe}}^{2-n}}{K_c (3n + 1/4n)^n}. \tag{25}$$

Therefore, the surge-swab pressure in the annulus can be calculated. Similar to the closed pipe string condition, the wellbore pressure at any given position is obtained:

Table 1: Trajectory data of the horizontal well.

Parameter	Value	Unit
Length of the vertical section	1956.3	m
Inclination at the kick off point	0	°
Dogleg severity of the build-up section	20.55	°/100 m
Inclination at the end of the build-up section	90	°
Length of the horizontal section	1500	m

Table 2: Input data of the model.

Parameter	Value	Unit
Outer diameter of the pipes	137.9	mm
Inner diameter of the pipes	118.6	mm
Diameter of the casing section	224.41	mm
Diameter of the open-hole section	215.9	mm
Drilling fluid density	1500	$\mathrm{Kg/m^3}$
Consistency coefficient	0.75	$\mathrm{Pa{\cdot}m^n}$
Liquidity index	0.67	—
Tripping out/in velocity	0.65	m/s
Clinging constant in casing section	0.418	—
Clinging constant in open-hole section	0.426	—
Porosity	0.36	—
Cutting particle diameter	3	mm
Measured depth of the cutting bridge	2500	m
Length of the cutting bridge	1	m

$$p_w = p_g + \Delta p_h + \Delta p_s. \tag{26}$$

3.3.2. Impermeable Cutting Plug. For the condition with the open pipe string and the impermeable cutting plug, the drilling fluid is divided into two spaces (Figure 5): (a) the space of the annulus above the impermeable cutting plug; (b) the

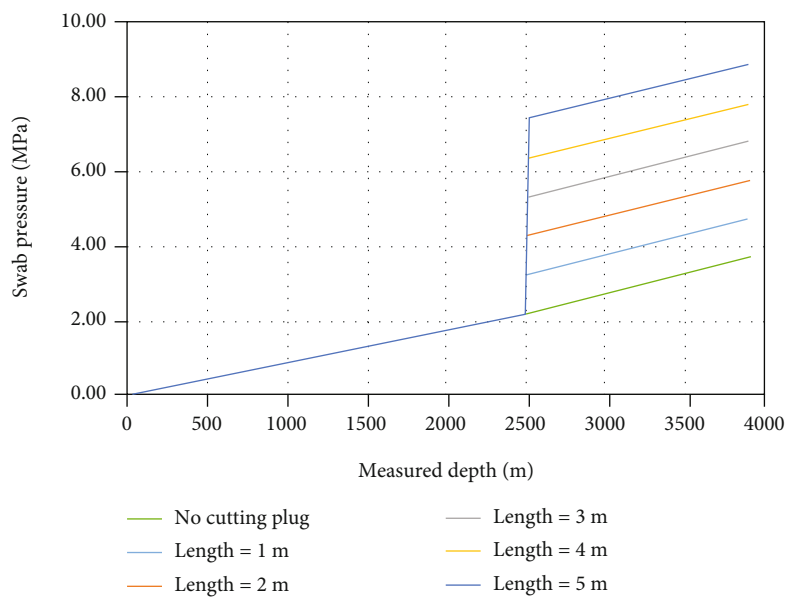

Figure 6: The effect of cutting plug length on the swab pressures in a closed pipe condition.

space composed by the annulus below the impermeable cutting plug, the wellbore below the bit, and the inside of the pipe string. The wellbore pressures (annulus pressures) in these two spaces should be calculated separately.

Due to the existence of the impermeable cutting plug, there is no flow rate in the annuli of both spaces. Therefore, the surge-swab pressures in the annuli are caused only by the clinging velocity:

$$v_{\mathrm{ae}} = v_c. \tag{27}$$

The wellbore pressure in the annulus above the impermeable cutting plug can be calculated with the surge-swab pressure and the hydrostatic pressure as usual, whereas the calculation in the annulus below the cutting plug is more complicated. The wellbore pressure p_{a0} at the bottom of the pipe string, equal to the pipe pressure p_{b0}, is required as the boundary condition. p_{a0} is calculated with the hydrostatic pressure and the frictional pressure loss inside the pipes, in which the flow rate Q_p is

$$Q_p = -\frac{\pi\left(D_{\mathrm{po}}^2 - D_{\mathrm{pi}}^2\right)v_t}{4}. \tag{28}$$

Therefore, the wellbore pressure above the cutting plug is

$$p_w = p_g + \Delta p_h + \Delta p_s. \tag{29}$$

The wellbore pressure between the cutting plug and the end of the pipe string is

$$p_w = p_{a0} - \Delta p_h - \Delta p_s. \tag{30}$$

The wellbore pressure below the end of the pipe string is

$$p_w = p_{a0} + \Delta p_h. \tag{31}$$

4. Results and Discussion

A horizontal well [39–41] is adopted to conduct a case study, consisting of a vertical section, a build-up section, and a horizontal section. The trajectory data and the input data of model calculation are separately presented in Tables 1 and 2. The length of the horizontal section is assumed as 1500 m. The casing shoe of the intermediate casing is assumed at the end of the build-up section (2394.3 m) for simplification. The case study is conducted for the swab pressure, while the surge pressure is exactly of the same magnitude with an opposite sign. The swab pressures are all calculated with the bit at the bottom of the wellbore (3894.3 m). The length of the cutting plug is only considered in the calculation of the osmotic pressure loss and ignored in the calculation of the wellbore pressure distribution.

4.1. Closed Pipe String. For a closed pipe string, the swab pressure distributions in tripping out processes with and without a cutting plug are compared in Figure 6, along with the effect of the cutting plug length. The swab pressures are calculated with of the length of 1 to 5 m, respectively. Results show that, under the given condition, the swab pressures above the measured depth of the cutting plug (2500 m) are correspondingly identical, while below the cutting plugs, the swab pressures are all greater than those in a wellbore without a cutting plug. The swab pressures below the cutting plug increase with the increase of the cutting plug length, due to the greater osmotic pressure loss caused by a longer cutting plug. At the bottom of the wellbore, the swab pressure is 8.82 MPa with a 5 m cutting plug, increasing by 244.9% of the swab pressure without a cutting plug (3.60 MPa).

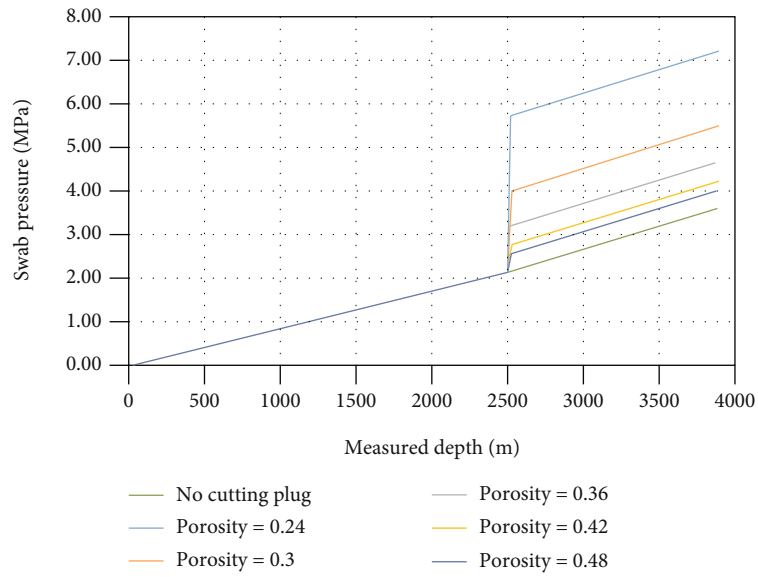

Figure 7: The effect of cutting plug porosity on the swab pressures in a closed pipe condition.

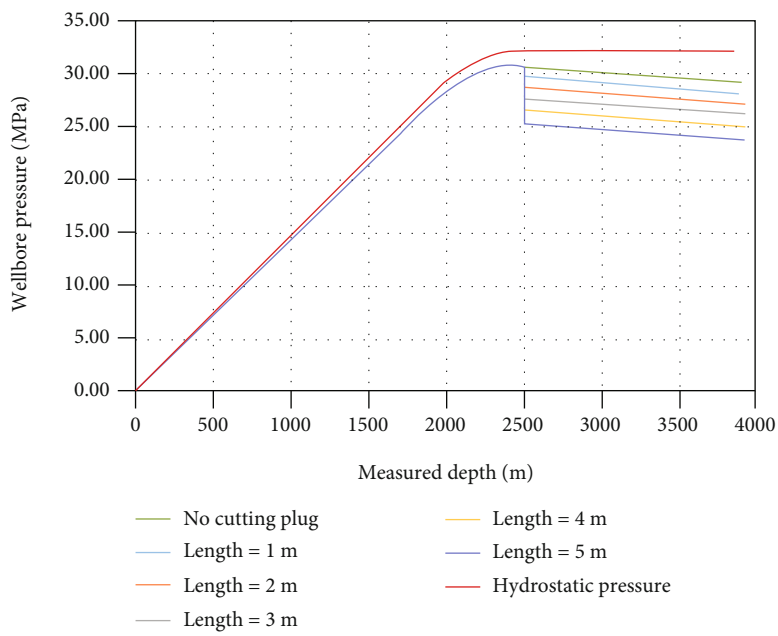

Figure 8: The effect of cutting plug length on the wellbore pressures in a closed pipe condition.

The effect of the porosity of the cutting plug on swab pressures is investigated and shown in Figure 7. The swab pressures are calculated with 0.24, 0.3, 0.36, 0.42, and 0.48 porosity, respectively. Similar with the trend of different cutting plug length, the results show that a lower porosity leads to a greater osmotic pressure loss, resulting in greater swab pressures below the measured depth of the cutting plug. At the bottom of the wellbore, the swab pressure is 7.18 MPa with a 0.24 porosity, increasing by 199.0% of the swab pressure without a cutting plug.

Consequently, the wellbore pressures differ among the cutting plug conditions above. The effect of the cutting plug length on the wellbore pressures is shown in Figure 8. The wellbore pressures above the measured depth of the cutting plug (2500 m) are correspondingly identical. Those below the cutting plug decrease with the increase of the cutting plug length, due to the greater swab pressures. At the bottom of the well, the hydrostatic pressure is 32.86 MPa, the wellbore pressure without a cutting plug is 29.25 MPa, and the wellbore pressure with a 5 m cutting plug is 24.03 MPa, 5.22 MPa lower than that in the condition without a cutting plug. The effect of the porosity on the wellbore pressures is shown in Figure 9. The wellbore pressures below the cutting plug decrease with the decrease of the cutting plug porosity. At the bottom of the well, the wellbore pressure with a cutting plug featuring a porosity

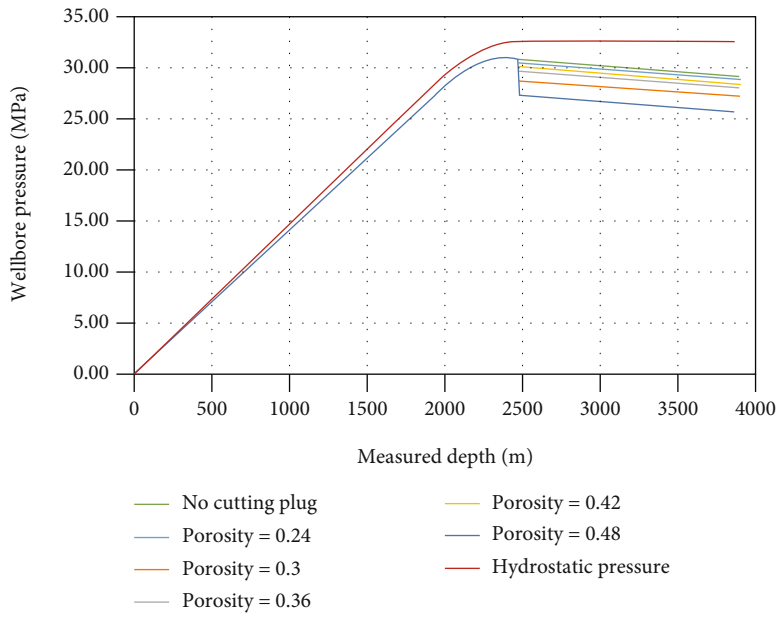

Figure 9: The effect of cutting plug porosity on the wellbore pressures in a closed pipe condition.

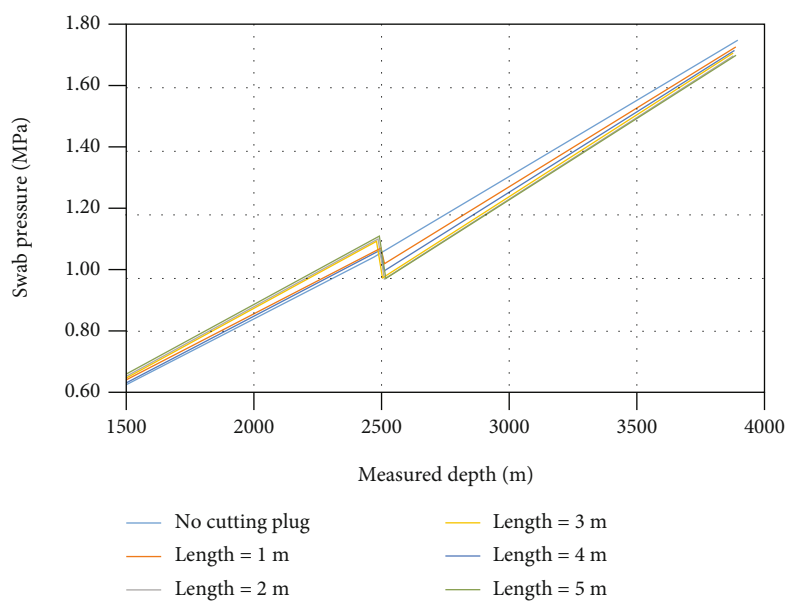

Figure 10: The effect of cutting plug length on the swab pressures in an open pipe condition.

0.24 is 25.68 MPa, 3.57 MPa lower than that in the condition without a cutting plug.

As analyzed above, an overestimation of the wellbore pressure would be generated by the previous no-cutting-plug model for a condition with cutting plugs. The overestimation is greater with the existence of a longer or low-porosity cutting plug, resulting in more risk on the wellbore stability.

4.2. Open Pipe String. The swab pressures are also calculated for an open pipe string with different cutting plug lengths, as shown in Figure 10. The swab pressures above the cutting plug measure depth are greater than those without a cutting plug, while the swab pressures below are lower. The difference increases with the length and is maximal near the cutting plug. Thus, the curve of swab pressures with shorter cutting plug is closer to the curve of no cutting plug. In the terms of quantity, at the measured depth of 2500 m, the swab pressure of the no-cutting-plug condition is 1.05 MPa, while it is 1.11 MPa of the 5 m cutting plug condition. At the measured depth of 2520 m, the swab pressure of the no-cutting-plug condition is 1.06 MPa, while it is 0.97 MPa of the 5 m cutting plug condition.

Similar tendency exists among different porosities of the cutting plug, as shown in Figure 11. With lower porosity, the swab pressures are higher above the cutting plug and lower

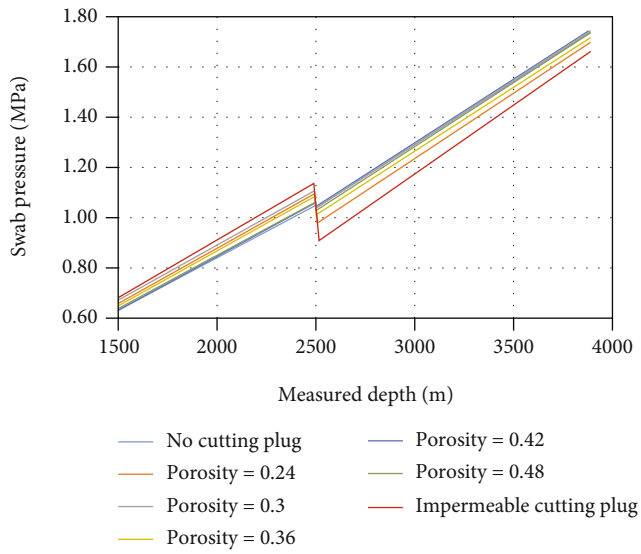

Figure 11: The effect of cutting plug porosity on the swab pressures in an open pipe condition.

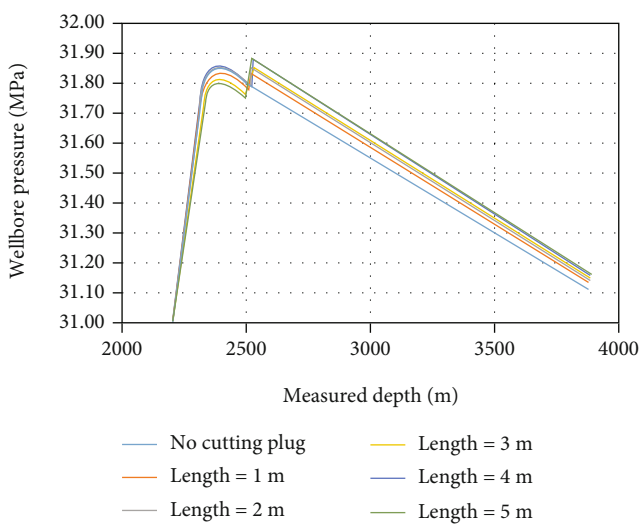

Figure 12: The effect of cutting plug length on the wellbore pressures in an open pipe condition.

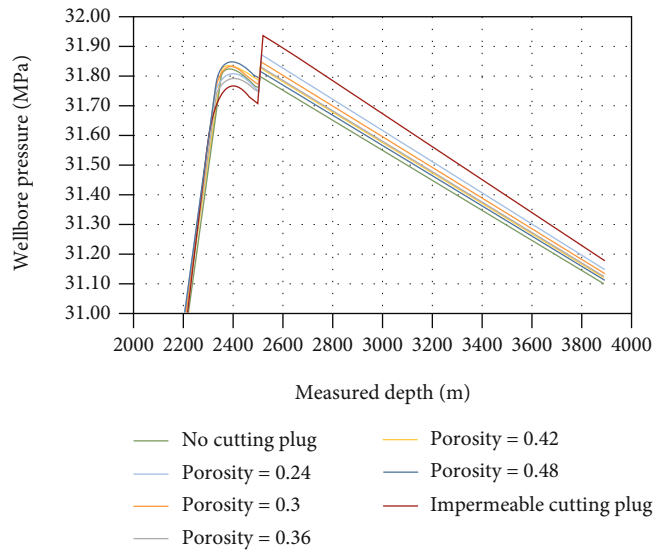

Figure 13: The effect of cutting plug porosity on the wellbore pressures in an open pipe condition.

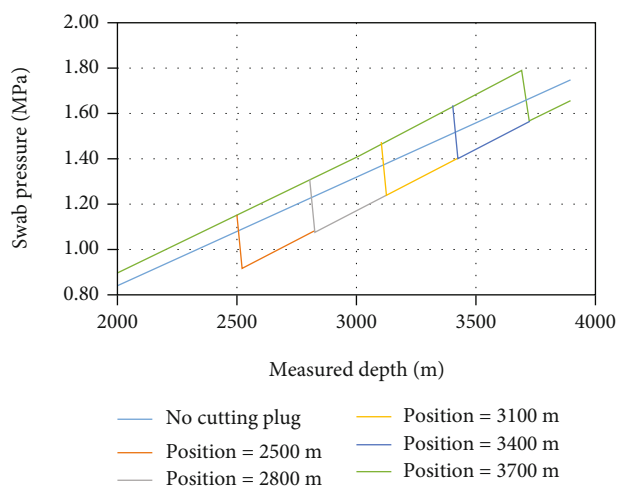

Figure 14: The effect of cutting plug position on the swab pressures in an open pipe condition.

below. The porosity of an impermeable cutting plug can be regarded as the lowest as 0. Even the calculation of the impermeable cutting plug is different from that of a porous one, the result still satisfies the tendency. In the terms of quantity, the swab pressure of the impermeable cutting plug condition is 1.14 MPa at the measured depth of 2500 m and 0.92 MPa at 2520 m.

The effect of the cutting plug length on the wellbore pressures is shown in Figure 12. Resulting from the swab pressure distribution, compared to the condition without a cutting plug, the wellbore pressures above the cutting plug are lower, and those below the cutting plug are higher. The wellbore pressure is 31.80 MPa at 2500 m for the no-cutting-plug wellbore, while it is 31.75 MPa above the 5 m cutting plug at the same measured depth. The wellbore pressure is 31.79 MPa at 2520 m for the no-cutting-plug wellbore, while it is 31.88 MPa below the 5 m cutting plug at the same measured depth.

The effect of the cutting plug porosity on the wellbore pressures has a similar trend with the cutting plug length, shown in Figure 13. The cutting plug with lower porosity results in greater differences of wellbore pressures from those without a cutting plug. Therefore, the impermeable cutting plug has the greatest influence. In the terms of quantity, the wellbore pressure at 2500 m above the impermeable cutting plug is 31.71 MPa and is 31.93 MPa at 2520 m below it.

The difference of wellbore pressure distribution between the open pipe and the closed pipe conditions results from the difference between their annulus flow rates. In the condition of a closed pipe string, the flow rate in the annulus is independent on the length and the porosity of the cutting plug, whereas in the condition of an open pipe string, the flow rate

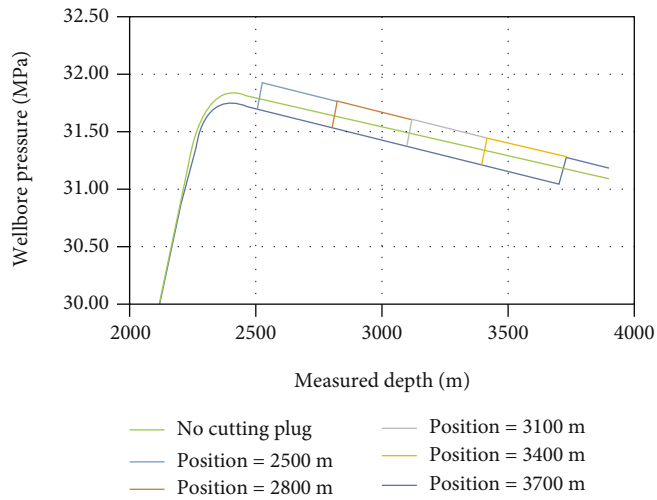

Figure 15: The effect of cutting plug position on the wellbore pressures in an open pipe condition.

decreases with the increase of the length and the decrease of the porosity of the cutting plug to satisfy the pressure balance at the joint of the annulus and the pipe inside.

The effect of the position of the cutting plug on the swab pressures is investigated. Swab pressures with an impermeable cutting plug at 2500 m, 2800 m, 3100 m, 3400 m, and 3700 m are calculated, shown in Figure 14. Besides the aforementioned results, the swab pressure difference varies with the cutting plug position. The difference between of swab pressures above the cutting plug between the conditions with and without a cutting plug increases with the cutting plug measured depth, which means the error of the previous swab pressure model applied on a cutting-plug condition is greater. In the terms of quantity, the swab pressure above the 2500 m cutting plug is 1.14 MPa and is 1.05 MPa without a cutting plug, resulting in a difference of 0.09 MPa, while the swab pressure above the 3700 m cutting plug is 1.80 MPa and is 1.65 MPa without a cutting plug, resulting in a difference of 0.15 MPa. Correspondingly, the difference of wellbore pressures above the cutting plug increases with the measured depth of it, shown in Figure 15. Consequently, the wellbore instability risk of application of the previous swab pressure model in a cutting plug condition is higher with a deeper cutting plug.

5. Conclusions

(1) A surge-swab pressure model is established considering the effect of cutting plugs, which is not considered in existing surge-swab pressure models. Both the open pipe string and closed pipe string conditions are considered. Cutting plug might develop from a porous one into an impermeable one due to clay hydration and dispersion of shale, resulting in the difference of pressure calculation

(2) A cutting plug in the closed pipe string condition has significant influence on surge-swab pressures. The surge-swab pressures above the cutting plug measured depth are identical to those without a cutting plug, while the surge-swab pressures below increase with the increase of the cutting plug length and the decrease of the cutting plug porosity. Quantitively, at the bottom of the wellbore, the swab pressure is 8.82 MPa with a 5 m cutting plug (porosity = 0.36) and 7.18 MPa with a 0.24 porosity (cutting plug length = 1 m), respectively, 244.9% and 199.0% of the swab pressure without a cutting plug (3.60 MPa). Consequently, the previous model overestimates the wellbore pressure for 5.22 MPa with a 5 m cutting plug and for 3.57 MPa with a 0.24 porosity cutting plug, resulting in the risk of inappropriate wellbore pressure management

(3) A cutting plug in the open pipe condition brings in more complicated influence on surge-swab pressures. Compared to the condition without a cutting plug, the surge-swab pressures are higher above the cutting plug measured depth and lower below. The difference increases with the decrease of the cutting plug porosity and the distance from the cutting plug and the increase of the length of the cutting plug. The difference above the cutting plug increases with the measured depth of the cutting plug. Quantitively, at the measured depth of 2500 m, the swab pressure of the no-cutting-plug condition is 1.05 MPa, while it is 1.11 MPa of the 5 m cutting plug condition and 1.14 MPa of the impermeable cutting plug condition. Compared to the cutting plug at 2500 m, the swab pressure above the 3700 m impermeable cutting plug is 1.80 MPa and is 1.65 MPa of the no-cutting-plug condition

(4) The model proposed in this work reveals extra surge-swab pressures and hazardous wellbore pressures under the effect of cutting plugs ignored by previous models, detecting potential wellbore instability risk of previous models. The model can be applied in field practice to guide the optimization of tripping parameters and guarantee the wellbore stability of shale drilling

Appendix

The calculation procedure for all four cases of the model in Section 3 (establishment of model) is systematized for the convenience of readers and users. Relevent references are denoted in Section 3.

A.1. Closed Pipe String with a Porous Cutting Plug

Calculate the flow rate in the annulus Q_a:

$$Q_a = -\frac{\pi D_{\mathrm{po}}^2 v_t}{4}. \tag{A.1}$$

Calculate the average velocity v_a of drilling fluid in the annulus:

$$v_a = \frac{4Q_a}{\pi\left(D_w^2 - D_{\mathrm{po}}^2\right)}. \tag{A.2}$$

Calculate the clinging velocity v_c of drilling fluid in the annulus:

$$v_c = -Cv_t. \tag{A.3}$$

Combining Eq. (A.2) and Eq. (A.3), calculate the effective velocity v_{ae} of drilling fluid in the annulus:

$$v_{\mathrm{ae}} = v_a + v_c. \tag{A.4}$$

Calculate the Reynolds number of the flow in the annulus:

$$\mathrm{Re} = \frac{12^{1-n}\rho\left(D_w - D_{\mathrm{po}}\right)^n |v_a|^{2-n}}{K_c(2n + 1/3n)^n}. \tag{A.5}$$

For laminar flow, constants a and b are:

$$\begin{cases} a = 24, \\ b = 1. \end{cases} \tag{A.6}$$

For turbulent flow, constants a and b are

$$\begin{cases} a = \dfrac{\lg n + 3.93}{50}, \\ b = \dfrac{1.75 - \lg n}{7}. \end{cases} \tag{A.7}$$

Calculate the frictional factor in the annulus f_a:

$$f_a = \frac{a}{\mathrm{Re}^b}. \tag{A.8}$$

Combining Eq. (A.4) and Eq. (A.8), calculate the frictional pressure loss in the annulus Δp_a:

$$\Delta p_a = \frac{2f_a L\rho v_{\mathrm{ae}}^2}{D_w - D_{\mathrm{po}}}. \tag{A.9}$$

Calculate the hydraulic radius R_h:

$$R_h = \frac{\phi D_c}{6(1-\phi) + (4D_c/D_w)}. \tag{A.10}$$

Calculate the capillary radius R_c:

$$R_c = 2R_h \tag{A.11}$$

Calculate the osmotic pressure Δp_o:

$$\Delta p_o = \frac{2K_c\left(4Q_a/\left(D_w^2 - D_p^2\right)\pi\right)}{\phi^n(n/3n+1)^n R_c^{1+n}} L_p. \tag{A.12}$$

Combining (A.9) and (A.12), calculate the surge-swab pressure Δp_s:

$$\Delta p_s = \Delta p_a + \Delta p_o. \tag{A.13}$$

Calculate the wellbore pressure p_w:

$$p_w = p_g + \Delta p_h + \Delta p_s. \tag{A.14}$$

A.2. Closed Pipe String with an Impermeable Cutting Plug

$$\Delta p_b = \frac{4\Delta F_{\mathrm{ax}}}{\pi D_b^2}. \tag{A.15}$$

Calculate the wellbore pressure p_w:

$$p_w = p_g + \Delta p_h + \Delta p_b. \tag{A.16}$$

A.3. Open Pipe String with a Porous Cutting Plug

Trial-and-error is needed to calculate the effective fluid velocity v_{ae} and the flow rates Q_a in the annulus due to the unknown Q_p.

Assume an initial Q_p, calculate the effective velocity v_{ae} of drilling fluid in the annulus:

$$v_{\mathrm{ae}} = -v_t\left(C + \frac{D_{\mathrm{po}}^2 - D_{\mathrm{pi}}^2}{D_w^2 - D_{\mathrm{po}}^2}\right) - \frac{4Q_p}{\pi\left(D_w^2 - D_{\mathrm{po}}^2\right)}. \tag{A.17}$$

Calculate the frictional pressure loss Δp_a with Eq. (A.9).

Calculate the flow rate in the annulus Q_a:

$$Q_a = -\frac{\pi\left(D_{\mathrm{po}}^2 - D_{\mathrm{pi}}^2\right)v_t}{4} - Q_p. \tag{A.18}$$

Calculate the osmotic pressure Δp_o with Eq. (A.12).

Calculate the surge-swab pressure Δp_s with Eq. (A.13).

Calculate the wellbore pressure p_w at the bottom of the pipe string with Eq. (A.14), namely, p_{a0}:

$$p_{a0} = p_w. \tag{A.19}$$

Calculate the velocity of drilling fluid in pipes v_p:

$$v_p = \frac{4Q_p}{\pi D_{\mathrm{pi}}^2}. \tag{A.20}$$

Calculate the effective velocity of drilling fluid in pipes:

$$v_{\mathrm{pe}} = v_p - v_t. \tag{A.21}$$

Calculate the Reynolds number for the flow in pipes:

$$\mathrm{Re} = \frac{8^{1-n}\rho D_{\mathrm{pi}}^n v_{\mathrm{pe}}^{2-n}}{K_c(3n + 1/4n)^n}. \tag{A.22}$$

For laminar flow, constants a and b are

$$\begin{cases} a = 16, \\ b = 1. \end{cases} \tag{A.23}$$

For turbulent flow, constants a and b refer to Eq. (A.7).

Calculate the friction factor in the pipes f_p:

$$f_p = \frac{a}{\mathrm{Re}^b}. \tag{A.24}$$

Calculate the frictional pressure loss in pipes Δp_p:

$$\Delta p_p = \frac{2f_p L\rho v_{\mathrm{pe}}^2}{D_{\mathrm{pi}}}. \tag{A.25}$$

Calculate the wellbore pressure p_w at the bottom of the pipe string, namely p_{p0}:

$$p_{p0} = p_g + \Delta p_h + \Delta p_p. \tag{A.26}$$

With Eq. (A.19) and Eq. (A.25), adjust Q_p until the pressure equality at the bottom of the pipe string is satisfied:

$$p_{p0} = p_{a0}. \tag{A.27}$$

With determined Q_p, all the parameters for calculating p_w with Eq. (A.14) is obtained.

A.4. Open Pipe String with an Impermeable Cutting Plug

Calculate the effective velocity v_{ae} of drilling fluid in the annulus:

$$v_{\mathrm{ae}} = v_c. \tag{A.28}$$

Calculate the frictional pressure loss in the annulus Δp_a with Eq. (A.9).

Calculate the surge-swab pressure Δp_s:

$$\Delta p_s = \Delta p_a. \tag{A.29}$$

Calculate the flow rate in the pipes Q_p:

$$Q_p = -\frac{\pi\left(D_{\mathrm{po}}^2 - D_{\mathrm{pi}}^2\right)v_t}{4}. \tag{A.30}$$

With Eq. (A.26), calculate the wellbore pressure p_w at the bottom of the pipe string, namely, p_{p0}.

Calculate the wellbore pressure above the cutting plug:

$$p_w = p_g + \Delta p_h + \Delta p_s. \tag{A.31}$$

Calculate the wellbore pressure between the cutting plug and the end of the pipe string:

$$p_w = p_{p0} - \Delta p_h - \Delta p_s. \tag{A.32}$$

Calculate the wellbore pressure below the end of the pipe string

$$p_w = p_{p0} + \Delta p_h. \tag{A.33}$$

Nomenclature

a: Constant for frictional factor calculation, dimensionless
b: Constant for frictional factor calculation, dimensionless
C: Mud clinging constant, dimensionless
D_b: Diameter of the bit, m
D_c: Cutting particle diameter, m
D_w: Diameter of the wellbore, m
D_{po}: Outer diameter of the pipe string, m
D_{pi}: Inner diameter of the pipe string, m
f_a: Frictional factor in the annulus, dimensionless
f_p: Frictional factor in the pipes, dimensionless
K_c: Consistency coefficient, Pa·m^{n}
L: Length of the flow channel, m
L_p: Length of the cutting plug, m
n: Flow behavior index, dimensionless
p_g: Wellbore pressure at the ground surface, Pa
p_{a0}: Annulus pressure at the bottom of the pipe string, Pa
p_{p0}: Pipe pressure at the bottom of the pipe string, Pa
p_w: Wellbore pressure, Pa

Q_a: Flow rate in the annulus, m^3/s
Q_p: Flow rate in the pipes, m^3/s
R_c: Capillary radius of the porous cutting plug, m
R_h: Hydraulic radius of the porous cutting plug, m
Re: Reynolds number, dimensionless
v_a: Average velocity of drilling fluid in the annulus, m/s
v_{ae}: Effective velocity of drilling fluid in the annulus, m/s
v_p: Average velocity of drilling fluid in the pipes, m/s
v_{pe}: Effective velocity of drilling fluid in the pipes, m/s
v_c: Clinging velocity of drilling fluid, m/s
v_t: Tripping velocity of the pipe string, m/s
ΔF_{ax}: Pipe string axial force applied on the bit, N
Δp_a: Frictional pressure loss in the annulus, Pa
Δp_b: Difference of the hydraulic pressure applied on the bit, Pa
Δp_h: Hydrostatic pressure, Pa
Δp_o: Osmotic pressure loss, Pa
Δp_p: Frictional pressure loss in the pipes, Pa
Δp_s: Surge-swab pressure, Pa
ρ: Drilling fluid density, kg/m^3
ϕ: Porosity of the porous cutting plug, dimensionless

Data Availability

The data used to support the findings of this study are included within the article.

Conflicts of Interest

The authors declare that there are no conflicts of interest regarding the publication of this paper.

Acknowledgments

The authors gratefully acknowledge the support of the National Natural Science Foundation of China (U19B6003; 51734010) and the Strategic Cooperation Technology Projects of CNPC and CUPB (ZLZX2020-01).

References

[1] C. N. Zou, Z. Yang, J. W. Cui et al., "Formation mechanism, geological characteristics and development strategy of non-marine shale oil in China," *Petroleum Exploration and Development*, vol. 40, no. 1, pp. 15–27, 2013.

[2] Z. J. Jin, Z. R. Bai, B. Gao, and M. W. Li, "Has China ushered in the shale oil and gas revolution," *Oil & Gas Geology*, vol. 40, no. 3, pp. 451–458, 2019.

[3] Q. Lei, D. W. Weng, S. C. Xiong et al., "Progress and development directions of shale oil reservoir stimulation technology of China National Petroleum Corporation," *Petroleum Exploration and Development*, vol. 48, no. 5, pp. 1198–1207, 2021.

[4] Q. Fu, "The status, challenge and prospect of shale oil exploration and development in China," *Oil Drilling & Production Technology*, vol. 27, no. 4, pp. 58–62, 2015.

[5] X. Li, D. L. Gao, Y. C. Zhou, and W. K. Cao, "General approach for the calculation and optimal control of the extended-reach limit in horizontal drilling based on the mud weight window," *Journal of Natural Gas Science and Engineering*, vol. 35, pp. 964–979, 2016.

[6] Y. H. Shi, H. Q. Xia, M. Peng, Y. Chen, and Y. J. Chen, "New accurate prediction method of safe window of drilling fluid density," *Fault-block Oil & Gas Field*, vol. 26, no. 2, pp. 248–252, 2019.

[7] H. Wang, R. Sweatman, B. Engleman et al., "Best practice in understanding and managing lost circulation challenges," *SPE Drilling & Completion*, vol. 23, no. 2, pp. 168–175, 2008.

[8] X. W. Jiang, *Drilling Accidents and Complex Problems*, Petroleum Industry Press, Beijing, 2006.

[9] N. Khakzad, F. Khan, and P. Amyotte, "Quantitative risk analysis of offshore drilling operations: a Bayesian approach," *Safety Science*, vol. 57, pp. 108–117, 2013.

[10] H. H. Fan, *Practical Drilling Fluid Mechanics*, Petroleum Industry Press, Beijing, 2014.

[11] G. E. Cannon, "Changes in hydrostatic pressure due to withdrawing drill pipe from the hole," in *Drilling and Production Practices*, pp. 42–47, One Petro, 1934.

[12] A. Wolski, S. L. M. Junqueira, and C. O. R. Negrão, "A steady-state approach for evaluation of surge and swab pressures in flows with free surface boundary conditions," *Journal of Petroleum Science and Engineering*, vol. 122, pp. 208–215, 2014.

[13] S. M. He, R. Srivastav, M. Tang, and R. Ahmed, "A new simplified surge and swab pressure model for yield-power-law drilling fluids," *Journal of Natural Gas Science and Engineering*, vol. 28, pp. 184–192, 2016.

[14] S. Krishna, S. Ridha, S. Campbell, S. U. Ilyas, I. Dzulkarnain, and M. Abdurrahman, "Experimental evaluation of surge/swab pressure in varying annular eccentricities using non-Newtonian fluid under Couette-Poiseuille flow for drilling applications," *Journal of Petroleum Science and Engineering*, vol. 206, article 108982, 2021.

[15] G. R. Samuel, A. Sunthankar, G. McColpin, P. Bern, and T. Flynn, "Field validation of transient swab-surge response with real-time downhole pressure data," *SPE Drilling & Completion*, vol. 18, no. 4, pp. 280–283, 2003.

[16] R. Srivastav, M. Enfis, F. Crespo, R. Ahmed, A. Saasen, and M. Laget, "Surge and swab pressures in horizontal and inclined wells," in *In Paper SPE 152662 Presented at the SPE Latin America and Caribbean Petroleum Engineering Conference*, Mexico City, Mexico, 2012.

[17] E. H. Clark, "Bottom-hole pressure surges while running pipe," in *In Paper 54-PET-22 Presented at the Petroleum Mechanical Engineering Conference*, Los Angeles, California, USA, 1954.

[18] J. A. Burkhardt, "Wellbore pressure surges produced by pipe movement," *Journal of Petroleum Technology*, vol. 13, no. 6, pp. 595–605, 1961.

[19] J. E. Fontenot and R. K. Clark, "an improved method for calculating swab and surge pressures and circulating pressures in a drilling well," *Society of Petroleum Engineers Journal*, vol. 14, no. 5, pp. 451–462, 1974.

[20] H. G. Wang and X. S. Liu, "Study on steady surge pressure for yield-pseudoplastic fluid in a concentric annulus," *Applied Mathematics and Mechanics*, vol. 17, no. 1, pp. 15–23, 1996.

[21] H. G. Wang, X. S. Liu, and J. Dong, "Approximate solution of stable fluctuation pressure of Newtonian fluid in eccentric annular," *Oil Drilling & Production Technology*, vol. 18, no. 2, pp. 18–21, 1996.

[22] F. Crespo, R. Ahmed, M. Enfis, A. Saasen, and M. Amani, "Surge-and-swab pressure predictions for yield-power-law drilling fluids," *SPE Drilling & Completion*, vol. 27, no. 4, pp. 574–585, 2012.

[23] F. Crespo and R. Ahmed, "A simplified surge and swab pressure model for yield power law fluids," *Journal of Petroleum Science and Engineering*, vol. 101, pp. 12–20, 2013.

[24] M. Tang, J. Y. Xiong, and S. M. He, "A new model for computing surge/swab pressure in horizontal wells and analysis of influencing factors," *Journal of Natural Gas Science and Engineering*, vol. 19, pp. 337–343, 2014.

[25] A. Ettehadi and G. Altun, "Functional and practical analytical pressure surges model through Herschel Bulkley fluids," *Journal of Petroleum Science and Engineering*, vol. 171, pp. 748–759, 2018.

[26] S. Krishna, S. Ridha, P. Vasant, S. U. Ilyas, S. Irawan, and R. Gholami, "Explicit flow velocity modelling of yield power-law fluid in concentric annulus to predict surge and swab pressure gradient for petroleum drilling applications," *Journal of Petroleum Science and Engineering*, vol. 195, article 107743, 2020.

[27] A. Lubinski, F. Hsu, and K. Nolte, "Transient pressure surges due to pipe movement in an oil well," *Oil & Gas Science Technology*, vol. 32, no. 3, pp. 307–348, 1977.

[28] M. Lal, "Surge and swab modeling for dynamic pressures and safe trip velocities," in *In Paper IADC/SPE 11412 Presented at the IADC/SPE 1983 Drilling Conference*, New Orleans, Louisiana, USA, 1983.

[29] R. F. Mitchell, "Dynamic Surge/Swab pressure predictions," *SPE Drilling Engineering*, vol. 3, no. 3, pp. 325–333, 1988.

[30] R. F. Mitchell, "Surge pressures in low-clearance liners," in *In Paper IADC/SPE 87181 Presented at the IADC/SPE Drilling Conference*, Dallas, Texas, USA, 2004.

[31] V. Tikhonov, O. Bukashkina, V. Liapidevskii, and L. Ring, "Development of model and software for simulation of surge-swab process at drilling," in *In Paper SPE 181933 Presented at the SPE Russian Petroleum Technology Conference and Exhibition*, Moscow, Russia, 2016.

[32] A. Willersrud, L. Imsland, and M. Blanke, "Early pack-off diagnosis in drilling using an adaptive observer and statistical change detection," *IFAC-PapersOnLine*, vol. 48, no. 6, pp. 177–182, 2015.

[33] X. Li, D. L. Gao, Y. C. Zhou, H. Zhang, and Y. C. Yang, "Study on the prediction model of the open-hole extended-reach limit in horizontal drilling considering the effects of cuttings," *Journal of Natural Gas Science and Engineering.*, vol. 40, pp. 159–167, 2017.

[34] Z. Q. Yang, J. Lu, Y. Wang et al., "Column penetration grouting mechanism for power-law fluids considering tortuosity effect of porous media," *Chinese Journal of Rock Mechanics and Engineering.*, vol. 40, no. 2, pp. 410–418, 2021.

[35] X. Y. Kong, *Advanced Seepage Mechanics*, University of Science and Technology of China Press, Hefei, 2010.

[36] J. S. Wu, *Analysis of Resistance for Flow through Porous Media [M.S. thesis]*, Huazhong University of Science and Technology, Wuhan, 2006.

[37] X. W. Tian, P. Wang, and S. M. Xu, "Flow resistance characteristics of power law fluid flow through granular porous medium," *Journal of Harbin Institute of Technology*, vol. 49, no. 1, pp. 126–132, 2017.

[38] X. Li, D. L. Gao, B. P. Lu, Y. J. Zeng, J. C. Zhang, and S. M. Zhou, "Study on the prediction model of extended-reach limit length in horizontal drilling with dual-channel drillpipe in shale formation," *Journal of Petroleum Science and Engineering*, vol. 177, pp. 570–578, 2019.

[39] X. Li, D. L. Gao, B. P. Lu, Y. J. Zeng, and J. C. Zhang, "Study on modified maximum extension length prediction model for horizontal wells considering differential sticking," *Journal of Petroleum Science and Engineering.*, vol. 183, article 106371, 2019.

[40] T. G. Chen, Z. C. Guan, and X. S. Liu, *Theories and Technologies of Drilling Engineering*, China University of Petroleum Press, Dongying, 2006.

[41] K. Lin, J. J. Wang, Z. X. Shen, W. H. Liu, J. D. Wang, and F. S. Shangguan, *Drilling Handbook: Chapter 3*, Petroleum Industry Press, Beijing, 2013.

Hindawi
Geofluids
Volume 2021, Article ID 9906500, 18 pages
https://doi.org/10.1155/2021/9906500

Research Article

Quantitative Characterization of Pore Space for the Occurrence of Continental Shale Oil in Lithofacies of Different Types: Middle Jurassic Lianggaoshan Formation in Southeastern Sichuan Basin of the Upper Yangtze Area

Xiangfeng Wei,[1,2] Kun Zhang,[3,4,5,6] Qianwen Li,[1,7] Dongfeng Hu,[2] Zhihong Wei,[2] Ruobing Liu,[2] Zhujiang Liu,[2] and Jiayi Liu[1,7]

[1]*State Key Laboratory of Shale Oil and Gas Enrichment Mechanisms and Effective Development, Beijing 100083, China*
[2]*Sinopec Exploration Company, Chengdu 610041, China*
[3]*School of Geoscience and Technology, Southwest Petroleum University, Chengdu 610500, China*
[4]*State Key Laboratory of Oil and Gas Reservoir Geology and Exploitation, Southwest Petroleum University, Chengdu 610500, China*
[5]*Key Laboratory of Tectonics and Petroleum Resources (China University of Geosciences), Ministry of Education, Wuhan 430074, China*
[6]*Energy and Geoscience Institute, University of Utah, Salt Lake City, Utah 84108, USA*
[7]*Sinopec Petroleum Exploration and Production Research Institute, Beijing 100083, China*

Correspondence should be addressed to Kun Zhang; shandongzhangkun@126.com

Received 25 August 2021; Accepted 18 October 2021; Published 27 October 2021

Academic Editor: Amer Syed

In addition to marine and marine-continental transitional strata, the continental ones are also widely distributed in various oil and gas-bearing basins in China. The continental shale generally provides favorable material bases for hydrocarbon generation, such as wide distribution, large thickness, multiple series of strata, high TOC content, nice organic matter type, and moderate thermal evolution. Part of such shale contains shale oil, but the pore space characteristics for the occurrence of this oil are not thoroughly studied. In order to accurately and quantitatively characterize the pore space where the continental shale oil in different types of lithofacies occurs, we sampled the rock cores from the Middle Jurassic Lianggaoshan Formation in the southeastern Sichuan Basin of the Upper Yangtze Area. The TOC content and mineral composition were analyzed, and we also carried out experiments on CO_2 and N_2 adsorptions, high-pressure mercury injection, and wash oil. Results show significant differences in pore space characteristics for the occurrence of shale oil in different types of lithofacies. In organic-rich mixed and clayey mudstones with the highest TOC content, the free shale oil, occupying the largest reservoir space, mainly occurs in macropores and mesopores, and the adsorbed shale oil, occupying the largest reservoir space, mainly occurs in mesopores. In the organic-bearing clayey mudstone, which has a higher TOC content, the free shale oil takes a larger reservoir space and mainly occurs in macropores, followed by mesopores, and the absorbed one, occupying a larger reservoir space, mostly occurs in micropores and then the mesopores. The organic-bearing mixed mudstone has a moderate TOC content, in which the free shale oil occupies a smaller reservoir space and primarily occurs in mesopores, followed by macropores, and the absorbed one, which takes a larger reservoir space, all occurs in mesopores. In the fine sandstone, the free shale oil occupies a smaller reservoir space and primarily occurs in mesopores, while the absorbed one occupies a smaller reservoir space and all occurs in mesopores.

1. Introduction

The change in geological concepts and the achievements made in horizontal well drilling and fracturing technologies in recent years brought a remarkable breakthrough in China's exploration of marine shale gas, and various shale gas fields have been successively built at Jiaoshiba, Weiyuan, Changning, Fushun-Yongchuan, Zhaotong, Luzhou, etc. [1–7] Besides, continental strata are also widely distributed in China's oil and gas-bearing basins, including Sichuan, Junggar, and Bohai Bay Basins. In particular, the continental shale in Jianghan Basin is featured with wide distribution, large thickness, multiple series of strata, high TOC content, moderate thermal evolution, and good kerogen type. Therefore, oil companies, such as PetroChina and the Sinopec Group, have attached great importance to the geological research on continental shale oil and gas and have planned to exert more efforts in exploration during China's "14th Five-Year Plan" [8–14].

Since shale pores are major reservoir spaces and seepage channels of shale oil, it is urgent to study the pore space characteristics for shale oil occurrence. Li et al. [15] argued that since shale oil mainly occurs in shale pores, research into the pore structure characteristics is the key to understand the mechanism of shale oil accumulation. In the lower third member of the continental Shahejie Formation in the Zhanhua Sag, shale micro-nanopore structure is qualitatively and quantitatively characterized with FE-SEM, CO_2 adsorption, N_2 adsorption, and high-pressure mercury injection [15]. Taking the continental shale of Zhanhua Sag in the Jiyang Depression of the Bohai Bay Basin as the examples, Su et al. used microscope and nuclear magnetic resonance (NMR) to examine the hydrocarbon generation and expulsion of nitrogen adsorption, reservoir properties, and oil-gas bearing capacity of different shale lithofacies [16]. To reveal the effects of shale reservoir characteristics on the movability of shale oil and its action mechanism in the lower third member of the Shahejie Formation, Ning et al. selected samples with different features and analyzed them using N_2 adsorption, high-pressure mercury injection capillary pressure (MICP), nuclear magnetic resonance (NMR), high-speed centrifugation, and displacement image techniques [17].

In this work, the continental shale was sampled from the Middle Jurassic Lianggaoshan Formation in southeastern Sichuan Basin of the Upper Yangtze Area in South China, and the key TY1 exploration well was selected to study the characteristics of pore space where the continental shale oil in different types of lithofacies occurs (Figure 1). First, the shale lithofacies were classified by TOC content and mineral composition. Then, the shale samples collected from the same depth were divided into two groups. For one of them, the experiments on CO_2 and N_2 adsorptions and high-pressure mercury injection were conducted to characterize the distribution features of micropores, mesopores, and macropores, thus quantitatively characterizing the full-scale pore structure of these samples before extraction. For the other group, the shale oil was first extracted from samples by wash oil, and the above experiments were repeated to obtain the same kind of data. Finally, the data before and after extraction were compared to obtain the pore space characteristics.

2. Geological Settings

2.1. Tectonic Framework. The study area, located at the high-steep fault-fold zone of East Sichuan, is an arcuate tectonic belt composed of a series of arcuate mountains. It is bounded by the Huayingshan Fault Zone, is adjacent to the Central Sichuan Uplift in the west, and stretches eastwards to the Qiyueshan Fault Zone on the Sichuan-Hubei border. The structural lineament mainly develops in the direction of NNE, extends towards NEE, and finally converges in the north [18–20]. In this tectonic belt, mountains are formed by high-steep anticlines with Permian-Triassic cores and asymmetrical wings, of which the gentle wing generally shows a stratigraphic dip of 20° ~30°, while the steep one shows a stratigraphic dip of 40° ~70° or a vertically inverted stratum. Besides, the broad valleys between these mountains are formed by wide and gentle synclines, which are developed in the Jurassic period and show a typical partition style both in structure and landform [21–24].

2.2. Sedimentology and Stratigraphy. The studied area in the Lianggaoshan Formation is divided into three members, of which both the first and second ones can be further divided into upper and lower submembers [25–30]. Meanwhile, this formation develops a set of gray siltstone, silty shale, black gray-dark gray shale, and fine gray siltstone. Besides, the dark gray shale primarily deposits in the upper submember of the first member and the lower submember of the second member, which are the strata suitable for the development of organic-rich shale (Figure 2). The Lianggaoshan Formation undergoes a complete cycle of lake transgression and regression during the sedimentation. Thereinto, the first member of this formation has sufficient provenance supply at the early stage of sedimentation and then experiences the lake transgression. The second member, mainly developing the shallow and semideep lacustrine deposits, reaches the maximum flood surface in the early stage and later experiences the lake regression. It is a favorable facies belt for the development of organic-rich shale. The third member primarily develops the coarse clastic materials in the delta front. Moreover, the upper submember of the first member and the lower submember of the second member are major strata, in which the dark argillaceous shale is developed [31–34].

3. Samples, Experiments, and Data Sources

In this study, the shale was sampled from the Lianggaoshan Formation in the TY1 well according to 14 depths, with the sample number shown in Table 1. First, the shale lithofacies were classified by measuring the TOC content of samples at the same depth with a Sievers 860 TOC analyzer and by performing the X-ray diffraction analysis on whole rocks and minerals with a YST-I mineral analyzer. Then, the shale samples collected from the same depth were equally divided into two groups. For one group, the BSD-PM1/2

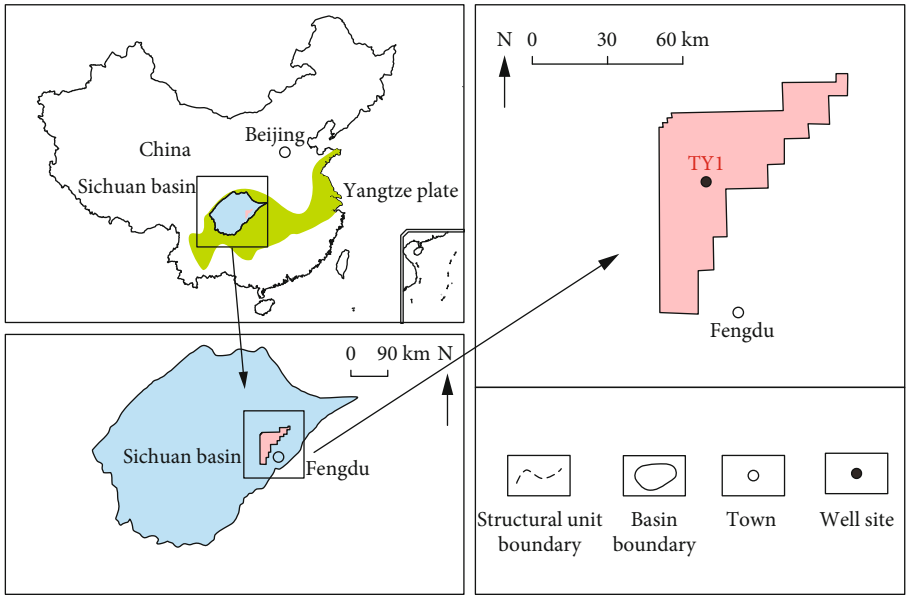

Figure 1: Locations of southeastern Sichuan Basin in South China and TY1 well site.

instrument was used for the CO_2 adsorption experiment to obtain the pore size distribution characteristics of micropores (<2 nm), the BSD-PS1/2/4 instrument was used for the N_2 adsorption experiment to obtain such characteristics of mesopores (2~50 nm), and the 3H-2000PS2 instrument was used for the high-pressure mercury injection experiment to obtain such characteristics of macropores (>50 nm). Then, the data about these three experiments were combined to determine the joint characterization for the full-scale pore structure of samples before the shale oil was extracted.

As for the other group, the DY-6 instrument was used for the wash oil experiment to extract the shale oil from samples at the same depth. Similarly, the CO_2 adsorption experiment was conducted with the BSD-PM1/2 instrument to obtain the pore size distribution characteristics of micropores (<2 nm), the N_2 adsorption experiment was conducted with BSD-PS1/2/4 instrument to obtain such characteristics of mesopores (2~50 nm), and the high-pressure mercury injection experiment was conducted with a 3H-2000PS2 instrument to obtain such characteristics of macropores (>50 nm). Then, the data about these three experiments were combined to determine the joint characterization for the full-scale pore structure of samples after the shale oil was extracted. Finally, the characterization results before and after extraction were compared to obtain the quantitative characterization of pore space for the occurrence of shale oil in different types of lithofacies.

4. Results and Discussion

4.1. Division of Shale Lithofacies. In previous studies, the shale lithofacies were divided based on the mineral composition and TOC content. (1) It is classified into 4 types according to the mineral composition: clayey shale (clay minerals ≥ 50%), calcareous shale (carbonate minerals ≥ 50), and mixed shale (siliceous, clay, and carbonate minerals < 50%) (Figure 3). (2) It is classified into 3 types according to the TOC content: organic-lean shale (TOC content = 0% ~ 1%), organic-bearing shale (TOC content = 1% ~ 2%), and organic-rich shale (TOC content ≥ 2%). When the two classification methods are integrated, there will be $3 \times 4 = 12$ types of lithofacies [35–42]. Table 1 shows different types of shale lithofacies divided based on the TOC content and mineral composition of 14 shale samples.

4.2. Pore Structure Characteristics for Different Types of Shale Lithofacies before and after the Extraction of Shale Oil. In the Lianggaoshan Formation, the pore volume and surface area provide the occurrence space for free and absorbed shale oils, respectively [43–45]. In this paper, the shale samples at the same depth were divided into two groups, one of which was analyzed to quantitatively characterize the full-scale pore size of samples containing the shale oil by characterizing the distribution features of micropores, mesopores, and macropores through experiments on CO_2 and N_2 adsorptions and high-pressure mercury injection, respectively [46–55].

For the other group, the wash oil was used to extract and remove the shale oil from sample pores at the same depth. Then similarly, the distribution features of micropores, mesopores, and macropores were characterized by experiments on CO_2 and N_2 adsorptions and high-pressure mercury injection, respectively, thus quantitatively characterizing the full-scale pore size of samples without shale oil [56–60], as shown in Figures 4 and 5.

4.2.1. Pore Volume Characteristics for the Occurrence of Shale Oil. The analysis on pore volume characteristics of rock reservoirs adopted the experimental data after the

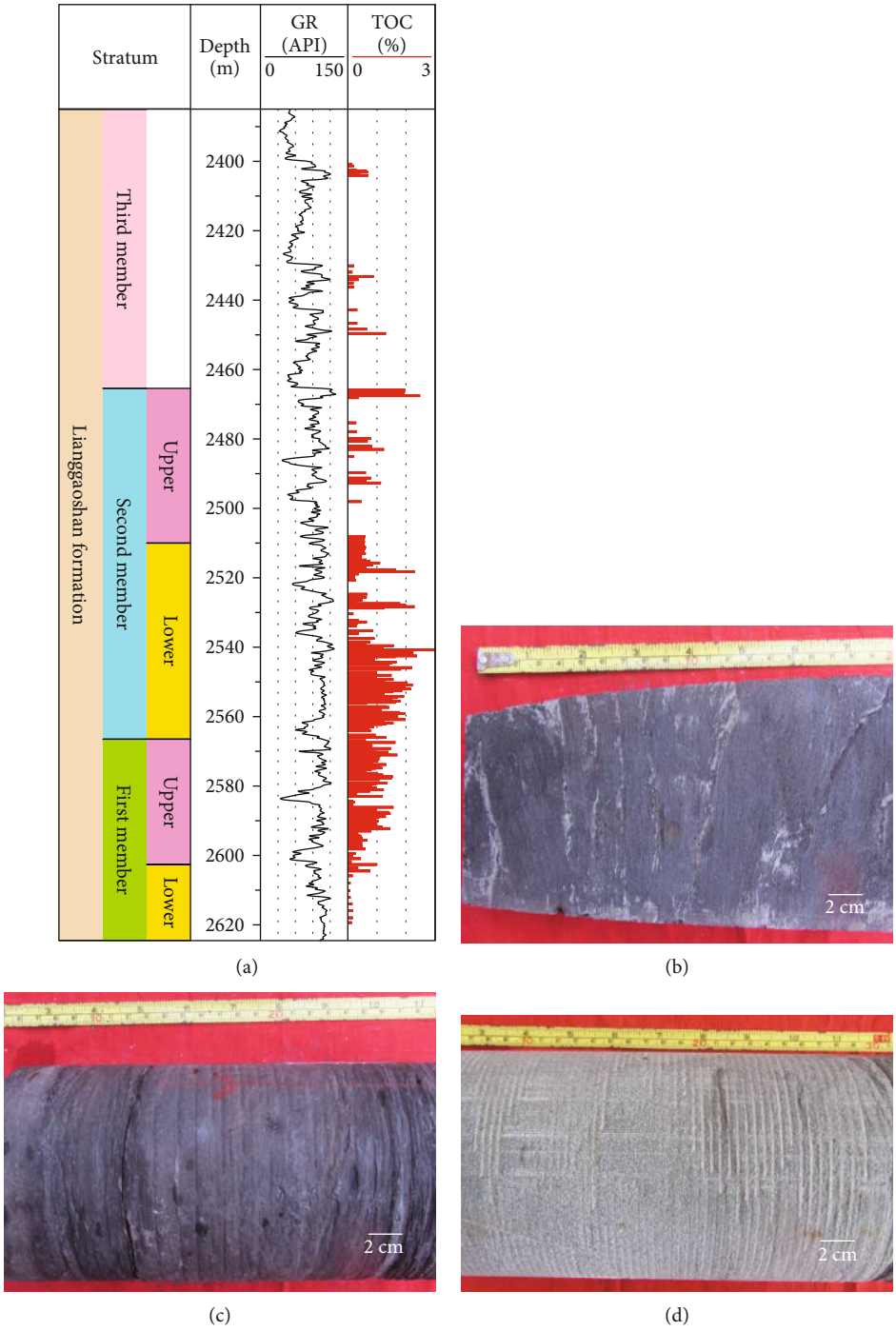

Figure 2: Column diagram and core photos of the Middle Jurassic Ranggosan Formation stratigraphy in well TY1. (a) Stratigraphic column diagram of the TY1 well; (b) dark gray shale of the upper subsection of the first section of the Ryanggosan Formation in TY1 well, 2579 m; (c) gray-black shale of the lower subsection of the second section of the Ryanggosan Formation in TY1 well, 2542 m; (d) gray fine sandstone of the third section of the Ryanggosan Formation in TY1 well, 2421 m. See Figure 1 for the well locations.

Table 1: Experimental sample depth, layer section, and petrographic classification.

Sample number	Depth (m)	Formation	Lithofacies
1	2403.93	The third member of Lianggaoshan Formation	Organic-bearing mixed shale
2	2466.7	Upper submember of the second member of Lianggaoshan Formation	Organic-rich clayey shale
3	2470.82	Upper submember of the second member of Lianggaoshan Formation	Fine sandstone
4	2515.82	Lower submember of the second member of Lianggaoshan Formation	Organic-bearing clayey shale
5	2527.04	Lower submember of the second member of Lianggaoshan Formation	Organic-rich clayey shale
6	2540.45	Lower submember of the second member of Lianggaoshan Formation	Organic-rich clayey shale
7	2542.24	Lower submember of the second member of Lianggaoshan Formation	Organic-rich clayey shale
8	2547.35	Lower submember of the second member of Lianggaoshan Formation	Organic-rich mixed shale
9	2552.98	Lower submember of the second member of Lianggaoshan Formation	Organic-rich clayey shale
10	2555.65	Lower submember of the second member of Lianggaoshan Formation	Organic-rich clayey shale
11	2573.32	Upper submember of the first member of Lianggaoshan Formation	Organic-rich mixed shale
12	2576.98	Upper submember of the first member of Lianggaoshan Formation	Organic-bearing clayey shale
13	2579.45	Upper submember of the first member of Lianggaoshan Formation	Organic-bearing clayey shale
14	2589.7	Upper submember of the first member of Lianggaoshan Formation	Organic-bearing clayey shale

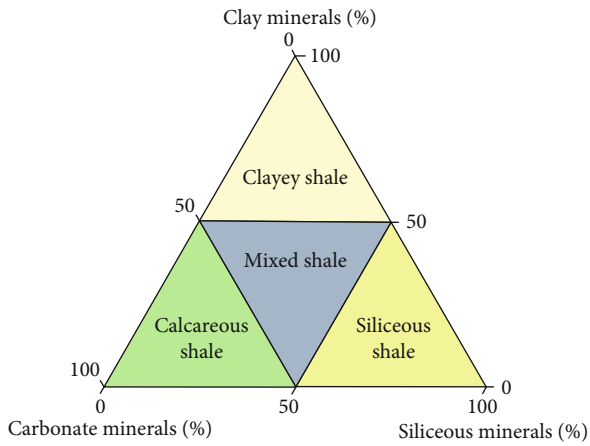

Figure 3: Shale petrographic diagram based on mineralogical composition.

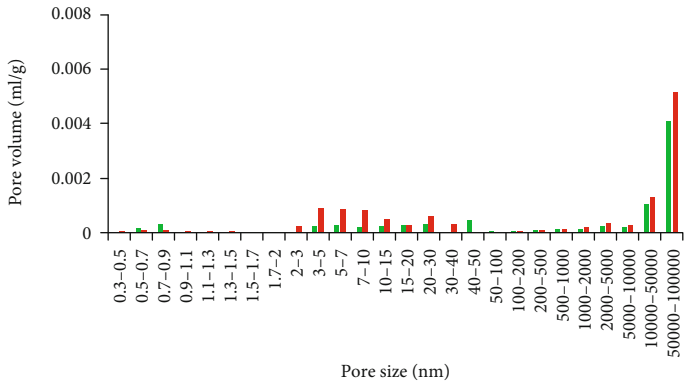

(a) 2403.93 m, organic-bearing mixed shale

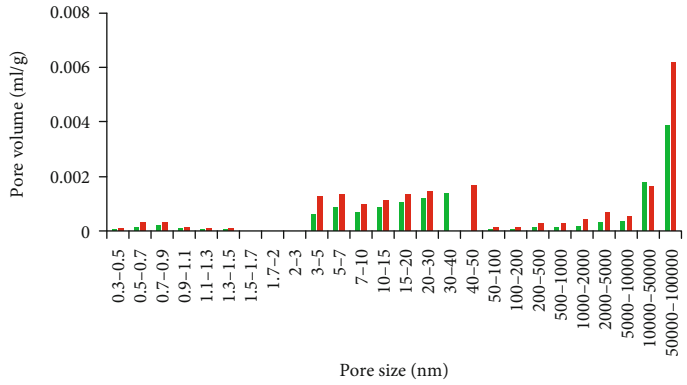

(b) 2466.7 m, organic-rich clayey shale

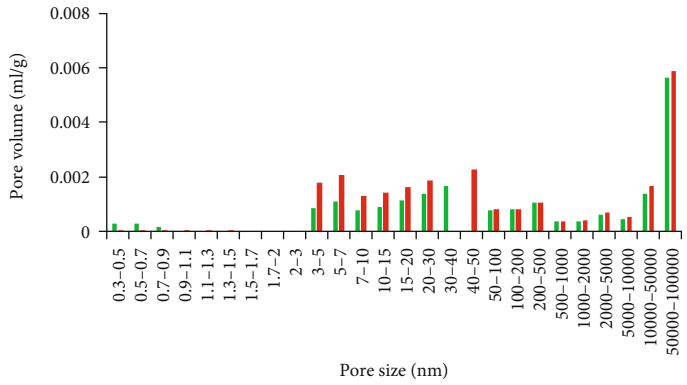

(c) 2470.82 m, fine sandstone

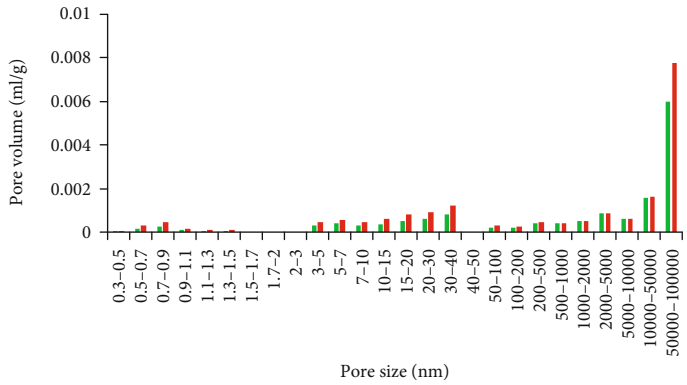

(d) 2515.82 m, organic-bearing clayey shale

Figure 4: Continued.

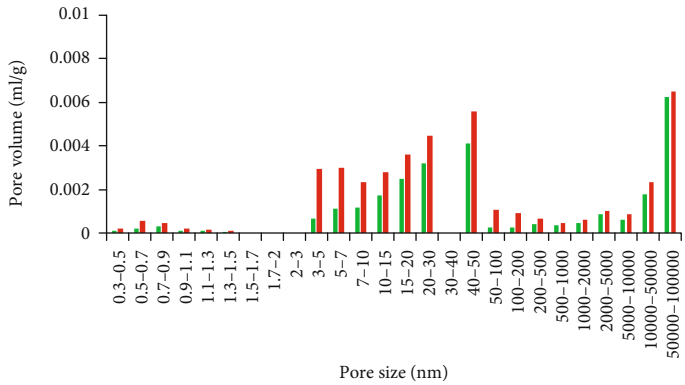

(e) 2527.04 m, organic-rich clayey shale

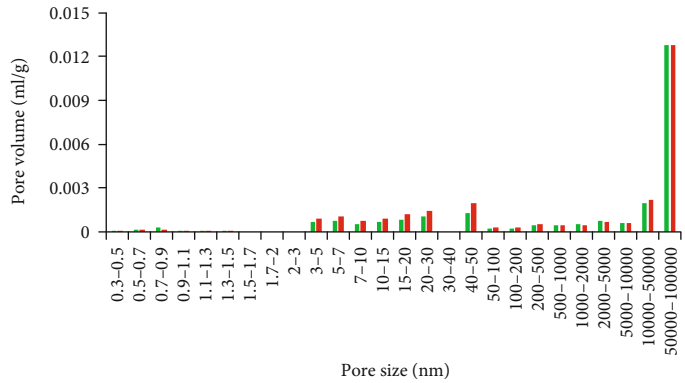

(f) 2540.45 m, organic-rich clayey shale

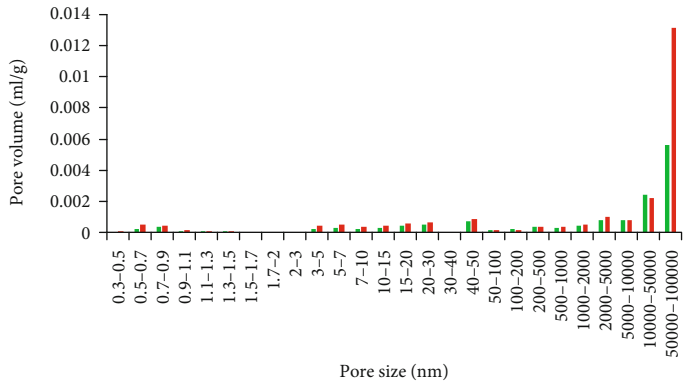

(g) 2542.24 m, organic-rich clayey shale

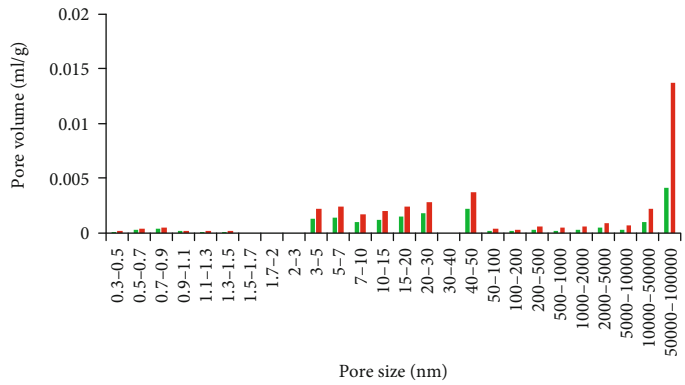

(h) 2547.35 m, organic-rich mixed shale

Figure 4: Continued.

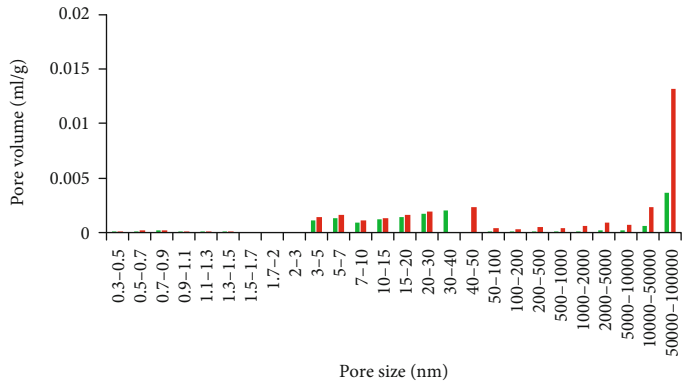

(i) 2552.98 m, organic-rich clayey shale

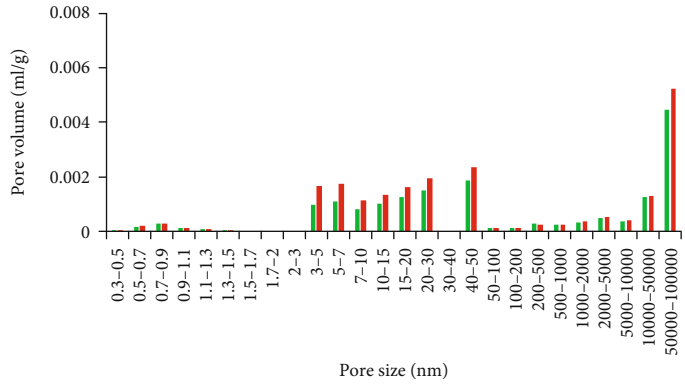

(j) 2555.65 m, organic-rich clayey shale

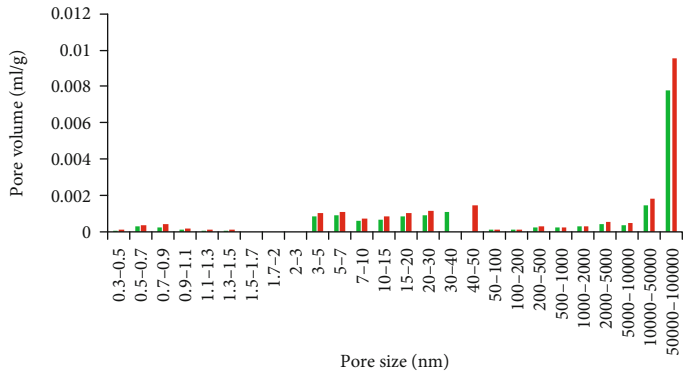

(k) 2573.32 m, organic-rich mixed shale

Figure 4: Continued.

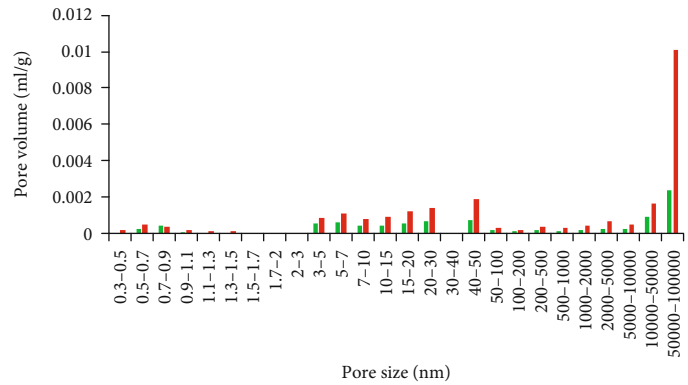

(l) 2576.98 m, organic-bearing clayey shale

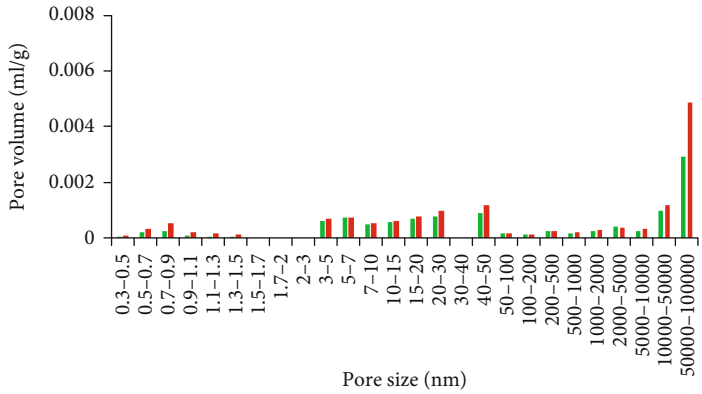

(m) 2579.45 m, organic-bearing clayey shale

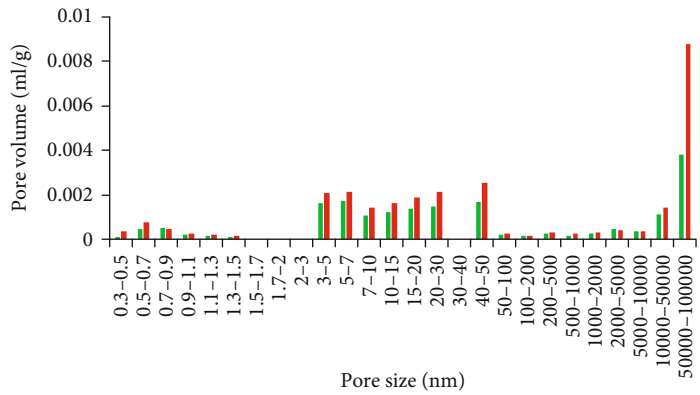

(n) 2589.7 m, organic-bearing clayey shale

Figure 4: Pore volume features based on the joint characterization for full-scale pore size of different shale samples in TY1 well. Green: pore volume data of shale samples before the extraction of shale oil; Red: pore volume data of shale samples after the extraction of shale oil.

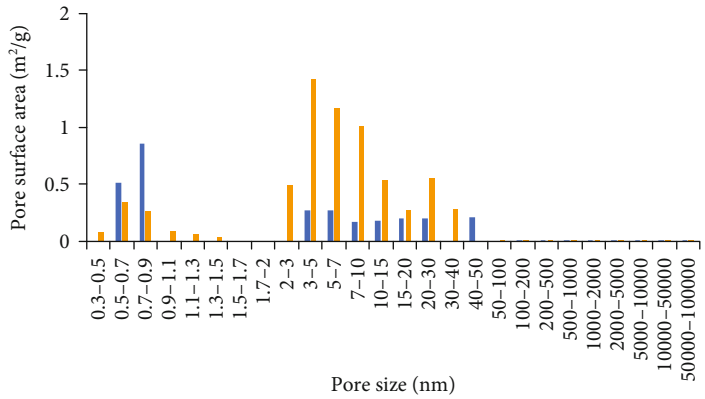

(a) 2403.93 m, organic-bearing mixed shale

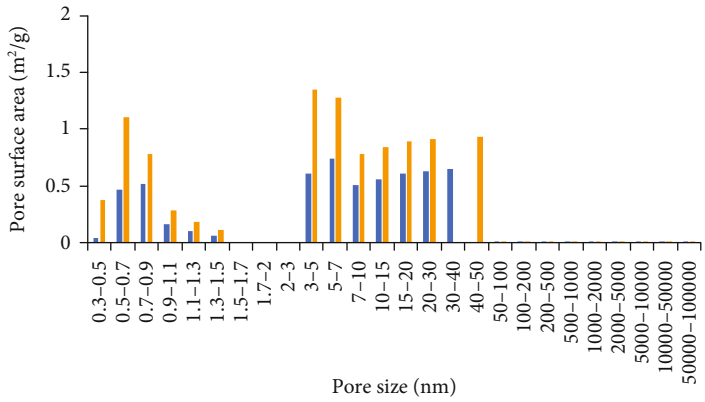

(b) 2466.7 m, organic-rich clayey shale

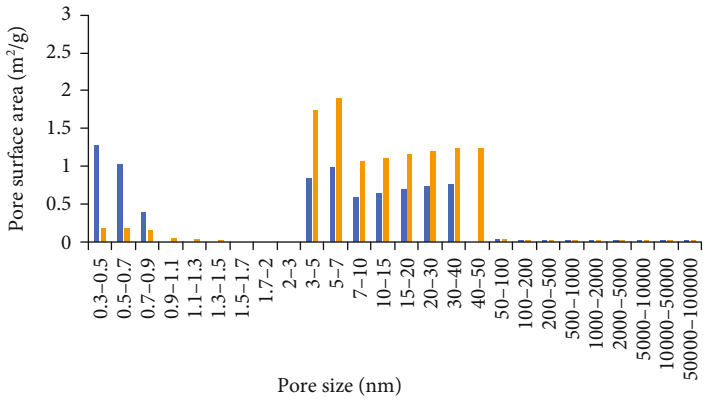

(c) 2470.82 m, fine sandstone

Figure 5: Continued.

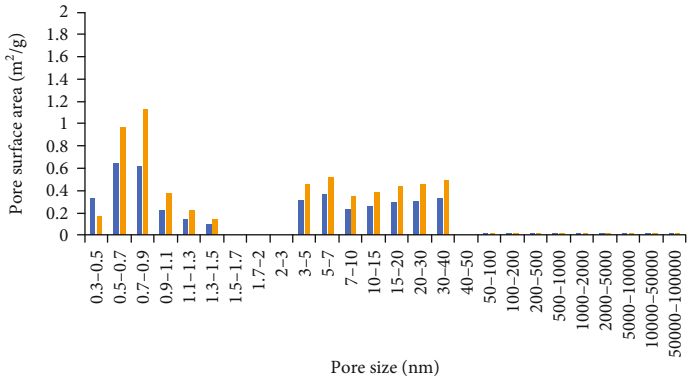

(d) 2515.82 m, organic-bearing clayey shale

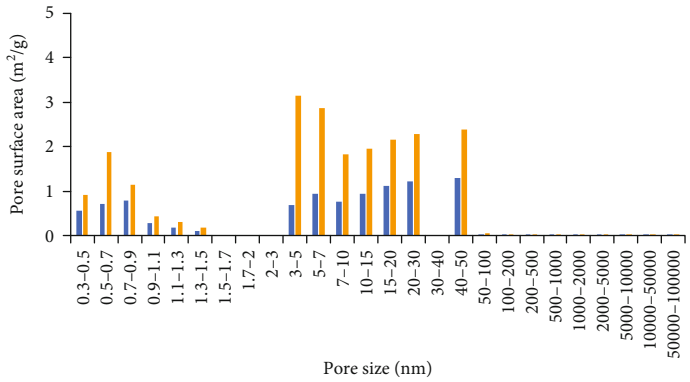

(e) 2527.04 m, organic-rich clayey shale

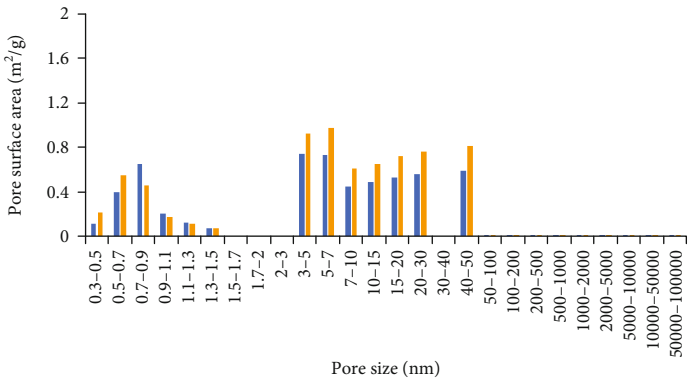

(f) 2540.45 m, organic-rich clayey shale

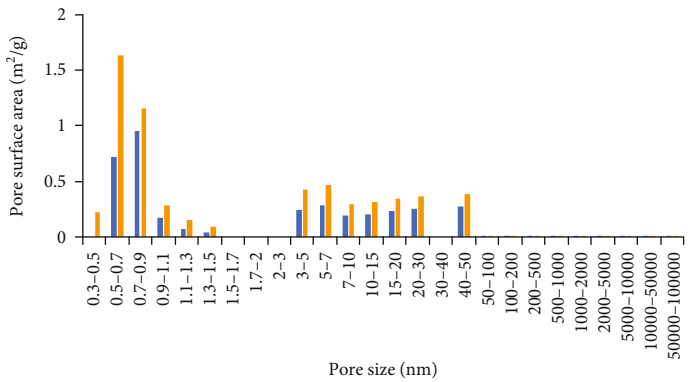

(g) 2542.24 m, organic-rich clayey shale

Figure 5: Continued.

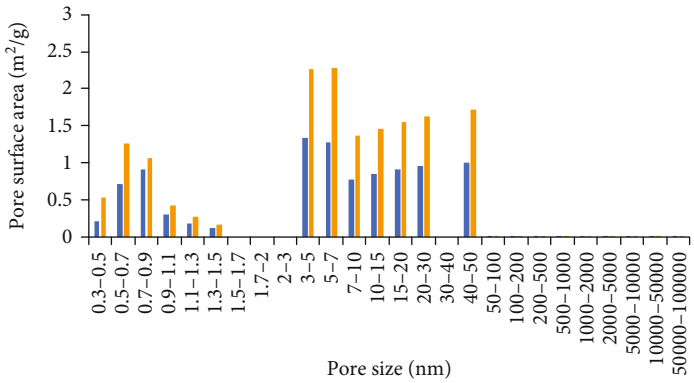

(h) 2547.35 m, organic-rich mixed shale

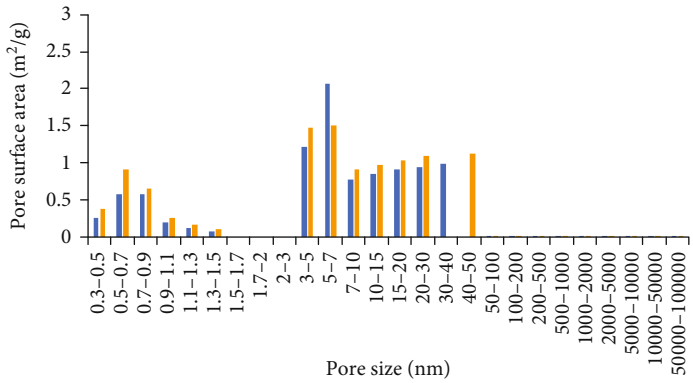

(i) 2552.98 m, organic-rich clayey shale

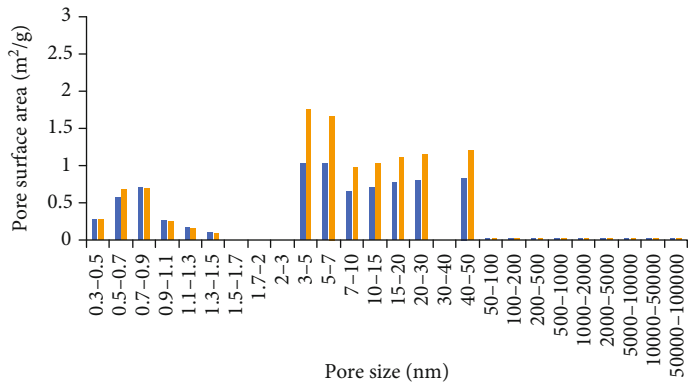

(j) 2555.65 m, organic-rich clayey shale

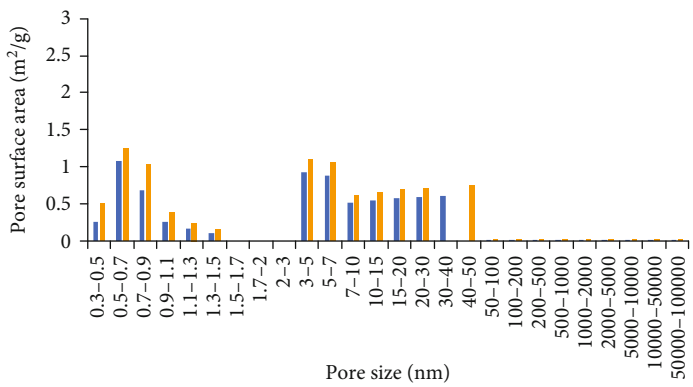

(k) 2573.32 m, organic-rich mixed shale

Figure 5: Continued.

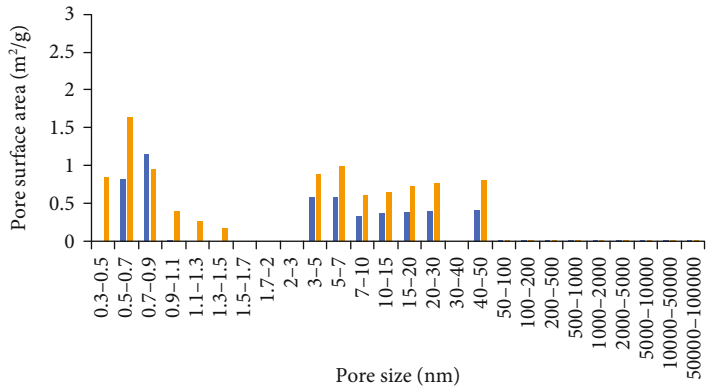

(l) 2576.98 m, organic-bearing clayey shale

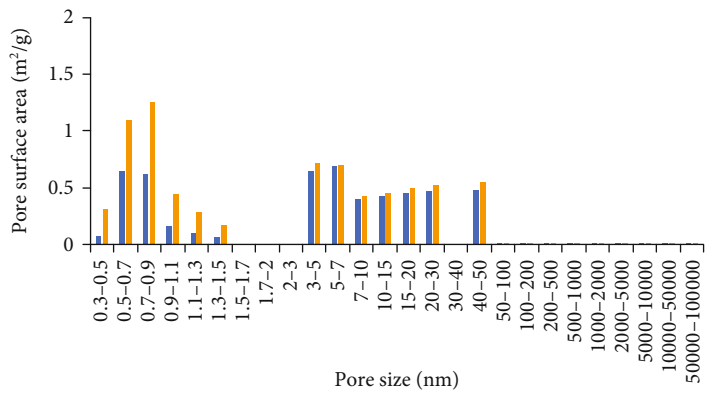

(m) 2579.45 m, organic-bearing clayey shale

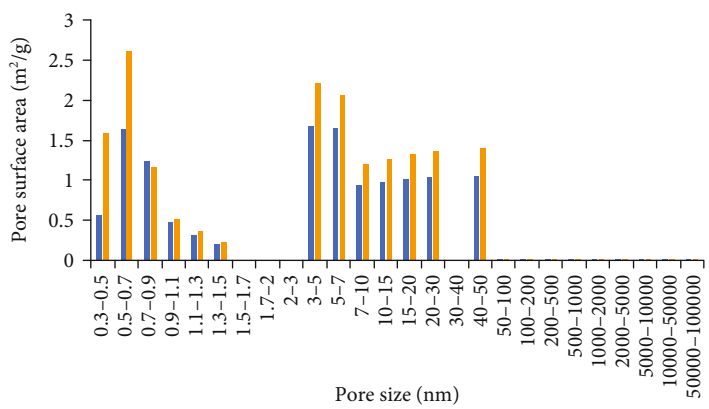

(n) 2589.7 m, organic-bearing clayey shale

Figure 5: Pore surface area features based on the joint characterization for full-scale pore size of different shale samples in TY1 well. Blue: pore surface area data of shale samples before the extraction of shale oil; Yellow: pore surface area data of shale samples after the extraction of shale oil.

shale oil was extracted. Thereinto, the organic-rich mixed and clayey mudstones have the highest pore volume of about 0.03 ml/g, which is followed by the value of about 0.025 ml/g in the fine sandstone; the organic-bearing clayey mudstone has a relatively low value of about 0.02 ml/g; and the organic-bearing mixed mudstone's pore volume is the lowest, showing a value of about 0.013 ml/g. In all types of lithofacies, the pore volume is predominantly provided by macropores (50% ~60%) and then by mesopores (about 40%).

By calculating the difference of the pore volume before and after extraction, the volume of pores where the free shale oil occurs can be obtained. As shown in Figure 6(a), the free shale oil contained in organic-rich clayey shale occupies the largest pore volume of about 0.01 ml/g, which is followed by the value of about 0.008 ml/g in organic-rich mixed shale and organic-bearing clayey shale; this oil contained in fine sandstone approximately occupies a pore volume of 0.005 ml/g; and it occupies the smallest pore volume of about 0.004 ml/g in organic-bearing mixed shale.

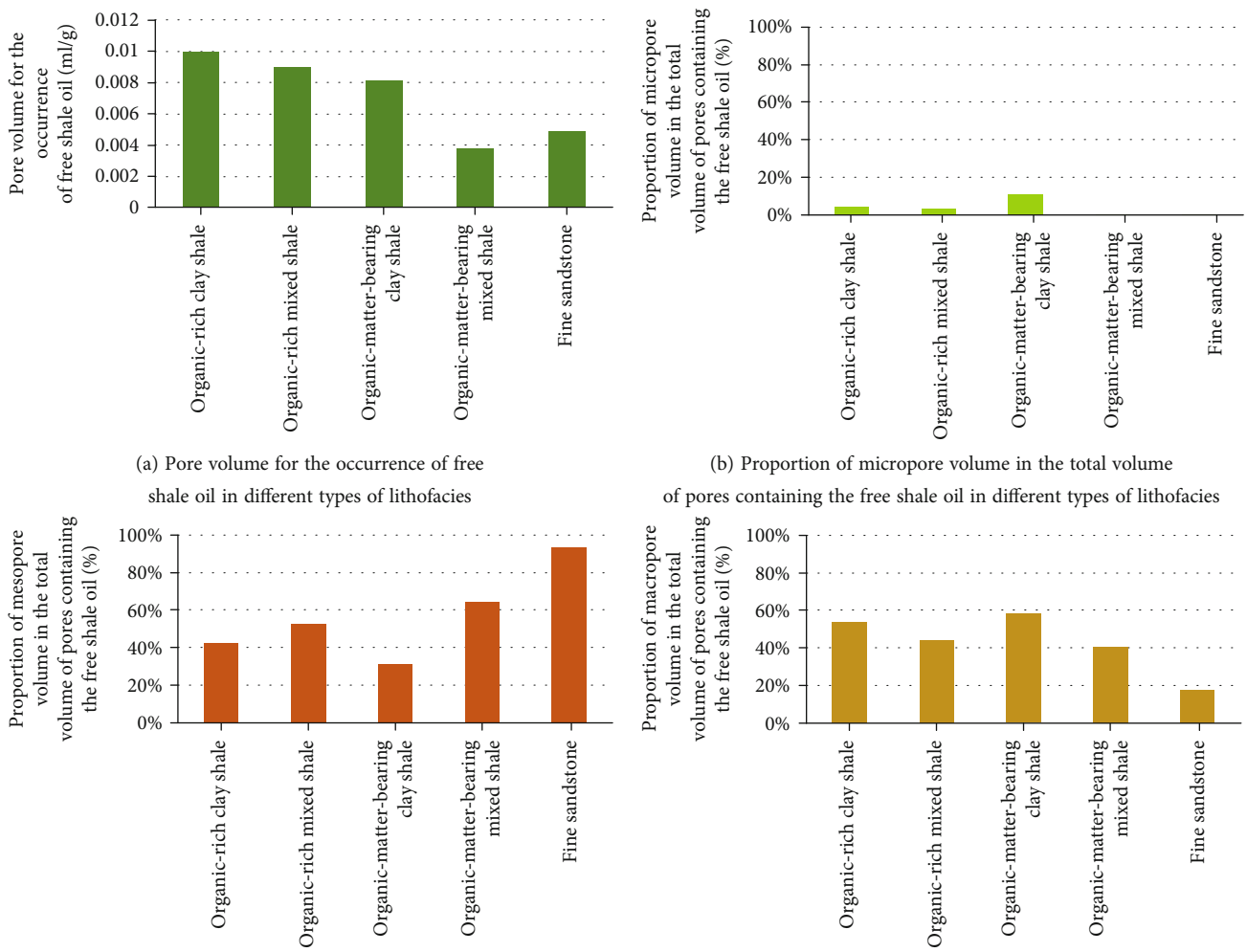

(a) Pore volume for the occurrence of free shale oil in different types of lithofacies

(b) Proportion of micropore volume in the total volume of pores containing the free shale oil in different types of lithofacies

(c) Proportion of mesopore volume in the total volume of pores containing the free shale oil in different types of lithofacies

(d) Proportion of macropore volume in the total volume of pores containing the free shale oil in different types of lithofacies

Figure 6: Pore volume characteristics for the occurrence of free shale oil in different types of lithofacies in TY1 well.

The main contributing pore types to the pore volume of the oil-bearing pores in the free state shale differ between the petrographic phases. According to Figures 6(b)–6(d), the free shale oil contained in organic-rich and organic-bearing clayey shales mainly occurs in macropores, which are followed by mesopores; that contained in organic-rich and organic-bearing mixed shales occurs mainly in mesopores, followed by macropores; and that contained in the fine sandstone primarily occurs in mesopores.

4.2.2. Pore Surface Area Characteristics for the Occurrence of Shale Oil. Similar to the pore volume, the analysis on the pore surface area characteristics of rock reservoirs also adopted the experimental data after the shale oil was extracted. The organic-rich clayey mudstone shows the highest pore surface area of about 12 m^2/g; the organic-rich mixed mudstone, organic-bearing clayey mudstone, and fine sandstone have a value of about 10 m^2/g; and the organic-bearing mixed mudstone shows the lowest value of 6.5 m^2/g. In all types of lithofacies, the pore surface area is primarily provided by mesopores (60%~90%) and then by micropores (5%~40%).

The difference of pore surface area before and after extraction helps to determine the surface area of pores where the absorbed shale oil occurs. As shown in Figure 7(a), the absorbed shale oil contained in organic-rich clayey shale occupies the largest pore surface area of over 4 m^2/g, and the values are similar in organic-rich mixed shale, organic-bearing clayey shale, organic-bearing mixed shale, and fine sandstone, fluctuating around 3 m^2/g.

Similarly, the pore surface area for the occurrence of shale oil in various types of lithofacies is provided by different pore types. According to Figures 7(b)–7(d), the absorbed shale oil contained in organic-bearing mixed shale and fine sandstone all occurs in mesopores; that contained in organic-rich clayey and mixed shales primarily occurs in mesopores, which are followed by micropores; and that contained in organic-bearing clayey shale mainly occurs in micropores, which are followed by mesopores.

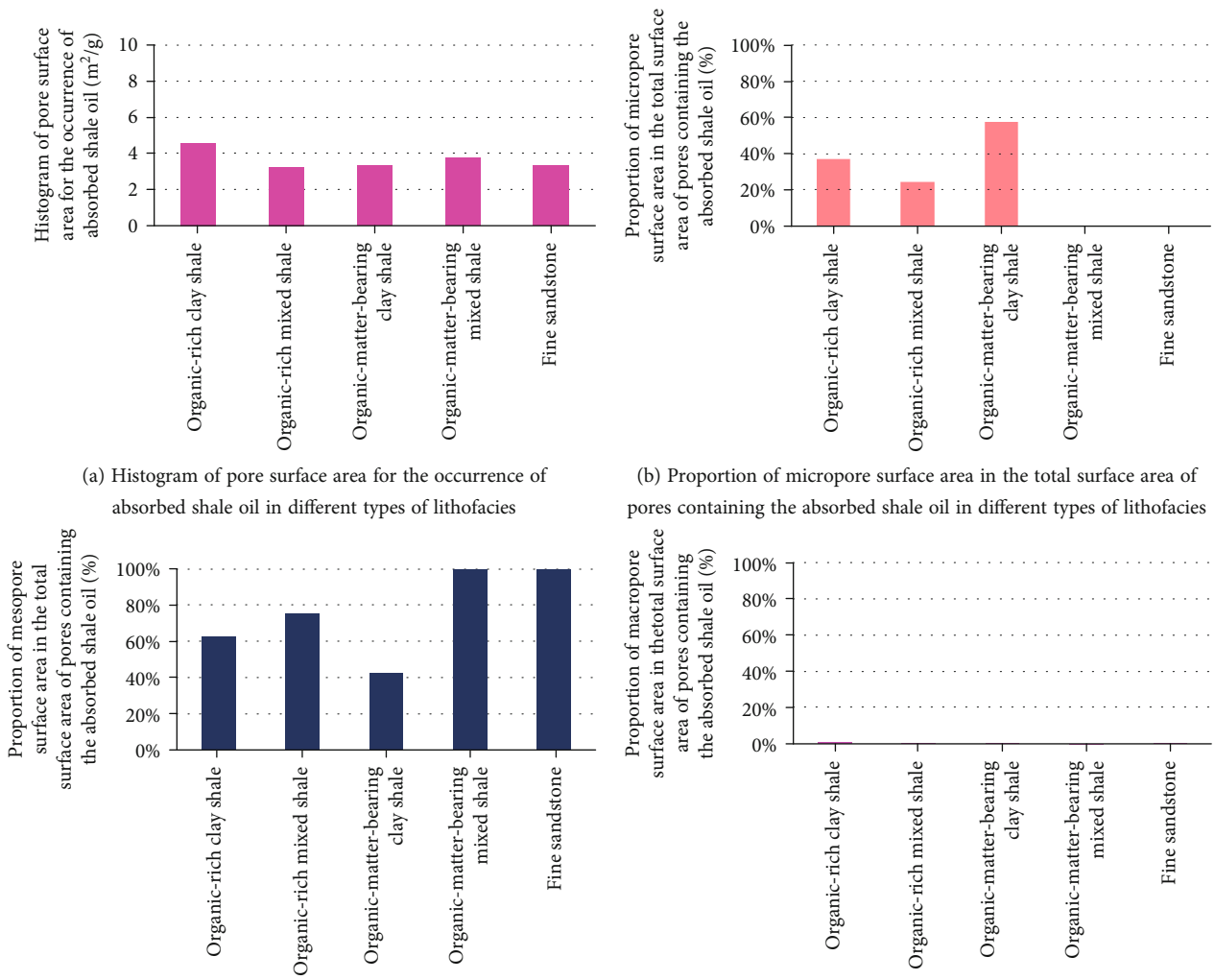

(a) Histogram of pore surface area for the occurrence of absorbed shale oil in different types of lithofacies

(b) Proportion of micropore surface area in the total surface area of pores containing the absorbed shale oil in different types of lithofacies

(c) Proportion of mesopore surface area in the total surface area of pores containing the absorbed shale oil in different types of lithofacies

(d) Proportion of macropore surface area in the total surface area of pores containing the absorbed shale oil in different types of lithofacies

Figure 7: Pore surface area characteristics for the occurrence of absorbed shale oil in different types of lithofacies in TY1 well.

5. Conclusions

In this paper, the rock cores are sampled from the Middle Jurassic Lianggaoshan Formation in southeastern Sichuan Basin of the Upper Yangtze area and are studied based on their TOC content, mineral composition, and shale lithofacies. Meanwhile, the experiments on CO_2 and N_2 adsorptions and high-pressure mercury injection are carried out before and after the shale oil is extracted by wash oil to compare the quantitative characterizations for the full-scale pore size and structure of samples before and after such extraction, thus obtaining the pore space characteristics for shale oil occurrence in different types of lithofacies. The following conclusions have been drawn.

(1) The characteristics of reservoirs vary significantly in different types of lithofacies. The organic-rich mixed and clayey mudstones, with the highest TOC content and the largest pore volume and surface area, provide abundant space for the occurrence of shale oil. Among them, macropores and mesopores contribute to the pore volume and surface area, respectively. In these two types of lithofacies, the free shale oil occupies the most reservoir space and predominantly occurs in macropores and mesopores; and the absorbed one occupies the largest reservoir space and primarily occurs in mesopores

(2) The organic-bearing clayey mudstone, with higher TOC content and larger pore volume and surface area, provides a certain space for the occurrence of shale oil. Notably, the pore volume and surface area originate from macropores and mesopores, respectively. In these lithofacies, the free shale oil occupies a larger space and mainly occurs in macropores, followed by mesopores, and the absorbed one also occupies a larger space and primarily occurs in micropores and then the mesopores

(3) The organic-bearing mixed mudstone has moderate TOC content and smaller pore volume and surface area, offering certain space for shale oil occurrence. Its pore volume and surface area are provided by macropores and mesopores, respectively. In this lithofacies, the free shale oil occupies a smaller reservoir space and mostly occurs in mesopores and then the macropores, and the absorbed one occupies a larger reservoir space and all occurs in mesopores

(4) The fine sandstone has a larger pore volume and surface area, which originate from macropores and mesopores, respectively, providing great space for the occurrence of shale oil. In these lithofacies, the free shale oil occupies a smaller reservoir space and mostly occurs in mesopores, and the absorbed one occupies a smaller reservoir space and all occurs in mesopores

Data Availability

Some of the data are contained in a published source cited in the references. All the data in this article are accessible to the readers.

Conflicts of Interest

The authors declare that they have no conflicts of interest.

Acknowledgments

This study was supported by the open funds from the National Natural Science Foundation of China (No. 42102192, No. 42130803, and No. 42072174); the State Key Laboratory of Shale Oil and Gas Enrichment Mechanisms and Effective Development (G5800-20-ZS-KFGY012); the Open Fund of Key Laboratory of Tectonics and Petroleum Resources (China University of Geosciences), Ministry of Education, Wuhan (TPR-2020-07); the Open Funds from the State Key Laboratory of Petroleum Resources and Prospecting (PRP/open-2107); and the Science and Technology Cooperation Project of the CNPC-SWPU Innovation Alliance.

References

[1] J. B. Curtis, "Fractured shale-gas systems," *AAPG Bulletin*, vol. 86, no. 11, pp. 1921–1938, 2002.

[2] X. Guo, Y. Li, T. Borjigen et al., "Hydrocarbon generation and storage mechanisms of deep-water shelf shales of Ordovician Wufeng Formation-Silurian Longmaxi Formation in Sichuan Basin, China," *Petroleum Exploration and Development*, vol. 47, no. 1, pp. 204–213, 2020.

[3] Z. He, S. Li, H. Nie, Y. Yuan, and H. Wang, "The shale gas "sweet window": "the cracked and unbroken" state of shale and its depth range," *Marine and Petroleum Geology*, vol. 101, no. 101, pp. 334–342, 2019.

[4] R. Wang, Z. Hu, L. Dong et al., "Advancement and trends of shale gas reservoir characterization and evaluation," *Oil & Gas Geology*, vol. 42, no. 1, pp. 54–65, 2021.

[5] R. Wang, H. Nie, Z. Hu, G. Liu, B. Xi, and W. Liu, "Controlling effect of pressure evolution on shale gas reservoirs: a case study of the Wufeng–Longmaxi Formation in the Sichuan Basin," *Natural Gas Industry*, vol. 40, no. 10, pp. 1–11, 2020.

[6] R. Wang, Z. Hu, S. Long et al., "Differential characteristics of the upper Ordovician-lower Silurian Wufeng-Longmaxi shale reservoir and its implications for exploration and development of shale gas in/around the Sichuan basin," *Acta Geologica Sinica-English Edition*, vol. 93, no. 3, pp. 520–535, 2019.

[7] X. Guo, D. Hu, Y. Li, Z. Wei, X. Wei, and Z. Liu, "Geological factors controlling shale gas enrichment and high production in Fuling shale gas field," *Petroleum Exploration and Development*, vol. 44, no. 4, pp. 513–523, 2017.

[8] Z. O. Caineng, P. A. Songqi, J. I. Zhenhua et al., "Shale oil and gas revolution and its impact," *Acta Petrolei Sinica*, vol. 41, no. 1, pp. 1–12, 2020.

[9] H. U.. Suyun, Z. H. A. O. Wenzhi, Y. A. N. G. Zhi et al., "Development potential and technical strategy of continental shale oil in China," *Petroleum Exploration and Development*, vol. 47, no. 4, pp. 877–887, 2020.

[10] K. Zhang, Y. Song, C. Jia et al., "Vertical sealing mechanism of shale and its roof and floor and effect on shale gas accumulation, a case study of marine shale in Sichuan basin, the upper Yangtze area," *Journal of Petroleum Science and Engineering*, vol. 175, no. 2019, pp. 743–754, 2019.

[11] K. Zhang, C. Jia, Y. Song et al., "Analysis of lower Cambrian shale gas composition, source and accumulation pattern in different tectonic backgrounds: a case study of Weiyuan block in the upper Yangtze region and Xiuwu Basin in the lower Yangtze region," *Fuel*, vol. 263, no. 2020, p. 115978, 2020.

[12] C. Zou, D. Dong, Y. Wang et al., "Shale gas in China: characteristics, challenges and prospects (II)," *Petroleum Exploration and Development*, vol. 43, no. 2, pp. 182–196, 2016.

[13] C. Zou, D. Dong, Y. Wang et al., "Shale gas in China: characteristics, challenges and prospects (I)," *Petroleum Exploration and Development*, vol. 42, no. 6, pp. 753–767, 2015.

[14] C. Zou, Q. Zhao, D. Dong et al., "Geological characteristics, main challenges and future prospect of shale gas," *Journal of Natural Gas Geoscience*, vol. 2, no. 5-6, pp. 273–288, 2017.

[15] T. Li, Z. Jiang, C. Xu et al., "Shale micro–nano pore structure characteristics in the lower third member of the continental Shahejie Formation, Zhanhua Sag," *Petroleum Science Bulletin*, vol. 2017, no. 4, pp. 445–456, 2017.

[16] S. Su, Z. Jiang, X. Shan et al., "Effect of lithofacies on shale reservoir and hydrocarbon bearing capacity in the Shahejie Formation, Zhanhua Sag, eastern China," *Journal of Petroleum Science and Engineering*, vol. 174, no. 174, pp. 1303–1308, 2019.

[17] C. Ning, Z. Ma, Z. Jiang et al., "Effect of shale reservoir characteristics on shale oil movability in the lower third member of the Shahejie Formation, Zhanhua Sag," *Acta Geologica Sinica - English Edition*, vol. 94, no. 2, pp. 352–363, 2020.

[18] S. Su, Z. Jiang, S. Xuanlong et al., "The effects of shale pore structure and mineral components on shale oil accumulation in the Zhanhua Sag, Jiyang Depression, Bohai Bay Basin, China," *Journal of Petroleum Science and Engineering*, vol. 165, no. 165, pp. 365–374, 2018.

[19] K. Zhang, Z. Jiang, L. Yin et al., "Controlling functions of hydrothermal activity to shale gas content-taking lower Cambrian in Xiuwu Basin as an example," *Marine and Petroleum Geology*, vol. 85, no. 2017, pp. 177–193, 2017.

[20] Z. C. Wang, W. Z. Zhao, Z. Y. Li, X. F. Jiang, and J. Li, "Role of basement faults in gas accumulation of Xujiahe Formation,

Sichuan Basin," *Petroleum Exploration and Development*, vol. 35, no. 5, pp. 541–547, 2008.

[21] Z. Juan, J. Tao, L. Xuesong, W. Tengqiang, G. Ruiying, and B. Rong, "Evaluation on exploration potentials of lower Jurassic reservoirs in eastern Sichuan Basin," *China Petroleum Exploration*, vol. 23, no. 4, 2018.

[22] K. Zhang, J. Peng, W. Liu et al., "The role of deep geofluids in the enrichment of sedimentary organic matter: a case study of the late Ordovician-early Silurian in the upper Yangtze region and early Cambrian in the lower Yangtze region, South China," *Geofluids*, vol. 2020, Article ID 8868638, 12 pages, 2020.

[23] C. Li, D. He, G. Lu, K. Wen, A. Simon, and Y. Sun, "Multiple thrust detachments and their implications for hydrocarbon accumulation in the northeastern Sichuan Basin, southwestern China," *AAPG Bulletin*, vol. 105, no. 2, pp. 357–390, 2021.

[24] K. Su, J. Lu, G. Zhang et al., "Origin of natural gas in Jurassic Da'anzhai Member in the western part of central Sichuan Basin, China," *Journal of Petroleum Science and Engineering*, vol. 167, no. 167, pp. 890–899, 2018.

[25] Y. Qing, Z. Lü, J. Wu et al., "Formation mechanisms of calcite cements in tight sandstones of the Jurassic Lianggaoshan Formation, northeastern Central Sichuan Basin," *Australian Journal of Earth Sciences*, vol. 66, no. 5, pp. 723–740, 2019.

[26] Z. Pang, S. Tao, Q. Zhang et al., "Enrichment factors and sweep spot evaluation of Jurassic tight oil in central Sichuan Basin, SW China," *Petroleum Research,*, vol. 4, no. 4, pp. 334–347, 2019.

[27] K. Zhang, Y. Song, S. Jiang et al., "Mechanism analysis of organic matter enrichment in different sedimentary backgrounds: a case study of the lower Cambrian and the upper Ordovician-lower Silurian, in Yangtze region," *Marine and Petroleum Geology*, vol. 99, no. 2019, pp. 488–497, 2019.

[28] X. Wang, S. He, X. Guo, B. Zhang, and X. Chen, "The resource evaluation of Jurassic shale in north Fuling area, eastern Sichuan Basin, China," *Energy & Fuels*, vol. 32, no. 2, pp. 1213–1222, 2018.

[29] C. Zou, S. Tao, Y. Fan, and X. Gao, "Characteristics of hydrocarbon accumulation and distribution of tight oil in China: an example of Jurassic tight oil in Sichuan Basin," *AAPG Search and Discovery*, vol. 2012, article 10386, pp. 1–6, 2012.

[30] J. Li, S. Z. Tao, Z. C. Wang, C. N. Zou, X. H. Gao, and S. Q. Wang, "Characteristics of Jurassic petroleum geology and main factors of hydrocarbon accumulation in NE Sichuan Basin," *Natural Gas Geoscience*, vol. 5, 2010.

[31] X. Lu, M. Li, X. Wang et al., "Distribution and geochemical significance of rearranged hopanes in Jurassic source rocks and related oils in the center of the Sichuan Basin, China," *ACS Omega*, vol. 6, no. 21, pp. 13588–13600, 2021.

[32] Z. Liu, G. Liu, Z. Hu et al., "Lithofacies types and assemblage features of continental shale strata and their implications for shale gas exploration: a case study of the middle and lower Jurassic strata in the Sichuan Basin," *Natural Gas Industry B*, vol. 7, no. 4, pp. 358–369, 2020.

[33] T. Li, Z. Jiang, P. Su et al., "Effect of laminae development on pore structure in the lower third member of the Shahejie shale, Zhanhua sag, eastern China," *Interpretation*, vol. 8, no. 1, pp. T103–T114, 2020.

[34] H. Guo, S. Liu, J. He, P. Zhu, and Q.-L. Zhang, "Hydrocarbon pooling conditions of the Jurassic Lianggaoshan Formation in Guangan area, central Sichuan Basin," *Natural Gas Industry*, vol. 28, no. 4, 2008.

[35] T. Li, Z. Jiang, C. Xu et al., "Effect of pore structure on shale oil accumulation in the lower third member of the Shahejie formation, Zhanhua sag, eastern China: evidence from gas adsorption and nuclear magnetic resonance," *Marine and Petroleum Geology*, vol. 88, no. 88, pp. 932–949, 2017.

[36] P. Wang, Z. Jiang, W. Ji et al., "Heterogeneity of intergranular, intraparticle and organic pores in Longmaxi shale in Sichuan Basin, South China: evidence from SEM digital images and fractal and multifractal geometries," *Marine and Petroleum Geology*, vol. 72, no. 72, pp. 122–138, 2016.

[37] W. Ji, Y. Song, Z. Jiang, X. Wang, Y. Bai, and J. Xing, "Geological controls and estimation algorithms of lacustrine shale gas adsorption capacity: a case study of the Triassic strata in the southeastern Ordos Basin, China," *International Journal of Coal Geology*, vol. 134-135, pp. 61–73, 2014.

[38] P. Wang, Z. Jiang, P. Li, C. Jin, X. Li, and P. Huang, "Organic matter pores and evolution characteristics of shales in the lower Silurian Longmaxi Formation and the lower Cambrian Niutitang Formation in periphery of Chongqing," *Natural Gas Geoscience*, vol. 29, no. 7, pp. 997–1008, 2018.

[39] X. Tang, Z. Jiang, S. Jiang, L. Cheng, and Y. Zhang, "Characteristics and origin of in-situ gas desorption of the Cambrian Shuijingtuo Formation shale gas reservoir in the Sichuan Basin, China," *Fuel*, vol. 187, no. 187, pp. 285–295, 2017.

[40] P. Wang, Z. Jiang, L. Chen et al., "Pore structure characterization for the Longmaxi and Niutitang shales in the upper Yangtze Platform, South China: evidence from focused ion beam-He ion microscopy, nano-computerized tomography and gas adsorption analysis," *Marine and Petroleum Geology*, vol. 77, no. 77, pp. 1323–1337, 2016.

[41] W. Ji, Y. Song, Z. Jiang et al., "Micro-nano pore structure characteristics and its control factors of shale in Longmaxi Formation, southeastern Sichuan Basin," *Acta Petrolei Sinica*, vol. 37, no. 2, pp. 182–195, 2016.

[42] F. Yang, S. Xu, F. Hao et al., "Petrophysical characteristics of shales with different lithofacies in Jiaoshiba area, Sichuan Basin, China: implications for shale gas accumulation mechanism," *Marine and Petroleum Geology*, vol. 109, pp. 394–407, 2019.

[43] W. Ji, Y. Song, Z. Jiang et al., "Fractal characteristics of nanopores in the lower Silurian Longmaxi shales from the upper Yangtze Platform, South China," *Marine and Petroleum Geology*, vol. 78, pp. 88–98, 2016.

[44] T. Li, Z. Jiang, Z. Li et al., "Continental shale pore structure characteristics and their controlling factors: a case study from the lower third member of the Shahejie Formation, Zhanhua Sag, Eastern China," *Journal of Natural Gas Science and Engineering*, vol. 45, no. 45, pp. 670–692, 2017.

[45] W. Ji, Y. Song, Z. Jiang et al., "Estimation of marine shale methane adsorption capacity based on experimental investigations of lower Silurian Longmaxi formation in the upper Yangtze Platform, South China," *Marine and Petroleum Geology*, vol. 68, pp. 94–106, 2015.

[46] F. Yang, Z. Ning, Q. Wang, R. Zhang, and B. M. Krooss, "Pore structure characteristics of lower Silurian shales in the southern Sichuan Basin, China: insights to pore development and gas storage mechanism," *International Journal of Coal Geology*, vol. 156, pp. 12–24, 2016.

[47] F. Yang, B. Hu, S. Xu, Q. Meng, and B. M. Krooss, "Thermodynamic characteristic of methane sorption on shales from oil, gas, and condensate windows," *Energy & Fuels*, vol. 32, no. 10, pp. 10443–10456, 2018.

[48] F. Yang, B. Lyu, and S. Xu, "Water sorption and transport in shales: an experimental and simulation study," *Water Resources Research*, vol. 57, no. 2, 2021.

[49] K. Zhang, Y. Song, S. Jiang et al., "Shale gas accumulation mechanism in a syncline setting based on multiple geological factors: an example of southern Sichuan and the Xiuwu Basin in the Yangtze region," *Fuel*, vol. 241, no. 2019, pp. 468–476, 2019.

[50] K. Zhang, J. Peng, X. Wang et al., "Effect of organic maturity on shale gas genesis and pores development: a case study on marine shale in the upper Yangtze region, South China," *Open Geosciences*, vol. 12, no. 1, pp. 1617–1629, 2020.

[51] B. Liu, S. He, L. Meng, X. Fu, L. Gong, and H. Wang, "Sealing mechanisms in volcanic faulted reservoirs in Xujiaweizi extension, northern Songliao Basin, northeastern China," *AAPG bulletin*, vol. 105, no. 8, pp. 1721–1743, 2021.

[52] B. Liu, J. Sun, Y. Zhang et al., "Reservoir space and enrichment model of shale oil in the first member of Cretaceous Qingshankou Formation in the Changling sag, southern Songliao Basin, NE China," *Petroleum Exploration and Development*, vol. 48, no. 3, pp. 608–624, 2021.

[53] H. Huang, R. Li, Z. Jiang, J. Li, and L. Chen, "Investigation of variation in shale gas adsorption capacity with burial depth: insights from the adsorption potential theory," *Journal of natural gas science and engineering*, vol. 73, article 103043, 2020.

[54] Z. Gao and Q. Hu, "Pore structure and spontaneous imbibition characteristics of marine and continental shales in China," *AAPG Bulletin*, vol. 102, no. 10, pp. 1941–1961, 2018.

[55] Z. Gao, Z. Liang, Qinhong Hu, Z. Jiang, and Q. Xuan, "A new and integrated imaging and compositional method to investigate the contributions of organic matter and inorganic minerals to the pore spaces of lacustrine shale in China," *Marine and Petroleum Geology*, vol. 127, article 104962, 2021.

[56] P. Wang, Z. Jiang, L. Yin et al., "Lithofacies classification and its effect on pore structure of the Cambrian marine shale in the upper Yangtze Platform, South China: evidence from FE-SEM and gas adsorption analysis," *Journal of Petroleum Science and Engineering*, vol. 156, no. 2017, pp. 307–321, 2017.

[57] K. Zhang, Z. Li, S. Jiang et al., "Comparative analysis of the siliceous source and organic matter enrichment mechanism of the upper Ordovician–lower Silurian shale in the upper-lower Yangtze area," *Minerals*, vol. 8, no. 7, p. 283, 2018.

[58] K. Zhang, Z. Jiang, X. Xie et al., "Lateral percolation and its effect on shale gas accumulation on the basis of complex tectonic background," *Geofluids*, vol. 2018, Article ID 5195469, 11 pages, 2018.

[59] X. Tang, Z. Jiang, Y. Song et al., "Advances on the Mechanism of Reservoir Forming and Gas Accumulation of the Longmaxi Formation Shale in Sichuan Basin, China," *Energy & Fuels*, vol. 35, no. 5, pp. 3972–3988, 2021.

[60] K. Zhang, Y. Song, S. Jiang et al., "Accumulation mechanism of marine shale gas reservoir in anticlines: a case study of the southern Sichuan Basin and Xiuwu Basin in the Yangtze region," *Geofluids*, vol. 2019, Article ID 5274327, 14 pages, 2019.

Hindawi
Geofluids
Volume 2021, Article ID 4093895, 12 pages
https://doi.org/10.1155/2021/4093895

Research Article

The Impact of Pore Structure on Kerogen Geomechanics

Saad Alafnan

College of Petroleum Engineering and Geosciences, KFUPM, Dhahran 31261, Saudi Arabia

Correspondence should be addressed to Saad Alafnan; safnan@kfupm.edu.sa

Received 5 July 2021; Revised 21 August 2021; Accepted 3 September 2021; Published 15 September 2021

Academic Editor: Jihui Ding

Production stimulation techniques such as the combination of hydraulic fracturing and lateral drilling have made exploiting unconventional formations economically feasible. Advancements in production aspects are not always in lockstep with our ability to predict and model the extent of a fracturing job. Shale is a clastic sedimentary rock composed of a complex mineralogy of clay, quartz, calcite, and fragments of an organic material known as kerogen. The latter, which consists of large chains of aromatic and aliphatic carbons, is highly elastic, a characteristic that impacts the geomechanics of a shale matrix. Following a molecular simulation approach, the objective of this work is to investigate kerogen's petrophysics on a molecular level and link it to kerogen's mechanical properties, considering some range of kerogen structures. Nanoporous kerogen structures across a range of densities were formed from single macromolecule units. Eight units were initially placed in a low-density cell. Then, a molecular dynamic protocol was followed to form a final structure with a density of 1.1 g/cc; the range of density values was consistent with what has been reported in the literature. The structures were subjected to petrophysical assessments including a helium porosity analysis and pore size distribution characterization. Mechanical properties such as Young's modulus, bulk modulus, and Poisson ratio were calculated. The results revealed strong correlations among kerogen's mechanical properties and petrophysics. The kerogen with the lowest porosity showed the highest degree of elasticity, followed by other structures that exhibited larger pores. The effect temperature and the fluid occupying the pore volume were also investigated. The results signify the impact of kerogen's microscale intricacies on its mechanical properties and hence on the shale matrix. This work provides a novel methodology for constructing kerogen structures with different microscale properties that will be useful for delineating fundamental characteristics such as mechanical properties. The findings of this work can be used in a larger scale model for a better description of shale's geomechanics.

1. Introduction

Rock geomechanics is a crucial branch of oil and gas reservoir development. The role of geomechanics is even more influential in unconventional formations, where permeability is mostly attributed to the hydraulic fractures generated. While hydraulic fracturing technologies have advanced, allowing for the efficient stimulation of newly drilled wells and restoration of productivity in old wells, the ability to describe and model the initiation, propagation, and dynamics of induced hydraulic fractures is lacking. Shale is a highly heterogeneous sedimentary rock consisting of a complex mineralogy of clay, quartz, calcite, and fragments of organic matter known as kerogen [1–3]; it is this complexity that causes shale petrophysics and geomechanics to deviate from those of conventional sedimentary rocks.

The extent and pattern of hydraulic fractures are determined by the fracturing fluid, as well as the geology of the formation. Highly viscous fluids are used to increase the propagation of the fracture, while low-viscosity fluids are employed to bridge formation discontinuities [4, 5]. A high rate of injectivity is used to enlarge the stimulated reservoir volume SRV, while a lower rate targets interconnecting discontinuities [6]. The formation's geological characteristics, however, fall beyond predesign control. Hydraulic fractures are likely to progress in the direction of existing natural fractures, where stress accumulation is the highest [7];though, clay minerals and other fragments may act as a barrier to propagation [8, 9]. Fracture geometry is controlled by the depth of the well. Shallow wells tend to form a network of fractures rather than a biwing fracture [10, 11]. The contents of brittle materials, characterizable by lower ranges in the

Poisson ratio, correlate positively with the formation of a complex fracture geometry [12, 13]. Generally, four types of fractures are anticipated: simple, fishbone-like, fishbone-like with a fissure opening, and multilateral fishbone-like. The fracture category is determined by several factors, including bedding discontinuity, the presence of natural fractures and faults, and rock mineralogy [14]. The macroscopic mechanical properties of shale depend on the properties of the different constituents on a microscopic level [15, 16]. In general, shale is a composite materials, with clay and quartz serving as the matrix and organic matter present as inclusions [17, 18].

The geomechanics of shale has been determined through traditional uniaxial and triaxial testing methods and laboratory scale fracturing experiments [19–24]. Such tests are based on the qualitatively linking of mechanical properties to the mineralogy. Hence, the models developed are vulnerable to a high level of discrepancy when applied to other samples with different mineralogical distributions [25]. Micromechanical testing methods such as quasistatic nanoindentation, mapping by nanoindentation, and atomic force microscope AFM have been employed to study variations in mechanical properties, with shale matrices revealing highly heterogeneous behaviors of feldsbar, carbonate, quarts, and organic matter [26–34]. Young's modulus of inorganic inclusions is in the range of 50 GPa, while it is less than 10 GPa for organic matter [27–29]. Inorganic constituents exhibit higher anisotropic behavior compared to those that are organic in nature [35–37]. Microscopic mechanical properties vary beyond the elastic region, impacting the development of hydraulic fractures. The extent and complexity of the induced hydraulic fractures are determined by the microstructural constituents of the shale matrix [38–40].

Organic matter, characteristically different from inorganic components, is often the target of micromechanical testing. High and low organic matter in shale samples have been tested for tensile failures, unconfined tensile strength, and fracture behavior, revealing some dependency of the geomechanics on the contents of the organic matter [41]. The heterogeneity and complexity of the mineralogy render isolating the impact of organic matter on geomechanics rather challenging. The organic matter consists of kerogen and bitumen. While the latter is soluble in organic solvents, the former represents a solid, best thought of as micro- or mesoporous material [3]. Chemical bonding and intermolecular interactions change with kerogen type and level of maturation, altering the chemical and physical properties (including the geomechanical behavior) and hence impacting the macroscopic geomechanics of shale. Experimental characterization of such kerogen requires extraction, followed by typical petrophysical and geomechanical assessments. Obtaining comprehensive insights into the relationship between the kerogen's structure and geomechanics means gathering samples containing kerogen that are characteristically different, a task that is both laborious and dubious.

The ability to represent naturally occurring or synthetically derived structures on a computational molecular platform has provided an unprecedented degree of flexibility in the study of complex research problems, moving the practice well beyond laboratory-based work. The goal of the present research is to recreate a range of representative kerogen configurations on a molecular level to delineate the relationship between kerogen's structure and its mechanical behavior.

1.1. Molecular Simulation of Kerogen. The first attempt to classify kerogens was based on the observation that kerogens contained in coals share a great deal of similarity with the matrix itself (e.g., a graphene-like structure), while kerogens found in other formations contain higher fraction of aliphatic chains [42, 43]. The current classification of kerogens relies on detailed elemental and spectroscopic analyses. In particular, hydrogen to carbon (H/C) and oxygen to carbon (O/C) ratios have been interpreted to determine the degree of aromaticity and oxidation level. Hence, kerogens can be ordered according to their origin (type) and rank (maturation) [44, 45]. Kerogens, generally, are categorized as type I, II, III, or IV, based on their origin. Each kerogen type is subject to a sequence of diagenesis, catagenesis, and mutagenesis processes. Hence, kerogens exist on a spectrum of maturity level [45, 46]. Some references classify type IV as the same as type III, due to their intrinsic similarities [47]. Type I is characterized by relatively high H/C and low O/C ratios, making it more aliphatic in nature [47]. Conversely, type II contains a larger amount of aromatic and cyclic aliphatic fractions, which decreases the H/C ratio [48]. Being originated in an oxygen-rich environment, type III is associated with larger contents of oxygen appearing in the functional groups or connecting cyclic chains of aromatic moieties [48, 49].

Through identifying the primary functional groups, complete modeling of the kerogen chemical structures was achieved where two distinct groups of kerogens were recognized. The first was island-like aromatic structures fused by alkoxy or ether while the second was more aliphatic. Large building blocks, also known as macromolecules, were derived based on hypothetical models constrained to match elemental ratios [50–54]. These kerogen macromolecules, when upscaled, failed to match macroscopic experimentally measured parameters such as density, a condition at least partially attributable to the lack of proper description of their three-dimensional (3D) spatial configuration [55]. Nevertheless, representing kerogens from different origins and thermal maturity levels has been achieved for type I and type II at diagenesis, beginning, and end of catagenesis [56, 57]. With the computational power of computer-based techniques, more types have been obtained. Ungerer et al. [58, 59] derived six representative models (i.e., IA, IIA, IIB, IIC, IID, and IIIA) [58, 59]. It is noteworthy to state that the prototypes listed in this review and some others were meant to provide structures that could reproduce the general macroscopic characteristics of kerogens to facilitate thorough investigation of different petrophysical, transport, and other related aspects. In this research, the advancement in the molecular representation of kerogen has been utilized to create representative structures, facilitating a thorough geomechanical analysis.

1.2. Atomistic Simulations of Mechanical Properties. Theoretical calculations of the mechanical properties of materials have attracted increasing interest for use in a wide range of engineering applications. Particularly, they have been adopted to study advanced composite materials under a wide range of conditions. The steering principle behind the approach is based on relating structural deformation to the applied stress field, after restoring mechanical equilibrium through energy minimization [60]. Theodorou and Suter [60] conducted a mechanical behavior study of atactic polypropylene at 233 K, considering 15 independent configurations; the authors found Young's modulus to be within 10% of what was measured experimentally. Commercial software packages have facilitated the creation of various amorphous structures. Fan and Hsu [61] conducted a molecular characterization of aromatic polysulfone elastic moduli within an acceptable range of accuracy and uncertainty. Hutnik et al. [62] considered a more complex system of glassy polycarbonate of 4,4′-isopropylidenediphenol for an analysis of the elastic and plastic properties, observing a high degree of uncertainty attributable to the number of configurations considered. Fan et al. [63] studied a similar system and reduced the uncertainty by considering more configurations. Raaska et al. [64] calculated elastic constants, using both static and dynamic stress-strain concepts. The reported Young's modulus value was comparable to that which was obtained experimentally. Kerogen, a set of naturally occurring materials consisting of carbon, hydrogen, oxygen, nitrogen, and sulfur and connected chemically through aliphatic, cyclic, and aromatic structures, was found to primarily be similar in chemistry to the aforementioned polymerized compounds. The success achieved in the calculation of the mechanical properties of polymers rendered an atomistic approach a reliable proxy, providing useful insights into kerogen geomechanics and the factors controlling it [65–70]. These studies shed some light on the mechanical properties of kerogen in a general sense. However, a detailed study of how kerogen heterogeneity influences the geomechanics of kerogen is not exhaustive. In this study, the impact of pore structure is linked to the mechanical behavior through an integrated study considering some range of kerogen configurations, temperature, and fluid effects.

In the next section, the nanostructure construction of kerogen is detailed, followed by the molecular algorithms utilized to characterize the structure for its relevant petrophysical aspects. The mechanical properties simulation adopted in this research is also presented.

1.3. Realistic Kerogen Structures. To study kerogen's geomechanics, a realistic structure epitomizing kerogen is required to serve as nanoporous media. In this research, a novel molecular modelling approach was followed to construct a nanoporous kerogen model virtually. The extraction of organic matter in sufficient quantities for a petrophysical assessment is arduous. The process generally requires the application of etching agents and/or thermal treatment. Additionally, the desired conditions of pressure and temperature at which different analyses are performed can be experimentally challenging. Attributed to its unprecedented flexibility, molecular modeling framework has the advantage of controlling the petrophysical properties of kerogen during the initiation phase where different kerogen types, bonding strengths, and other chemical properties can be changed in order to independently isolate their impact. The geomechanical assessments carried out in this study relied on the novel work of the kerogen models derived by Ungerer et al. [59]. These units are understood to cover the basic kerogen types (see Figure 1 and Table 1).

In this study, kerogen type IIA was used as a representative of the organic matter in shale. Type IIA kerogen macromolecules were recreated on a molecular level, see Figure 2 for a graphic representation of the various kerogen types. Polymer-consistent forcefield plus (PCFF+) was used to parameterize the atoms present in kerogen as center forces [71, 72]. Each center is defined and assigned a charge. Lennard Jones 6-9 was employed to describe the interactions between different center forces. The PCFF+ is very well known for its ability to configure organic compounds complementing earlier efforts of forcefields such as with COMPASS and CFF93 [71, 72].

An initial low-density structure containing eight units of kerogen IIA was created in relatively large cell volume to avoid any issues caused by larger sized kerogen macromolecules. The final kerogen structure was then formed utilizing a large-scale atomic/molecular massively parallel simulator LAMMPS. The simulation proceeded to a final condition of 20.67 MPa and 350 K which are deemed to represent typical reservoir conditions. The molecular dynamic steps began with initializing the cell by assigning 9.5 cutoff value and 2.0 skin with periodic boundaries, that was followed by a proper configuration of the molecular positions and velocity through energy minimization. Next, two stages of isochoric-isothermal NVT and isobaric-isothermal NPT for 250 ps and 200 ps, respectively, were run at 900 K. Then, the temperature was gradually reduced from 900 K to the final temperature through three consecutive NPT stages. The gradual decrease to the final targeted temperature assured faster convergence of kerogen units. The density of the final kerogen structure was around 1.1 g/cm^3, which is close to the measured experimental one for the same type [59]. During the creation of the initial cell, a number of dummy molecules were added to act as a placeholder. The dummy molecules were removed when the final structure was formed, leaving behind a certain number of voids. The same process was repeated with an increasing number of dummy molecules, yielding a total of seven configurations across a range of density values (see Table 2). A description of the molecular construction protocol is given in Figure 1.

1.4. Petrophysical Characterization. Helium–kerogen interactions in a Gibbs Monte Carlo simulation was used as a proxy for determining the void space, through the following relationship:

$$N^m = N^a - \rho_a V_P. \tag{1}$$

Here, ρ_a is the density of the helium, N_m is the number of excess helium, and N_a is the number of adsorbed molecules

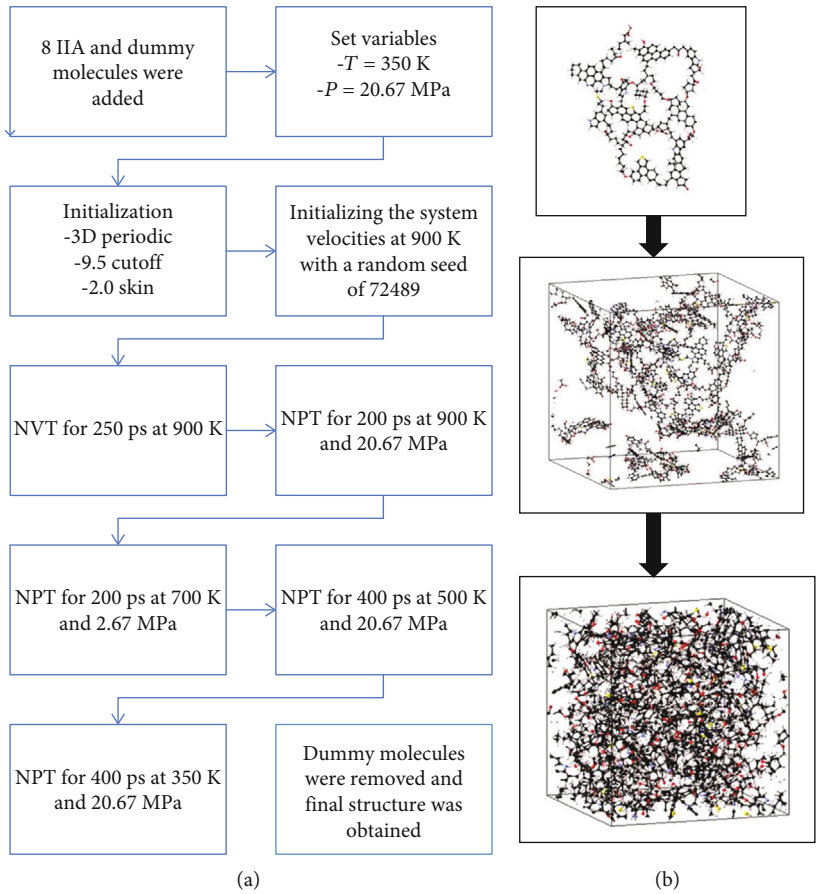

Figure 1: (a) LAMMPS protocol workflow for creating kerogen nanostructures. (b) from a single kerogen unit to the final kerogen structure [82].

Table 1: Kerogen prototypes presented by Ungerer [58], reproduced from Alafnan [82].

Kerogen type	Maturity level	H/C	O/C	N/C	S/C
KIA	Immature	1.530	0.052	0.028	0.012
KIIA	Immature	1.170	0.095	0.024	0.012
KIIB	Top of oil window	1.120	0.060	0.022	0.009
KIIC	Middle end of oil window	0.905	0.054	0.021	0.008
KIID	Overmature	0.580	0.051	0.023	0.011
KIIIA	Immature	0.870	0.116	0.017	0.000

of helium. The pore volume V_P can be calculated assuming no excess adsorption which is reasonably justified by the confined spaces in kerogen. Once the pore volume is estimated, the porosity could then be calculated when divided by the bulk volume. The calculations were performed on all kerogen structures, revealing increasing void ratios as the number of dummy molecules increased (see Table 1).

Porosity, which is an indicator of the total pore volume, can be used to describe the total voids of porous media. A detailed distribution of pore sizes, however, is needed to fully characterize a kerogen structure. For this purpose, a pore size distribution (PSD) analysis was carried out for all seven nanoporous kerogen structures. The insertion of nonoverlapping spheres to fill the void spaces was used to determine the PSD distribution. The process involves predefining a threshold radius (i.e., a sphere was created in a certain location if its radius was greater than or equal to 0.15 nm in this study) [73]. An example of the PSD calculations performed can be found in Figure 3. The PSD and cumulative distribution function are given in Figures 4 and 5, respectively. The analysis revealed an increasing number of larger pores as the number of dummy molecules increased (i.e., larger pores were found to be positively correlated with porosity).

1.5. Mechanical Properties. The kerogen's molecular structure, initially at equilibrium, was deformed by changing the

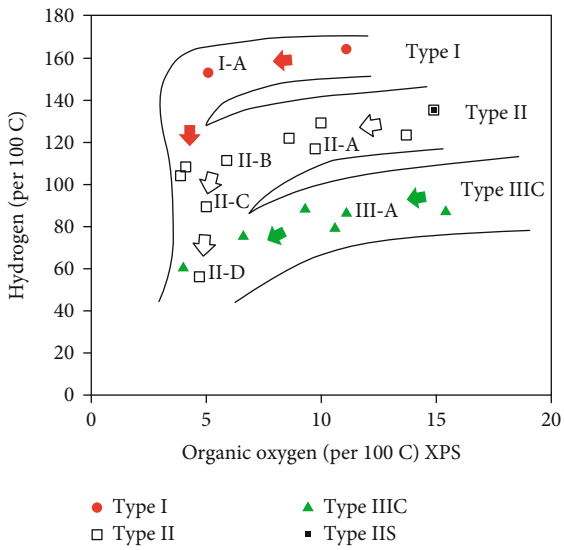

Figure 2: Van Krevelen diagram of kerogen maturation [59].

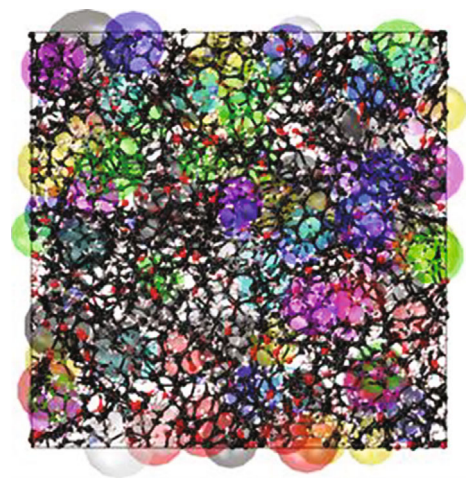

Figure 3: Visual illustration of the PSD algorithm for one of the kerogen structures [82].

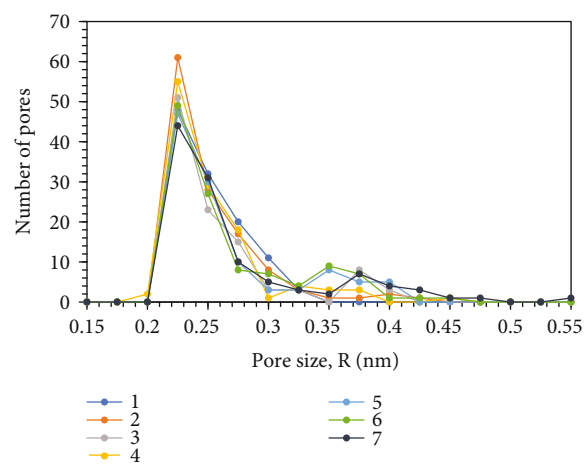

Figure 4: PSD of the kerogen configurations.

Table 2: Seven kerogen configurations constructed.

Configuration	Number of dummy molecules	Density (g/cm^3)	Porosity
1	0	1.114	6.45%
2	5	1.096	8.11%
3	10	1.082	9.36%
4	15	1.058	11.43%
5	20	1.041	13.48%
6	25	1.023	14.77%
7	35	0.963	19.68%

lattice vector $R = (a, b, c)$ to a disturbed cell $R' = (a', b', c')$, using a strain matrix e [74–76].

$$R' = R\begin{pmatrix} 1 + e_{xx} & \frac{1}{2}e_{xy} & \frac{1}{2}e_{xz} \\ \frac{1}{2}e_{yx} & 1 + e_{yy} & \frac{1}{2}e_{yz} \\ \frac{1}{2}e_{zx} & \frac{1}{2}e_{zy} & 1 + e_{zz} \end{pmatrix}. \quad (2)$$

The changes imposed led to a shift in the total energy of the system:

$$U = \frac{E_{\text{tot}} - E_0}{V_0} = \frac{1}{2}\sum_{i=1}^{6}\sum_{j=1}^{6} C_{ij}e_ie_j, \quad (3)$$

where U is the stress per unit volume, V_0 is the initial volume of the cell, E_0 is the energy of prior deformation, E_{tot} is the energy after deformation, and C_{ij} is the element of the stiffness matrix. Both i and j run from one to six {xx, yy, zz, yz, xz, xy}, yielding a stress tensor of 36 elements. Assuming symmetry, the total number of elements was reduced to three for a cubic cell.

A predefined strain e was defined across one direction (i.e., one component of the lattice). All other strain components were set to zero. The energy change U, defined by Equation (3), reduced as follows [77].

$$U = \mathrm{C}_{11}\frac{e^2}{2}. \quad (4)$$

The above equation was used to calculate element C_{11}. Similarly, the diagonal strains was set as $e_{yz} = e_{zy} = 1/2\, e$, and all other strain components were set to zero. The energy change equation could then be reduced to calculate C_{44} [77].

$$U = \mathrm{C}_{44}\frac{e^2}{2}. \quad (5)$$

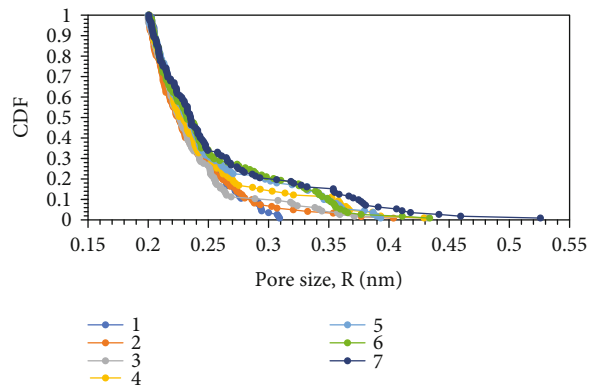

Figure 5: Cumulative distribution function of the PSD for the seven configurations.

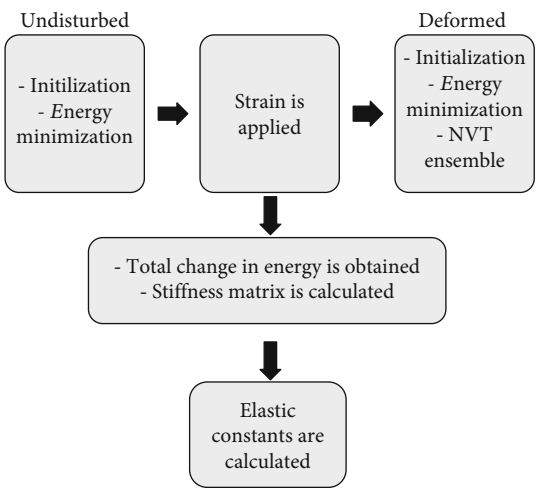

Figure 6: LAMMPS-based molecular approach used to calculate mechanical properties.

The bulk modulus, an elastic coefficient representing the response to a uniform applied stress, was calculated by setting $e_{xx} = e_{yy} = e_{zz} = e$, while the shear modulus, a coefficient of the elastic response to shear stress, was estimated by setting $e_{zz} = e$ and $e_{xx} = e_{yy} = -1/2\, e$ [78]. For estimating the elastic moduli, smaller value of strains is used. Elastic moduli are obtained at two values of strains to assure consistency (i.e., 0.02 and 0.04 strains were selected).

The aforementioned approach was applied to the different kerogen configurations. The strain implementation and energy calculations were conducted through LAMMPS and assisted by a MedeA interface. The molecular dynamic protocol consisted of initialization with a 3D periodic boundary, 9.5 cutoff distance, and 2.0 skin, followed by energy minimization to optimize the positions of the atoms. Then, strains were applied in predefined directions. The energy was subsequently minimized, and NVT ensemble was run at the specified temperature, allowing for a calculation of the total change in energy and stiffness matrix. The data were then used to estimate the elastic moduli. A summary of the molecular approach is given in Figure 6.

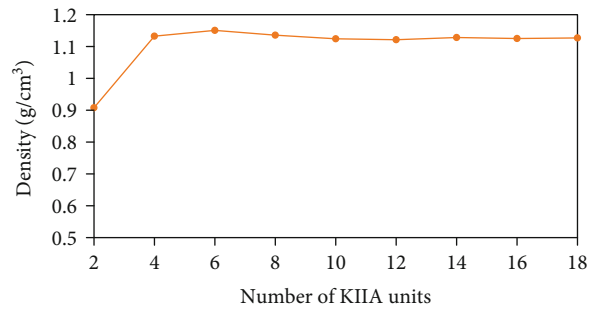

Figure 7: Density convergence of kerogen structures built using an increasing number of kerogen units.

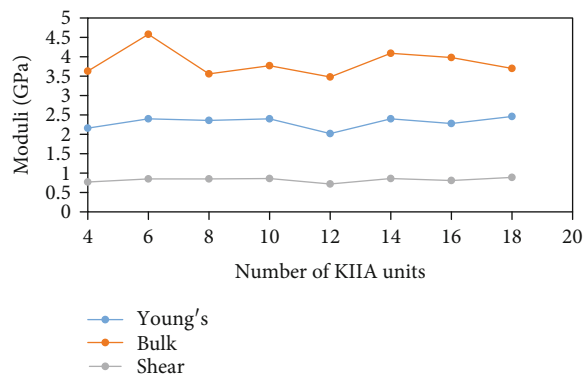

Figure 8: Elastic moduli of kerogen structures, revealing an acceptable degree of reproducibility for kerogen constructed from more than four units.

The above concept was extended beyond the elastic region by continuously deforming the structure at an incremental strain and minimizing the energy before and after deformation to mimic tensile, compression, and shear failure tests.

Kerogen is anticipated to exhibit both elastic and plastic behaviors during the shale stimulation phase and production span. In this study, elastic property and tensile failure tests were carried out to develop a comprehensive understanding of kerogen's geomechanics. The details are presented in the next section.

2. Results and Discussion

2.1. Porosity Effect. The lattice dimension of the seven configurations ranged from 3.6 nm to 3.8 nm, corresponding to a bulk volume of 46.656 nm^3 to 54.872 nm^3 (i.e., the outcome of applying the construction protocol summarized in Figure 1). To assure that the selected number of kerogen macromolecules was sufficient to yield representative geomechanics, a pragmatic approach of checking the effect of increasing the number of kerogen units was followed. A kerogen structure built from two kerogen units was created, and its density was obtained. The same process was repeated at an increasing number of kerogen units. It was evident that the density converged to the same value for kerogen containing more than four units, while the structure consisting of two

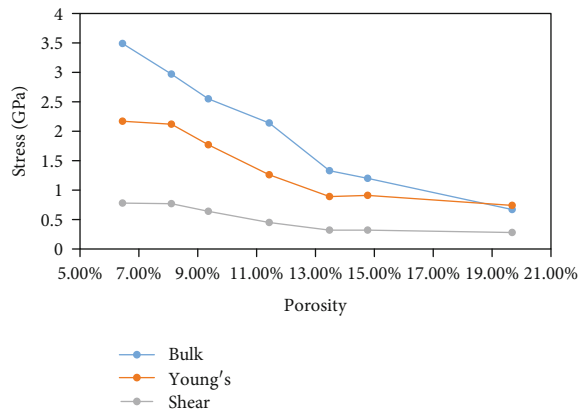

Figure 9: Elastic moduli as a function of porosity for kerogen containing eight units.

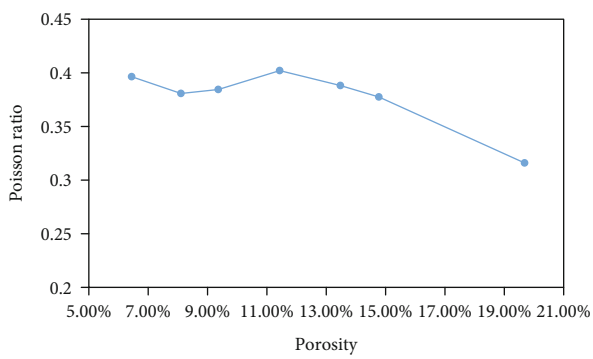

Figure 10: Poisson's ratio for kerogen as a function of porosity.

units deviated significantly (see Figure 7). The convergence in the density is consistent with estimated mechanical moduli as shown in Figure 8. Similar observations of the number of units needed to form a realistic kerogen structure are reported in the literature [79–84].

Next, the impact of the kerogen pore structure on its geomechanics was explored in the seven configurations, with porosity values ranging from 6.45% to 19.68% (see Table 2). The analysis began with extraction of the elastic moduli. The results showed that kerogen's elastic moduli decreased as porosity increased, an observation suggesting a higher probability of plastic deformation as the void ratio increases (see Figure 9). The elastic moduli were then utilized to calculate the Poisson ratio.

$$\nu = \frac{E}{2G} - 1, \tag{6}$$

where E is Young's modulus, G is the shear modulus, and ν is the Poisson ratio.

The Poisson ratio is a coefficient used to characterize the tendency of materials to expand in a direction perpendicular to the direction of compression. In geomechanics, it is an indicator of a rock's likelihood to fracture. For kerogen, the ratio was found to negatively correlate with porosity with some fluctuations at a lower range of porosity (see Figure 10). The obtained results of elastic moduli in this computational study are consistent with the experimental work reported in the literature. The experimental approach primarily utilizes nanoindentation coupled with atomic force microscopy to extract Young's modulus and Poisson's ratio (see Table 3).

Table 3: Experimental assessments of Young's modulus and Poisson's ratio of kerogen samples taken from different shale formations.

Formation	Poisson's ratio	Young's modulus (GPa)
Kumar et al., [85]		
Woodford shale (USA)	0.3	6.2
Kimmeridge (USA)	0.3	5
Eliyahu et al., [26]		
Upper Jurassic Source Rock (USA)	0.3	Up to 2.5
Ahmadov et al., [86]		
Bazhenov (Russia)	0.35	5.2
	0.45	4.7

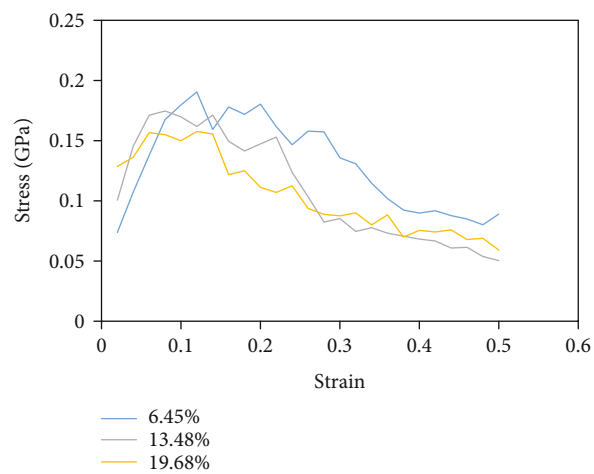

Figure 11: Tensile mechanical deformation of kerogen structures with a porosity range of 6.45% to 19.68%. Three cases were shown to avoid overlapping.

Deformation and fracturing occur outside the elastic region. Thus, the stress-strain relationship detailed in Section 2.3 was used to explore the mechanisms of mechanical failure. As described previously, an incremental strain was applied along the z-direction to the seven kerogen configurations, with a total strain of 0.4 (see Figure 11).

The kerogen with the lowest porosity exhibited a prolonged elastic region with an ultimate strength of 0.191 GPa. It showed early signs of failure at a 0.08 strain. The failure progressed through a series of strains, a behavior intrinsically different from what is typically observed for the inorganic constituents of sedimentary rocks. A complete fracture was not observed until a strain value of approximately 0.3. The other kerogen configurations showed similar trends, but with

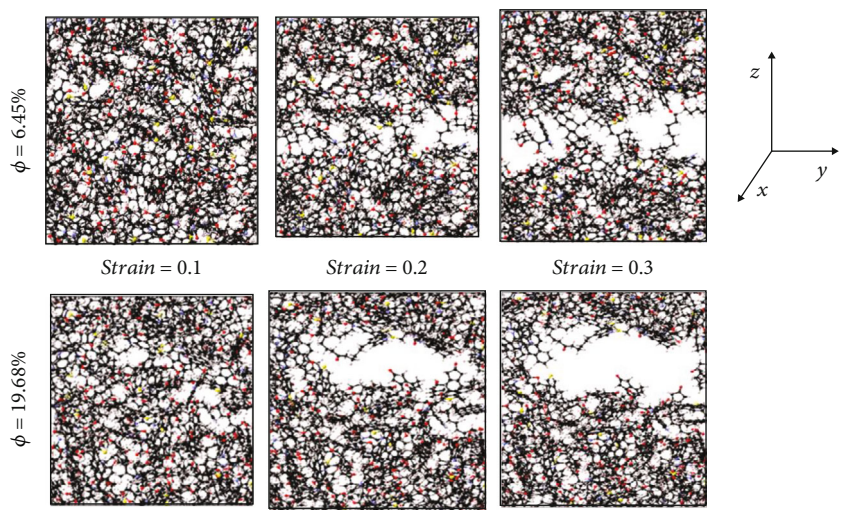

Figure 12: Visualization of the evolution of tensile deformation for two kerogen structures. The first had a porosity of 6.45% and the second of 19.68%.

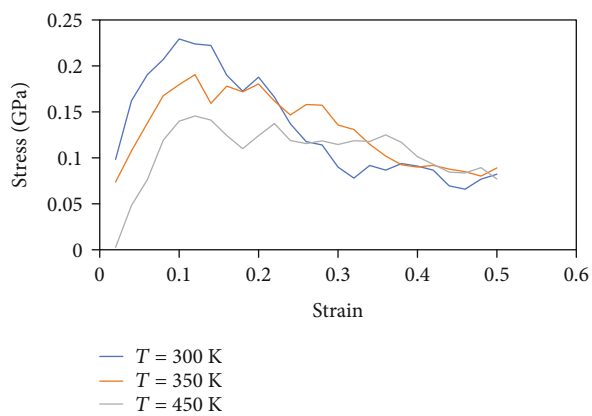

Figure 13: Tensile mechanical deformation of 6.45% porosity kerogen structure at 300 K, 350 K, and 450 K.

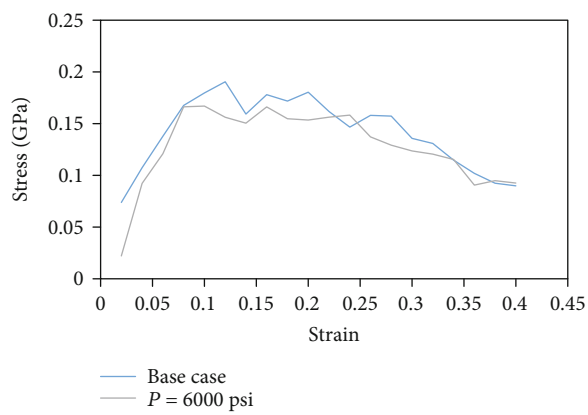

Figure 14: Tensile mechanical deformation of 6.45% porosity kerogen structure for empty and filled with methane cases at 6000 psi.

a decreasing order of ultimate strength as porosity increased. The kerogen configurations with the highest porosity experienced the earliest signs of failure, at a 0.05 strain.

The geomechanical behavior of the different kerogen configurations intuitively matched the petrophysical analysis conducted in Section 2.2. As porosity increased, larger pores were introduced into the structures. These pores tended to serve as points of stress accumulation, enhancing fracture initiation and propagation at smaller magnitudes of applied stresses. A visual evolution of tensile deformation for the two kerogen structures with the lowest and highest porosity values is given in Figure 12. It can be seen that the structure with higher porosity began to deform more severely at a lower strain, in alignment with the larger pores.

2.2. Temperature Effect. The mechanical behavior of oncrystalline materials such as kerogen is more vulnerable to be influenced by changes in the temperature. The mechanical assessment of kerogen in the previous section is conducted at 350 K, which is deemed to be a representative of average reservoir temperature. However, reservoir temperature may vary depending on the depth and the location of the reservoir. The adopted framework in this study is capable of addressing the effect of temperature as the construction of the structure, and the quantification of its energy is performed honoring the selected temperature. The stress-strain relationship revealed high sensitivity of the mechanical behavior on the temperature (see Figure 13). As the temperature increases, kerogen seems to undergo prolonged plastic deformation before failure.

2.3. Pore Fluid Effect. The reported data in the previous sections were made considering only kerogen with empty pores. However, in the reservoir, pore volume is occupied with fluids in quantities that are determined by the conditions of pressure, temperature, and the available pore volume. To study the effect of fluids, kerogen pore volume was saturated with natural gas (i.e. primarily represented by methane in this study) through running Gibbs Monte Carlo simulation. Two structures (highest and lowest porosity)

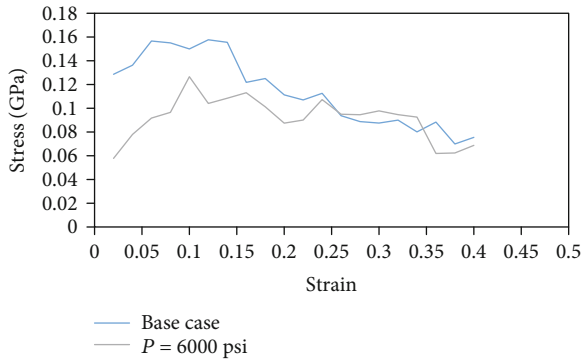

Figure 15: Tensile mechanical deformation of 19.68% porosity kerogen structure for empty and filled with methane cases at 6000 psi.

were subjected to interactions with methane. The output is the number of methane molecules trapped in the structure. The calculations were performed using MedeA interface. Methane fugacity, which is needed for the calculations, was estimated using Peng-Robinson equation of state. In this study, Gibbs Monte Carlo simulation was performed at 6000 psi (i.e., the fugacity is 35.84 MPa at this pressure).

Kerogen structures filled with methane were then assessed for their mechanical behavior (see Figures 14 and 15). It is evident that the contained methane in pore volume altered the mechanical response of kerogen especially for the high porosity case (i.e., with high porosity, more methane molecules are occupying the structure).

3. Conclusion

The geomechanical behavior of shale is governed by its individual constituents, including kerogen. The presence of kerogen as finely dispersed fragments renders it inaccessible to traditional mechanical testing methods. In this study, a novel molecular modeling approach was followed to construct, characterize, and mechanically test kerogen configurations across a range of petrophysical properties, in order to determine their geomechanical characteristics. The results revealed that the kerogen exhibited both elastic and plastic deformations. The kerogen with the lowest porosity had the maximum ultimate strength and highest elastic moduli. The higher porosity kerogen showed a higher probability of failure, which was attributable to the presence of larger pores. Kerogen mechanical behavior was found also sensitive to the conditions of temperature and the fluid occupying the pore volume. The findings of this work can be used in a larger scale computational modeling of shale's geomechanics. It is recommended that this work be validated and the findings of this study experimentally correlated.

Abbreviations

$\varnothing$: Porosity, dimensionless parameter
R: Pore radius, nm
T: Temperature, K
P: Presssure, psi, MPa, or Pa
V_P: Pore volume, $m^{3.}$
E: Young's modulus, GPa
B: Bulk modulus, GPa
G: Shear modulus, GPa
ν: Poisson ratio, dimensionless parameter.

Data Availability

The molecular simulation data including the constructed kerogen structures that were used to support the findings of this study are available from the corresponding author upon request.

Additional Points

Highlights. (i) Organic materials, known as kerogen, are believed to be finely dispersed in the source rocks matrix. (ii) Seven different kerogen structures were recreated at molecular level starting from single macromolecules. The models represent some range of porosity.(iii) Kerogens revealed geomechanical behavior that is characteristically different than that of typical rocks. (iv) Elastic moduli were found to be negatively correlated with porosity. (v) Kerogen with the highest porosity was more vulnerable to fracture under applied stresses than kerogen of low porosity.(vii) The temperature and the fluid occupying the pore volume influence the mechanical behavior

Conflicts of Interest

The author declares that they have no conflicts of interest.

Acknowledgments

The author acknowledges the support provided by the College of Petroleum Engineering and Geosciences at King Fahd University of Petroleum and Minerals in Saudi Arabia. The results reported in this study has been achieved by MedeA interface.

References

[1] S. Zhou, G. Yan, H. Xue, W. Guo, and X. Li, "2D and 3D nanopore characterization of gas shale in Longmaxi formation based on FIB-SEM," *Marine and Petroleum Geology*, vol. 73, pp. 174–180, 2016.

[2] J. Klaver, G. Desbois, R. Littke, and J. L. Urai, "BIB-SEM pore characterization of mature and post mature Posidonia Shale samples from the Hils area," *Germany. Int. J. Coal Geol*, vol. 158, pp. 78–89, 2016.

[3] C. Yang, J. Zhang, S. Han, B. Xue, and Q. Zhao, "Classification and the developmental regularity of organic-associated pores (OAP) through a comparative study of marine, transitional, and terrestrial shales in China," *Journal of Natural Gas Science and Engineering*, vol. 36, pp. 358–368, 2016.

[4] C. L. Cipolla, E. P. Lolon, and B. Dzubin, "Evaluating stimulation effectiveness in unconventional gas reservoirs," in *In: paper SPE 124843 presented at SPE annual technical conference and meeting*, pp. 4–7, New Orleans, Louisiana, USA, 2009.

[5] Y. S. Zou, S. C. Zhang, T. Zhou, Y. S. Xiao, and J. Gao, "Experimental investigation into hydraulic fracture network propagation in gas shales using CT scanning technology," *Rock Mechanics and Rock Engineering*, vol. 49, pp. 33–45, 2016.

[6] L. J. L. Beugelsdijk, C. J. de Pater, and K. Sato, "Experimental hydraulic fracture propagation in a multi-fractured medium," in *In: SPE 59419 presented at the Asia Pacific conference on integrated modeling for asset management*, pp. 25-26, Yokohama, Japan, 2000.

[7] T. L. Blanton, "Propagation of hydraulically and dynamically induced fractures in naturally fractured reservoirs," in *Paper SPE 15261 Presented at Unconventional Gas Technology Symposium*, Louisville, Kentucky, 1986.

[8] R. Rickman, M. Mullen, E. Petre, B. Grieser, and D. Kundert, "A practical use of shale petrophysics for stimulation design optimization: all shale plays are not clones of the Barnett shale," in *In: paper SPE 115258 presented at SPE annual technical conference and exhibition*, pp. 21–24, Denver, Colorado, USA, 2008.

[9] J. E. Olson, B. Bahorich, and J. Holder, "Examining hydraulic fracture—natural fracture interaction in hydrostone block experiments," in *In: paper SPE 152618 presented at the SPE hydraulic fracturing technology conference*, pp. 6–8, woodlands, Texas, 2012.

[10] N. R. Warpinski and L. W. Teufel, "Influence of geologic discontinuities on hydraulic fracture propagation (includes associated papers 17011 and 17074)," *Journal of Petroleum Technology*, vol. 39, no. 2, pp. 209–220, 1987.

[11] N. K. Fisher, B. M. Davidson, E. O. Goodwin, W. S. Buckler, and N. P. Steinberger, "Integrating fracture mappig technologies to optimize stimulations in the Barnett Shale," in *In: paper SPE 77441 presented at the SPE annual technical conference and exhibition*, San Antonio, Texas, 2002.

[12] T. N. Olsen, T. R. Bratton, and M. J. Thiercelin, "Quantifying proppant transport for complex fractures in unconventional formations," in *In: paper SPE 119300 presented at the SPE hydraulic fracturing technology conference*, pp. 19–21, woodlands, Texas, 2009.

[13] B. Hou, M. Chen, Z. M. Li, Y. H. Wang, and C. Diao, "Propagation area evaluation of hydraulic fracture networks in shale gas reservoirs," *Petroleum Exploration and Development*, vol. 41, no. 6, pp. 833–838, 2014.

[14] P. Tan, Y. Jin, K. Han et al., "Analysis of hydraulic fracture initiation and vertical propagation behavior in laminated shale formation," *Fuel*, vol. 206, pp. 482–493, 2017.

[15] M. M. Labani and R. Rezaee, "The importance of geochemical parameters and shale composition on rock mechanical properties of gas shale reservoirs: a case study from the Kockatea shale and Carynginia formation from the Perth Basin, Western Australia," *Rock Mechanics and Rock Engineering*, vol. 48, pp. 1249–1257, 2015.

[16] H. Sone and M. D. Zoback, "Mechanical properties of shale-gas reservoir rocks—part 2: ductile creep, brittle strength, and their relation to the elastic modulus," *Geophysics*, vol. 78, pp. D393–D402, 2013.

[17] G. Wang and T. R. Carr, "Methodology of organic-rich shale lithofacies identification and prediction: a case study from Marcellus Shale in the Appalachian basin," *Computational Geosciences*, vol. 49, pp. 151–163, 2012.

[18] S. Chen, Y. Zhu, H. Wang, H. Liu, W. Wei, and J. Fang, "Shale gas reservoir characterisation: a typical case in the southern Sichuan Basin of China," *Energy*, vol. 36, pp. 6609–6616, 2011.

[19] H. Daigle, N. W. Hayman, E. D. Kelly, K. L. Milliken, and H. Jiang, "Fracture capture of organic pores in shales," *Geophysical Research Letters*, vol. 44, pp. 2167–2176, 2017.

[20] F. Amann, E. A. Button, K. F. Evans, V. S. Gischig, and M. Blümel, "Experimental study of the brittle behavior of clay shale in rapid unconfined compression," *Rock Mechanics and Rock Engineering*, vol. 44, pp. 415–430, 2011.

[21] B. Yang, L. Xue, and K. Zhang, "X-ray micro-computed tomography study of the propagation of cracks in shale during uniaxial compression," *Environment and Earth Science*, vol. 77, p. 652, 2018.

[22] T. Guo, S. Zhang, Z. Qu, T. Zhou, Y. Xiao, and J. Gao, "Experimental study of hydraulic fracturing for shale by stimulated reservoir volume," *Fuel*, vol. 128, pp. 373–380, 2014.

[23] J. Zhou, M. Chen, Y. Jin, and Z. G-q, "Analysis of fracture propagation behavior and fracture geometry using a tri-axial fracturing system in naturally fractured reservoirs," *International Journal of Rock Mechanics and Mining Sciences*, vol. 45, pp. 1143–1152, 2008.

[24] J. Tang, J. Li, M. Tang et al., "Investigation of multiple hydraulic fractures evolution and well performance in lacustrine shale oil reservoirs considering stress heterogeneity," *Engineering Fracture Mechanics*, vol. 218, p. 106569, 2019.

[25] J. Zhao and D. Zhang, "Dynamic microscale crack propagation in shale," *Engineering Fracture Mechanics*, vol. 228, 2020.

[26] M. Eliyahu, S. Emmanuel, R. J. Day-Stirrat, and C. I. Macaulay, "Mechanical properties of organic matter in shales mapped at the nanometer scale," *Marine and Petroleum Geology*, vol. 59, pp. 294–304, 2015.

[27] T. M. Wilkinson, S. Zargari, M. Prasad, and C. E. Packard, "Optimizing nano-dynamic mechanical analysis for high-resolution, elastic modulus mapping in organic-rich shales," *Journal of Materials Science*, vol. 50, pp. 1041–1049, 2015.

[28] J. Zhao, D. Zhang, T. Wu et al., "Multiscale approach for mechanical characterization of organic-rich shale and its application," *International Journal of Geomechanics*, vol. 19, article 04018180, 2018.

[29] K. C. Bennett, L. A. Berla, W. D. Nix, and R. I. Borja, "Instrumented nanoindentation and 3D mechanistic modeling of a shale at multiple scales," *Acta Geotechnica*, vol. 10, pp. 1–14, 2015.

[30] X. W. Gu, M. Jafary-Zadeh, D. Z. Chen et al., "Mechanisms of failure in nanoscale metallic glass," *Nano Letters*, vol. 14, pp. 5858–5864, 2014.

[31] W. Cao, C. Marvel, D. Yin et al., "Correlations between microstructure, fracture morphology, and fracture toughness of nanocrystalline Ni–W alloys," *Scripta Mater*, vol. 113, pp. 84–88, 2016.

[32] G. Sernicola, T. Giovannini, P. Patel et al., "In situ stable crack growth at the micron scale," *Nature Communications*, vol. 8, p. 108, 2017.

[33] B. N. Jaya and V. Jayaram, "Fracture testing at small-length scales: from plasticity in Si to brittleness in Pt," *JOM*, vol. 68, pp. 94–108, 2016.

[34] Y. Deng, B. R. S. Rogne, and A. Barnoush, "In-situ microscale examination of hydrogen effect on fracture toughness: a case study on B2 and D03 ordered iron aluminides intermetallic alloys," *Engineering Fracture Mechanics*, vol. 217, p. 106551, 2019.

[35] M. Goodarzi, M. Rouainia, A. Aplin, P. Cubillas, and M. de Block, "Predicting the elastic response of organic-rich shale

using nanoscale measurements and homogenization methods," *Geophysical Prospecting*, vol. 65, pp. 1597–1614, 2017.

[36] F.-J. Ulm and Y. Abousleiman, "The nanogranular nature of shale," *Acta Geotechnica*, vol. 1, pp. 77–88, 2006.

[37] J. C. Zeszotarski, R. R. Chromik, R. P. Vinci, M. C. Messmer, R. Michels, and J. W. Larsen, "Imaging and mechanical property measurements of kerogen via nanoindentation," *Geochimica et Cosmochimica Acta*, vol. 68, pp. 4113–4119, 2004.

[38] H. Ouchi, S. Agrawal, J. T. Foster, and M. M. Sharma, "Effect of small scale heterogeneity on the growth of hydraulic fractures," in *SPE Hydraulic Fracturing Technology Conference and Exhibition*, The Woodlands, TX, USA, 2017.

[39] T. Peng, J. Yan, H. Bing et al., "Laboratory investigation of shale rock to identify fracture propagation in vertical direction to bedding," *Journal of Geophysics and Engineering*, vol. 15, p. 696, 2018.

[40] J. Zhou, H. Huang, and M. Deo, "Numerical study of critical role of rock heterogeneity in hydraulic fracture propagation," in *50th US Rock Mechanics/Geomechanics Symposium*, Houston, TX, USA, 2016.

[41] K. L. Hull, Y. N. Abousleiman, Y. Han et al., "Nanomechanical characterization of the tensile modulus of rupture for kerogen-rich shale," *SPE Journal*, vol. 22, pp. 1024–1033, 2017.

[42] A. L. Down and G. W. Himus, "A preliminary study of the chemical constitution of kerogen," *Journal of the Institute of Petroleum*, vol. 27, pp. 426–445, 1941.

[43] J. P. Forsman and J. M. Hunt, "Insoluble organic matter (kerogen) in sedimentary rocks," *Geochimica et Cosmochimica Acta*, vol. 15, no. 3, pp. 170–182, 1958.

[44] D. W. van Krevelen, *Coal: typology–chemistry–physics–constitution, first*, Elsevier, The Netherlands, 1961.

[45] B. Durand and J. Espitalie, "Evolution de la matie're organique au cours de l'enfouissement des se'diments," *Compte rendus de l'Acade'mie des Sciences (Paris)*, vol. 276, pp. 2253–2256, 1973.

[46] B. Tissot, B. Durand, J. Espitalie, and A. Combaz, "Influence of nature and diagenesis of organic matter in formation of petroleum," *American Association of Petroleum Geologists Bulletin*, vol. 58, pp. 499–506, 1974.

[47] B. Durand, G. Nicaise, J. Roucache, M. Vandenbroucke, and H. W. Hagemann, *1977b. Etude ge'ochimique d'une se'rie de charbons*, R. Campos and I. J. Gon, Eds., Advances in Organic Geochemistry, ENADIMSA, Madrid, 1975.

[48] B. Tissot and M. Vandenbroucke, "Geochemistry and pyrolysis of oil shales," in *Geochemistry and Chemistry of Oil Shales, ACS Symposium Series*, F. P. Miknis and J. F. McKay, Eds., vol. 230, pp. 1–11, American Chemical Society, Washington D. C, 1983.

[49] P. Albrecht, M. Vandenbroucke, and M. Mandengue, "Geochemical studies on the organic matter from the Douala Basin (Cameroon)–I. Evolution of the extractable organic matter and the formation of petroleum," *Evolution of the extractable organic matter and the formation of petroleum. Geochimica et Cosmochimica Acta*, vol. 40, no. 7, pp. 791–799, 1976.

[50] J. P. Forsman, "Geochemistry of kerogen," in *Organic Geochemistry, Earth Series Monograph*, I. A. Breger, Ed., vol. 16, pp. 148–182, Pergamon Press, Oxford, 1963.

[51] A. L. Burlingame, P. A. Haug, H. K. Schnoes, and B. R. Simoneit, "Fatty acids derived from the Green River formation oil shale by extractions and oxidations – a review," in *Advances in Organic Geochemistry 1968*, P. A. Schenck and I. Havenaar, Eds., pp. 85–129, Pergamon Press, Oxford, 1969.

[52] M. Djuricic, R. C. Murphy, D. Vitorovic, and K. Biemann, "Organic acids obtained by alkaline permanganate oxidation of kerogen from the Green River (Colorado) shale," *Geochimica et Cosmochimica Acta*, vol. 35, no. 12, pp. 1201–1207, 1971.

[53] T. F. Yen, "Structural aspects of organic components in oil shales," in *Oil Shale, Developments in Petroleum Science*, T. F. Yen and G. V. Chilingarian, Eds., vol. 5, pp. 129–148, Elsevier, Amsterdam, 1976.

[54] B. Tissot, G. Deroo, and A. Hood, "Geochemical study of the Uinta Basin: formation of petroleum from the Green River formation," *Geochimica et Cosmochimica Acta*, vol. 42, no. 10, pp. 1469–1485, 1978.

[55] M. Vandenbroucke and C. Largeau, "Kerogen origin, evolution and structure," *Organic Geochemistry*, vol. 38, no. 5, pp. 719–833, 2007.

[56] M. Vandenbroucke, "Structure of kerogens as seen by investigations on soluble extracts," in *Kerogen*, B. Durand, Ed., pp. 415–443, Insoluble Organic Matter from Sedimentary Rocks. Editions Technip, Paris, 1980.

[57] F. Behar and M. Vandenbroucke, "Chemical modelling of kerogens," *Organic Geochemistry*, vol. 11, no. 1, pp. 15–24, 1987.

[58] P. Ungerer, D. Rigby, B. Leblanc, and M. Yiannourakou, "Sensitivity of the aggregation behaviour of asphaltenes to molecular weight and structure using molecular dynamics," *Molecular Simulation*, vol. 40, no. 1–3, pp. 115–122, 2014.

[59] P. Ungerer, J. Collell, and M. Yiannourakou, "Molecular modeling of the volumetric and thermodynamic properties of kerogen: influence of organic type and maturity," *Energy & Fuels*, vol. 29, pp. 91–105, 2014.

[60] D. N. Theodorou and U. W. Suter, "Atomistic modeling of mechanical properties of polymeric glasses," *Macromolecules*, vol. 19, no. 1, pp. 139–154, 1986.

[61] C. Fan and S. Hsu, "Application of the molecular simulation technique to characterize the structure and properties of an aromatic polysulfone system. 2. Mechanical and thermal properties," *Macromolecules*, vol. 25, 1992.

[62] M. Hutnik, A. S. Argon, and U. W. Suter, "Simulation of elastic and plastic response in the glassy polycarbonate of 4, 4'-isopropylidenediphenol," *Macromolecules*, vol. 26, no. 5, pp. 1097–1108, 1993.

[63] C. Fan, T. Cagin, Z. Chen, and K. Smith, "Molecular Modeling of Polycarbonate. 1. Force Field, Static Structure, and Mechanical Properties," *Macromolecules*, vol. 27, 1994.

[64] T. Raaska, S. Niemela, and F. Sundholm, "Atom-based modeling of elastic constants in amorphous polystyrene," *Macromolecules*, vol. 27, no. 20, pp. 5751–5757, 1994.

[65] C. Bousige, C. M. Ghimbeu, C. Vix-Guterl et al., "Realistic molecular model of kerogen's nanostructure," *Nature Materials*, vol. 15, no. 5, pp. 576–582, 2016.

[66] L. Brochard, G. Hantal, H. Laubie, F. J. Ulm, and R. J. Pellenq, "Capturing material toughness by molecular simulation: accounting for large yielding effects and limits," *International Journal of Fracture*, vol. 194, no. 2, pp. 149–167, 2015.

[67] G. Hantal, L. Brochard, R. J. M. Pellenq, F. J. Ulm, and B. Coasne, "Role of interfaces in elasticity and failure of clay–organic nanocomposites: toughening upon Interface weakening?," *Langmuir*, vol. 33, no. 42, pp. 11457–11466, 2017.

[68] L. Huang, Z. Ning, Q. Wang et al., "Kerogen deformation upon CO2/CH4 competitive sorption: implications for CO_2 sequestration and enhanced CH_4 recovery," *Journal of Petroleum Science and Engineering*, vol. 183, p. 106460, 2019.

[69] T. Wu and A. Firoozabadi, "Mechanical properties and failure envelope of kerogen matrix by molecular dynamics simulations," *The Journal of Physical Chemistry C*, vol. 124, no. 4, pp. 2289–2294, 2020.

[70] T. Wu and A. Firoozabadi, "Fracture toughness and surface energy density of kerogen by molecular dynamics simulations in tensile failure," *The Journal of Physical Chemistry C*, vol. 124, no. 29, pp. 15895–15901, 2020.

[71] H. Sun, "COMPASS: An ab initio force-field optimized for cndensed-phase applicationsoverview with details on alkane and benzene compounds," *The Journal of Physical Chemistry. B*, vol. 102, no. 38, pp. 7338–7364, 1998.

[72] H. Sun, S. J. Mumby, J. R. Maple, and A. T. Hagler, "An ab initio CFF93 all-atom force field for polycarbonates," *Journal of the American Chemical Society*, vol. 116, no. 7, pp. 2978–2987, 1994.

[73] C. B. Barber, D. P. Dobkin, and H. Huhdanpaa, "The Quickhull Algorithm for Convex Hulls," *ACM Transactions on Mathematical Software*, vol. 22, no. 4, pp. 469–483, 1996.

[74] U. Suter and B. Eichinger, "Estimating elastic constants by averaging over simulated structures," *Polymer*, vol. 43, 2002.

[75] L. J. Walpole, "On bounds for the overall elastic moduli of inhomogeneous systems I," *Journal of the Mechanics and Physics of Solids*, vol. 14, pp. 151–162, 1966.

[76] L. J. Walpole, "On bounds for the overall elastic moduli of inhomogeneous system II," *Journal of the Mechanics and Physics of Solids*, vol. 14, pp. 289–301, 1966.

[77] Y. Page and P. Saxe, "Symmetry-general least-squares extraction of elastic coefficients from ab initio total energy calculations," *Physical Review B*, vol. 63, 2001.

[78] Y. Page and P. Saxe, "Symmetry-general least-squares extraction of elastic data for strained materials from ab initio calculations of stress," *Physical Review B*, vol. 65, 2002.

[79] S. Alafnan, T. Solling, and M. Mahmoud, "Effect of kerogen thermal maturity on methane adsorption capacity: a molecular modeling approach," *Molecules*, vol. 25, no. 16, 2020.

[80] S. Alafnan, A. S. Sultan, and J. Aljaberi, "Molecular fractionation in the organic materials of source rocks," *ACS Omega*, vol. 5, no. 30, pp. 18968–18974, 2020.

[81] S. Alafnan, F. Yusuf, O. Mansour, K. Alsamadony, A. Awotunde, and M. Aljawad, "Enhanced recovery from organic-rich shales through carbon dioxide injection: molecular-level investigation," *Energy & Fuels*, vol. 34, 2020.

[82] S. Alafnan, "Petrophysics of kerogens based on realistic structures," *ACS Omega*, vol. 6, no. 14, pp. 9549–9558, 2021.

[83] J. Aljaberi, S. Alafnan, G. Glatz, A. S. Sultan, and C. Afagwu, "The impact of kerogen tortuosity on shale permeability," *SPE Journal*, vol. 26, 2020.

[84] C. Afagwu, S. Al-Afnan, S. Patil, J. Aljaberi, M. A. Mahmoud, and J. Li, "The impact of pore structure and adsorption behavior on kerogen tortuosity," *Fuel*, vol. 303, p. 121261, 2021.

[85] V. Kumar, C. H. Sondergeld, and C. S. Rai, "Nano to macro mechanical characterization of shale," *Proc. - SPE Annu. Tech. Conf. Exhib.*, vol. 4, pp. 3421–3443, 2012.

[86] R. Ahmadov, T. Vanorio, and G. Mavko, "Confocal laser scanning and atomic-force microscopy in estimation of elastic properties of the organic-rich Bazhenov formation," *The Leading Edge*, vol. 28, pp. 18–23, 2009.